Maik Kaiser

High Energy X-Ray Diffraction On Ultrasound Excited Crystals

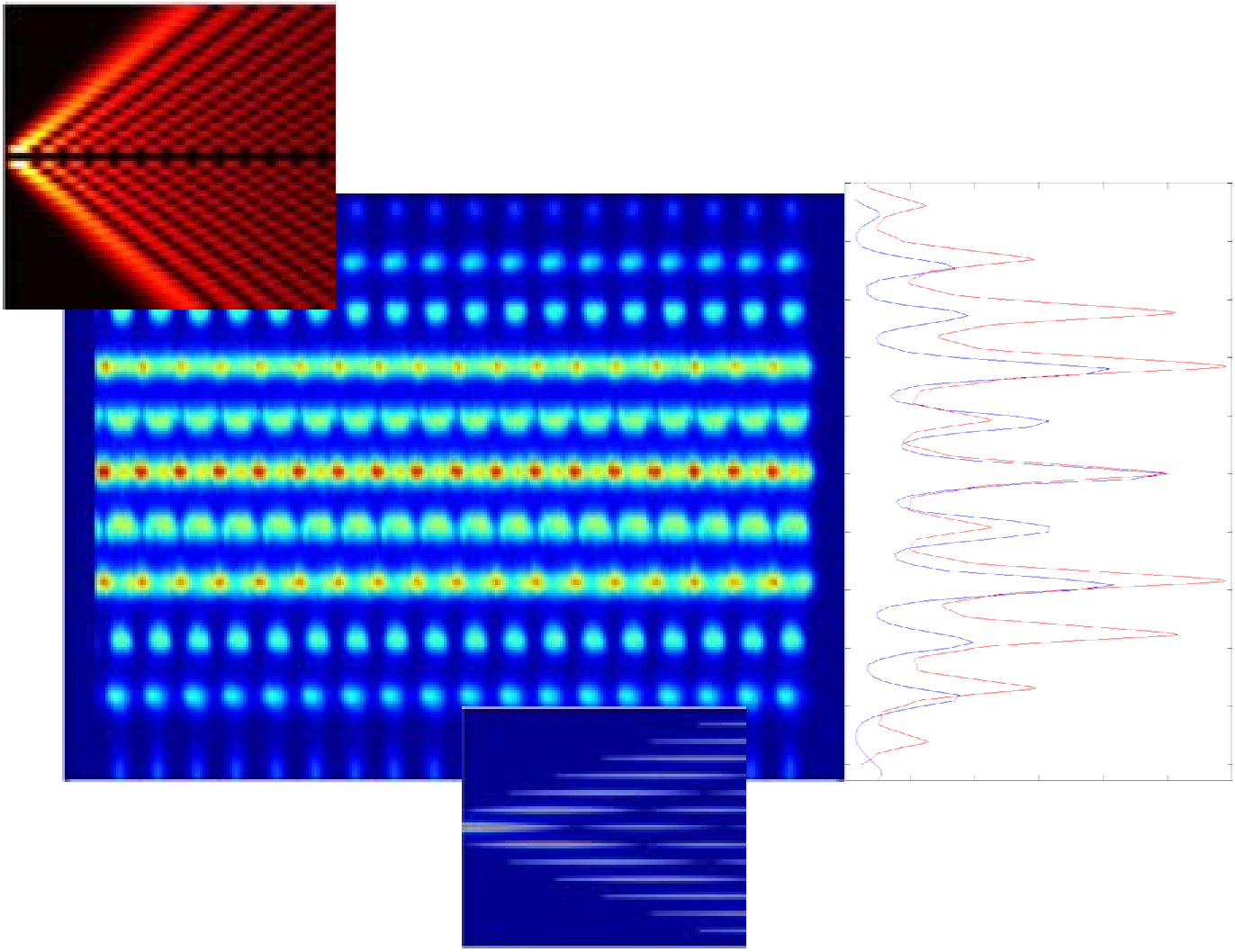

Cuvillier Verlag Göttingen

High energy x-ray diffraction on ultrasound excited crystals

Den Naturwissenschaftlichen Fakultäten
der Friedrich-Alexander-Universität Erlangen-Nürnberg
zur
Erlangung des Doktorgrades

vorgelegt von

Maik Kaiser

aus Mainz

Bibliografische Information Der Deutschen Bibliothek
Die Deutsche Bibliothek verzeichnet diese Publikation in der Deutschen Nationalbibliografie; detaillierte bibliografische Daten sind im Internet über http://dnb.ddb.de abrufbar.
1. Aufl. - Göttingen : Cuvillier, 2005
Zugl.: Erlangen-Nürnberg, Univ., Diss., 2004
ISBN 3-86537-394-1

Als Dissertation genehmigt von den Naturwissenschaftlichen

Fakultäten der Universität Erlangen-Nürnberg

Tag der mündlichen Prüfung: 23.03.2004

Vorsitzender der
Promotionskommission: Prof. Dr. L. Dahlenburg

Erstberichterstatter: Prof. Dr. R. Hock

Zweitberichterstatter: Prof. Dr. H. Fuess

© CUVILLIER VERLAG, Göttingen 2005
Nonnenstieg 8, 37075 Göttingen
Telefon: 0551-54724-0
Telefax: 0551-54724-21
www.cuvillier.de

Alle Rechte vorbehalten. Ohne ausdrückliche Genehmigung des Verlages ist es nicht gestattet, das Buch oder Teile daraus auf fotomechanischem Weg (Fotokopie, Mikrokopie) zu vervielfältigen.
1. Auflage, 2005
Gedruckt auf säurefreiem Papier

ISBN 3-86537-394-1

Zusammenfassung

Die vorliegende Arbeit behandelt zeitintegrierte und zeitaufgelöste Hochenergie-Röntgenbeugung an ultraschallangeregten Silizium Kristallen. Mit hochenergetischer Synchrotronstrahlung einer Energie über 80 keV und einem hochauflösenden Dreiachsendiffraktometer mit einer maximalen Winkelauflösung von 0.01 Bogensekunden wurden in Laue-Streugeometrie erstmals ultraschallinduzierte Satellitenreflektionen aus dem Volumen des Kristalls nachgewiesen. Es konnte gezeigt werden, welche Propagationsrichtung die durch einen Schallwandler angeregten Wellen im Hochfrequenzbereich annehmen. Der Hochfrequenzbereich definiert sich dabei über das Verhältnis der Extinktionslänge eines gemessenen Röntgenreflexes zur Wellenlänge des Ultraschalls, die für die durchgeführten Experimente typischerweise zwischen 10 μm und 150 μm liegt. Statt einer longitudinalen Schallmode in [111]-Richtung des Silizium-Kristalls wird eine transversale Welle in [012]-Richtung angeregt. Zur Aufklärung dieses Sachverhaltes trugen hochaufgelöste zweidimensionale Scans der Beugungsebene bei, mit Hilfe derer sich die Projektion eines aus der Beugungsebene zeigenden Ultraschallausbreitungsvektors messen lassen. Zusammen mit der Ausbreitungsgeschwindigkeit der angeregten Wellenmode von 5823 m/s sind die Winkelpositionen der gemessenen Satellitenreflektionen bestätigt worden.

Um die gemessenen zeitunabhängigen und zeitabhängigen Intensitätsprofile der Haupt- und Satellitenreflektionen zu rekonstruieren, wurde ein Simulationsprogramm entwickelt. Dieses Programm erlaubt, zeitintegrierte und zeitaufgelöste Rockingkurven verschiedener Kristallreflektionen als Funktion der Energie der gebeugten Strahlung, der Ultraschallfrequenz und der Ultraschallamplitude zu berechnen.

Die Simulationsrechnungen basieren auf einer für schallangeregte Kristallgitter modifizierten dynamischen Beugungstheorie, die sowohl Haupt- als auch Satellitenreflektionen im Grenzfall dicker Kristalle behandelt. Dicke Kristalle zeichnen sich dadurch aus, dass die von der Röntgenenergie abhängige Extinktionslänge einer Reflektion wesentlich kleiner ist als die tatsächliche Dicke des Kristalls. Da unter den hier gewählten experimentellen Randbedingungen von Röntgenenergien zwischen 80

keV und 250 keV und Kristalldicken von 5 mm das Kriterium des dicken Kristalls stets erfüllt ist, schliesst sich eine Behandlung im Rahmen der kinematischen Theorie aus.
Die Simulationsrechnungen zeigen unter anderem folgende generellen Aspekte der Beugung von hochenergetischer Röntgenstrahlung an ultraschallangeregten Kristallen:

1. Die Halbwertsbreiten der Satellitenreflektionen sind deutlich kleiner als die Halbwertsbreite der Auflösungsfunktion des Diffraktometers von 0.065 Bogensekunden bei 200 keV.
2. Die Satellitenreflektionen besitzen wie die Hauptreflektionen alle die gleiche Reflektivität von 0.5.

Im Gegensatz zur Simulation unterscheiden sich im Experiment die Satellitenintensitäten in der Höhe deutlich von denen der Mutterreflektionen und auch untereinander. Die Faltung der Auflösungsfunktion des Diffraktometers mit der gerechneten Intensitätsverteilung am Beispiel der (-571)-Reflektion bei einer Anregungsfrequenz des Ultraschall von 96 MHz ergibt eine deutliche Annäherung an die gemessene Intensitätsverteilung.
Messungen der Rockingkurven bei unterschiedlichen Röntgenenergien im Bereich von 199keV bis 225 keV klären qualitativ die Ursache der noch verbleibenden Intensitätsunterschiede zwischen Simulation und Messung. Die Satellitenreflektionen ändern in diesem Energiebereich ihre Peakintensität periodisch, was nur mit einem volldynamischen Beugungsverhalten der Satellitenreflektionen zu erklären ist. Dies bedeutet, dass die Extinktionslängen der Satellitenreflektionen deutlich grösser als die der Mutterreflektionen sind und sich im Bereich der doppelten Kristalldicke bewegen. Die Durchstimmung der Röntgenenergie bewirkt dabei eine Vergrösserung der Extinktionslängen der Satelliten über den Wert der doppelten Kristalldicke hinaus und damit ein periodisches Verhalten der Peakintensitäten der Satelliten.
Aus derjenigen Röntgenenergie, bei der die Satellitenreflektion erster Ordnung die gleiche Intensität wie die Hauptreflektion annimmt, lässt sich über das Verhältnis von Extinktionslänge und Kristalldicke die Lösungsmenge der möglichen tatsächlich im Kristall angeregten Schallamplitude bestimmen. Messungen von Rockingkurven bei verschiedenen Ultraschallamplituden bestätigen das dynamische Beugungsverhalten der Satellitenreflektionen.

Schliesslich war es möglich, die Intensität der Satellitenreflektionen als Funktion der Zeit mit einer Auflösung von 200 ps zu beobachten. Die mit der Schallfrequenz periodisch über die doppelte Kristalldicke getriebenen Extinktionslängen führen zu einem zweimaligen Aufblitzen der Maximalintensität der Satelliten innerhalb einer Schwingungsperiode von 5.2 ns.

Contents

1. Introduction **1**

2. Basic dynamical diffraction theory **5**

2.1. Equations of the kinematical diffraction theory 5

2.2. Fundamental equation of the dynamical diffraction theory 7

2.3. The dispersion surface 8

2.4. Atomic scattering factor, structure factor and the dielectric susceptibility 11

2.5. Extinction length and Pendellösung 13

2.6. Intensity distributions of diffracted x-rays 18

2.7. Absorption and the Borrmann effect 21

3. Current research state: X-ray diffraction on ultrasound excited crystals **23**

3.1. X-ray diffraction on volume acoustic waves 25

3.1.1. Acousto-electric phonons 25

3.1.2. X-ray diffraction under the condition of x-ray acoustic resonance 30

3.1.3. High frequency volume acoustic waves 34

3.1.4. Low frequency volume acoustic waves 39

3.2. X-ray diffraction on surface acoustic waves 43

3.3. Applications 46

4. Theory and simulations: X-ray diffraction on ultrasound excited crystals **49**

4.1. Theoretical background 49

4.1.1. Limit of small ultrasound amplitudes 51

4.1.2. Large ultrasound amplitudes 55

4.1.3. Angular positions of ultrasound excited satellite reflections 57

4.1.4. The FWHM of ultrasound excited satellite reflections 59

4.2. The computer code SIMSAT 60

4.3. Simulation results 63

4.3.1. Limit of small ultrasound amplitudes 63

4.3.2. Large ultrasound amplitudes 79

4.3.3. Angular positions of ultrasound excited satellite reflections 85

4.3.4. The FWHM of ultrasound excited satellite reflections 86

5. Experimental part **89**
5.1. The high-energy beamline ID 15 89
5.2. Peculiarities of high-energy x-ray diffraction 93
5.3. The high-resolution triple-axis diffractometer 98
5.4. Scanning procedures / the non-dispersive set-up 99
5.5. High angular resolution 102
5.6. The instrument resolution function 104
5.7. The sample: ultrasound in crystals 105
5.8. Time-resolution in x-ray diffraction: The timing electronics 112

6. Results and discussion: Comparison of experimental data and simulations 117
6.1. Ultrasound propagation direction and angular satellite positions 117
6.2. Comparison of measured intensity distribution and simulation 124
6.3. Analysis of x-ray energy scans 130
6.3.1. Extinction length of the first diffraction satellite and determination of the ultrasound amplitude 136
6.3.2. Determination of the superlattice's structure factor 141
6.3.3. Higher order satellites 141
6.4. Ultrasound amplitude scans 143
6.5. Time resolved evolution of the ultrasound excited satellite system 145

7. Conclusions and outlook **149**

Appendix **153**
A.1. Deviation parameter dT and thickness parameter A 153
A.2. List of ultrasound directions projected onto the scattering plane 155

List of symbols and acronyms **159**

Bibliography **163**

Acknowledgments **181**

Chapter 1

Introduction

This thesis deals with time integrated and time resolved high energy x-ray diffraction on ultrasound excited crystals. Time resolved investigation of condensed matter gives the opportunity to understand the dynamics in solids and fluids. In particular, time resolved x-ray diffraction enables one to observe time dependent structural changes on the atomic scale. With modern third generation synchrotron sources like the European Synchrotron Radiation Facility (ESRF) short-pulsed x-radiation sources with a pulse duration of 100 ps are available. In principle all time dependent phenomena in condensed matter can be investigated which show a time dependence on the picosecond or slower time scales. Thereby periodically repetitive events can be the subject of matter as well as single but reversible perturbations. Non-reversible sample changes are more difficult to investigate since the single shot intensity of an x-ray pulse may not be sufficient. Sacrificing time resolution in taking longer x-ray pulses make non-reversible changes still possible to investigate. In the present work the time evolution of rocking curve intensity profiles of ultrasound excited silicon single crystals was investigated by stroboscopic x-ray diffraction, in which the generation of the ultrasonic waves is synchronized with x-ray pulses emitted from the storage ring.

Since the influence of acoustic excitation in crystals on the x-ray diffracted intensity was discovered for the first time [Fox 31], this field of research found a growing interest. The demand of the semiconductor industry in the 1960's to grow perfect crystals was accompanied by several experimental verifications of the dynamical diffraction theory, which was developed at the beginning of the 20^{th} century [Dar 14a, Dar 14b, Ewa 16a, Ewa 16b, Ewa 17, Lau 31]. Ultrasound excitation as a periodic and controllable perturbation triggered investigations of x-ray-acoustic interactions to study the dispersion surface and to experimentally confirm the diffraction theory of perturbed crystals. This lead only very recently to interesting applications: The optimization of x-ray flux and bandwidth via acoustic excitation in synchrotron x-ray monochromators is one example

[Pol 94, Rev 95, Pol 99a, Pol 99b], the acoustic control of x-ray beams in space and time another one [Ros 92, Pol 98]. The high sensitivity of acoustically induced diffraction effects to small intrinsic strains lead to propositions of methods to characterize the structural quality of semiconductors [Zol 93]. The dynamical focusing of x-rays through crystals subjected to ultrasound was investigated in [Nos 94a, Nos 94b]. Furthermore ultrasound excited crystals were proposed as x-ray beam choppers [Tuc 98] and fast x-ray switches with switching times between 50 and 100 ps [Iol 95b]. The study of diffraction phenomena in complex dynamic deformation fields is therefore a challenging task. Through all the years difficulties related to the interpretation of experimental data accompanied the research field due to the complexity of dynamical diffraction phenomena, not at least because the effects had to be manifested experimentally by measuring the integrated intensity due to missing angular resolution capabilities (comments in [LeR 75], [Zol 95a]). The goal of the present work is to resolve acoustically induced satellite reflections in space and time and to measure and explain their dependence on the ultrasound parameters frequency and amplitude and the x-ray parameters energy and choice of reflection. The interpretation of measured data is thereby based on simulations of the interaction of dynamical x-ray diffraction with a periodic and dynamic (i.e. time dependent) elastic perturbation in the crystal. This work will contribute to further understand the effects of vibrating disturbances to the diffraction process.

Chapter two reviews the mathematical and physical concepts of kinematical and dynamical diffraction theory. The geometrical concept of the dispersion surface as well as expressions like the atomic susceptibility, the extinction length and the pendulum solution are introduced. Rocking curve intensity distributions of diffracted x-rays in the framework of dynamical theory of perfect crystals are presented along with a discussion of the absorption aspect and the Borrmann anomalous transmission through thick perfect crystals. The definitions of thick and thin crystals are given together with the range of application of these approximations and the connection to the kinematical diffraction theory will be shown.

In chapter three the previous work in the field of x-ray diffraction on ultrasound excited crystals will be reviewed as required for understanding the present work. Due to the large

amount of available publications it was necessary to clearly distinguish between investigations on volume acoustic waves, surface acoustic waves, diffraction topography studies and optically excited phonons. The discussion is thereby focused on the investigation of x-ray diffraction on volume acoustic waves, even though hints for the explanation of a part of newly discovered effects could be found in the literature of the entire field. A further separation in the subfield of x-ray diffraction on volume acoustic waves with respect to the ultrasound frequency was undertaken. In fact, it has to be distinguished between low frequency ultrasound (LFVAW), where the acoustic wavelength is larger than the extinction length of the x-rays, the x-ray acoustic resonance (XAR), where it has the same value (taking into account the geometry), and high frequency ultrasound (HFVAW), with an acoustic wavelength being much smaller than the value of the extinction length. The appearance of satellite reflections in the diffraction pattern due to ultrasound excited superstructures is closely connected to the frequency range above the x-ray acoustic resonance condition. During the course of this thesis ultrasound excited satellite reflections of volume acoustic waves have been resolved for the first time.

Chapter four treats simulations of x-ray diffraction on ultrasound excited silicon crystals with the main emphasis on the high ultrasound frequency regime. After the presentation of the computer code SIMSAT, which was developed in this work to calculate rocking curve intensity distributions of x-rays diffracted by ultrasound excited crystals, simulations for different reflections, x-ray energies, ultrasound frequencies and amplitudes are discussed. Due to differences in the theoretical approach it is of great importance to distinguish between the small and the large ultrasound amplitude regime. The distinction is based on the relation of the applied ultrasound amplitude with respect to the absolute value of the diffraction vector, i.e., the lattice spacing. If the ratio of the ultrasound amplitude and the lattice spacing is smaller than one, the amplitudes are considered as small. If the ratio is exceeding unity, one is talking about large amplitudes.

In order to evaluate the chances to resolve diffraction satellites with the given mechanical resolution of the diffractometer of 0.01 arcsec, the full width at half maximum (FWHM) of satellite reflections as well as the angular separation between main reflections and satellite reflections are calculated. Theoretical approaches dealing with the time resolved

evolution of the intensity distribution of satellite reflections are rarely investigated [Pol 98]. To our knowledge no treatment is available for large ultrasound amplitudes.

Chapter five describes the experimental conditions for the investigation of ultrasound excited crystals with high energy x-ray diffraction. It starts with a brief presentation of the high energy beamline ID 15 of the European Synchrotron Radiation Facility (ESRF), where the experiments were carried out within the framework of an ongoing collaboration with the Institut für Kristallographie und Strukturphysik of the Friedrich-Alexander Universität Erlangen-Nürnberg. The advantages of high energy x-ray diffraction with respect to penetration depth and high angular resolution are explained along with a description of the high resolution triple axis diffractometer. The scanning procedures as well as the instrumental resolution function are shown. The mechanisms to excite ultrasonic waves in the silicon samples, a more general description of the propagation of elastic waves in crystals and the scattering geometry are described. Finally, the time-resolving electronics to obtain x-ray diffraction measurements with 200 ps resolution is presented.

In chapter six the experimental results are analyzed and the comparison to simulated data is discussed. Apart from the measurement of angular and time resolved diffraction patterns of ultrasound excited satellite reflections it was possible to measure and understand rocking curves at different x-ray energies and ultrasound amplitudes. The oscillation of satellite intensities as a function of the x-ray energy is explained by a dynamical diffraction behavior of the satellite reflections. The extinction lengths of the satellite reflections are discussed together with the determination of the absolute value of the superlattice structure factor. Reciprocal space maps were most helpful to determine the unexpected propagation direction of the sound waves.

Chapter seven concludes this thesis, summarizes the obtained results and will give an outlook to possible future research directions.

Chapter 2

Basic Dynamical Diffraction Theory

2.1. Equations of the kinematical diffraction theory

After the discovery of x-rays by W.C. Röntgen in 1895 and the proposition of Laue in 1912 that crystals could serve as natural diffraction gratings for x-rays, both the electromagnetic wave nature of x-rays and the periodic structure of crystals were proofed. A main contribution to the rapid development of the field of x-ray diffraction on crystals represents the improvement of the experimental technique due to W.H. and W.L. Bragg. Since the wavelength λ of x-radiation is of the same order of magnitude or smaller than the interatomic distances of the smallest lattice periods in crystals ($\approx 10^{-10}$ m), interference maxima of the diffracted waves can be measured at conveniently large scattering angles. If $\mathbf{k_i}$ and $\mathbf{k_f}$ are the incident and diffracted (final) wave vectors, the Laue vector equation (2.1) describes the direction of the diffraction maxima, whereas the scattering vector **G** has to be a vector of the reciprocal lattice given in equation 2.2.

$$\vec{k}_f - \vec{k}_i = \vec{G} \tag{2.1}$$

$$\vec{G} = h\vec{b}_1 + k\vec{b}_2 + l\vec{b}_3 \tag{2.2}$$

The indices h,k,l are the Miller indices of a family of lattice planes and the **b**'s are the base vectors of the reciprocal lattice. The reciprocal lattice vector **G** stands perpendicular to the associated set of lattice planes with an absolute value reciprocal to the lattice spacing d_{hkl} (equation 2.3).

$$|\vec{G}| = \frac{1}{d_{hkl}} \tag{2.3}$$

The equation of the lattice spacing for a cubic crystal with the lattice parameter a_0 = 5.43 Å for silicon is given by equation 2.4 [War 69].

$$d_{hkl} = \frac{a_0}{\sqrt{h^2 + k^2 + l^2}} \tag{2.4}$$

For elastic scattering ($k_i = k_f = 1/\lambda$) at an angle θ between the incident wave vector and the set of lattice planes with spacing d_{hkl} the well-known Bragg equation follows from equation 2.1 and 2.3. The scattering angle is 2θ and θ is called the Bragg angle (equation 2.5). The x-ray wavelength is denoted by λ.

$$\lambda = 2d_{hkl}\sin\theta \tag{2.5}$$

A simple geometrical construction in the reciprocal lattice of diffraction vectors associated with a given incident direction and wavelength is most useful for the discussion of the various experimental methods to bring reciprocal lattice points on the so-called Ewald sphere of reflection and thus to observe diffraction maxima (figure 2.1). Therefor the incident beam ends at the origin of the reciprocal lattice. The sphere around the origin of the incident beam is the Ewald sphere. Constructive interference occurs if a reciprocal lattice point (hkl) lies on the Ewald sphere. Then the diffracted beam forms together with the incident beam and the reciprocal lattice vector **G** a closed triangle. The experimental methods to bring reciprocal lattice points on the Ewald sphere are described in several textbooks on solid state physics and x-ray diffraction (for example [Ash 76] and [War 69]). In this work the angle of incidence θ is varied by rotating the sample crystal in order to bring reciprocal lattice points onto the Ewald sphere.

The geometrical part of the diffraction problem concerns only the directions of the diffraction maxima. The detailed intensity distribution of scattered x-rays requires more theoretical investigations. The intensity distribution due to the kinematical theory is included in the dynamical diffraction theory in the limit of thin crystals. The basics of the dynamical diffraction theory are described in the following paragraphs.

2.2. Fundamental equation of the dynamical diffraction theory

A brief presentation of the dynamical theory of x-ray diffraction for perfect crystals is given now. The common approach in dynamical diffraction theory is to treat the propagation of the x-ray wave-field inside and outside the crystal by Maxwell's equations (i.e. classical electrodynamics) and the interaction of the field with the electrons of the crystal by quantum mechanics. This interaction comes into consideration in the description of the electric susceptibility χ [Pin 78]. Neglecting weak magnetic interactions and assuming the electrical conductivity to be zero, the wave equation 2.6 can be derived from Maxwell's equations [Bru 76].

$$\mathrm{curlcurl}\mathbf{E} = 4\pi k^2 (1+\chi)\mathbf{E} \tag{2.6}$$

Here the relation $k = 1/\lambda$ with the vacuum x-ray wavelength λ was used. The electric field waves **E** are assumed to be of the Bloch wave type,

$$\mathbf{E} = \sum_{hkl} \mathbf{E}_{hkl} \exp 2\pi i (\mathbf{k}_{hkl}\mathbf{r} - \nu t) \tag{2.7}$$

where ν is the x-ray frequency and **r** the propagation vector.
Since the crystal lattice is periodic, the electric susceptibility χ can be expanded as a Fourier series.

$$\chi = \sum_{hkl} \chi_{hkl} \exp(2\pi i \mathbf{G}_{hkl}\mathbf{r}) \tag{2.8}$$

Substitution of equation 2.7 and 2.8 in the wave equation 2.6 leads to the fundamental equation of the dynamical diffraction theory [Hae 01],

$$(k^2 - \mathbf{k}_m^2)\mathbf{E}_m + k^2 \sum_n \chi_{m-n}\mathbf{E}_n = 0 \tag{2.9}$$

2.3. The dispersion surface

The fundamental equation (2.9) has nontrivial solutions if the determinant is vanishing, which leads to the dispersion relation in the two-wave approximation (i.e. two reciprocal lattice points m = 0 and m = (hkl) lie close to the Ewald sphere),

$$\left(K^2 - k_0^2\right)\left(K^2 - k_{hkl}^2\right) = k^4 C^2 \chi_{hkl}^2 \chi_{\overline{hkl}}^2 \tag{2.10}$$

with the abbreviation $K^2 = k^2(1+\chi_0)$. The polarization factor C equals 1 for σ-polarization and cos2θ for π-polarization.

The concept of the dispersion surface based on this equation is very helpful for the comprehension of the diffraction process. The dispersion equation describes the relation between k_{hkl} and k. We draw spheres of radius k about the origin 0 and the reciprocal lattice point (hkl). Figure 2.1 shows a section through these spheres. The intersection of the spheres in the scattering plane is called the Laue point. Only close to this point the Laue equation (2.1) is satisfied and strong diffraction will occur. If no diffracted wave exists the wavevector in the crystal is multiplied by the refractive index of the material compared to the wavevector in vacuum. The radius of the sphere due to the refracted wave in the crystal is therefore $k(1+\chi_0)^2$. Since the dielectric susceptibility is small compared to unity (chapter 2.4) for x-ray wavelengths, the radius of the second pair of spheres is commonly approximated as $k(1+\chi_0/2)$.

The intersection of the refraction corrected spheres is called the Lorentz point. Close to the Lorentz point diffraction occurs and the relation between k_o and k_{hkl} is defined by equation 2.10. Hence the tails of incoming and diffracted wavevector can not lie on the spheres. If the spheres are approximated by planes (the radii of the spheres are very large compared to the intersection region), the section of the drawn dispersion surface is a hyperbola asymptotic to the circles away from the intersection region. This equals the linearization of equation 2.10 in order to transform it from a fourth order into a second order equation. The degeneracy of the intersection is lifted into two branches of the dispersion surface, the upper and lower branch indicated in figure 2.1. In general there are four branches in the approximation of two strong waves, two branches for each

polarization state. For a very small Bragg angle like it is the case for high energy x-rays, the branches for different polarization states are nearly on top of each other. The polarization factor in equation 2.10 can therefore be set to unity.

When an incoming plane wave hits the crystal surface, the tangential component of the wavevectors has to be conserved. The incident vacuum wave represented by a wavevector k_i close to the Laue point will create two wavefields represented by the intersection with both branches of the dispersion surface of the normal through the origin of k_i to the entrance surface. One incident plane wave thus gives rise to two waves with forward character from which two waves with diffracted character are generated in the crystal. Two wavefields are therefore propagating in the crystal, one for each branch of the dispersion surface. Each wavefield consists of two waves with wavevectors of forward and diffracted-wave character. The propagation directions of the two wavefields are different since they are propagating along the normal to the dispersion surface at the excitation points [Pin 78, Bat 64].

In addition to describing the wavevectors in the crystal and thus the directional properties of the excited waves, the construction of the dispersion surface also characterizes the ratio of the field amplitudes of the waves. They can be determined from a combination of equation 2.10 with equation 2.9 for the two waves E_0 and E_{hkl}, which yields [Bat 64]:

$$\frac{E_{hkl}}{E_0} = -\frac{kC\chi_{hkl}}{2(k_{hkl} - K)} \tag{2.11}$$

Together with the boundary conditions at the crystal surface the relative intensity distribution of diffracted x-rays for perfect crystals are obtained from the square of the field amplitudes (equation 2.11). The results for diffraction on a plane parallel plate like it is the case in our experiments are discussed in paragraph 2.6.

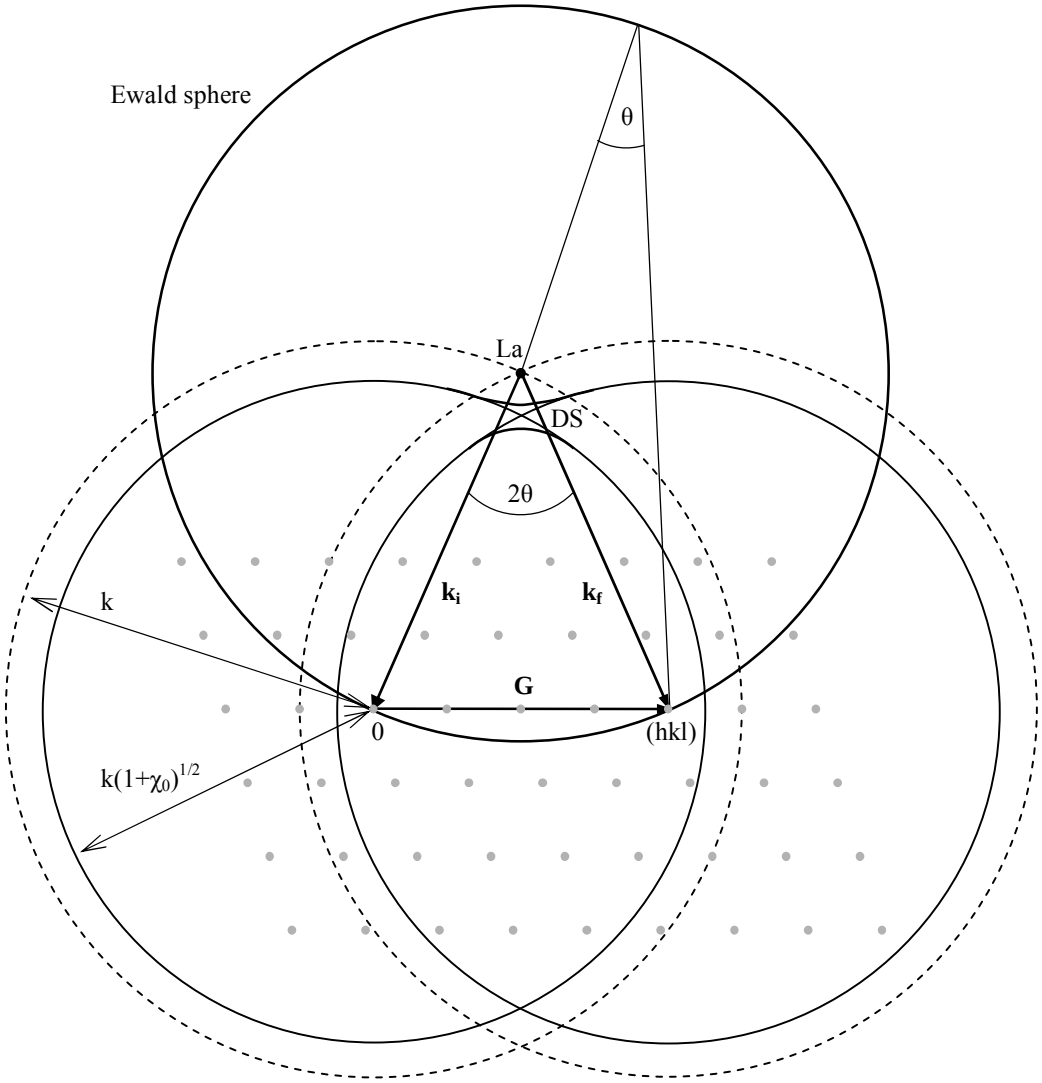

Figure 2.1: Ewald construction (bold) and the construction of the dispersion surface. The two spheres around 0 and (hkl) intersect in the scattering plane at the Laue point (dashed line), the refraction-corrected spheres at the Lorentz point. Close to this point diffraction occurs. The degeneracy at the Lorentz point, i.e. at the Brillouin zone boundary is lifted due to the crystal potential. This leads to the dispersion surface on which the tails of incoming and diffracted wave vector have their origin in the treatment due to dynamical diffraction theory. The grey dots represent reciprocal lattice points.

2.4. Atomic scattering factor, structure factor and the dielectric susceptibility

The structure factor can be expressed in the usual form, where f_n denotes the atomic scattering factor of atom n. The values x_n, y_n and z_n define the positions of atom n in the real space unit cell.

$$F_{hkl} = \sum_n f_n \exp 2\pi i(hx_n + ky_n + lz_n) \tag{2.12}$$

The atomic scattering factor f depends on the chosen reflection of a given crystalline material. Atomic scattering factors are tabulated for example in [War 69, Int 74, XOP 01]. Figure 2.2 shows the atomic scattering factor f_0 of elemental silicon. The tabulated values are calculated based on self-consistent wave function methods, variational wave functions or obtained from the Thomas-Fermi-Dirac statistical model.

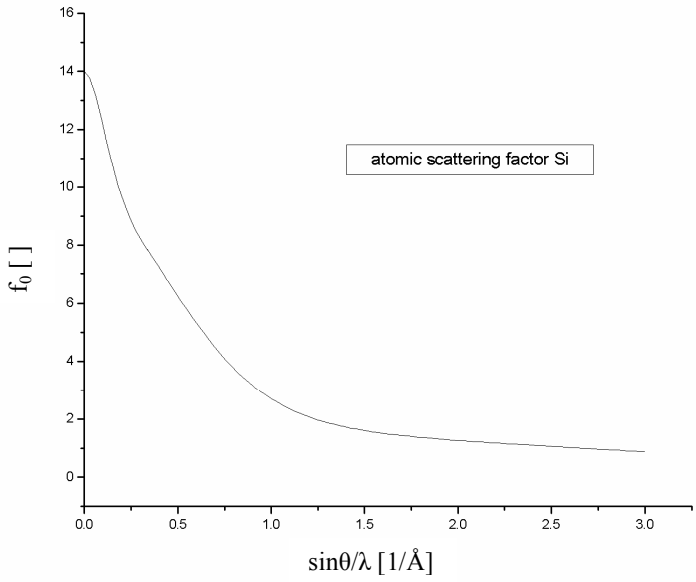

Figure 2.2: The atomic scattering factor f_0 of silicon. It has no further dependence on the x-ray energy but on the momentum transfer of the incident and scattered photon. In the forward direction the scattering factor equals the number of electrons in the scattering atom. The data is taken from [XOP 02]

The susceptibility is related to the structure factor F_{hkl} as expressed by [Zac 45]

$$\chi_{hkl} = -\frac{e^2}{4\pi\varepsilon_0 mc^2} \cdot \frac{\lambda^2}{\pi V} \cdot F_{hkl} \tag{2.13}$$

V denotes the volume of the unit cell, what equals a_0^3 for a cubic silicon crystal. The susceptibility represents the ability of an atom to be polarized. Equation 2.13 shows also that it depends on the square of the x-ray wavelength, thus high energies in the 80-200 keV range dramatically decrease the values of χ down to the order of 10^{-8}. This is two orders of magnitude smaller compared to energies around 10-20 keV.

Figure 2.3 shows the real and imaginary part of the atomic susceptibility as a function of the x-ray energy for the (-571)-reflection of silicon. The small values of the susceptibility for high energies have interesting consequences concerning the diffraction on ultrasound excited crystals with respect to the full width at half maximum (FWHM) of satellite reflections, what will be clear once the experimental observations are analysed in chapter 6.

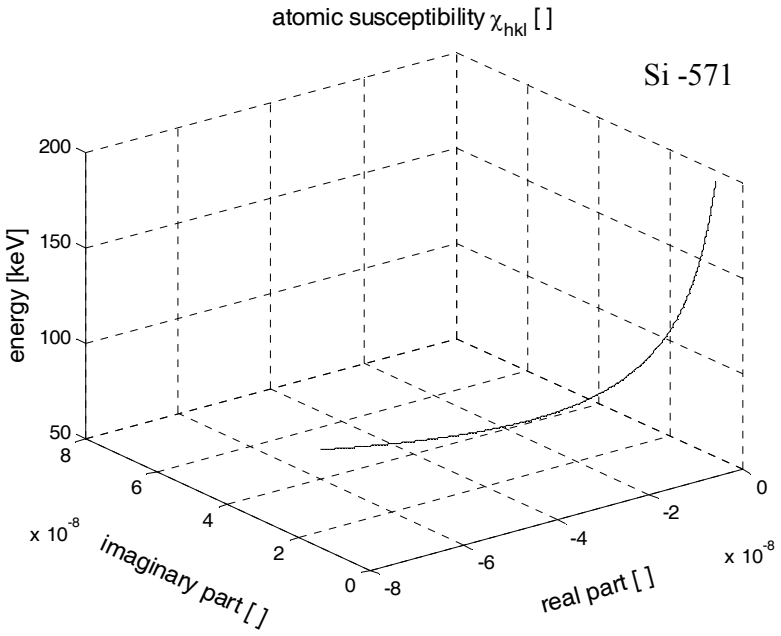

Figure 2.3: Real and imaginary part of the electric (or atomic) susceptibility for the (-571) silicon reflection as a function of the x-ray energy between 50 keV and 200 keV. At these high energies the susceptibility is two orders of magnitude smaller than for energies around 20 keV.

Whenever the susceptibility takes part in calculations throughout this work, the square root of the susceptibility multiplied with the susceptibility value for the reflection with opposite sign is needed. For silicon as a centro-symmetric crystal the product equals the multiplication with its conjugate complex value and thus the square root equals the absolute value of the susceptibility (equation 2.14), if no absorption is taken into account [Aut 69]. Therefore in all equations χ has to be understood as an abbreviation for $|\chi|$, if not otherwise mentioned.

$$\left|\chi_{hkl}\right| = \sqrt{\chi_{hkl}\chi_{\overline{hkl}}} \tag{2.14}$$

2.5. Extinction length and Pendellösung

If both wavefields from the upper and the lower branch of the dispersion surface described in 2.3 overlap throughout their propagation in the crystal, interference effects occur. The small difference in the wavevectors of both branches has a minimum in the center of the dispersion surface in symmetrical Laue geometry, where it equals the diameter of the dispersion hyperbola. This distance in reciprocal space is called Pendellösung [Aut 61] and its reciprocal is the extinction length Λ. Some authors call the extinction length the Pendellösung period instead. Since the energy swaps back and forth from the diffracted to the forward-diffracted beam as a function of depth, the extinction length gives the depth, after which there is no diffracted but only a forward-diffracted beam. Equation 2.15 gives the extinction length not only in the center of the dispersion hyperbola, but also as it deviates from the exact Bragg condition [Pin 78].

$$\Lambda = \frac{\lambda\sqrt{\gamma_h\gamma_0}}{C_s\left|\chi_{hkl}\right|\sqrt{dT^2+1}} \tag{2.15}$$

The asymmetry parameters γ_h and γ_0 are the cosines of the angles between the Bragg planes and the incident and diffracted beams respectively. The deviation parameter dT is commonly used in dynamical diffraction theory to describe the deviation from the Bragg angle in units of the FWHM of a given reflection (equation 2.16).

The intensity distribution of the diffracted beam is governed by its extinction length. It plays a crucial role for the understanding of extinction beats in the intensity distributions of diffracted x-rays, which could in principle interfere with ultrasonically excited satellite reflections. The intensity distribution of diffracted x-rays will be discussed in paragraph 2.6. The evaluation of extinction length and the Pendellösung gives the opportunity to discuss the influence of asymmetric reflections on the intensity profiles. Asymmetric reflections are reflections where the investigated lattice planes are not parallel to the surface normal of the crystal. Such reflections were measured in this work due to more advantageous conditions to resolve ultrasound excited satellite reflections (chapter 6).

The dependence of the extinction length as a function of x-ray energy and the deviation from the exact Bragg angle is visualised in figure 2.4. The curves are calculated for the (-571)-reflection of silicon based on equation 2.15, the surface normal is assumed to point in the (111)-direction and thus an asymmetric reflection is considered.

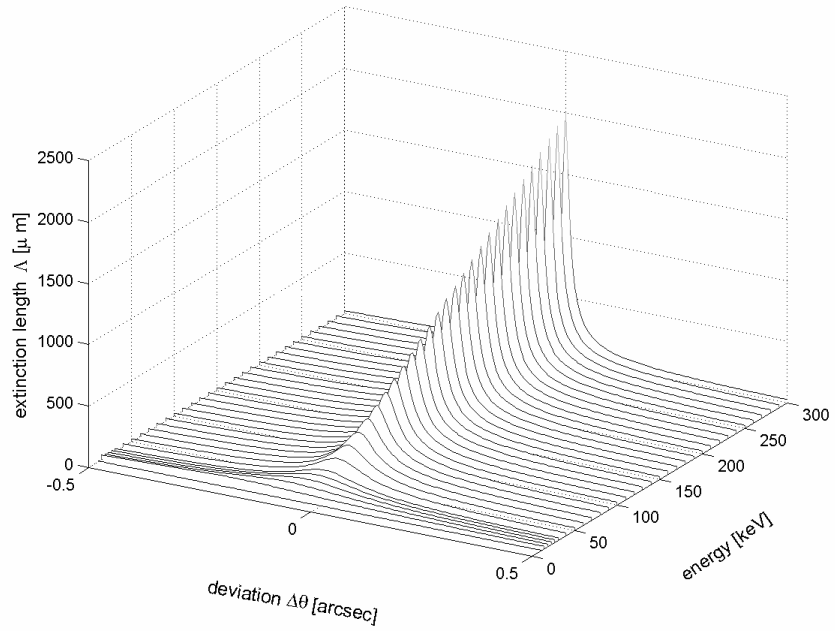

Figure 2.4: The extinction length for the silicon (-571)-reflection as a function of the deviation from the Bragg angle Δθ and the x-ray energy. For high energies above 80 keV it reaches the mm-range.

The extinction length increases at higher energies. It can reach several millimetres for energies above 300 keV. For this particular asymmetric reflection and the x-ray energy of 100 keV for example, the value of the extinction length amounts to 0.662 mm. In addition, the angular width of the extinction length decreases at higher energies with respect to the diffraction angle. At low energies, the peak position of the extinction length deviates from the kinematical expected Bragg angle due to the asymmetry of the chosen reflection. At high energies this deviation is much smaller. This fact becomes more obvious after displaying its pendellösungs-length. As already mentioned, the pendellösungs-length Γ represents the pendant of the extinction length in reciprocal space with $\Gamma = 1/\Lambda$. It describes the distance of the two sheets of the dispersion surface at different angles. Figure 2.5a shows the pendellösungs-length as a function of energy and deviation from the Bragg angle, still for the above mentioned geometrical conditions of asymmetric Laue diffraction. The influence of the asymmetry is striking at low energies. For comparison, the dependence of the Γ for the same parameter range is plotted for the symmetric Laue case in figure 2.5b. To maintain symmetric conditions, the reflection was kept to be (-571), but the angle between the surface and the diffraction vector was set to zero. This is comparable to a different crystal cut: A surface normal direction of (534) instead of (111) and (-571) parallel to the crystal surface instead of (-110).

The percentage difference in the pendellösungs-length Γ between the asymmetric and the symmetric Laue case is visualized in figure 2.5c. At low energies the different scattering geometry has a tremendous effect on the Γ, at high energies the difference becomes less dominant. This is also evident from figure 2.5d, for which the absolute values of the pendellösungs-length are extracted at the exact Bragg angle. At the x-ray energy of 100 keV, the difference of the pendellösungs-length for asymmetric and symmetric diffraction geometry amounts to a peak value of slightly more than 6% close to the exact Bragg angle (figure 2.5e). Even if the influence of the asymmetry plays a less important role on the pendellösungs-length, the extinction length and therefore also for the intensity distribution of scattered x-rays at higher energies, the asymmetric Laue case was implemented in the calculations of the simulation program SIMSAT (chapter 4). The reason is threefold. First, the simulations should also be valid for lower energies, and second, the influence of the asymmetric geometry as an error source should be avoided

also for higher energies. Third, the experiments in this study were performed in asymmetric diffraction geometry. The results presented here are important for the analysis and the interpretation of the experimental data. As will be discussed in chapter 3, the literature published on ultrasonically excited crystals deals with symmetrical Laue diffraction, both in theory and experiment. Furthermore, experimental arrangements were normally chosen to measure under symmetric conditions. In the experiments described in this work, asymmetric conditions are more advantageous for reasons of higher resolution.

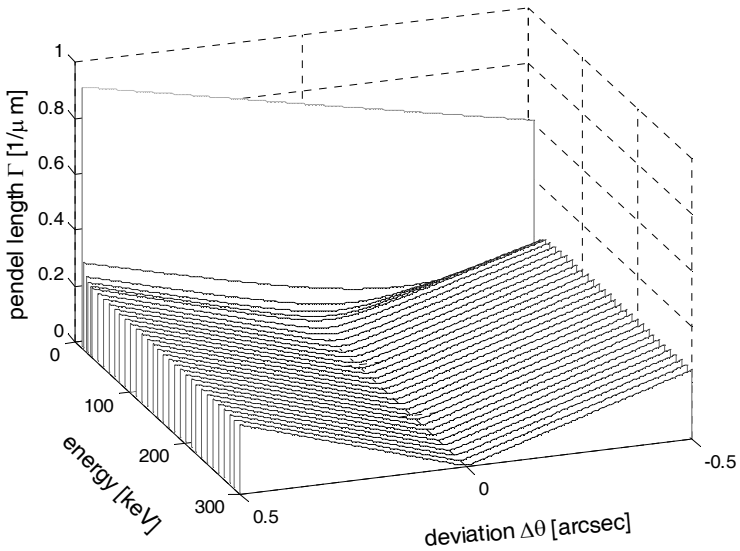

Figure 2.5a

Figure 2.5b

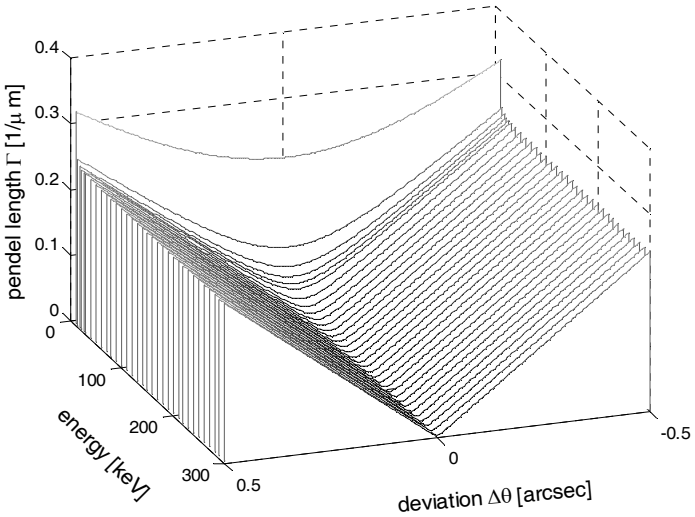

Figure 2.5a-b: The pendellösungs-length for the silicon (-571)-reflection as a function of the deviation from the Bragg angle and the x-ray energy. In 2.5a the (-571)-reflection as an asymmetric reflection, in 2.5b as a symmetric one.

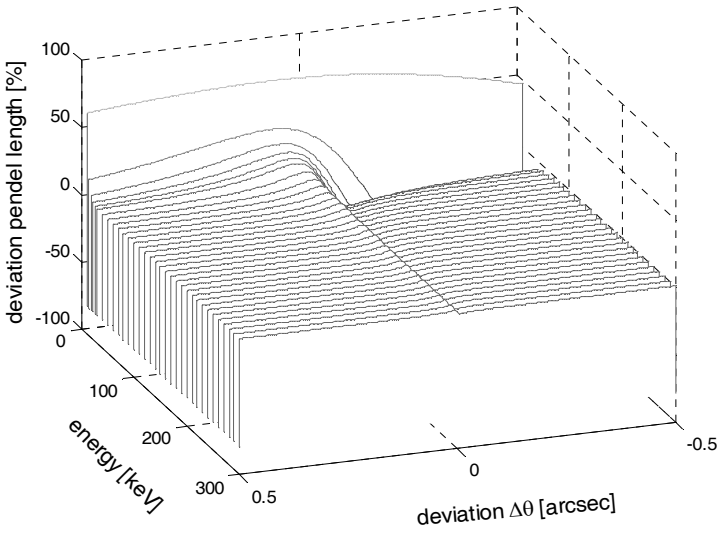

Figure 2.5c

Figure 2.5c-e: The difference in pendellösungs-length Γ between the asymmetric and symmetric (-571)-reflection, in 2.5c as a function of the deviation from the Bragg angle and the x-ray energy; in 2.5d at the exact Bragg angle and in 2.5e at the x-ray energy of 100 keV.

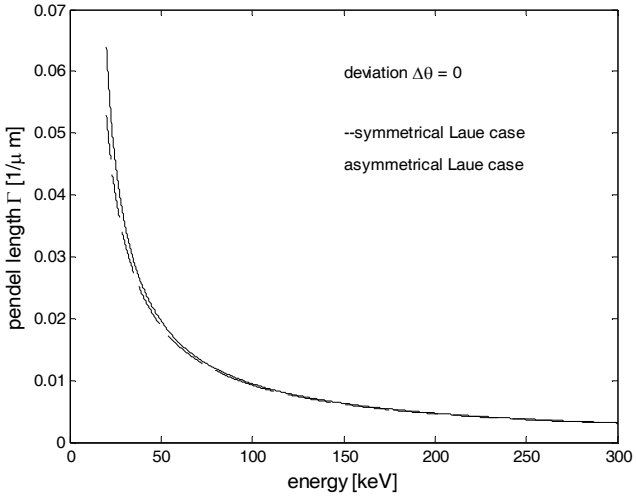

Figure 2.5d

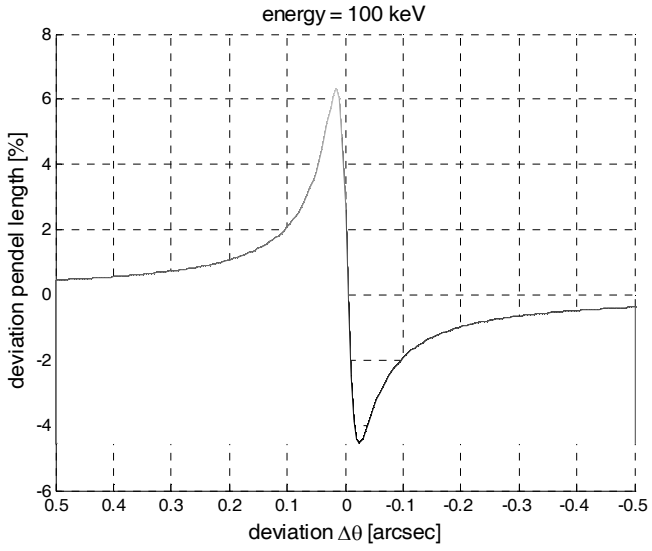

Figure 2.5e

2.6. Intensity distribution of diffracted x-rays

After Zachariasen [Zac 45] two dimensionless quantities are introduced in dynamical diffraction theory. The deviation parameter dT = dT(Δθ,E,h,k,l) is defined by equation 2.16 and the thickness parameter A = A(T,E,h,k,l) by equation 2.17. The parameter dT describes the deviation from the Bragg angle in units of the FWHM of the corresponding reflection. Parameter A describes the crystal thickness T in units of the double extinction length.

$$dT = \frac{\Delta\theta \cdot \sin 2\theta + 1/2 \cdot |\chi_0| \cdot (\gamma_h/\gamma_0 - 1)}{C_s \cdot |\chi_{hkl}| \cdot \sqrt{|\gamma_h|/\gamma_0}} \tag{2.16}$$

$$A = \pi \cdot k \cdot C_s \cdot |\chi_{hkl}| \cdot \frac{T}{\sqrt{|\gamma_h \gamma_0|}} \tag{2.17}$$

Experimentally, the deviation parameter dT can be adjusted through the angle Δθ, the x-ray energy and the chosen reflection. The parameter A changes via crystal thickness, x-ray energy and reflection. In Appendix A.1 both parameters are plotted for the (-351) and the (-571) - reflection of silicon.

The intensity distribution for diffraction on a plane parallel plate without absorption in Laue scattering geometry can then be written as:

$$I = \frac{\sin^2\left(A\sqrt{dT^2+1}\right)}{dT^2+1} \tag{2.18}$$

The diffraction pattern shows interference fringes because of the $\sin^2$ – term in the numerator. If the thickness T and therefore also A increases, these interference fringes come close together. Assuming that the crystal thickness is no longer sharply defined, the numerator can be replaced by its average value of ½. This thick crystal approximation is valid for A >> 1 and the equation for the intensity distribution takes the following form:

$$I = \frac{1}{2 \cdot \left(dT^2 + 1 \right)} \tag{2.19}$$

The mean diffraction pattern is shown as a function of dT in figure 2.6a. The maximum value of ½ is found at the center of the diffraction pattern.

The thin crystal approximation is applied for A << 1. Equation 2.18 reduces then to [Zac 45]

$$I = \frac{\sin^2 \left(A \cdot dT \right)}{dT^2} \tag{2.20}$$

The kinematical diffraction is embedded in the dynamical diffraction theory in the limit of thin crystals. Only the positions of the diffraction maxima on the θ-scale deviate from the Bragg angle due to refraction, which is not taken into account in the kinematical theory.

In figure 2.6a the approximations are compared. The mean diffraction profile for a thick crystal has a maximum value of ½ at the center and no oscillations on the tail. For a thin crystal A = 0.1 was taken as an example. Since it seems to be a flat line on the scale of figure 2.6a, a zoom is shown in figure 2.6b. For the intermediate range of A ≈ 1 the value π is taken, where equation 2.18 must be considered. The diffraction profile has a minimum of 0 at the center and oscillations on the tail.

The diffraction pattern due to the exact equation 2.18 is calculated for an A-range of 0 to 30 in figure 2.6c. The maximum intensity at the center of the diffraction pattern oscillates with $\sin^2 A$ (dT = 0 in equation 2.18) between 0 and unity. This can be understood as follows. If the crystal is thin with respect to the extinction length, only a small amount of the energy from the incident intensity can flow in the diffracted direction. As the crystal thickens until it reaches one-half of the extinction length, the energy flow increases progressively until all the energy flows into the diffracted beam direction (the relative intensity of the maxima is unity). When the crystal thickness increases to one full extinction length, there is no diffracted beam, and all the energy flows in the forward diffracted beam. This oscillation in diffracted intensity with thickness persists until absorption extinguishes this effect or irregularities in the thickness produce the averaging

effect manifested in the thick crystal approximation (equation 2.19). The intensity exhibits always then maxima in the center of the diffraction profile, when a certain number of extinction lengths plus half an extinction length fits into the crystal (equation 2.21). The integer number of extinction lengths in the crystal gives thereby the number of oscillations on the tail of the intensity profile for a given thickness (figure 2.6a and 2.6c).

$$T = (2n+1) \cdot \frac{\Lambda}{2} \tag{2.21}$$

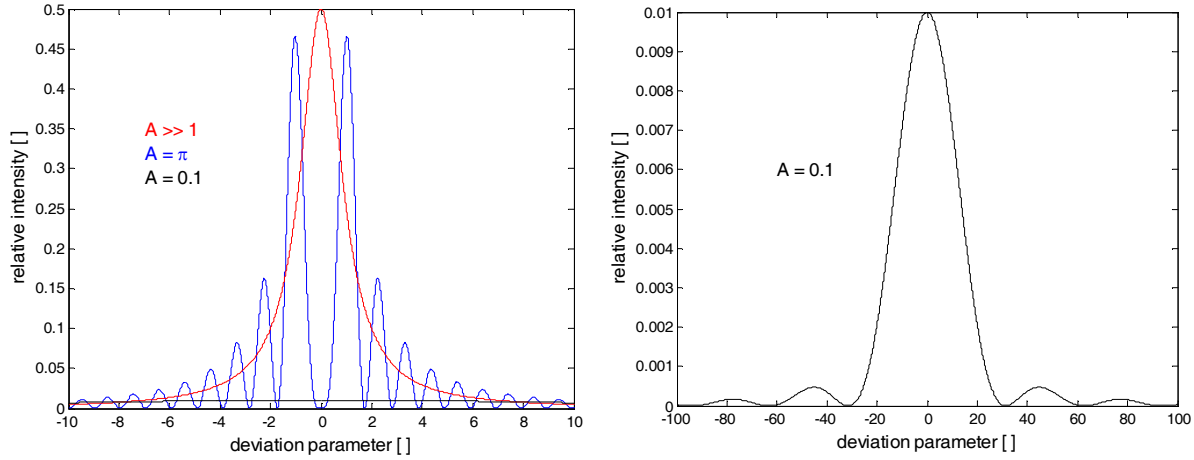

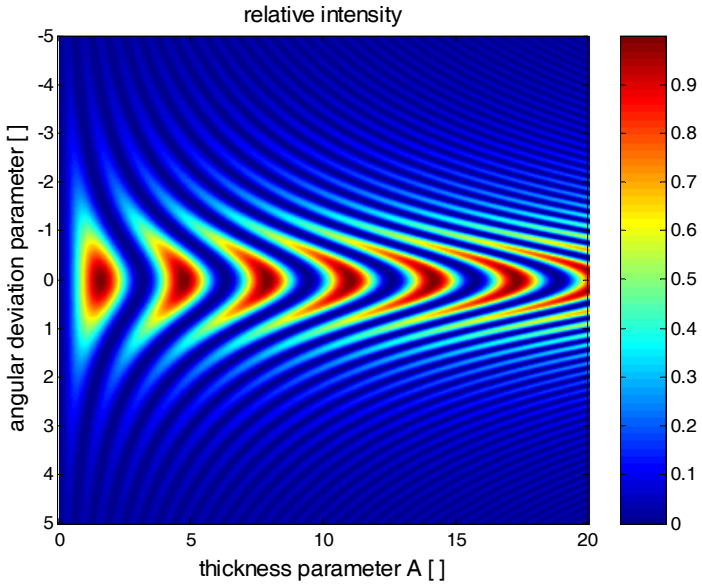

Figure 2.6a (top left): Intensity profiles for different values of the thickness parameter A. A >> 1 represents the thick crystal limit, A = 0.1 the kinematical approximation and A = π the intermediate range.
Figure 2.6b (top right): Zoom of figure 2.6a for the value A = 0.1.
Figure 2.6c: Intensity distribution as a function of the angular deviation parameter dT and the thickness parameter A after the dynamical diffraction theory (Laue transmission geometry). The intensity is oscillating in both variables ('extinction beats'). Details can be found in the text.

2.7. Absorption and the Borrmann effect

Absorption is taken into account via additional components of the atomic scattering factor. We can write

$$f = f_0(\sin\theta/\lambda)+f'(E)+if''(E) \tag{2.22}$$

Anomalous dispersion occurs at x-ray energies in the vicinity of an absorption edge, which is expressed by an additional, energy dependent component f′. Photoelectric absorption in a material is described by the imaginary part if″ of the complex atomic scattering factor. The anomalous dispersion correction is negligible far away from absorption edges, which is true in our experiments on silicon above 80 keV. The linear absorption coefficient μ of a material is linked to the imaginary part of the atomic scattering factor as

$$\mu = \frac{e^2}{2\pi\varepsilon_0 mc^2 V}\lambda\sum_n f''_n \quad , \tag{2.23}$$

whereby the sum runs over all atoms n in the crystallographic unit cell.

It can be shown that for a thick absorbing crystal anomalous transmission (Borrmann effect) through the crystal can occur [Bor 43]. The dynamical diffraction theory predicts a standing wave pattern inside the crystal with nodal planes parallel to the atomic planes (figure 2.7) [Bat 64]. The wavefields from the two different branches of the dispersion surface (chapter 2.3) have two different solutions. The wavefield emerging from the dispersion sheet closer to the Laue point has intensity minima at the atomic planes, for the second wavefield maxima occur [Bat 64].

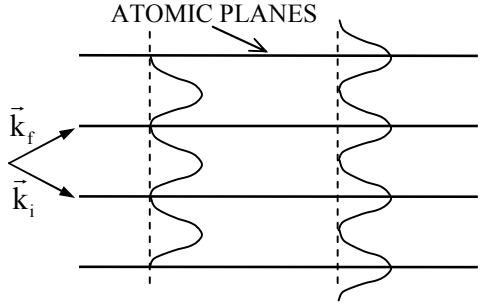

Figure 2.7: Standing wave pattern produced by two coherent, traveling plane waves with wave vectors $\mathbf{k_i}$ and $\mathbf{k_f}$. Nodes of curve on the right-hand side coincide with antinodes of the curve on the left-hand side. When such a pattern exists relative to the atomic planes, the normal photoelectric absorption is radically altered (after [Bat 64]).

The wavefields suffer absorption mainly by the photoelectric process in the crystal, and as the electron density is greatest at the atomic sites, the Bloch wave with intensity maxima at the atomic planes will have the greater photoelectric absorption cross-section. On the other hand, if nodal planes of the electric field coincide with the atoms of the diffracting planes, much smaller than normal absorption occurs. It is therefore possible to obtain a transmitted wave through crystals whose product of the average linear absorption coefficient μ and thickness T is over 10, even though the normal intensity reduction is expected to be exp(-10) (after equation 5.3).

After [Bat 64] it can be distinguished between $\mu T << 1$, where the crystal can be considered as thin with respect to absorption and $\mu T >> 1$ for absorbing crystals. Additionally, at values $\mu T \gtrsim 6$ the influence of the anomalous Borrmann transmission has to be taken into account for the intensity distribution of diffracted x-rays in nearly perfect crystals. The extent to which absorption and the Borrmann effect influence the diffraction process for our experimental conditions regarding x-ray energy and crystal thickness will be estimated in chapter 5.2.

Chapter 3

Current research state: X-ray diffraction on ultrasound excited crystals

It is quite useful to distinguish between x-ray diffraction of volume acoustic waves (VAW) and surface acoustic waves (SAW). The part about volume acoustic waves is separated into low frequency volume acoustic waves (LFVAW), diffraction under x-ray acoustic resonance (XAR), high frequency volume acoustic waves (HFVAW), and acousto-electrically amplified phonons (AE phonons). Acoustoelectric phonons are very high-frequent ultrasound waves. This distinction is not required for surface acoustic waves, since the experiments are entirely carried out in the high frequency regime. The part about surface waves is followed by a discussion of the applications of discovered effects.

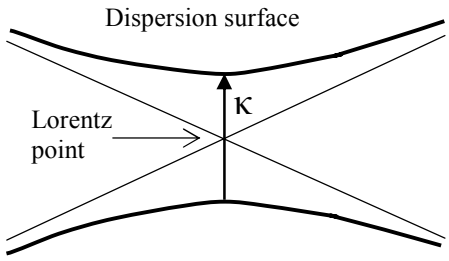

Figure 3.1: An enlarged schematic view of the dispersion surface (bold) drawn in figure 2.1. The thin lines represent a sector of the refraction-corrected spheres around the origin of the reciprocal lattice and the lattice point (hkl), respectively. They are approximated by straight lines due to the large radii of the spheres compared to the intersection region. The spheres intersect in the Lorentz point. If the ultrasound wavevector **κ** matches the splitting of the dispersion surface, the x-ray acoustic resonance occurs. The low ultrasound frequency regime is obtained, if κ is smaller, and the high frequency regime is reached, if κ is larger than the splitting of the dispersion surface. The figure is drawn for symmetrical Laue geometry and an ultrasound propagation direction **κ** perpendicular to the scattering vector **G**.

The physical background for this distinction is visualized in figure 3.1. If a nearly perfect crystal is excited by ultrasonic waves, the diffraction of x-rays on the crystal structure is influenced by the additional lattice vibration. The ultrasound propagation is described by the wavevector **κ** and the amplitude **a**. The absolute value of the wavevector $\kappa = 1/\lambda_{usw}$ is determined by the reciprocal of the ultrasound wavelength λ_{usw}. If **κ** matches the splitting of the dispersion surface (chapter 2.3), the x-ray acoustic resonance occurs. If **κ** is not

large enough to cause mixing of the energy levels between the sheets of the dispersion surface, the low ultrasound frequency regime is obtained. The high frequency regime is reached for $\boldsymbol{\kappa}$ being larger than the splitting of the dispersion surface. In the high frequency regime ultrasound excited satellite reflections may be observed by x-ray diffraction, in the low frequency regime a broadening of the corresponding rocking curve. The strength of the ultrasound influence on the diffraction process in the crystal is determined by the ultrasound amplitude **a**. If the absolute value of **a** exceeds the lattice spacing d (equations 2.3 and 2.4), the large amplitude regime is reached. In vector notation it can therefore be distinguished between the limit of small amplitudes, if the scalar product of the scattering vector **G** and the ultrasound amplitude **a** is $\mathbf{Ga} < 1$, and the regime of large amplitudes, if $\mathbf{Ga} > 1$. In the low frequency range the ultrasound amplitude causes the increase of diffracted intensity for a nearly perfect crystal, in the high frequency regime it determines the number of excited satellite reflections, insofar they are resolvable by x-ray diffraction experiments. The resolution of ultrasound excited satellite reflections is not obvious, since the wavelengths of ultrasonic waves in crystals in the μm-range are much longer than typical lattice spacing of several Ångstrøm. Additional reciprocal lattice points due to the ultrasound excitation lie thus close to the originally unperturbed lattice point.

In this work ultrasound excited satellite reflections were successfully resolved in the experiments. Their angular positions, their detailed intensity distribution as well as their dependence on the x-ray energy, the ultrasound frequency, the ultrasound amplitude and as a function of time could not be fully explained by the basic kinematical diffraction theory. This required a treatment due to the dynamical diffraction theory of modulated crystals including some modifications adapted for our diffraction geometry (chapter 5). A deeper look in the published literature in this field will provide the necessary tools to tackle this problem, which flow into the extensive simulations undertaken in chapter 4 and prepare the ground to accurately describe the experimental results presented in chapter 6. Special attention is paid to the resolution of satellite reflections, their angular positions together with ultrasonic mode conversion. Numerical values for ultrasound amplitudes play an important role as well as nonlinearities in the diffracted intensity as a function of the amplitude. Information about the theoretical treatment of ultrasonic waves

in crystals is an important issue in order to find an applicable approach for our own experiments. A further goal is to extract time-resolved investigations of ultrasound excited crystals in theory and experiment.

3.1. X-ray diffraction on volume acoustic waves

3.1.1. Acoustoelectric phonons

The pioneering work in the group of Köhler, Möhling, Peibst mostly treats the case of very high frequency ultrasonic waves in crystals. They discuss theoretical aspects as well as experimental results. In [Möh 70] they present their method to investigate lattice vibrations based on the acoustoelectric effect in CdS crystals. In order to avoid too much Joule heating, they proposed to carry out the measurements with 10 - 100 μs voltage pulses. The detector, a conventional scintillation counter, was simultaneously gated for this time period with a resolution of 1 μs. The angular resolution of their instrument was 1 arcsec and the quality of their samples was controlled beforehand by recording diffraction topographs. The influence on the carrier concentration was varied by irradiation with filtered light from a halogene lamp. Experimental results together with a theoretical concept were presented in [Köh 70]. Their angular resolution only permitted then to record a broadening of the Rocking curve of the main reflection rather than to resolve individual satellites. Thus they measured the integrated intensity versus the applied voltage. At low excitation voltages a linear increase was observed in the integrated intensity, which began to level off at higher voltages. With their model they are able to calculate the ultrasound amplitude. The model was based on von Laue's description of dynamical scattering and introduced a corrected atomic susceptibility by replacing the atomic position vector in the susceptibility function with the difference between this position vector and the lattice displacement vector induced by ultrasound vibrations. This leads to an additional exponential term in the expression for the susceptibility with the periodic lattice displacement in the exponent. Its expansion yields

a modulation of the susceptibility with Bessel functions. Including this corrected susceptibility in Maxwell's wave equation, they calculated the altered integrated intensities for the Laue scattering geometry. Following their line of argumentation, the only possible verification of the calculated amplitudes based on this model is to compare the measured results from different reflection orders of identical sets of lattice planes, which should give the same results for the amplitudes. Indeed, both selected reflections show roughly the same linear behaviour, when plotting the amplitude versus the applied voltage. However, the linear behaviour shows obviously that they excited the crystal still in the low amplitude regime. They mentioned that the data was taken from the same crystal region, since the ultrasound amplitudes increase exponentially with the distance from the electrodes. The crystal thickness was 20 μm, but thickness effects in the diffracted intensity were not discussed.

In [Kie 73, Köh 73] they showed also the reflection profiles as a function of the rocking angle. In addition, they plotted the differences between the intensities of the vibrating and the stationary crystal. This gives the impression to obtain diffraction satellites, but applying their theory they conclude to having measured a superposition of several satellite orders. Furthermore, they conclude that the ultrasound amplitudes were not large enough to reach kinematical diffraction conditions, but a nonlinearity in the behaviour of the ultrasound amplitude versus higher applied voltages indicates the onset of the transition. They assume higher harmonics in the oscillation to be responsible for the nonlinearity. They state that with increasing amplitude the number of excited satellites should increase, whereas the average intensity of each satellite decreases simultaneously. This leads to a limiting value in the overall diffracted intensity of the satellite system and thus approaches the kinematical description. In [Köh 74a] a second vibrational harmonic is taken into account for several values of the phase angle between the fundamental and the harmonic vibration, which results in an asymmetric integrated intensity distribution. The last publication in the series [Köh 74b] is a roundup of the previous work including an essay to determine the amplitudes of the second harmonic vibration as well as to give a threshold, at which amplitude the satellites can be treated kinematically. This value is mainly based on the fact that the extinction length of a satellite reflection must greatly exceed the crystal thickness. To complete here, the group published also already in 1970

a paper entitled '*Acousto-electric phonon distributions measured by x-ray Brillouin scattering*' [Lem 70]. Therein, the authors developed a theory called '*Brillouin scattering in the language of kinematical theory of x-ray diffraction*', applying it to the same measuring method as presented in [Möh 70] and concluding that the results indicate higher phonon frequencies as obtained by Brillouin scattering with light. They state also that the '*evaluation of phonon distributions from satellites of x-ray Bragg reflections is complicated by convolutions with spectral and angular distributions of the primary beam*', not at least because it was not possible to directly resolve them.

Somehow the same experimental procedure as in [Möh 70] was also used in [Car 71] to investigate piezoelectrically amplified acoustic waves in GaAs. The method to subtract the measured intensities with and without excitation signal gives a maximum at 50 ± 8 GHz, which is in good agreement with the maximum net gain according to the linear acousto-electric theory. They point out that this value is an order of magnitude larger than what is possible to study with the Brillouin scattering technique. A Cu x-ray source together with a 22 μm thick crystal at 77 K was used for the experiments.

The first time angular resolved satellite peaks from acousto-electrically amplified phonons in double-crystal x-ray diffraction measurements were reported in [LeR 75]. They investigated InSb single crystals since these are anyway opaque at wavelengths below some μm and hence no data was available from optical Brillouin scattering. They state that the extension to the x-ray regime allows to studying much higher frequency phonons on other materials than those optically transparent. The AE- amplification of phonons from the thermal-equilibrium background provides the possibility to investigate in detail the interaction of phonons with x-rays under more controlled conditions, such as phonon frequency, propagation and polarization directions as, for example, in the diffuse or thermal scattering background. The philosophy of the experiments still resembles the one presented in [Möh 70]. But due to the electrical properties of InSb at 77 K it was possible to extend the short-pulse operation, applied in earlier experiments, to 2 ms, which facilitates the entire data collection and thus avoids drift effects. Furthermore, applying a magnetic field to systems with high electron mobility enhances not only the AE-gain, but permits also effective phonon amplification for relatively low electric fields. This, however, restricts the measurements to samples of relatively low carrier

concentration and thus to relatively low phonon frequencies, which achieve their maximum AE-gain at less than 10 GHz. They managed to resolve satellite peaks corresponding to phonon frequencies between 0.9 and 6.4 GHz depending on the electron concentration, the electron mobility and on the applied electric and magnetic field. The mechanical instrumental resolution is not indicated, but it should be around 1-2 arcsec and is thus comparable to the value in [Möh 70]. The harder x-radiation of a Mo source and likely the better crystal quality of the samples narrowed the resolution element, the unperturbed rocking curve. The authors also criticize the interpretation of previous experiments [LeR 75]: '*These studies were made at relatively low resolution and thus revealed only a broadening of the x-ray diffraction profiles. The satellite profiles (…) were obtained by subtracting the undisturbed profile obtained without AE phonons. However, when satellites are not resolved from the Bragg elastic peak, the diffraction profile is the result of multi-beam diffraction, and the physical meaning of subtracting the undisturbed profile is not clear. Furthermore, the subtraction procedure ignores the possible effect of the phonons on the elastic Bragg peaks themselves.*' They obtain a representative value for the phonon amplitude of 0.3 Å from the integrated intensities of the separated satellites corresponding to an amplification factor on the order of 10^8 with respect to the Debye spectrum. They observe higher-order satellites, which still grow even when the first-order satellites already tend to saturate with increasing voltage. In addition, the appearance of phonon-induced satellites is accompanied by a dramatic reduction of the height and the half-width of the elastic central peak. On the other hand, peak intensities, intensity distributions and FWHM of the satellites and the main peak are not quantitatively discussed. Further experiments from the same group [LeR 76] took advantage of the fact that amplified phonon beams can attenuate anomalous transmission of x-rays in thick crystals with $\mu T > 10$. They conclude that it is possible to evaluate the atomic displacement and the associated strain with this method and they detect '*weakly enhanced phonon modes other than those predicted by the acoustoelectric theory*'. Possible reasons for this are i) mode conversions at the end face of the sample, ii) the continuous attenuation of phonon beams via nonlinear interactions populating other modes, or iii) the large amplitude vibrations entailing the importance of higher-order terms in the potential expansion at the atomic sites. They also comment on the fact that

they did not observe satellites in this experiment. In their opinion this indicates that inelastically scattered x-rays do not undergo anomalous transmission. That is probably not the case, since the extinction lengths of the satellites can be much larger than those of the elastic reflection (see chapter 6) and thus the satellites are not in the Borrman regime leading to a very small intensity under these experimental conditions. Chapman et. al. [Cha 83] report in addition about time resolved experiments with a resolution of 0.5 μs to monitor the behaviour of the acoustic flux. They conclude that the phonons, which do not travel in the expected direction [LeR 76], results '*in part from mode conversion at the end wall of the crystal, and in part from direct conversion within the forward-travelling acoustic domain*'.

Another way to excite ultrasonic waves in a crystal is to bond a transducer device, driven by a sinusoidal voltage, to the crystal. In this excitation mode the investigated ultrasonic frequencies are normally lower than in AE-excited devices. Frequencies in the low GHz range are considered as low compared to the phonon spectrum. At frequencies one order of magnitude below the phonon value, one generally speaks of ultrasound, even if this is nothing else than the coherent excitation of phonons in the lower linear part of the acoustic branch of the phonon dispersion curve, which is close to the origin of the Brillouin zone of a given material. In this case, however, frequencies around 100 MHz are already considered as high frequency ultrasonic waves. In addition, as lower the frequency of the excited phonons or ultrasonic waves become, the more difficult it is to resolve them in x-ray diffraction measurements. This is because they are coming closer and closer to the elastic Bragg peak and finally broaden it. The transducer excitation has the advantage that the excited waves are clearly monochromatic and the amplitude does not depend on the position in the crystal (compare [Köh 70]). Another advantage lies in the possibility to excite ultrasound waves with absolute values of the wave vectors close to the splitting of the dispersion surface, which gives the possibility to study resonance effects and, under certain conditions, even dynamical diffraction effects.

3.1.2. X-ray diffraction under the condition of x-ray acoustic resonance (xar)

Entin observed a resonant weakening of the anomalous transmission of x-rays if the ultrasound wavelength is equal to the extinction length (x-ray acoustic resonance) [Ent 77]. Therefore x-rays from the continuous spectrum of a copper anode passed a 7.85 mm thick perfect silicon crystal excited by ultrasound waves with the help of quartz converters at frequencies around 120 MHz. The integrated intensity of the diffracted beam, which passed through the crystal exploiting the Borrmann anomalous transmission effect, was detected at low excitation amplitudes. At a fixed excitation frequency, the x-ray wavelength and thus the splitting of the dispersion surface was changed by scanning the two-theta angle of the diffractometer with a step width of about 0.8 degrees. By comparing the detected integrated intensities with and without ultrasound excitation and plotted versus the x-ray wavelength, a dip corresponding to the suppression of the Borrmann effect was observed. Assuming that the position of the intensity minimum fulfilled the xar condition, the atomic scattering factor of the reflection was calculated and it agreed within its error bar with the published value. Further investigations were reported in [Ent 78a]. Using characteristic Mo radiation and varying the ultrasound frequency rather than the x-ray wavelength lead qualitatively to the same result as given in [Ent 77]. In addition, they measured an increased width of the resonance dip as a function of excitation voltage. If the excitation voltage is increased above at least 2 V, the anomalous transmission is even suppressed for any value of the ultrasound frequency. They concluded that the intensity of the anomalous transmission due to acoustic deformations is highly sensitive under resonance conditions. Numerical solution of Tagaki's differential equations for perturbed crystals in the approximation of a spherical incident wave confirms the suppression of anomalous transmission by the ultrasound wave.

An analytical solution of Takagi's equations for the two-wave approximation in Laue diffraction with a one-dimensional distortion field and an incident plane wave was tackled in [Ent 78b], still for small ultrasound amplitudes and for conditions close to the xar. The diffracted intensity distribution at the exit surface of the crystal can be

calculated, if the entrance slit width is small compared to the base of the Borrmann fan. Additionally, the field trajectories along the absorption rays must not be more divergent than the resonance region width. The second condition is most likely fulfilled for the central part of the Borrmann fan. The unperturbed intensity profile of the diffracted beam at the exit surface has its maximum in the centre of the fan and continuously decreases when approaching the edges. As a consequence of the ultrasound excitation, a couple of symmetrically located minima merge into the intensity profile at the exit surface close to the centre of the fan, their distance increases with increasing frequency. If the xar condition is precisely matched, the intensity distribution has a local minimum in the centre of the Borrmann fan. From the experimental point of view they improved the instrumental resolution by increasing the sample thickness and by using a 1 mm slit in front of the detector. The slit width in front of the sample was decreased to 0.25 mm. As a result a fine structure splitting in the intensity dip was observed, corresponding to the two different polarization states of the x-radiation.

The dip in the diffracted intensity under x-ray acoustic resonance conditions in the Borrmann regime should also occur by measuring the crystal reflection rocking curves. Consequently, Entin and Assur observed deep minima in the rocking curves with a high angular resolution setup [Ent 81]. The resolution of 0.1 arcsec was obtained by using a monolithic silicon double crystal of 10.8 and 10.7 mm thickness, respectively. The distance between the wafers was 10 mm and the relative orientation was changed via a magnetic coil mechanically attached to the monochromator crystal and a permanent magnet fixed to the second part of the monolithic crystal serving as the sample. Changing the current in the magnetic coil varied the angle between the ‘two’ crystals. A diffractometer with independent axes did not provide the necessary stability and resolution. Additional slits were placed in front of the monochromator and the sample crystal. The slit size of approximately 150 μm in front of the sample was chosen as a compromise between the beam divergence and its diffraction by the slits. The angular positions of the rocking curve intensity minima were dependent on the ultrasound frequency, a higher frequency leading to an increased distance between the minima. The rocking curve profiles for the transmitted and diffracted beam were simulated showing a qualitatively good agreement with the measured results. The simulations are based on the

multi-wave dynamical diffraction theory developed in [Ent 79]. Therein, the resonant interaction of the x-ray wave field in a thick absorbing crystal with the acoustic displacement field was investigated on the basis of the dynamic scattering theory for an ideal crystal [Ent 79]. Since the additional points in reciprocal space due to the ultrasound induced superlattice are close to the Ewald sphere, the diffraction is treated as a multi-wave problem with a plane wave Ansatz instead of a two-beam approach as it was used for high ultrasound frequencies in [Köh 74a]. With this approach the system of equations does not reduce to a two-wave problem. As a result, the ratio of diffracted intensity with and without ultrasound is expressed by the 0^{th} order Bessel function multiplied with an exponential function of the same argument with opposite sign [Ent 81]. The argument consists of the product of the crystal thickness multiplied with the absorption coefficient due to the multi-wave diffraction. It should be noted that the obtained theoretical values of the angular position of the minima in the rocking curves around the x-ray acoustic resonance equates the angular positions of the satellite maxima obtained in [Pol 94] for high frequency ultrasonic waves in crystals (see also chapter 4).

The method described in [Ent 78b] to measure the intensity minima at the crystal exit surface in the Borrmann regime was exploited to determine x-ray structure factors and extinction lengths in perfect or slightly imperfect crystals with a high precision, presumed that the sound velocity is known very accurately [Ent 91].

An oscillation of the integrated intensity in the centre of the diffraction profile at the exit surface of the crystal as a function of the ultrasound amplitude was recognized in [Ent 88]. The theoretical approach to describe the diffraction process is comparable to the one reported in [Ent 79] applied to the one-phonon case around the XAR, the experimental set-up is the same as in [Ent 78b] with a smaller slit size of 50 μm in front of the sample and the detector. They state: '*Since the periphery of the Borrmann delta only increases the background, the oscillation contrast should be increased by placing a narrow slit in front of the detector, passing the central part of the profile of the reflected beam.*' The intensity oscillation as a function of the ultrasound amplitude should in principle be observable at all ultrasound frequencies greater than the XAR-frequency, but the oscillations were only observed close to the x-ray acoustic resonance. This is due to the fact that the contrast in the centre of the Borrmann fan is significantly higher at the x-ray

acoustic resonance than for short wavelength ultrasound. However, for a crystal sufficiently thick compared to the ultrasound wavelength and at very small excitation voltages, the effect of intensity oscillation at the x-ray acoustic resonance offers the possibility to measure ultrasound amplitudes with high sensitivity and high local resolution by an absolute method. Structural distortion effects on the spatial distribution of the diffracted intensity under x-ray acoustic resonance conditions were investigated by Khrupa and Entin [Khr 91a]. Therefore, the intensity distribution at the exit surface of the Borrmann fan is examined to obtain the deformation level stemming from macroscopic distortions as well as to determine the static Debye-Waller factor.

A contribution to the investigation of the XAR was also given by Nosik and Iolin [Nos 93, Iol 95a]. The theoretical work of Nosik has to be seen in the framework of the results of Entin for thick crystals applying the Takagi-Taupin equations [Ent 77-79]. Nosik includes as well high amplitude multi-phonon scattering to match the XAR-condition between the dispersion sheets. The differential equations are solved with the help of perturbation theory and examined as exact solutions. He concludes that the presented approach is also valid for large ultrasound amplitudes and that wave vectors not large enough to match the splitting of the dispersion surface may nevertheless do so by multi-phonon scattering.

Iolin et. al. investigated the combination of deformations in a perfect crystal due to bending and exposure to ultrasound at the same time [Iol 95a]. They find that the sensitivity of the diffraction with respect to small static deformation is highest under x-ray acoustic resonance conditions. The qualitative explanation is the following: Because of the gradient of the static deformation, the tie points move adiabatically along the dispersion sheet. Under the condition of XAR the tie points interact many times with the ultrasonic wave and interbranch scattering is possible. They use the Takagi-Taupin equations to describe the symmetrical Laue diffraction on slightly distorted crystals in the two-wave approximation with an incident plane wave, and provide analytical solutions for the case of small static deformations in a Borrmann thick crystal applying the Born approximation. Roughly speaking, they find minima in the diffracted intensity whose position depends on the combination of the static deformation and the ultrasound

amplitude. The minima are deeply pronounced at the XAR in qualitative agreement with the experimental data.

3.1.3 High frequency volume acoustic waves (hfvaw)

Assur and Entin derived expressions for the position and width of satellite reflections due to dynamic diffraction by a superlattice formed by a standing acoustic wave at low amplitudes in a perfect silicon crystal [Ass 82]. The rocking curves were measured in Bragg geometry with a high-resolution setup based on a monolithic single crystal as already described [Ent 81]. They resolved one diffraction satellite on the tail of the rocking curve at an ultrasound frequency around 200 MHz measured with Ag-Kα radiation, but they did not compare the measured and calculated data quantitatively. The integrated reflection intensities were also measured as a function of the vibrational amplitude with white x-radiation in order to change the ratio Δ between the extinction length and the ultrasound wavelength at a constant excitation frequency. They observed a linear intensity increase at $\Delta > 1$, while the integrated intensity increases with a smaller slope at $\Delta < 1$. Moreover, Entin and Puchkova [Ent 84] found oscillations of the integrated intensities as a function of the vibrational amplitude superimposed on the linear increase at $\Delta > 1$ and low amplitudes, similar as reported in [Ent 88a] for $\Delta = 1$ (XAR condition). The experiment was carried out in Laue scattering geometry on a 400 μm thin silicon crystal with x-radiation from a silver anode, a 50 μm slit in front of the sample and a large aperture in front of the detector. A quartz transducer excited ultrasonic waves at about 114 MHz in the crystal. This frequency was chosen such that Δ was still close enough to $\Delta = 1$, otherwise intensity oscillations were hardly detectable. The oscillation contrast was stronger for a travelling rather than a standing ultrasonic wave. Furthermore, at higher ultrasound amplitudes the oscillation contrast tended to decrease. The oscillation period was twice the extinction length divided by the crystal thickness. The oscillations of the integrated intensity were explained by extinction beats of the (not resolved) satellite reflections. Calculations based on the numerical solution of the Takagi equations showed qualitative agreement with the measurement. Some years later, the

accumulated results about the integrated intensities of ultrasound excited crystals were put together in the sense that the author described the behavior for different frequencies and amplitudes over a wide range [Ent 88b]. For high ultrasound frequencies, the initial linear growth of the integrated intensity as a function of the ultrasound amplitude is replaced by a square-root dependence, both overlaid with an oscillatory behavior. In the regime of low frequencies the intensity increase shows to be quadratic for low amplitudes and linear for higher ones. Even higher amplitudes show a square-root dependence, because at large amplitudes the generation of higher harmonics may exhibit non-linear behavior. Finally, with a further increase of the amplitude, the kinematical limit of the integrated intensity is reached for both cases, high and low ultrasound frequencies. There, it should stay constant. But it can happen to be that the angular width exceeds the divergence of the incident radiation and the intensity decreases with the reciprocal of the ultrasound amplitude. The analytical solutions were derived for symmetrical Laue diffraction and a standing acoustic wave, whereas the ultrasound wave vector is perpendicular to the scattering vector. The crystal thickness exceeds in any case the ultrasound wavelength. The presence of two polarizations and the absorption were not taken into account. Measurements referring to this publication were presented in [Khr 91b]. The integrated reflectivity for high frequencies and fairly high amplitudes reached a plateau level indicating the transition to the kinematical case. Two more purely theoretical investigations were presented by Nosik [Nos 91a, Nos 91b]. In [Nos 91a] the construction of the four-wave approximation of the dynamic theory of x-ray diffraction in crystals distorted by ultrasound was performed. Recapitulating the results, if the extinction length is much longer than the ultrasound wavelength, the satellites can be regarded independently using the two-wave equations for each satellite order, otherwise the satellite positions depend also on the ultrasound amplitude. The results presented in [Nos 91b] are comparable to [Ent 88], but more weight is put on the dependence of the integrated intensity on the crystal thickness and the distinction between travelling and standing ultrasonic waves.

Entin reported about the suppression of the Borrmann effect by acoustic oscillations [Ent 85]. Compared to the investigations in the regime of the XAR, a theoretical development valid for the three different frequency ranges is presented. The development is based on

the solution of the fundamental system of dynamical diffraction equations for the multiwave case applying perturbation theory. The suppression factor of the Borrmann effect for high frequent ultrasonic waves is calculated. It is pointed out that the Debye-Waller factor describes the acoustically induced suppression only correctly especially in the high frequency range. Referring to the published experimental results of [Cha 83], a correct interpretation of the data is given to eliminate contradictions linked to the determination of the ultrasonic displacement amplitude.

Analytical expressions for the x-ray field diffracted on crystals being subjected to longitudinal or transverse ultrasonic waves in Bragg and Laue geometry taking also into account non-resonant x-ray waves were derived in [Pol 87, Pol 88]. The theory is valid for thick crystals, but not as thick as in the Borrmannn case. In [Pol 94] analytical expressions for the differential and integrated reflection coefficients of ultrasound excited crystals were derived also for large vibration amplitudes, still based on the theoretical approach developed in [Pol 87] and [Pol 88]. The time dependence of x-ray diffraction in crystals deformed by small-amplitude ultrasound is discussed in [Pol 98]. The theoretical developments in [Pol 87], [Pol 94] and [Pol 98] turned out to be quite useful, in an extended version, for the simulation of experimental situations described in this work. Therefore they will be discussed in more detail in the chapter 4. Another point of view of the theory developed in [Pol 87], [Pol 88] and [Pol 94] is presented in [Pol 96], which was originally written for crystals with laser-induced gratings, but could also be applied to crystals with differently induced periodic modulations of the electron density such as ultrasonic waves. Therein, diffracted intensities in the vicinity of a satellite as a function of, among other variables, the crystal thickness were derived. The influence of absorption on dynamical Bragg diffraction in crystals affected by high-frequency and high-amplitude ultrasound on the intensity gain of ultrasound excited Bragg monochromators is estimated in [Pol 97].

In the 90's, time-resolved investigations in the ps-range found more and more interest due to the availability of pulsed synchrotron sources. Apart from [Pol 98] (chapter 4), one more theoretical investigation for high frequency volume acoustic waves has to be mentioned. In [Iol 95b], the '*influence of a high-frequency standing acoustic wave on the angular spectrum of a diffracted beam in a perfect crystal*' was presented. A rapid

suppression and modulation of the diffracted intensity in the centre of the diffraction profile in Laue geometry with a characteristic duration much smaller than the period of the acoustic wave was found. This is valid for a thick crystal in the sense that several ultrasound wavelengths have to fit into the crystal, the suppression time being dependent on the number of matching wavelengths. As an example, a 100 MHz ultrasonic wave may suppress the intensity to 1% for the duration of 50 to 100 ps. Thereby the suppression factor is strongly dependent on the ultrasonic amplitude. The theoretical approach is based on the solution of the Takagi-Taupin equations with the transfer-matrix method. Time resolved experimental investigations were either done on low-frequency volume acoustic waves (chapter 3.1.4) or high-frequency surface acoustic waves (chapter 3.2).

The influence of high-frequency ultrasound on deformed single crystals was studied in [Iol 88], [Zol 92a] and [Zol 95a]. In these investigations an effect called '*anomalous dependence of diffraction intensity on ultrasound amplitude*' was found. The effect is based on the fact that in a smoothly deformed crystal the high frequency ultrasound wave makes transitions between the dispersion sheets possible and thus leads to a violation of the adiabaticity conditions for the motion of the representative excitation points on the dispersion surface. The reason behind is that in a slightly deformed crystal the dispersion surface is already excited in much more than only one point. In [Iol 88] the experiments were carried out at $\mu T \dot{c} 1$ (low absorption) so that the role of the Borrmann effect is not significant, but the crystal being still a thick one in the sense that the crystal thickness exceeds the extinction length by far. The ultrasound excitation results in a substantial decrease of the diffracted integrated intensity with increasing but small amplitudes. With a much further increase of the amplitude the diffracted intensity increases linearly before it reaches finally the kinematic limit. In between, a new type of Pendellösung beats was observed connected to interference phenomena in the presence of static strain together with high-frequency ultrasound under conditions, when ordinary extinction beats are already suppressed. They state: '*A nontrivial fact is that in absolute numbers the influence of the ultrasound is much more strongly manifested in diffraction in a strained crystal than for an ideal lattice.*' In a strained crystal excited by ultrasonic waves, multiphonon processes play already an important role even at low amplitudes, contrary to

ideal crystals where they have to be taken into account only in the high amplitude regime. In addition, the theoretical satellite positions shift in a deformed crystal depending on the value of static strain and ultrasound amplitude. The analytical solution of Tagaki type equations in two-wave approximation including static and ultrasonic (dynamic) deformation yielded this result. The diffractometer resolution did not permit to observe such shifts. A quantitative comparison of experimental data and theory was difficult because the excitation frequency of 60 MHz was close to the threshold of XAR. Another interesting feature of their experiments should be discussed. Since the static strain field was introduced by slight pressure on the sample holder, the strain distribution was not necessarily clear. To obtain an idea about the strain field, they measured the diffracted intensity by scanning the sample plate along the diffraction vector. Unstrained regions were identified via the unchanged diffracted intensity, largest strains via the maximum growth of the integrated intensity (up to roughly ten times higher). They examined then two regions, a low strained one and a high strained one. Scanning the ultrasound frequency showed an inversed behaviour in the diffracted intensity in the low strained compared to the high strained region. In the nearly perfect region the intensity curve has a distinct peak structure due to resonances of the acoustic system transducer-glue-silicon, but in the high strained region the same scan of the frequency leads to sharp dips in the otherwise higher intensity. This observation is used as an indication of the anomalous influence of the ultrasound on the diffraction in a strained crystal. Moreover, amplitude scans at the central resonance of the frequency scans showed an increasing intensity with higher amplitude in the nearly perfect region and a decrease of intensity at a higher base level in the highly strained region. In [Zol 92a] basically the same statements were given, solely the static strain was induced in a more controlled way with the help of a bending device. Additionally the dependence of the sound effect (the intensity gain) on the reciprocal static strain gradient was investigated, showing some maxima and minima representing the new type of Pendellösung beats mentioned in [Iol 88]. In [Zol 95a] a different theoretical approach of the diffraction in strained crystals including ultrasound excitation was investigated. The description is based on the visual concepts of the dispersion surface and Poynting vectors after [Pin 78]. The calculations yield diffraction profiles with sophisticated structures. Because most of the published work was dealing

with the easier measurements of integrated diffraction intensities, the authors write: '*Note that detailed measurements of diffraction profiles under ultrasonic excitation have not been performed even in perfect crystals, not to mention strained ones. (…). Thus, the amazing graphs (…) may be considered a challenge to x-ray groups having double-crystal diffractometers with angular accuracy of the order of 0.1".*'

3.1.4. Low-frequency volume acoustic waves (Lfvaw)

Already in 1967, Haruta [Har 67] investigated a piezoelectrically driven vibrating quartz plate in Laue scattering geometry. The conditions were not as to measure in the Borrmann regime, but in the non-absorbing range at $\mu T \sim 1$ and at a low ultrasound frequency of 230 kHz. Since the ultrasound induced vibrations are controllable lattice distortions, he wanted to find out the relationship between the diffracted intensity and these lattice distortions. Changes in the integrated intensity were measured as a function of the position in the crystal, as a function of the ultrasound amplitude and phase. To do so, he first used the topographic method to visualize intensity changes on a film and then he investigated the intensity changes by taking a smaller beam focused on this area of the sample and a scintillation detector in a common diffraction setup. He gated the detector for a fraction of the excitation cycle and by changing the phase he got a relation between the diffracted intensity and the excitation phase. Even if this kind of time resolution was strongly limited by the possibilities to gate the detector, the diffraction signal gave already the impression to be of sinusoidal form, but keeping in mind that the ultrasound frequency was only on the order of 230 kHz. For the semi quantitative analysis he used Kato's formulation of weakly distorted crystals. His conclusions were three-folded: First, the distortions must have a component along the diffraction vector. Second, during one cycle of the ultrasound excitation there are two maxima in the measured intensity because compression and expansion of the lattice leads to the same increase in the diffracted intensity. Third, the integrated intensity as a function of the ultrasound amplitude has a zero slope at very low amplitudes and a parabolic form with increasing amplitudes. A linear range at intermediate amplitudes is followed by saturation at high amplitudes.

Since it was only possible to express the amplitude as the driving current of the piezoelectric crystal, one possible reason for the saturation is that the ultrasound amplitude is no longer proportional to the applied current. Obviously the second possible reason was the transition of the crystal to an ideally imperfect one.

In an experiment of Hauer and Burns the reduction of the Borrmann transmission caused by a low-frequency standing acoustic wave was investigated [Hau 75]. A 2 mm thick silicon crystal was excited by 10 MHz longitudinal acoustic waves via a bonded piezoelectric ceramic transducer. The incident x-ray beam from a Cu Kα source was collimated to about 1˚, diffracted by the sample in Laue geometry and detected by a phototube, without neither moving the sample nor the detector. The transmitted x-ray intensity plotted versus the average input power into the transducer showed roughly a linear decrease, except for rather low input power values. To put this result in the context of previously described results, the following remarks are made. [LeR 76] measured Rocking curves on a Borrmann thick crystal for high frequency acoustoelectric phonons. The intensity decreased with increasing amplitude, but the decreasing rate was not analysed in detail. [Cha 83] measured as well the integrated intensity for acoustoelectric amplified phonons in the high frequency regime and a Borrmann thick crystal. They stated that the logarithm of the integrated intensity ratio should fall off linearly with the squared amplitude. [Nos 93] found theoretically a minimum or at least a plateau of the integrated intensity versus the ultrasound amplitude for the x-ray acoustic resonance in a Borrmann crystal. [Ent 78a] obtained experimentally a curved decreasing function, which may did not reach the minimum or inflection point, because the amplitude was not high enough. The results of [Ent 88a] have to be taken with caution in this regard. Bearing in mind that they measured an oscillating behavior of the integrated intensity as a function of the amplitude close to the x-ray acoustic resonance, it should not be forgotten that they put a narrow slit in front of the detector for part of the experiment. The idea was to cut out the central part of the Borrmann fan. Second, they measured thick crystals compared to the ultrasound wavelength, but the crystals were not as thick as to measure in the Borrmann regime. To summarize, it seems logic that in the Borrmann regime a perturbation by an ultrasonic wave of any frequency tends to destroy the effect with

increasing amplitude, even though this takes place at different levels and is maybe halted on a plateau around the x-ray acoustic resonance.

Hauer and Burns [Hau 75] also carried out time-resolved measurements to investigate the interruption of the Borrmann effect as an x-ray shuttering mechanism. A modulated excitation signal of 15 μs bursts together with a carrier frequency of 10 MHz, the electronics is coupled to the detector and the signal generator. Therewith they managed to produce an 'open shutter' for the transmitted x-ray intensity with duration of 25 μs. Furthermore, faster switch times by fast-rise-time acoustic fields or optical beams were proposed, a vision which was realized 26 years later and presented in [DeC 01b] together with some basic ideas published in [Buc 99].

A gain factor of 50 in the integrated intensity ratio was obtained in experiments presented in [Lis 97a]. A standing wave of longitudinal ultrasound at about 15 MHz was induced in a 4 mm thick silicon crystal. Since the experiments were carried out with synchrotron radiation at high x-ray energies of 90 keV, it was possible to penetrate such a thick crystal in Laue geometry without operating in the Borrmann regime. The experiments were performed on a high-resolution triple-axis diffractometer [Suo 95]. The authors resolved the line shape of the rocking curves at different voltage amplitudes applied to a $LiNbO_3$ transducer, which was coupled to the sample crystal. Applying the voltage to the transducer doubled and broadened immediately the rocking curve intensity distribution, increasing the voltage lead to a further broadening of the rocking curve and a slight decrease in the peak intensity at the same time. The integrated intensity gain plotted versus the applied voltage amplitude showed a linear increase. The achieved gain factor exceeded the previously obtained ones by far. This is because high x-ray energies were more favourable to reach the kinematical limit. Simulations based on a linear gradient crystal model with the measured FWHM as input parameters reflected qualitatively the shapes of the rocking curves. The calculated curves yielded box-shaped curves with a decreasing peak value at higher amplitudes. Operating the diffractometer in three crystal mode with the third crystal used as an analyzer allowed to mapping the complete intensity distribution in reciprocal space. This showed a broadening only in the sound propagation direction, what proofed the clear excitation mode and the longitudinal character of the induced wave. Finally, the peak-to-peak amplitude of the atomic

displacement of 210 Å was deduced from the FWHM of the broadest rocking curve. The same group provided also time-resolved measurements of high-energy x-ray diffraction on ultrasound excited crystals [Lis 97b]. The experimental conditions were similar as in [Lis 97a]; this time the thickness of the crystal was chosen to 10 mm and the x-ray energy to 258 keV. The ultrasound excitation frequency was of the same order as before. The time-resolved data was obtained in a stroboscopic way, taken at every data point of the rocking curve. The electronics to exploit the intrinsic time resolution of the germanium detector lead to a resolution of 20 ns, taking advantage of the bunch structure of the synchrotron allowed a resolution of 200 ps. The obtained time pattern of the whole rocking curve intensity distribution showed a periodic broadening and narrowing. Additionally the integrated intensity remained constant in time. Snapshots at moments when the lattice is mostly relaxed, at maximum strain and the time averaged data were compared to calculations based on the standing wave equation. An inverse circle function representing the probability to find a particular amplitude at a certain position and time in the crystal described the state of maximum strain, time averaging over one oscillation period lead to a complete elliptic integral of the first kind and described well the time averaged data. In [Lis 98] frequency scans were additionally presented. Therefore, the intensity distribution at different ultrasonic frequencies taken one arcsec besides the maximum rocking curve intensity was measured. It shows sharp acoustic resonances for the system transducer-bond-crystal and a broad bunch of resonances around the third transducer overtone. Furthermore, a time pattern as discussed previously taken close to a transducer resonance is shown. The time distribution is not very sinusoidal, giving evidence for a higher harmonic contamination. The authors state that it was not trivial to excite pure sound modes. The spatial behavior of the ultrasonic wave field was also measured. This was achieved by placing 200 μm slits in front of the sample and the detector and by translational scans along the ultrasonic field. At every point a time-resolved rocking curve was recorded. The data demonstrates a distorted near field close to the transducer and an improved quality deeper in the volume.

3.2. X-ray diffraction on surface acoustic waves (saw)

In [Zol 92c] the acoustic field in the multilayer acousto-optical device ZnO-SiO_2-Si is probed by x-ray diffraction in Bragg geometry. Interdigital electrodes on the ZnO layer were used to excite the surface acoustic wave. The main resonance frequency of the system was close to 80 MHz, which was falling in the high-frequency regime. The dependence of the diffraction intensity - measured on the top of the broadened rocking curve - on the ultrasound frequency confirmed the resonance frequency and additional lateral maxima. Measurements at another position on the sample gave differing results and thus demonstrated an inhomogeneity of the acoustic field.

The narrowing effect of rocking curves due to ultrasonic surface excitation in strained crystals is reported in [Zol 94], [San 95] and [Zol 97]. This effect is explained by possible transitions between the sheets of the dispersion surface away from the locus point due to the largely excited sheets following the static strain. Once the ultrasonically induced strain is stronger than the static strain, the rocking curves broaden as expected. X-ray Bragg diffraction on a multilayer mirror modulated by surface acoustic waves is studied in [Ros 97]. The x-ray plane wave from a rotating copper anode was reflected from a curved graphite monochromator with a linear focus and collimated by two 10 μm slits. After reflection from the ultrasound excited multilayer at a Bragg angle of about 0.8°, the intensity was recorded by a scintillation detector with a 10 μm aperture slit. The multilayer system was deposited on the acousto-active $LiNbO_3$ substrate and presented a resonance frequency of 218 MHz. Scans in ω-2θ space at different ultrasound amplitudes showed diffraction satellites with changing intensity distributions. In order to obtain the maximum energy diffracted towards a precise satellite, it was necessary to slightly shift the incident angle away from the exact Bragg angle of the multilayer. The satellite positions were calculated from the grating equation. The intensity distribution was simulated on the basis of the Takagi formalism taking into account the changed boundary conditions due to the modulated surface. The assumed ultrasound amplitude of 14 Å gave similar results as compared to the experimental data. A continuation of this work is reported in [Ros 98]. This time they applied a standing rather than a travelling surface acoustic wave by two superimposed travelling waves and provided also time-resolved

data. The main results were as follows. The diffracted intensity distribution accumulated in the detector scanning mode gave the same results for a standing and a travelling surface acoustic wave, thus the diffraction process on the superlattice was solely dependent on the ultrasound wavelength and amplitude. Furthermore, the diffracted intensity for a travelling wave was not dependent on time, contrary to the standing wave. There, the diffracted intensity at the angular position of the first order satellite was modulated in time by a sinusoidal law at twice the ultrasound frequency.

Zolotoyabko and Polikarpov measured surface acoustic waves as well on $LiNbO_3$ with monochromatic Cu-radiation in Bragg geometry in ω-2θ mode at an ultrasound frequency of 290 MHz [Zol 98]. At high ultrasound amplitudes the angular width and the integrated intensity of the reflection increased. Because of the limited angular resolution diffraction satellites could not be resolved. Special attention was paid to the maximum possible intensity gain with the background of tuneable synchrotron radiation monochromators. The experimentally achieved integral intensity gain was close to 3 at an ultrasound amplitude estimated to 0.17 nm together with a triplicate growth of the spectral angular width. The theoretical (kinematical) maximum gain for the integrated intensity was calculated to 4.7 for Cu-radiation. This value can in theory be increased when using shorter x-ray wavelengths. Basically the same device was investigated with grazing incidence diffraction in [Sau 98]. An increase of the diffracted intensity of up to 100% was measured. Simulations taking into account the varying structure factors by an additional Debye-Waller factor due to the lattice displacements induced by the surface wave lead to an estimate of the ultrasound amplitude for the longitudinal component of 0.04 nm for the highest applied voltage. In [Sau 99] diffraction experiments under almost 900 MHz surface acoustic wave excitation on GaAs were performed in normal Bragg geometry with synchrotron radiation at 12 keV. They were able to resolve up to 6 diffraction satellites on each side of the rocking curve and estimated the ultrasound amplitude to 0.2 nm. As the amplitude was increased up to this value, the number of appearing satellites also increased. Stroboscopic x-ray topography allowed them to image the wavefronts of a focussing and a parallel transducer.

[Tuc 00] investigated again the ZnO/Si device under surface acoustic wave excitation with high-resolution x-ray diffraction, this time with monochromatic synchrotron

radiation at 12 keV and at an ultrasound frequency of 365 MHz. They were able to resolve satellite reflections showing that the excited crystal acts as a dynamical diffraction grating. Measurements at different positions on the sample changed the intensity distribution and the angular satellite positions. They attributed this behavior to differing acoustic velocities at different distances from the acoustic source, either covered by the piezoelectric film or just on the surface of the pure silicon. Satellite reflections due to the interaction of x-ray Bragg diffraction with SAW propagating perpendicular to the scattering vector on single crystals of $LiNbO_3$ were systematically studied in [Tuc 01]. Parameters like the acoustic wavelength (4 μm, 12 μm, 30 μm), the acoustic amplitude (a few Angstrøm) and the x-ray energy (8 – 20 keV) were varied, which indicated that the intensity distribution depends on the ratio of x-ray and ultrasound penetration depths. The extinction lengths of the satellite reflections were much smaller than both of them. It should be noted that the FWHM of each satellite was identical to the main Bragg reflection without ultrasonic excitation. A model based on the kinematical approximation was established in order to derive the penetration depth and the amplitude of the ultrasonic wave. The model can not give adequate results if the x-ray penetration depth exceeds the acoustic penetration or if high-quality silicon crystals are investigated, because in both cases dynamical diffraction effects play a more important role. To finish the part about surface acoustic waves, very recently time-resolved diffraction measurements on the ZnO/Si device were presented in [Zol 02]. They excited a standing surface acoustic wave at a frequency of 580 MHz and observed diffraction satellites on the rocking curve in Bragg geometry with monochromatic x-ray energy of 21 keV. The satellite intensity reached 40 % of the main reflection oscillating sinusoidally as a function of time at twice the excitation frequency. The time dependence was measured at the intensity maxima position of the satellite reflection. The phase shift between the synchrotron x-ray bunches and the ultrasound excitation signal was changed with an electronic delay line in steps of 18 ps. A translation of the whole diffractometer along the incident x-ray beam was used as well to produce delay times of 100 ps. They state that diffractometer translation could be used to achieve and control delay times in the fs- and ps-range with a jitter of 1 fs dependent on the mechanical control of the diffractometer translation.

3.3. Applications

The discovered effects described in 3.1 and 3.2 were applied to characterize materials or to exploit them for x-ray beam optics. The very accurate determination of crystal structure factors and extinction lengths [Ent 91] was already discussed in 3.1.2 as well as the highly sensitive determination of crystal imperfection [Iol 95a, Khr 91a]. The improved analyses of crystal imperfection due to ultrasound exposition was also treated in [Zol 92b] and [Zol 93]. In [Zol 92b] the ratio of the integrated intensities of high amplitude – high frequency ultrasound excited crystal compared to an ambient one was measured. From the intensity difference between the theoretical kinematical limit and the measured ratio they deduced the grade of crystal quality. Zolotoyabko et. al. reported about the study of very small strains in semiconductor crystals [Zol 93]. The second silicon crystal in a double-crystal setup under Bragg diffraction condition and incident Cu-radiation was serving as the sample and was exposed to high-frequency surface acoustic waves close to the XAR-frequency. Applying small ultrasound amplitudes, they observed a narrowing of the rocking curve instead of the expected broadening due to unresolved satellite reflections. From the subtraction of both curves they deduced very small strain values, which would not have been possible to measure with normal diffraction methods without ultrasound excitation. The effect is qualitatively explained by the '*rectification*' of atomic planes due to the ultrasound influence. These planes were distorted by the intrinsic strain, such that the rocking curve tends to restore the ideal shape under ultrasound excitation. This narrowing of the rocking curve is only observed for this specific scattering geometry, since the simulations for the Laue geometry did not indicate such an effect [Zol 92a]. The application of ultrasound excited crystals to the focussing of x-rays is treated in [Mkr 85], [Nos 94a] and [Nos 94b]. In [Mkr 85] diffraction focussing of spherical x-radiation by a quartz crystal with a focal point outside the crystal is reported. A collimated MoKα x-ray beam is incident on the thin quartz crystal in Laue geometry, the diffracted beam is detected with an x-ray film. The source-to-crystal and the crystal-to-detector distances are varied. The focal point and its intensity are found to be dependent on the ultrasound amplitude; unfortunately the applied ultrasound frequency is not mentioned. In [Nos 94a] and [Nos 94b] the dynamical

diffraction focussing under the condition of X-ray acoustic resonance in vibrating perfect and elastically bent crystals are studied. The focal points are found to lie inside the crystal and are as well very sensitive to the ultrasound amplitude. These theoretical investigations treat a spherical X-ray wave diffracted in symmetric Laue geometry, the mathematical problem is analytically solved by applying the Takagi-Taupin equations.

In [Rev 95] a three-pole electromagnetic device was used to vibrate a perfect silicon crystal at about 100 Hz acting as a broadband vibrating Laue monochromator for synchrotron diffraction topography. In this experiment no ultrasonic waves were induced, but moreover the whole crystal was moved. The utilization of ultrasound excited crystals as monochromators with adjustable bandwidth and intensity throughput is discussed in [Pol 99a] and [Pol 99b], based on [Pol 94] and [Pol 97] (chapter 3.1.3). In [Pol 99a] an acoustically controlled $LiNbO_3$ double crystal Bragg-Bragg monochromator for synchrotron radiation was performed. The crystals were excited with 290 MHz surface acoustic waves by interdigital transducers, the technique to excite surface acoustic waves regularly used in the experiments of Zolotoyabko [Zol 92c]. It was possible to adjust the angular width of the diffraction profile and the flux for this ultrasound excited monochromator by varying the ultrasound amplitude. They were able to provide a 1.5-fold gain in the diffracted intensity and twice the FWHM of the diffraction profile when exciting both crystals at the same time. Higher excitation levels did not yield a higher gain. The resolution did not allow the observation of diffraction satellites even at this relatively high ultrasound frequency. In [Pol 99b] a Laue-Laue quartz double-crystal monochromator was studied. The intensity throughput could be increased six times due to the broadening of the rocking curve. The ultrasonic excitation was obtained via electrochemically deposited silver electrodes, the excitation frequency was around 6 MHz. The experiment was conducted with molybdenum radiation. No satellites were resolved, but the increase of the rocking curve width and the intensity gain as a function of the high frequency voltage showed a nearly linear behavior.

A double-crystal diffractive time-modulation of synchrotron radiation by the excitation of pulsed surface acoustic waves to both $LiNbO_3$-crystals is discussed in [Pol 98b]. The idea is the following. Since the application of ultrasound broadens the rocking curve, a slight misalignment of the crystals of a double-crystal Bragg monochromator with respect to the

exact Bragg condition forces its reflectivity close to zero when the ultrasound is switched off and nearly 100 % if the ultrasound is applied. If now the amplitude of the ultrasound is modulated in time by a pulsed-shaped signal, the x-ray intensity throughput will be modulated with the frequency of the modulation of the ultrasound. The frequency of the acoustic wave was 290 MHz, the logical function modulation frequency of 0.2 Hz during a rocking curve scan was chosen to show the feasibility of the switching between the rocking curve under ultrasonic excitation and the unexcited one. They obtained a diffraction efficiency of about 60%. The method is of course limited to the switching rapidity due to the modulation frequency signal.

The experiments published in [Tuc 97] are somehow based on the same philosophy. A high-frequency chopper for synchrotron radiation based on the grazing incidence diffraction of an x-ray beam on surface acoustic waves is presented. Pulsed SAW were synchronised to the synchrotron x-ray bunches and via the temporal structure of the satellite intensities certain x-ray flashes were selected out of the diffracted beam. The detector was detuned to the satellite positions. The technique opens the possibility of more flexibility in choosing the time structure of flashed x-rays for dedicated experiments. In [Tuc 98] basically the same subject is treated. It is pointed out that a mechanical chopper has more limitations than an ultrasound based one, which can work in the MHz-range.

Chapter 4

Theory and simulations: X-ray diffraction on ultrasound excited crystals

In the framework of this thesis the computer program SIMSAT (SIMulations of SATellites) was written. It serves to simulate x-ray diffraction patterns of ultrasound excited crystals in transmission scattering geometry (Laue case) and calculates the intensity distributions of ultrasound induced satellite reflections including their time dependence in a multi-parameter space with the parameters ultrasound frequency and amplitude, x-ray energy and Bragg reflection indices. The program is based on the dynamical diffraction theory of periodically modulated crystal structures as developed by Polikarpov [Pol 87, Pol 88, Pol 94, Pol 98], in part modified by the author to include asymmetric reflections and variable ultrasound propagation directions within the scattering plane. The basic underlying theoretical concept in the formulation given by Polikarpov and the adaptation for asymmetric reflections and variable ultrasound propagation directions is briefly discussed along with the simulation results separated into the small and large amplitude regime.

4.1. Theoretical background

Analytical expressions for the x-ray field diffracted on crystals in Bragg and Laue geometry being subjected to longitudinal or transverse ultrasonic waves taking into account non-resonant x-ray waves were derived in [Pol 87, Pol 88]. The approach is the following: The equations for the Bloch wave amplitudes were rewritten in a form analogous to the Schrödinger equation [Sak 94] and solved analytically, introducing the ultrasonic effect as a small perturbation and thus applicable for small ultrasonic amplitudes. In [Pol 88] the theoretical approach is extended to four-level x-ray acoustic resonance, which can appear in crystals modulated by transverse ultrasonic waves in

Bragg geometry because of the degeneracy of energy levels in ideal crystals. In [Pol 94] analytical expressions for the differential and integrated reflection coefficients of ultrasound excited crystals were derived also for large vibration amplitudes, based on the theoretical approach developed in [Pol 87] and [Pol 88]. The 'Ansatz' for the wave field in the crystal consists of an expansion into a series of slowly varying amplitudes including the additional lattice periodicity due to the ultrasound excitation. Insertion of this 'Ansatz' into Maxwell's equations leads to Bloch-wave solutions, which are rewritten in a matrix form analogous to Schrödinger's equation and solved analytically. Since this time the full expansion series is used, the resulting equations for the intensities of the diffracted waves in Laue geometry are in principle applicable also for large ultrasonic amplitudes and for the entire frequency range. Symmetrical Laue diffraction of plane-monochromatic waves in a crystal excited by high-frequency ultrasonic waves leads to a series of equally distant satellite reflections with the same peak value of 0.5 each, centered around the Bragg position of the main reflection. The integral intensity shows extinction beats as a function of the ultrasound amplitude due to the creation of new satellite reflections. The FWHM of the satellite reflections varies periodically as a function of the ultrasound amplitude like it was in principle observed in [Ent 88a]. Obviously the theory is valid for thick crystals, but not as thick as in the Borrmannn regime. The overall intensity of a double-crystal system and the energy resolution were also discussed, because the aim of the investigation was the application of an ultrasound excited crystal as part of a double-crystal synchrotron monochromator with an adjustable reflectivity for high-flux or optimized bandwidth experiments. Experimentally the satellites were not resolved. Experiments were carried out with silver-coated quartz plates in Laue-Bragg scattering geometry with Mo Kα radiation. Transverse ultrasonic waves were excited in the frequency range from 10 to 100 MHz. A three times broader Rocking curve and a nearly 3-fold enhancement of the peak intensity was observed by exciting only the first crystal. At a certain voltage applied to the electrodes (5-7 V), saturation of the intensity enhancement was reached.

With the availability of pulsed synchrotron sources time-resolved investigations in the ps-range found a growing interest in the 90's. The '*Resonance Time Modulation of X-ray Diffraction in Crystals Deformed by Ultrasound*' is discussed in [Pol 98]. Equations for

the time dependence of diffraction intensity of a crystal modulated by small-amplitude ultrasound were presented, based on the publications [Pol 87] and [Pol 94]. It was shown that the maximum time modulation of x-rays by ultrasonic vibrations is achieved at a frequency roughly $2^{1/2}$ times higher than the frequency for the x-ray acoustic resonance, being slightly dependent on the ultrasonic amplitude. This maximum time modulation strongly affects the satellite intensities close to the satellite peak positions. The theoretical developments in [Pol 87], [Pol 94] and [Pol 98] turned out to be quite useful, in an extended version, for the simulation of experimental situations described in this work.

4.1.1. Limit of small ultrasound amplitudes

A theory for the expected intensity distribution of x-rays diffracted in symmetric Laue geometry by ultrasonically excited crystals is published in [Pol 98]. The equation for the time-integrated intensity distribution derived by Polikarpov and Skadorov [Pol 98] is valid for all ultrasound frequencies and the limiting case of small ultrasound amplitudes. It has the following form:

$$I = \frac{1}{2(dT^2+1)} \cdot \left(1 + \frac{J_1{}^2 dT^2}{\left(\sqrt{dT^2+1} - \Delta\right)^2 + J_1{}^2} \right) \qquad 4.1$$

$J_1 = J_1(\mathbf{Ga})$ is the first order Bessel function of the first kind, its argument being the scalar product of the scattering vector **G** and the ultrasound amplitude vector **a**.

In equation 4.1 dT is the deviation parameter. Polikarpov [Pol 98] uses the deviation parameter in its limiting form for symmetrical Laue diffraction, here it is the general deviation parameter as defined in chapter 2 (equation 2.16), and thus includes the asymmetric Laue case.

The parameter Δ expresses the most general geometrical relation between the ultrasonic wavevector $\boldsymbol{\kappa}$ and the splitting of the dispersion surface. In the language used in chapter

2.6 it describes the extinction length of a reflection Λ in units of the ultrasound wavelength. It takes the following form:

$$\Delta = \frac{\kappa \cdot \sin(\theta-\alpha)}{k \cdot C_s \cdot \chi} \qquad 4.2$$

θ is the Bragg angle, α the angle between **κ** and **G**, k the absolute value of the x-ray wave vector, C_s the x-ray polarization factor and χ the electric susceptibility of a given reflection. In [Pol 98] the dimensionless parameter Δ was originally introduced for a particular geometry adapted for transverse ultrasonic waves: The ultrasonic wave vector was assumed to be perpendicular to the scattering vector (i.e., α = 90° in equation 4.2). Since the ultrasound wave vector may point in any direction within the scattering plane - which is the case in the experiments carried out during the course of this thesis - the equation for Δ was modified to include the general orientation of the ultrasound wave vector **κ** with respect to the scattering vector **G**.

To understand qualitatively the general dependence of the diffracted intensity distribution on both parameters Δ and the first order Bessel function J_1, which enter equation 4.1, the following two examples may serve. The dependence of the first order Bessel function on the amplitude of the ultrasonic wave is shown in figure 4.1 for four silicon reflections (440) and (220) as well as (-351) and (-571). To remind the reader, their reciprocal lattice vectors enter the calculation via the scalar product **Ga** in the argument of the Bessel function. These four particular reflections are chosen because they show i) the difference of the oscillatory dependence with increasing reflection order for the 220 and 440 reflections and ii) the other two reflections were most frequently measured on ID 15. The ultrasound amplitude vector is assumed to point along the [111]-direction in crystal space. The low amplitude case is defined by the condition **G**·**a** < 1 and is thus restricted to the linear part of the Bessel function close to a = 0.

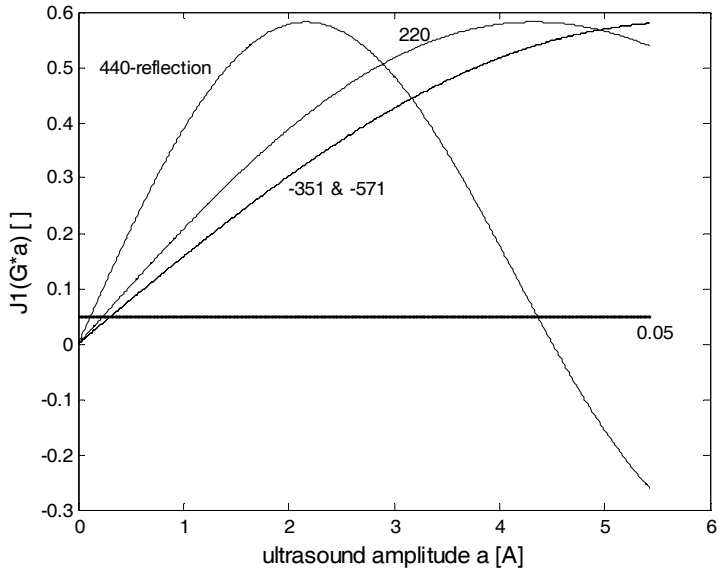

Figure 4.1: The first order Bessel function for the Si single crystal reflections (220), (440), (-351) and (-571) as a function of the ultrasound amplitude a. The period of the oscillation depends on the scalar product **Ga**. The amplitude direction is assumed to point in the [111]-direction, which leads to the same argument in the Bessel function for the (-571) and (-351)-reflection. For small amplitudes the dependence of J_1 on the sound amplitude is linear. This regime is the small amplitude limit of the diffraction theory. For a qualitative discussion of equation 4.1 on the parameters Δ and dT the value of the first order Bessel function is arbitrarily fixed to $J_1 = 0.05$, a value well within the validity regime of the small amplitude theory.

To visualize the qualitative dependence of the scattered intensity I (equation 4.1) on the two dimensionless variables Δ and dT, the value of the Bessel function can be fixed arbitrarily to any value close to the origin, here to 0.05, the same value as chosen by Polikarpov [Pol 98]. The intensity dependence can then be investigated as a function of Δ and dT alone, as it is done in the simulations presented at the beginning of chapter 4.3.1. Calculating the diffracted intensity distribution as a function of the dependent variables Δ and dT reduces the parameter space of independent variables and thus enables the visualization in three dimensions. The dependence of the scattered intensity on particular independent variables like the detailed ultrasound wave propagation and scattering geometry, the ultrasound frequency or x-ray energy are easily deduced by the functional dependence of Δ and dT on these variables. As an example the dependence of Δ on the ultrasound frequency and the energy of the primary x-ray beam is shown in figure 4.2 for the (-351) reflection of silicon and the [111] ultrasound propagation direction. Ultrasound

frequency and x-ray energy enter Δ in equation 4.2 via the wave vectors of the x-radiation and the ultrasonic wave for the ultrasound velocity of a given propagation direction. At a given x-ray energy and scattering geometry the greater Δ represents a higher ultrasonic frequency. Therefore Δ will often be called 'frequency parameter' throughout this work.

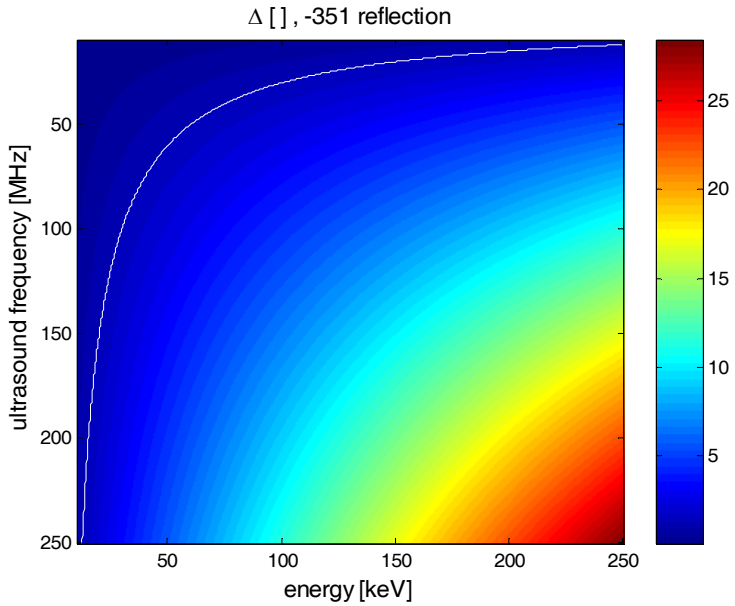

Figure 4.2: The dimensionless parameter Δ for the (-351)-reflection as a function of the ultrasound frequency and the x-ray energy. The white line indicates the maximum time modulation for ultrasound excited satellite reflections at $\Delta \approx 1.4$ (chapter 4.3.1).

The deviation parameter dT is visualized as a function of x-ray energy and deviation from the Bragg angle Δθ for the (-351) reflection of a (111) cut silicon crystal in appendix A.1 (figure A.1a) and for the (-571) reflection in figure A.1b.

Time dependent intensity distribution

In the low amplitude case the time-dependent intensity distribution IM can be written as the sum of a time-integrated (time-independent) part I (equation 4.1) and a time-modulated part M [Pol 98],

$$IM = I + M\cos\omega t \qquad 4.3$$

The parameter time is denoted as t, ω being the angular frequency of the ultrasonic wave. M takes the following form:

$$M = \frac{1}{dT^2 + 1} \cdot \left(\frac{J_1 dT\left(\sqrt{dT^2 + 1} - \Delta\right)}{\left(\sqrt{dT^2 + 1} - \Delta\right)^2 + {J_1}^2} \right) \qquad 4.4$$

The first order Bessel function J_1, the deviation parameter dT and the frequency parameter Δ have the same meaning as in the description of the time-integrated intensity distribution discussed above.

4.1.2. Large ultrasound amplitudes

The intensity distribution for x-rays diffracted in crystals strongly excited by high amplitude ultrasound was calculated in [Pol 94]. It is presented here in a different form. Equation 12 of [Pol 94] is rewritten in a form similar to the case of low amplitudes (equation 4.1). It becomes therefore possible to compare the structure of the mathematical expressions with more ease. In addition, the simulations for large ultrasound amplitudes (chapter 4.3.2) can then be discussed in the same way as in the limit of low amplitudes (chapter 4.3.1). Again, Δ and dT are modified in a way that it is possible to consider the ultrasonic wave vector pointing in any direction of the scattering plane and to treat asymmetric Laue cases (equations 4.2 and 2.16). The equation for the time-integrated intensity distribution takes then the following form:

$$I = \frac{1}{2(dT^2 + {J_0}^2)} \cdot \left({J_0}^2 + \sum_n \frac{{J_n}^2 dT^2}{\left(\sqrt{dT^2 + {J_0}^2} - n\Delta\right)^2 + {J_n}^2} \right) \qquad 4.5$$

J_0 and J_n being the zeroth and the n-th order Bessel function, respectively.

First, the reduction of equation 4.5 to equation 4.1 in the limiting case of small amplitudes is shown. The Bessel functions of orders zero to three and twenty are plotted in figure 4.3. The Bessel function of order zero is the only one starting like a cosine function for very small arguments, all the higher orders start like a sine function. Moreover, as higher the order of the Bessel function, as longer it remains zero as a function of the amplitude. In the required summation process in equation 4.5 higher orders come only into account, if the ultrasound amplitude is sufficiently large. For rather small ultrasonic amplitudes the zero order Bessel function can be approximated by the value one and the sum over n components reduces to the first order Bessel function. With these approximations equation 4.5 reduces to 4.1, thus the high amplitude case reduces to the equations for the low amplitude case.

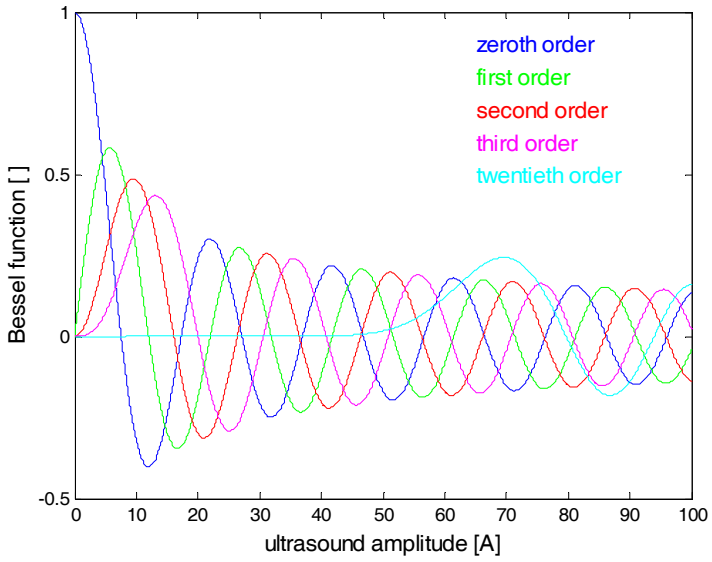

Figure 4.3: The Bessel functions of order zero to three and twenty as a function of the ultrasound amplitude. The diminishing maxima of the different orders are shifted.

In addition, the consistency of equations 4.1, 4.4 and 4.5 with the dynamical theory of diffraction should be noted. If no ultrasonic wave is excited in the crystal, the limiting cases of vanishing ultrasound frequency and amplitude have to be considered. In that case the time dependent component M approaches 0, $M \rightarrow 0$, and the time independent component I approaches for small and large ultrasound amplitudes the equation for the

Laue diffraction profile in the case of a thick crystal due to the dynamical theory with a Lorentzian line shape:

$$I = \frac{1}{2(dT^2 + 1)} \qquad 4.6$$

Without ultrasound excitation, no intensity changes with time can be expected and the intensity distribution accordingly agrees with the results from dynamical diffraction for a thick crystal (chapter 2.6).

4.1.3. Angular positions of ultrasound excited satellite reflections

A schematic view of the diffraction geometry is presented in figure 4.4. The sample has to be rotated around the tail of the diffraction vector (i.e. the origin of the reciprocal lattice) to bring the superlattice point $\mathbf{G} + \boldsymbol{\kappa}$ onto the Ewald sphere. Then the satellite intensity is diffracted to the detector with a large aperture. The kinematical (or geometrical) theory predicts satellite reflections at angular positions according to the equation:

$$\Delta\theta = \frac{\kappa \cdot \sin(\theta - \alpha)}{k \cdot \sin(2\theta)} \qquad 4.7$$

This equals the approximation x/G (the arc is approximated by x, the radius by G, figure 4.4), which is valid in all considerable cases of $\boldsymbol{\kappa}$ and $\mathbf{G}$ since the absolute value of the ultrasonic wave vector κ is much smaller than that of the diffraction vector G, the quotient being of the order of 10^{-4}.

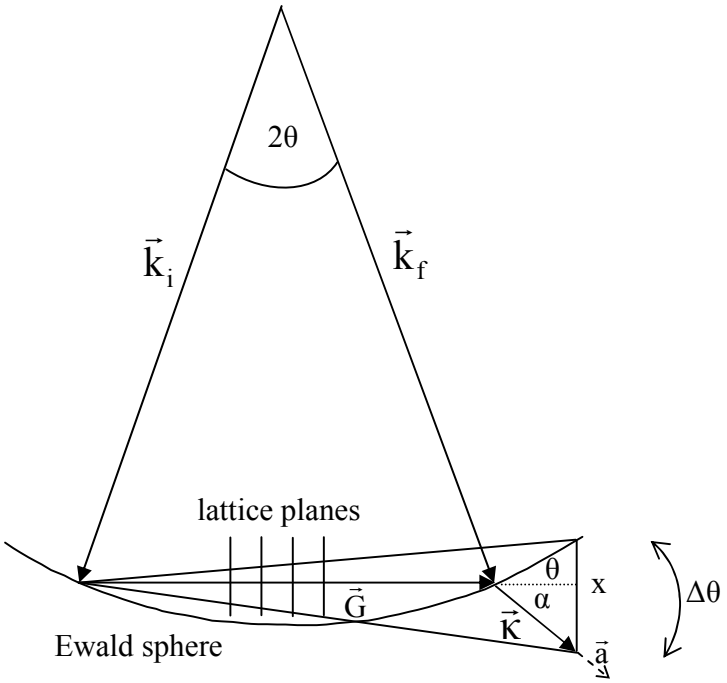

Figure 4.4: The geometrical construction for the determination of the angular positions of ultrasound excited satellite reflections.

Applying the dynamical diffraction theory leads to the following equation for the calculation of the satellite positions:

$$\Delta\theta = \pm\sqrt{\left(\frac{\kappa\cdot\sin(\theta-\alpha)}{k\cdot\sin(2\theta)}\cdot\sqrt{\frac{|\gamma_h|}{\gamma_0}}\right)^2-\left(\frac{C_s\cdot\chi}{\sin(2\theta)}\cdot\sqrt{\frac{|\gamma_h|}{\gamma_0}}\right)^2-\frac{\chi_0}{2\sin(2\theta)}\left(\frac{\gamma_h}{\gamma_0}-1\right)} \qquad 4.8$$

This equation is obtained as follows. Intensity maxima of the satellite reflections occur, if the bracketed term in the denominator of equation 4.5 equals 0. The resulting equation is solved for Δθ, which yields equation 4.8. This equation is similar to the one published in [Pol 94], but here it is also modified to include the asymmetric Laue case and ultrasonic

wave vectors pointing in any direction in the scattering plane, i.e. it is not restricted to ultrasound directions perpendicular to the diffraction vector. Note, however, that for the symmetric Laue case the last term equals to zero, and for high energies the atomic susceptibility χ becomes so small that the second bracketed term is negligible. Under these conditions equations 4.8 and 4.7 equal each other.

4.1.4. The FWHM of ultrasound excited satellite reflections

In the foregoing discussion of the intensity distributions, changes in the FWHM of the satellite reflections were not yet treated. The sound wave amplitude via the characteristics of the Bessel functions, the reflection order and the x-ray energy determine the FWHM of the satellite reflections. In this paragraph the FWHM of ultrasound excited satellite reflections is discussed in more detail. After [Pol 94] the halfwidth of the satellite reflection of order n can be calculated to:

$$\mathrm{FWHM} = \frac{2 \cdot \left| \chi_{hkl} \cdot J_n(\vec{G} \cdot \vec{a}) \right|}{\sin(2\theta)} \qquad 4.9$$

This equation does not take into account the asymmetry of the diffraction problem and is applicable for the ultrasound wave vector lying perpendicular to the diffraction vector. It can be taken as a very good approximation also for the asymmetric diffraction geometry and for ultrasonic wave vectors lying close enough to the direction perpendicular to the scattering vector. Close enough means here values up to 15°. The characteristics of the FWHM will not change because for high energies influences due to asymmetric reflections become less important since the Bragg angles are very small. High x-ray energies always lead to a value close to 1 for the asymmetry coefficient γ_h/γ_0.

After the choice of a reflection, the FWHM of the satellite reflections is a function of the x-ray energy (via the susceptibility and the diffraction angle θ), the ultrasound amplitude vector and the satellite order. Different satellite orders do not have the same FWHM. The ultrasound propagation direction and its oscillation mode (longitudinal, transversal, or

coupled) define thereby the ultrasound amplitude vector. In addition it should be noted that the FWHM of a satellite reflection does not depend on the ultrasonic frequency.

4.2. The computer code SIMSAT

As a part of this thesis the computer code SIMSAT was written in order to simulate x-ray diffraction patterns of ultrasound excited crystals in transmission scattering geometry (Laue case). SIMSAT calculates the intensity distributions of ultrasound induced satellite reflections including their time dependence in a multi-parameter space with the parameters ultrasound frequency and amplitude, x-ray energy and Bragg reflection indices. The program SIMSAT is written in the computing language 'Matlab' [Mat 02] and runs on a cluster of computing machines based on the operation system 'LINUX'. The advantage of such a highly developed computing language is the availability of readily implemented functions and visualization/graphical tools. To speed up the processing, it is very advantageous to vectorize the calculus as much as possible, thus to use matrix notations and matrix algebra rather than loops [Mat 02]. This is especially useful if calculations have to be carried out in a multi-parameter space. However, if the dimension of this space becomes too high, the use of loops is hardly avoidable. Nevertheless the program code SIMSAT was written in matrix notation as much as possible.

SIMSAT includes various subroutines. Each subroutine calculates a particular case, e.g., the time-integrated scattered intensity distribution in the limit of small ultrasound amplitudes or the time-dependent intensity distribution of satellite reflections for large ultrasound amplitudes. Subroutines to calculate basic crystallographic parameters like the atomic susceptibility, for example, are implemented in the main code as well as the calculation of ultrasound propagation parameters.

Initially, the program asks for input parameters which are listed in table 4.1 together with the output parameters. All of the input parameters can be chosen freely by the user, except for the atomic scattering factor f_0. For silicon, f_0 is plotted in chapter 2, figure 2.2, otherwise we refer to tabulated values [XOP 02, Int 92]. However, the values of f_0 for the reflections investigated in this work are already included in the program code.

The first set of parameters in table 4.1 written in black represents basic crystallographic quantities important for x-ray diffraction phenomena on crystals in general. They are independent of the modulation of the crystalline lattice by the ultrasonic wave. The middle part (in blue) denotes quantities which are needed to describe the excitation of ultrasonic waves within a crystal. The third set of parameters written in green are the output parameters calculated and plotted by SIMSAT. The independent variables required to calculate the dependent parameters are given in red in table 4.1.

Table 4.1: Input and output parameters of the simulation code SIMSAT.

Input parameters:	Dependent on:	Output parameters:	Dependent on:
Energy E [keV]		X-ray wavelength λ [Å]	(E)
lattice constant a_0 [Å]		d-spacing d [Å]	(a_0, h, k, l)
Miller indices h k l		reciprocal lattice vector |**G**| [1/ Å]	(d)
surface normal n1 n2 n3		structure factor F(hkl)	(f, h, k, l)
atomic scattering factor f	(sinθ/ λ)	atomic susceptibility χ	(a_0, λ, F(hkl))
polarization factor photons Cs		bragg angle θ [°]	(d, λ)
ultrasound frequency uswfreq [MHz]		asymetric angle β [°]	(n1, n2, n3, h, k, l)
ultrasound amplitude a [Å]		x-ray wavevector |**k**| [1/ Å]	(λ)
ultrasound direction uswh uswk uswl		extinction length [μm]	(E, a_0, h, k, l, n1, n2, n3, f, Cs)
angular range Δθ [arcsec]		zeroth order Bessel function Jo	(**G**,**a**)
time range t [ns]		n-th order Bessel function Jn	(**G**,**a**)
		ultrasound wavespeed c [m/s]	(uswh, uswk, uswl)
		ultrasound wavelength λusw [Å]	(c, uswfreq)
		ultrasound wavevector |**κ**| [1/ Å]	(λusw)
		angle α = ∢ (**G**, **κ**) [°]	(h, k, l, uswh, uswk, uswl)
		intensity distribution I	(all input parameters except t)
		satellite positions $\Delta\theta^n$ [arcsec]	(all input parameters)
		FWHM of the satellites $\Delta\theta^n_{HW}$ [arcsec]	(χ , Jn, θ, Cs)
		time-resolved intensity distribution IM	(all input parameters)

The structure of the program code SIMSAT is presented as a flow diagram in figure 4.5. Once started, the program asks to enter the input parameters. Since the calculations are

valid for the entire frequency range, we do not need to distinguish between low and high ultrasound frequencies, thus ‘all frequencies’ is marked there.

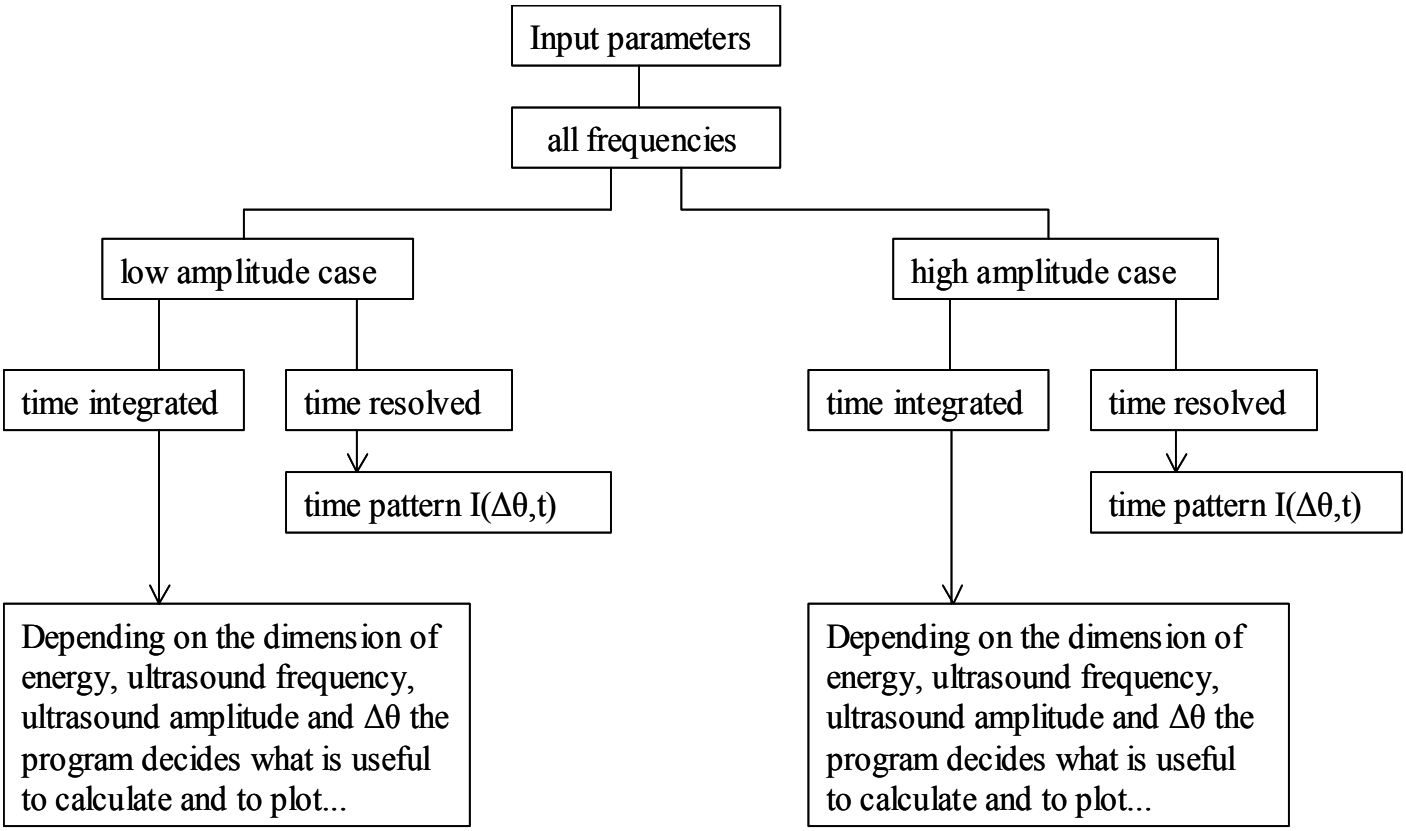

Figure 4.5: Structure of the different possibilities of the computer code SIMSAT.

After the user has chosen the frequency of the ultrasonic wave, the decision to calculate intensity distributions in the limit of low or high ultrasound amplitudes must be made. The criterion for the low amplitude case is thereby $\mathbf{G}\cdot\mathbf{a} < 1$ [Ent], given by the scalar product of the reciprocal lattice vector **G** with the ultrasound amplitude vector **a**. The next selection concerns the time dependence of the simulated intensity patterns. Choosing the time-resolved case then yields the time pattern $I(\Delta\theta,t)$ of the scattered intensity calculated over the time and angular range defined by the user. Single values rather than parameter ranges are allowed as an input for the x-ray energy, the ultrasound frequency and amplitude for the calculation of time-resolved intensity patterns. If the calculation of

the time-integrated intensity distribution is selected, the output depends on the dimension of the input parameters. If the user chooses for example an energy range, a range for the angular deviation from the Bragg angle but one single value for the ultrasound frequency and amplitude, a plot I(E,Δθ) for this particular frequency and amplitude will be generated. If also only one single value is chosen for the x-ray energy, the intensity distribution I(Δθ) for the otherwise constant parameters will be generated. In general, a maximum of two independent variables can enter the simulations as a range of parameters to be able to generate plots in three dimensions; all the other parameters are kept constant for this particular simulation.

4.3. Simulation results

In the following paragraphs simulation results of time-integrated and time-dependent ultrasound induced satellite diffraction patterns are presented for small and large ultrasound amplitudes. In the first part of 4.3.1 the diffraction patterns are calculated as a function of the dimensionless parameters Δ and dT to discuss the general observations. Later on, the diffracted intensity distribution is calculated as a function of the experimental observables x-ray energy, Bragg angle, reflection order as well as ultrasound frequency and amplitude.
Since the total observable intensity in the limit of small sound wave amplitudes can be written as a linear superposition of a time-integrated part I and a time-modulated part M (equation 4.3), separate simulations are presented for these individual contributions to the scattered time-dependent intensity IM.

4.3.1. Limit of small ultrasound amplitudes

The intensity distribution in dependence of the deviation parameter dT and the frequency parameter Δ is visualized in figure 4.4a. At Δ = 1, the x-ray acoustic resonance, a pair of ultrasound induced satellite reflections is excited and appears symmetrically with respect to the main reflection. The satellite reflections are much sharper than the main reflection,

the ratio of the FWHM between satellite and main reflection is 0.05. The satellite reflections achieve a maximum intensity value of 0.5 immediately beyond the x-ray acoustic resonance (figure 4.6a). This value is the theoretical limit of diffracted intensity for a thick crystal in the Laue case and the same than for the main reflection. With increasing frequency parameter the separation of the satellites from the main reflection continuously increases. The satellite positions follow thereby a square-root law in angle-frequency space, which will be discussed in further details in chapter 4.1.3. It should be noted that the main reflection is unaffected in position and intensity by the appearance of satellites with changing Δ. This is due to the fact that the ultrasound induced superlattice creates new reciprocal lattice points, which diffract independently from the lattice of the unperturbed crystal.

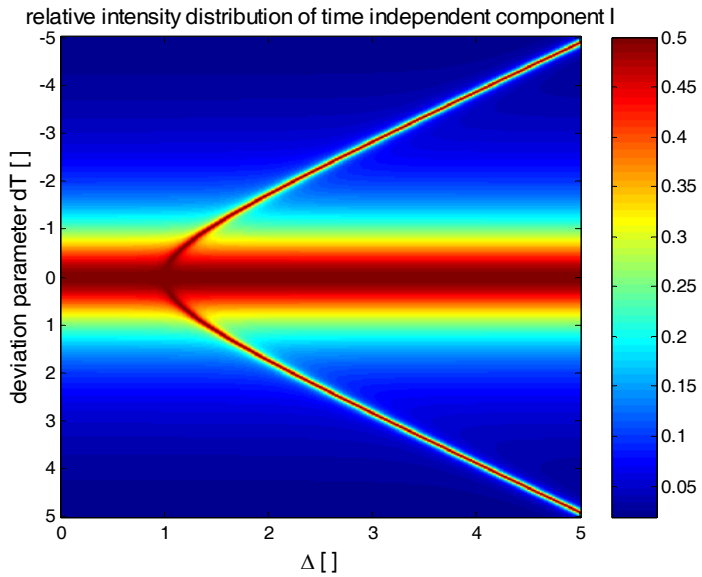

Figure 4.6a: Time integrated intensity distribution as a function of the frequency parameter Δ. Well above the x-ray acoustic resonance the angular distance from the main reflection is nearly linearly increasing.

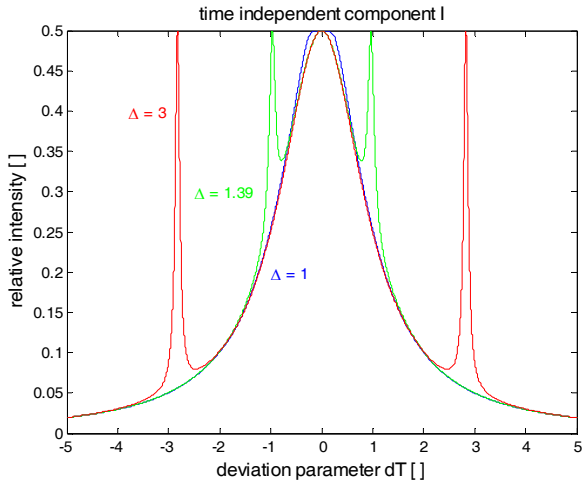

Figure 4.6b: The time integrated intensity distribution at the x-ray acoustic resonance (Δ = 1), the maximum time modulation of the satellite reflection (Δ = 1.39) and a higher value of Δ = 3.

Figure 4.6b shows the angular intensity distribution for the three different discrete values of the frequency parameter Δ = 1, 1.39 and 3. These values correspond to the x-ray acoustic resonance, the value Δ for which the maximum time modulation is achieved and a value, where the satellites are already well separated from the main reflection.

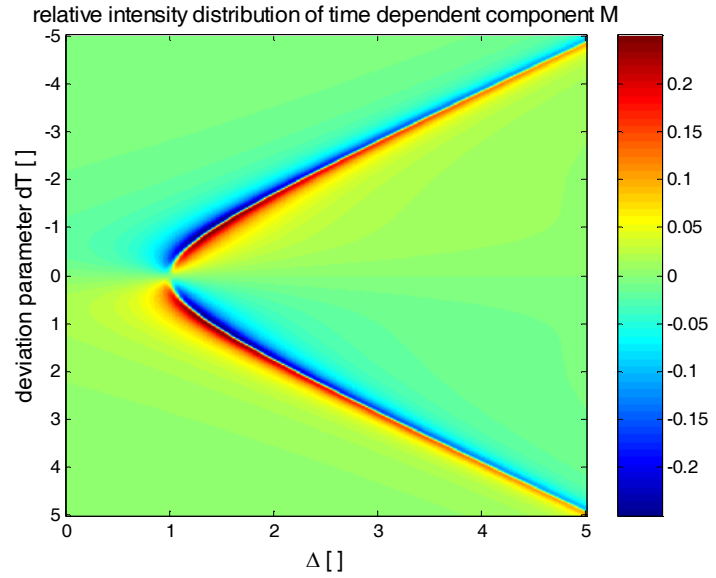

Figure 4.7a: Intensity distribution of the time modulated component M as a function of the frequency parameter Δ. The intensity modulation acts on the satellite intensities close to the peak position and leads to an asymmetry in the intensity distribution of M. At increasing Δ the time modulated component M becomes less important.

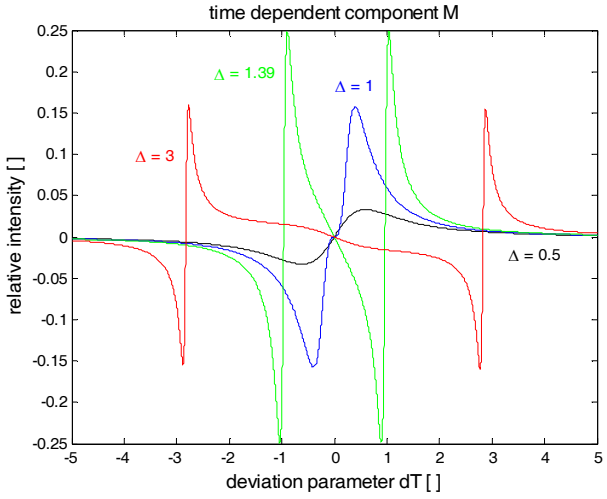

Figure 4.7b: The time modulated component M at the x-ray acoustic resonance (Δ = 1), the maximum time modulation of the satellite reflection (Δ = 1.39) and a higher value of Δ = 3.

Figure 4.7a visualizes the time-modulated component M of the satellite intensities as given by equation 4.4 up to a value of the frequency parameter Δ = 5. Figure 4.7b shows the angular intensity distribution of the time-modulated component M for the three different discrete values of the frequency parameter Δ = 1, 1.39 and 3. It should be pointed out that there is no time modulation of the reflection intensity at the exact

satellite position (figure 4.7b compared to figure 4.6b). Instead, the time modulation acts on the satellite intensities very close to the peak position and leads to an asymmetry in the intensity distribution of the satellites.

The strength of the time modulation depends on the frequency parameter Δ. The value for the strongest time modulation is the maximum value of M as a function of the frequency parameter Δ, which is determined to Δ = 1.39. Analytical results [Pol 98] give the value $\Delta = 2^{1/2} \pm J_1(\mathbf{Ga})$ for a maximum time modulation, thus the value is slightly dependent on the ultrasound amplitude for a given reflection. Since we fixed the value of the Bessel function in these simulations to 0.05, the analytical result yields Δ = 1.46 and Δ = 1.36 for the maximum time modulation. Apart from the weak dependence on the sound amplitude, the value of M for the maximum time modulation is independent from other influences. In addition, the value of the Bessel function is small by definition in the low amplitude limit, thus the value of Δ for the maximum time modulation will not change dramatically with varying ultrasound amplitudes. All values between $\Delta = 2^{1/2} + J_1(\mathbf{Ga})$ and $\Delta = 2^{1/2} - J_1(\mathbf{Ga})$ are very close to the maximum time modulation. This is manifested in the rather flat top in figure 4.7c. With increasing values of Δ the time modulated contribution to the diffraction pattern decreases and the observable time-dependent satellite intensities show less time modulation (figure 4.7c).

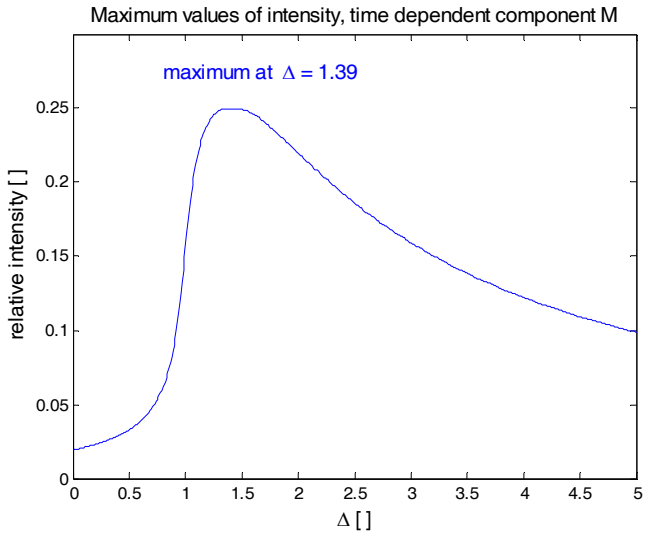

Figure 4.7c: The maximum values of the time modulated component M (figure 4.7a) as a function of Δ. The maximum value of M and thus the largest time modulation is found at Δ = 1.39.

Since we have now shown separately the contributions of the time-independent and time-modulated part of the satellite intensities to the diffraction pattern, in this section the superposition of both contributions will be discussed. This superposition is the observable intensity diffracted by an ultrasound excited crystal in a real time-resolved experiment.

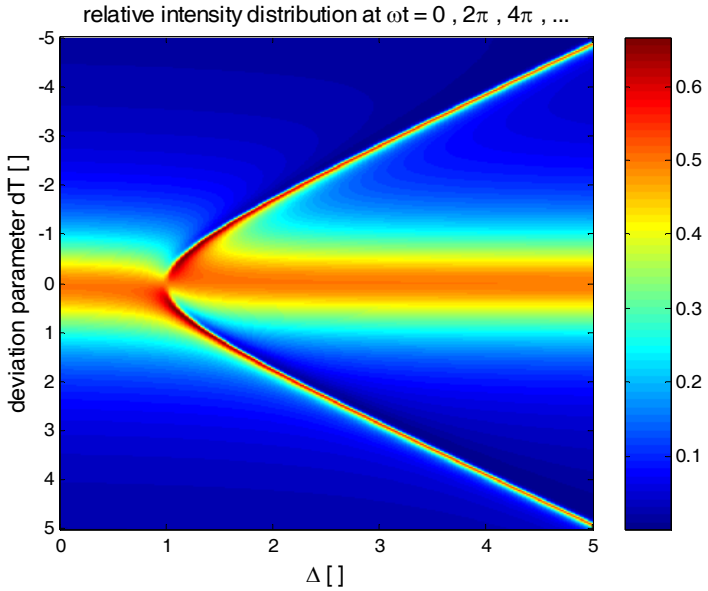

Figure 4.8a: The total time dependent intensity distribution IM = I + Mcosωt as a function of the frequency parameter Δ at time snapshots corresponding to cosωt = 1. At increasing Δ the contribution of M to the total intensity distribution decreases.

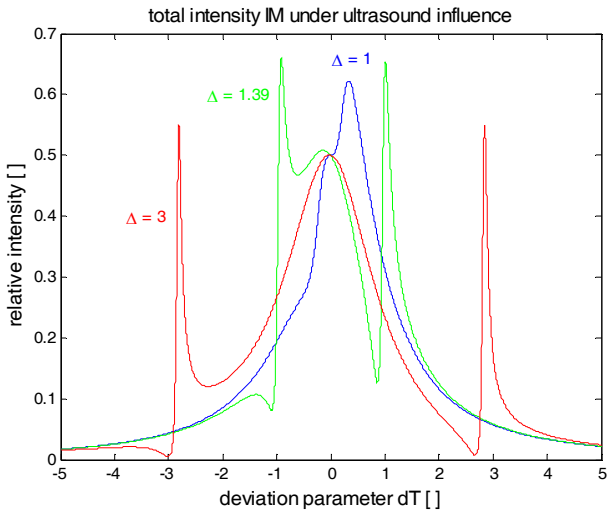

Figure 4.8b: The total time dependent intensity distribution IM for time snapshots corresponding to cosωt = 1 at the x-ray acoustic resonance (Δ = 1), the maximum time modulation of the satellite reflection (Δ = 1.39) and a higher value of Δ = 3.

Figure 4.8a shows the total time-dependent intensity distribution IM as a function of the frequency parameter Δ up to a value of Δ = 5, the sum of the time independent part I and the time modulated part M due to equation 4.3. The time-dependent intensity distribution IM is calculated for time snapshots corresponding to cosωt = 1. For the same snapshots

the time-dependent intensity distribution IM is visualized in figure 4.8b for the three different discrete values of the frequency parameter $\Delta = 1$, 1.39 and 3. The asymmetry of the time-modulated part M now shows up again in the total diffraction pattern. It is also due to the time-modulated part M that the satellite intensity in the observable diffraction pattern even exceeds the maximum intensity of the main reflection of 0.5 at this time instant (figure 4.8a and figure 4.8b).

After the discussion of the two contributions I and M to the total time-dependent intensity distribution IM and their dependence on the frequency parameter Δ, time-dependent intensity distributions are now shown as a function of time for particular values of Δ in figures 4.9 – 4.14. The time-dependent intensity distributions IM are visualized for values of the frequency parameter Δ below the x-ray acoustic resonance ($\Delta = 0.5$ and $\Delta = 0.8$), at the x-ray acoustic resonance ($\Delta = 1$), in the maximum of the time modulation ($\Delta = 1.39$), and well above the x-ray acoustic resonance ($\Delta = 2$ and $\Delta = 4$). These simulations give the experimentalist an idea about the strength of the expected time-dependent effects on the diffraction pattern. Already at values of Δ well below the x-ray acoustic resonance the intensity distribution in the main reflection starts to oscillate periodically from one side of the center of the main reflection to the other (figure 4.9 and 4.10). At the x-ray acoustic resonance intensity concentrates in distinct maxima greater than 0.5 with a separation of the ultrasound period. These intensity maxima develop on the trailing edge on both sides of the main reflection with a phase shift of half the ultrasound period. This is the onset of a satellite reflection (figure 4.11). At the strongest time modulation $\Delta = 1.39$, well separated satellites have appeared on both sides of the Bragg position. The maximum intensity of the satellite reflection oscillates periodically with the ultrasound frequency on each side of the main reflection (figure 4.12). With further increase of the frequency parameter Δ, the satellites become more separated from the main reflections Bragg position, but show less and less time modulation. The main reflection itself shows now again an oscillatory intensity like below the x-ray acoustic resonance, but with a smaller amplitude in the deviation parameter dT (figure 4.13 and 4.14).

Figure 4.9 – 4.14 (following page)**:** Time resolved intensity distribution IM for values of the frequency parameter $\Delta = 0.5$, 0.8, 1, 1.39, 2, 4. The angular separation of satellite reflections is larger at higher Δ, but the time modulation is less.

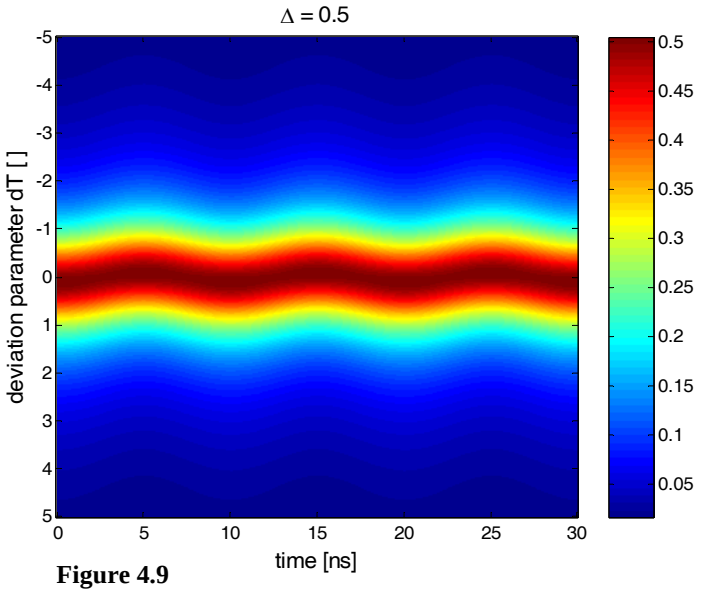

Figure 4.9

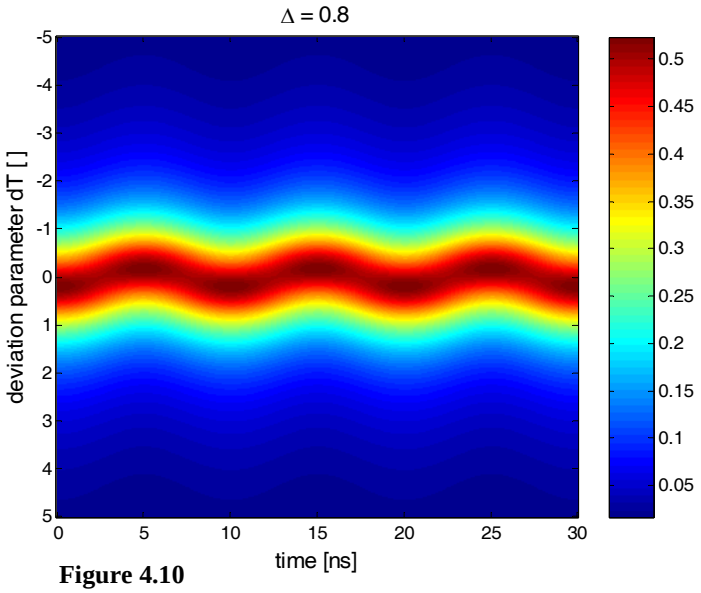

Figure 4.10

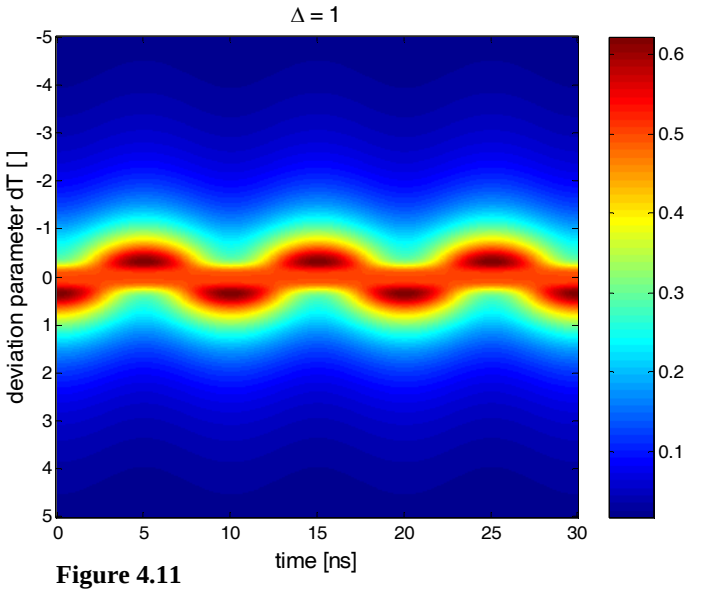

Figure 4.11

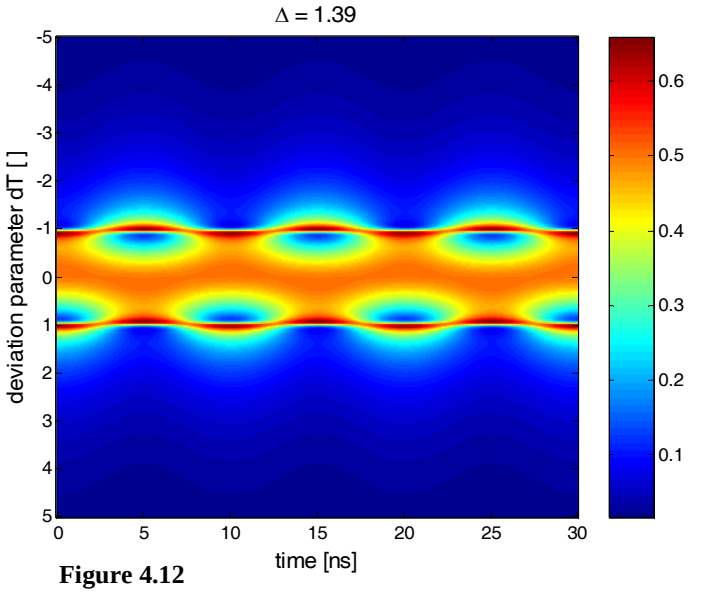

Figure 4.12

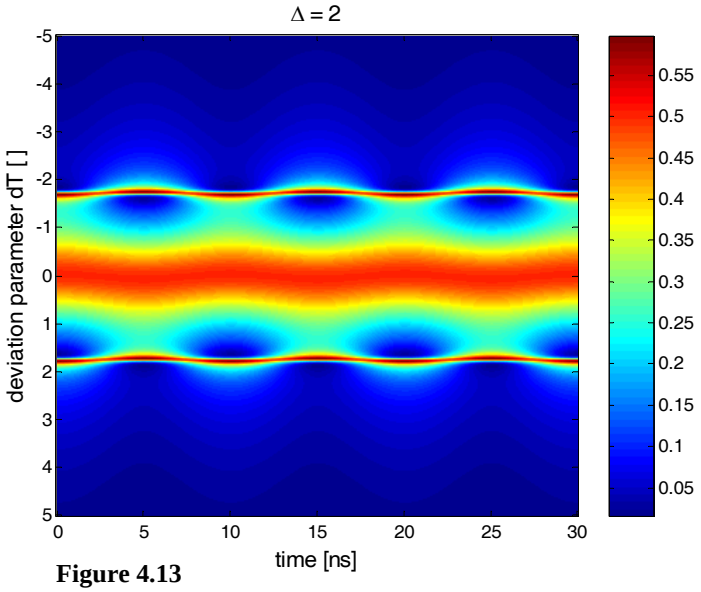

Figure 4.13

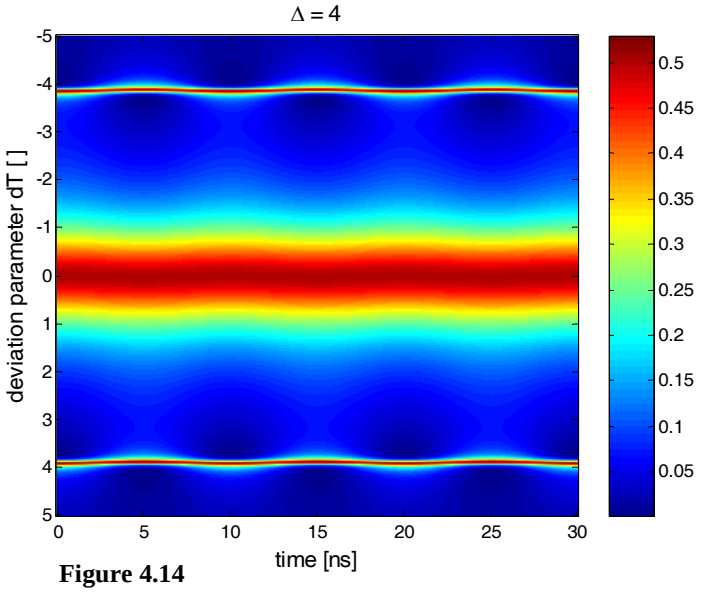

Figure 4.14

Until now, the general behavior of the time-integrated and time-resolved intensity distributions has been discussed. Next, simulations are presented, which are calculated in the space of experimentally accessible variables like the frequency and amplitude of the ultrasonic wave, the x-ray energy, the reflection order and the relative deviation from the diffraction angle $\Delta\theta$. This change from the dependent and dimensionless variables Δ and dT used in the dynamical diffraction theory to experimentally accessible independent quantities makes a direct comparison of experimental data with the simulations possible. Further it allows the experimentalist an easier design of the experiments concerning the choice of variables and parameter values. The transformation between the dimensionless and independent variables is achieved via equations 4.2 and 2.16. Δ is a function of the ultrasound frequency and the x-ray energy for a given reflection and ultrasound propagation direction (figure 4.2), the deviation parameter dT is a function of the Bragg angle deviation $\Delta\theta$ and the x-ray energy, once the reflection order is chosen (figures A.1a and A.1b). The white curve in figure 4.2 represents a constant height line indicating the value $\Delta = 1.39$ for the maximum time modulation.

Furthermore, reflectivity curves will be calculated as a function of the ultrasound amplitude, which implies that the Bessel function is no longer fixed to the value $J_1(\mathbf{Ga}) = 0.05$ as in the qualitative simulations in (Δ, dT)-space. Figure 4.3 shows the range of numerical values the Bessel function achieves in these simulations.

Most of the experiments on beamline ID 15 were carried out on the silicon reflections (-351) and (-571), and the simulations shown in this chapter are done for these two reflections. The x-ray energy of 100 keV and the ultrasound frequency of about 125 MHz represent as well typical experimental conditions. Amplitudes of the ultrasonic waves in the crystal are a priori unknown. The knowledge of the excitation voltage applied to the transducer does not allow to determining the ultrasound amplitude. The simulations are thus calculated on the basis on assumed amplitudes of the ultrasonic wave propagating in the crystal.

To get an idea about the influence of the different variables of the multi-parameter space on the satellite positions and intensity distributions, several computer experiments are carried out. Let us imagine to measure rocking curves of the (-351)-reflection of a (111)-

cut silicon crystal, excited by longitudinal ultrasonic waves propagating in the [111]-direction. A monochromatic x-ray beam is diffracted on the crystal in Laue transmission geometry. The angular resolution of the diffractometer is set to 0.001", an order of magnitude better as it is possible for a real experiment on the beamline ID 15, in order to resolve all details of simulated diffraction satellites with a FWHM down to 0.005". Now, apart from the relative rocking angle, there are three free parameters left: the x-ray energy, the ultrasound frequency and amplitude. Only one of these relevant parameters is changed in the simulations, the two others are kept constant.

The first parameter to be varied is the ultrasound frequency, at the x-ray energy of 100 keV and the low ultrasound amplitude of 0.2 Å. Calculating one rocking curve at every frequency value, the frequency is subsequently changed from 0 to 150 MHz in the simulation. The expected intensity distribution is shown in figure 4.15. This corresponds qualitatively to the plot of figure 4.6a in the dimensionless (Δ, dT)-space. In this particular example the x-ray acoustic resonance condition is met at a sound wave frequency of 20 MHz and diffraction satellites appear.

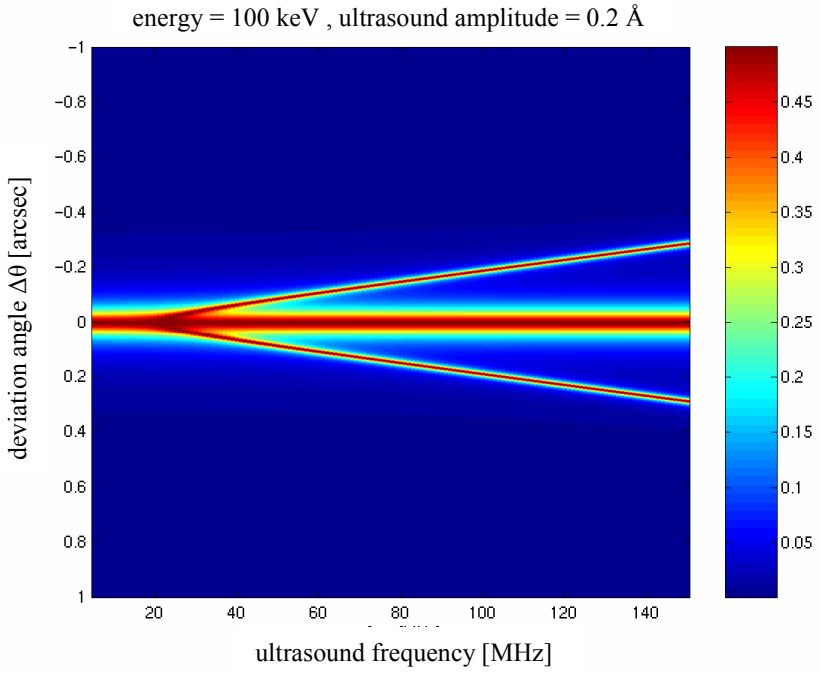

Figure 4.15: The intensity distribution as a function of the deviation angle Δθ and the ultrasound frequency at the x-ray energy of 100 keV and the ultrasound amplitude of 0.2 Å.

Already before the satellites begin to separate from the main reflection, a slight broadening of the rocking curve by the FWHM of the arising satellite reflections is observed. This is the regime of a gradient crystal. The gradient is induced by the time dependent strain. With increasing frequency, the satellites separate from the main reflection. This angular splitting from the main reflection is linear with increasing frequency. The satellites show a smaller FWHM than the main reflection and have the same maximum height of 0.5. This is valid for all frequencies higher than the x-ray acoustic resonance frequency.

In a second computer experiment the x-ray energy of the monochromatic beam is successively changed, at a constant ultrasound frequency of 125.6 MHz and an ultrasonic amplitude of 0.2 Å (figure 4.16). The resulting intensity distribution as a function of the x-ray energy is substantially different from the simulation at varying ultrasound frequency. At low x-ray energies, the asymmetry of the diffraction geometry plays an important role. This asymmetry of the diffraction profile is only dependent on the choice of reflection order and crystal cut, but the broadening is governed by the ultrasound amplitude. At the x-ray energy of about 20 keV satellite reflections appear. The asymmetry is still visible at this x-ray energy for which the x-ray acoustic resonance occurs. Close to the x-ray acoustic resonance, the separation of the satellite positions from the main reflection is not linear with increasing x-ray energy.

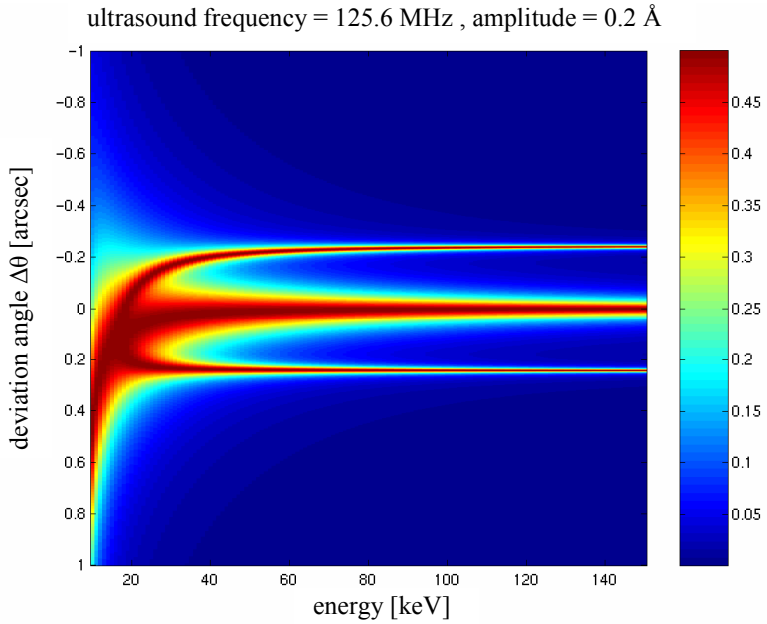

Figure 4.16: The intensity distribution as a function of the deviation angle Δθ and the x-ray energy at the ultrasound frequency of 125.6 MHz and the ultrasound amplitude of 0.2 Å.

Above an energy of 50 keV in this particular example, the separation of the satellites from the main reflection remains almost the same (figure 4.16). Higher energies do not lead to a still larger separation of the satellites. Both, the halfwidth of the main reflection and those of the satellites decrease with increasing x-ray energy. This is not the case as a function of the ultrasound frequency.

In a third computer experiment the ultrasound amplitude is smoothly increased at a constant x-ray energy of 100 keV and an ultrasound frequency of 125.6 MHz. Under these conditions satellites are excited and appear as soon as the sound wave has a non-zero amplitude. As it is for increasing frequency, the halfwidth of the main reflection then is again not affected as a function of increasing ultrasound amplitude. On the other hand, the satellite reflections are getting continuously broader with higher amplitudes (figure 4.17). The peak value 0.5 of the satellites intensity remains unchanged like in the two foregoing computer experiments. This is also valid for very small ultrasound amplitudes, which is hardly visible in figure 4.17 due to the scaling. Increasing the amplitude further than about 0.4 Å exits the range of validity of the theory for the low amplitude limit under the chosen experimental conditions.

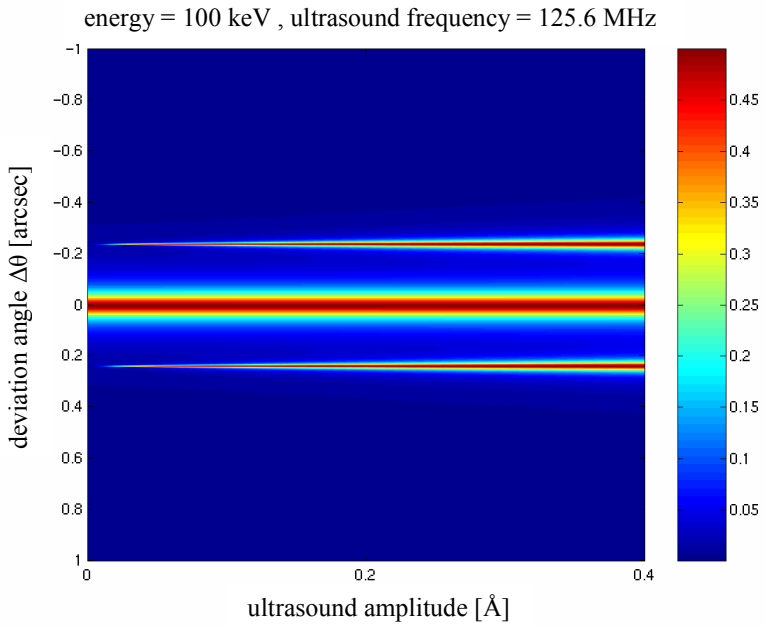

Figure 4.17: The intensity distribution as a function of the deviation angle Δθ and the ultrasound amplitude at the x-ray energy of 100 keV and the ultrasound frequency of 125.6 MHz. The FWHM of the satellite reflections is growing with higher amplitudes as long as the low amplitude theory is valid.

After the discussion of the influence of the different experimental parameters x-ray energy, ultrasound frequency and amplitude on the reflection profiles, experimental conditions for time-integrated and time-dependent intensity distributions can be better defined. The emphasis of the simulations shown in figures 4.18a - 4.21b for the (-351)-reflection lies in the comparison of time-integrated and time-dependent intensity distributions under otherwise identical experimental conditions. The results of these simulations can be summarized as follows. High ultrasound frequencies are more favorable to experimentally observe well-separated satellite reflections because the separation from the main reflection becomes larger (figure 4.20a). If the x-ray energy is low (10 keV in figures 4.18a-b), only a broadening of the main reflection is observed in the time integrated intensity distribution at the excitation frequency of 125.6 MHz, whereas the time dependent intensity distribution shows already a distinctive structure. Concerning their resolution by angular scans increasing x-ray energies would also be more favorable for the detection of the satellite reflections because the FWHM of the main reflection reduces. But since the FWHM of the satellite reflections also decreases with increasing x-ray energy, their detection will become more difficult, because their FWHM can easily achieve values below the instrumental resolution of 0.01 arcsec (figure 4.19a compared to 4.20a). Moreover, with increasing ultrasound frequencies the time modulation gets progressively reduced, being detrimental for the study of time-modulation effects (figure 4.19b and 4.21a compared to 4.20b and 4.21b). Depending on the goal of the experiment, the parameters x-ray energy and ultrasound frequency have therefore to be chosen as a compromise between high resolution and strong time modulation effects. Increasing the ultrasound amplitude broadens the satellites. If they are already well-separated from the main reflection, this increase in the FWHM results then in a facilitated detection, because their halfwidth is already close to the diffractometer resolution limit with a step size of 0.01 arcsec.

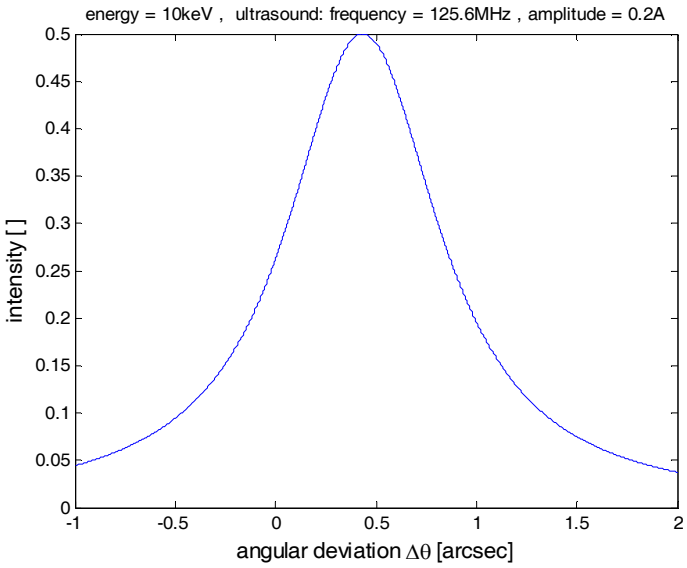

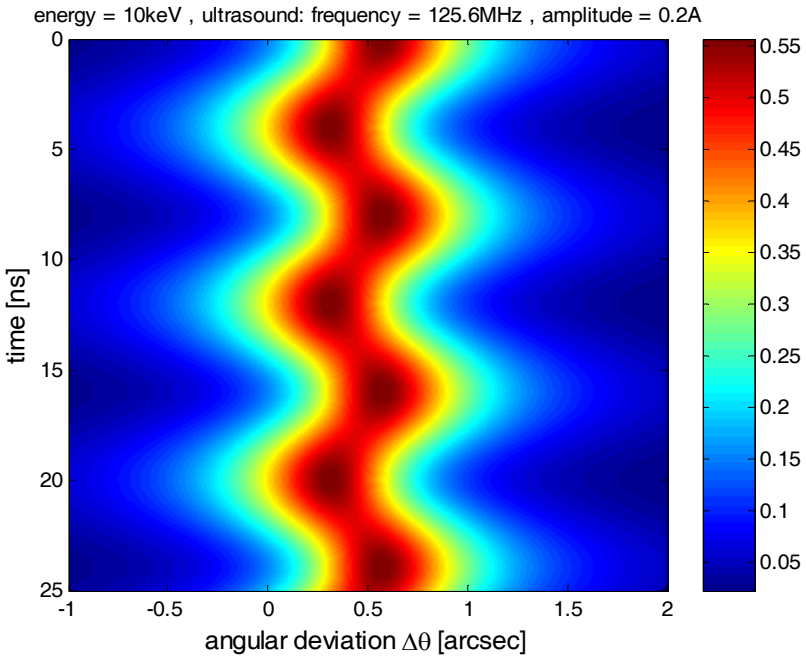

Figures 4.18a (top) and 4.18b (bottom): Time integrated and time dependent intensity distribution in the limit of small ultrasound amplitudes as a function of $\Delta\theta$ at the x-ray energy of 10 keV, the ultrasound excitation frequency of 125.6 MHz and ultrasound amplitude of 0.2 Å. The shift in $\Delta\theta$ is due to the low x-ray energy. The time dependent intensity distribution may already show a distinctive structure although the corresponding time integrated intensity distribution is only broadened.

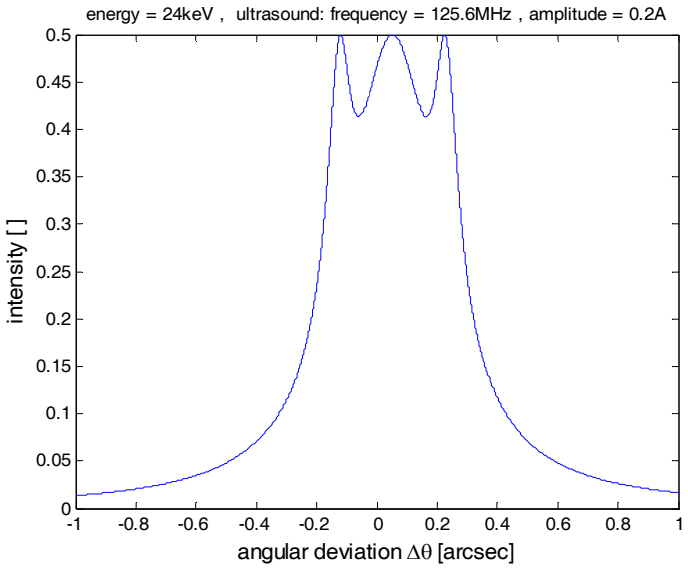

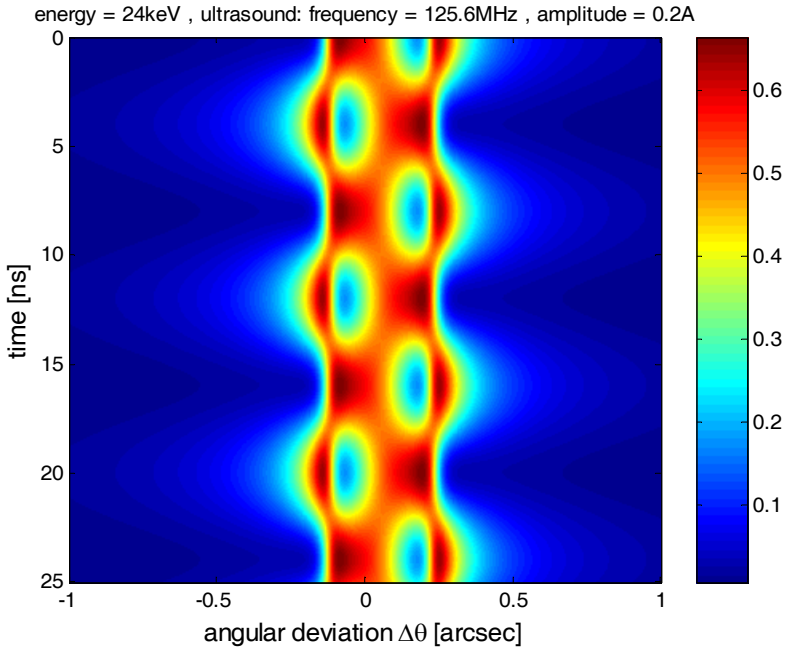

Figures 4.19a (top) and 4.19b (bottom): Time integrated and time dependent intensity distribution in the limit of small ultrasound amplitudes as a function of $\Delta\theta$ at the x-ray energy of 24 keV, the ultrasound excitation frequency of 125.6 MHz and ultrasound amplitude of 0.2 Å. In comparison to figures 4.18a and 4.18b the x-ray energy is increased. Satellite reflections are not yet completely separated from the main reflection, which makes it difficult to observe the time dependent intensity changes in a real time resolved diffraction experiment.

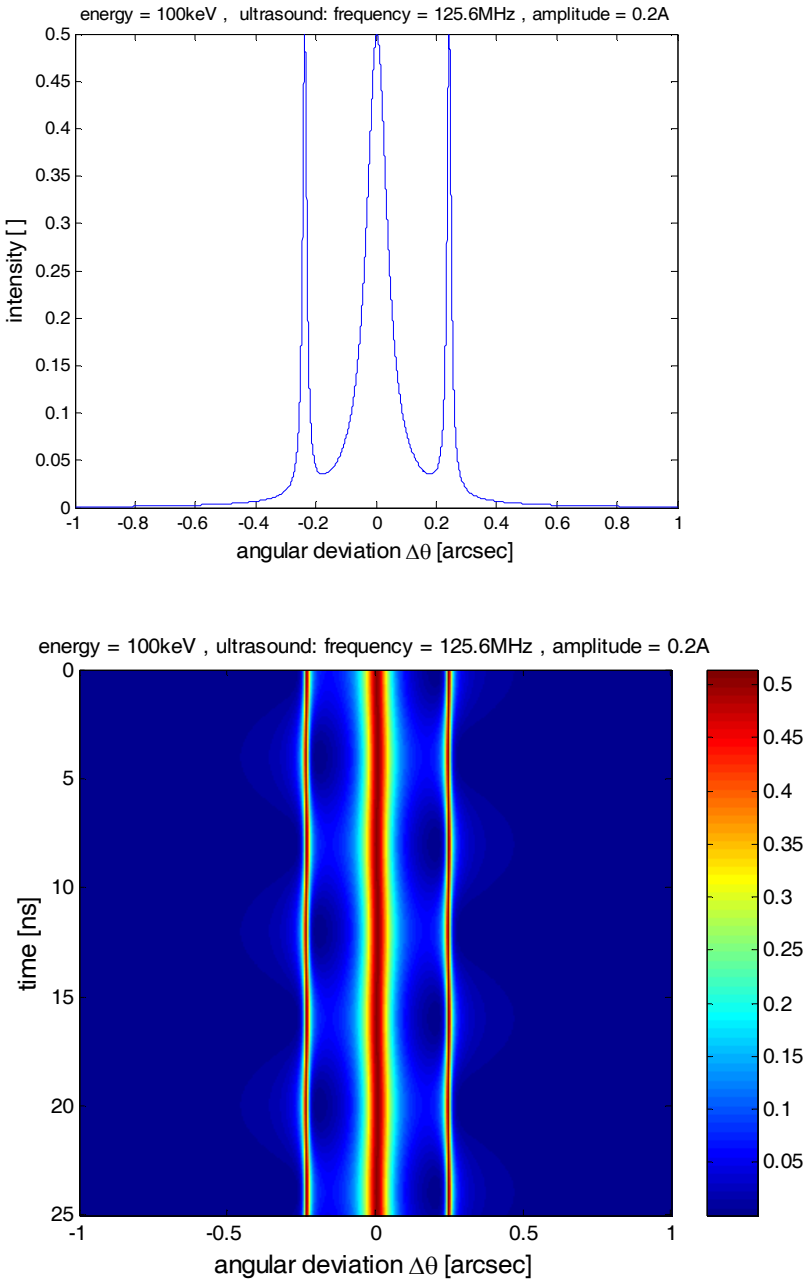

Figures 4.20a (top) and 4.20b (bottom): Time integrated and time dependent intensity distribution in the limit of small ultrasound amplitudes as a function of $\Delta\theta$ at the further increased x-ray energy of 100 keV, the ultrasound excitation frequency of 125.6 MHz and ultrasound amplitude of 0.2 Å. Satellite reflections are separated from the main reflection, but the time modulation of the satellite intensity distribution decreased.

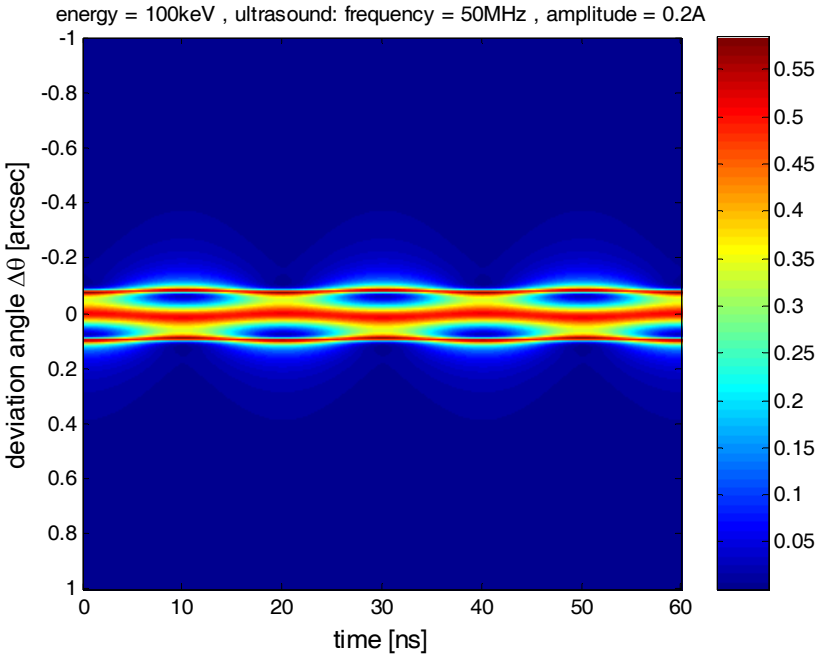

Figure 4.21a: Time dependent intensity distribution in the limit of small ultrasound amplitudes as a function of Δθ at the x-ray energy of 100 keV, the ultrasound excitation frequency of 50 MHz and ultrasound amplitude of 0.2 Å. Satellite reflections are just separating from the main reflection at this ultrasound frequency.

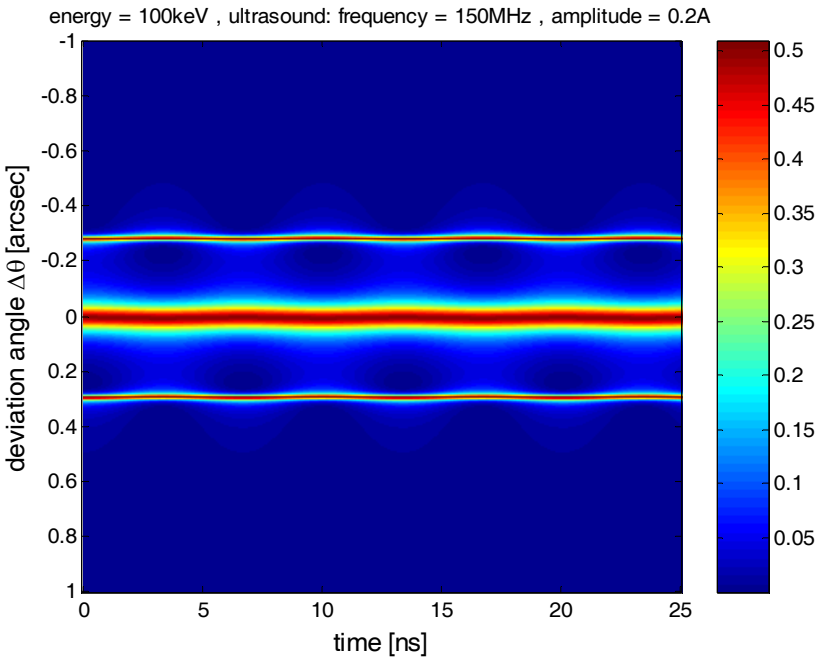

Figure 4.21b: Time dependent intensity distribution for the same parameters as in figure 4.21a apart from the increased ultrasound frequency of 150 MHz. The satellite reflections are now well separated from the main reflection, but the time modulation decreased.

4.3.2. Large ultrasound amplitudes

The simulations for large ultrasound amplitudes based on equation 4.5 can now be discussed in the same way as in the limit of small amplitudes. Like for small sound wave amplitudes the formation of satellites is also at large amplitudes dependent on the x-ray energy, the ultrasound frequency and amplitude. With increasing sound wave amplitude Bessel functions of order $n > 1$ now contribute to the diffraction pattern. This results in an increasing number of excited satellite reflections. Since the (-571)-reflection was measured in the experiments on ID 15, the simulations are calculated for this reflection. Thus the results can be compared to the experimental data shown in chapter 6. The longitudinal ultrasonic wave is still assumed to be excited in the [111]-direction. For this propagation direction the angle α between the scattering vector and the ultrasound vector is 78°.

The same three computer experiments as for small ultrasound amplitudes are carried out in order to show the dependence of the diffraction pattern on the ultrasound frequency, amplitude and x-ray energy. First we assume to excite a sound wave of amplitude 2 Å. The x-ray energy is set to 100 keV. For large ultrasound amplitudes, the onset of the first and higher order satellite reflections is shifted to lower ultrasound frequencies compared to the limit of small ultrasound amplitudes. If the ultrasound frequency is increased, the separation of the appearing satellites from the main reflection is again a linear function of the frequency (figure 4.22). The number of excited satellites depends on the ultrasound amplitude **a**. It enters the argument of the first and higher order Bessel functions in the scalar product **Ga**. The condition $\mathbf{Ga} \approx n$ gives approximately the number of satellites n, which leads to four satellites on both sides of the main reflection. Once separated from the main reflection, all satellites reach the same reflectivity of 0.5, but their FWHM are now all different. The sequence of halfwidths over the satellite pattern is dependent on the sound wave amplitude and the oscillatory behaviour of the Bessel functions. With increasing ultrasound amplitude satellite reflections with formerly small FWHM may become broad and vice versa.

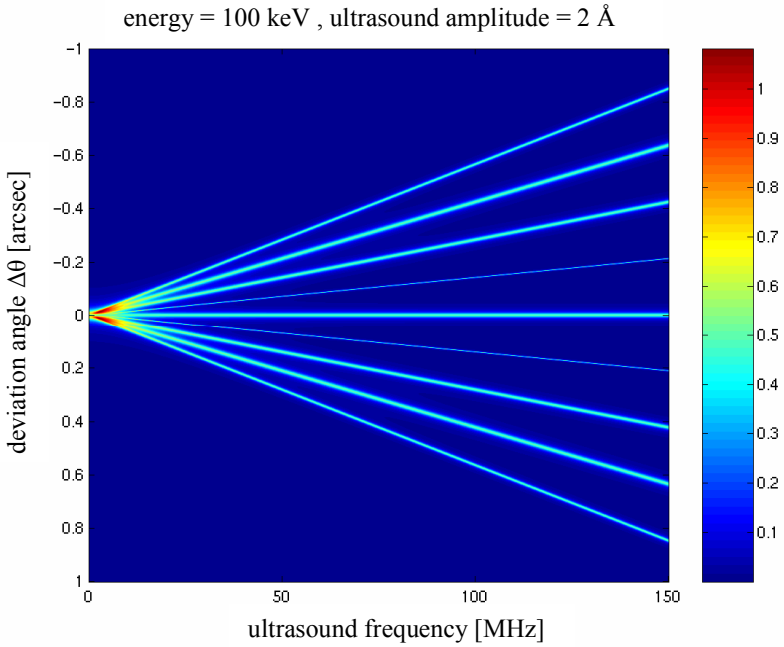

Figure 4.22: The intensity distribution as a function of Δθ and the ultrasound frequency at the x-ray energy of 100 keV and the ultrasound amplitude of 2 Å due to the high amplitude theory. Beyond the x-ray acoustic resonance several satellite reflections appear.

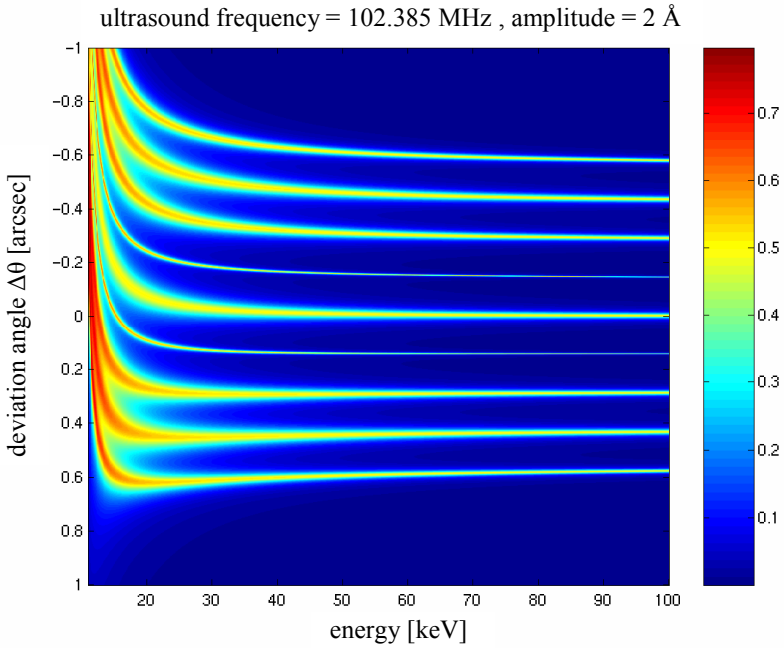

Figure 4.23: The intensity distribution as a function of Δθ and the x-ray energy at the ultrasound frequency of 102.385 MHz and the ultrasound amplitude of 2 Å due to the high amplitude theory. In the low energy range close to the x-ray acoustic resonance the influence of the asymmetric reflection is obvious.

In the second experiment the x-ray energy is increased at a fixed ultrasound frequency of 102.385 MHz and a sound wave amplitude of 2 Å. Because the ultrasound amplitude has not changed, again four satellites with different halfwidths develop on both sides of the main reflection (figure 4.23). As in the small amplitude limit the FWHM of the main reflection and the satellites decreases with increasing x-ray energy. Apart from the fact that more satellites emerge at high ultrasound amplitudes, no qualitative changes of the diffracted intensity distribution can be observed as a function of the x-ray energy compared to the low amplitude regime.

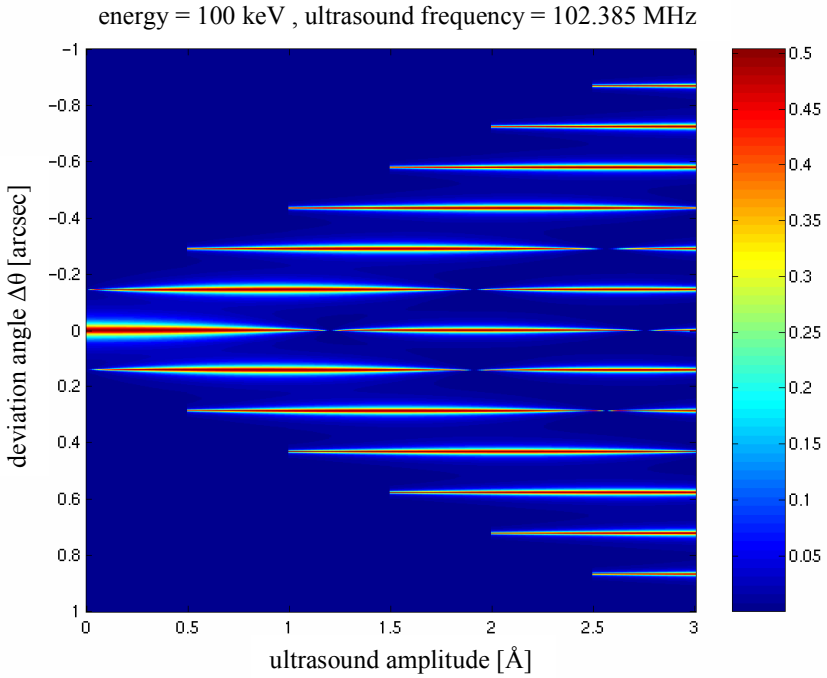

Figure 4.24: The intensity distribution as a function of Δθ and the ultrasound amplitude at the x-ray energy of 100 keV and the ultrasound frequency of 102.385 MHz due to the high amplitude theory. The number of excited satellite reflections depends on the ultrasound amplitude. The FWHM of the satellite reflections is oscillating with increasing ultrasound amplitude. The maximum FWHM is shifted for different satellite orders.

The striking difference is reflected in the third computer experiment, where the ultrasound amplitude is continuously increased at the x-ray energy of 100 keV and an ultrasound frequency of 102.385 MHz. The result of the simulation is shown in figure 4.24. Since more and more Bessel functions contribute to the diffraction pattern with increasing ultrasound amplitude, the number of excited satellites increases accordingly.

Each of them, including the main reflection, is periodically breathing with respect to their FWHM. The periodically changing halfwidth is explained through the properties of the periodic Bessel functions. The maxima of the Bessel functions of different orders are shifted in phase with respect to each other (figure 4.3). For this reason the satellite reflections achieve their maximum halfwidth at different ultrasound amplitudes. The main reflection is affected by this behavior, too, because the intensity distribution of the original reflection is governed by the Bessel function of order zero, which shows similar characteristics at large amplitudes. This is a qualitatively new observation compared to the small amplitude limit, because now the FWHM of the main reflection may be smaller than the FWHM of the satellite reflections for certain sound wave amplitudes. Moreover, it is even possible that the intensity of the main reflection vanishes at ultrasound amplitudes, for which the satellite reflections can be observed (figure 4.24).

Selected time-integrated intensity distributions for large ultrasound amplitudes and the (-571) - reflection are shown in figures 4.25a – 4.26. It is clear from figure 4.25a that ultrasonic frequencies below a certain threshold lead to overlapping satellites, which makes it difficult to resolve them in a real diffraction experiment. At 100 keV, 30 MHz and 5 Å for example, one expects more likely to measure a rectangular shaped rocking curve (figure 4.25a) rather than resolved satellites, because the FWHM of the instrument resolution function of 0.065 arcsec (chapter 5.6) does not allow to resolve a separation of the satellite reflections of 0.04 arcsec. At the same x-ray energy of 100 keV and an ultrasound frequency of 102.385 MHz it will already be possible to resolve distinct satellite reflections (figure 4.25b) and even more clearly at 150 MHz (figure 4.25c). The influence of the choice of the reflection on the diffraction pattern is shown in figure 4.26. For the (153)-reflection the angle α to the [111]-direction is calculated to 28°. The smaller the angle between the scattering vector and the ultrasonic wave vector is, the closer the ultrasound induced satellite reflections are spaced. Even for the rather high ultrasound frequency of 100 MHz - ‘high’ in the sense of ‘well above the x-ray acoustic resonance’ - and a main reflection of small FWHM due to the scattering of 100 keV x-rays, satellites are much more difficult to resolve than for the (-571)-reflection. Therefore the main reflection, i.e. the angle between the ultrasound propagation and the scattering

vector, has to be selected carefully to resolve the satellite system. To work out this dependence in detail, the expected angular positions of ultrasound excited diffraction satellites are now discussed.

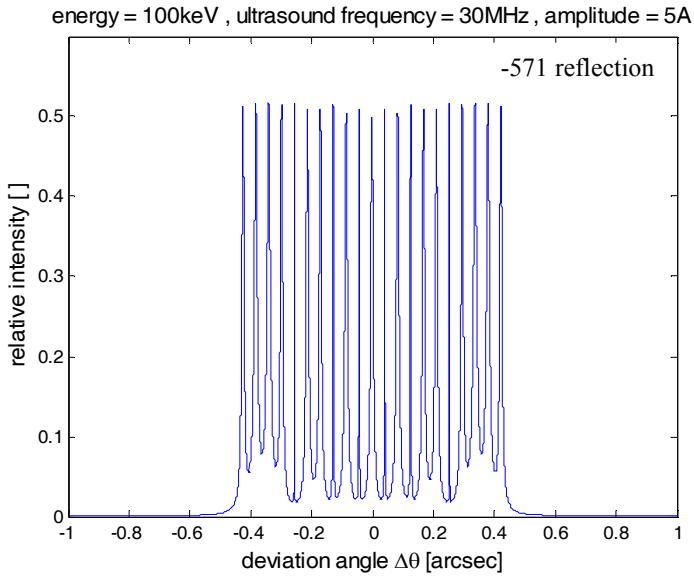

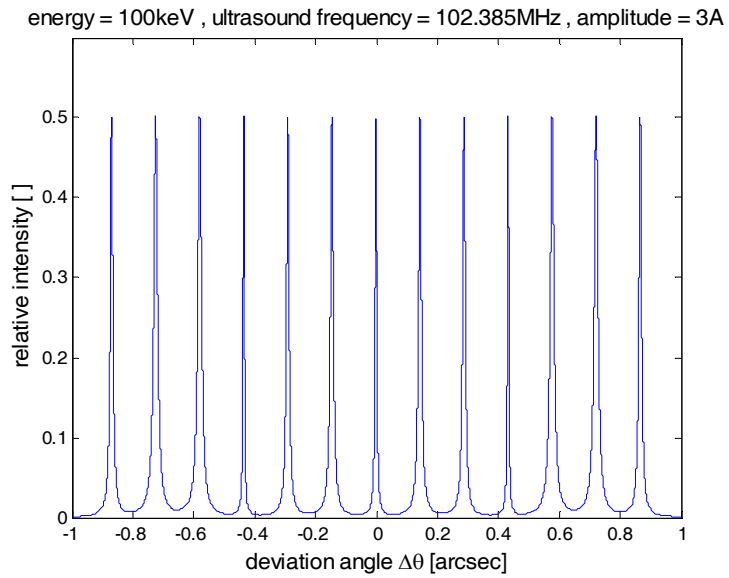

Figure 4.25a (top): Satellite intensity distribution at 100 keV and an ultrasound amplitude of 5 Å for the (-571)-reflection at the ultrasound frequency of 30 MHz. Due to the low ultrasound frequency the satellite reflections lie very close together.
Figure 4.25b (bottom): Satellite intensity distribution at 100 keV and an ultrasound amplitude of 3 Å for the (-571)-reflection at the ultrasound frequency of 102.385 MHz. As higher the frequency as easier it is to resolve the satellite reflections. The ultrasound amplitude determines the number of excited satellites and their FWHM.

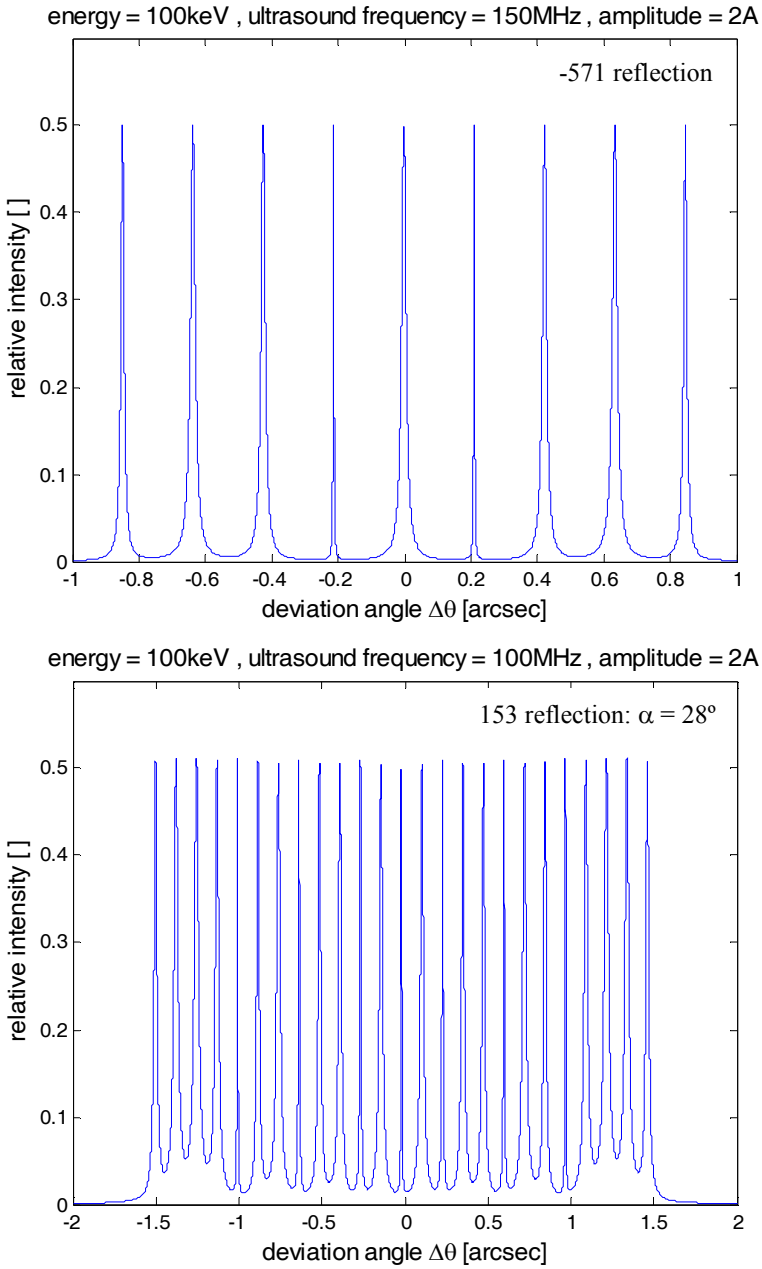

Figure 4.25c (top): Satellite intensity distribution at 100 keV and an ultrasound amplitude of 2 Å for the (-571)-reflection at the ultrasound frequency of 150 MHz. The further increase of the ultrasound frequency compared to figures 4.25a and 4.25b leads to an increased separation of the satellite reflections. The change of the ultrasound amplitude to 2 Å results in a different distribution of the FWHM of consecutive satellite reflections compared to figure 4.25b.

Figure 4.26 (bottom): Satellite intensity distribution at the x-ray energy of 100 keV, the ultrasound frequency of 100 MHz and the ultrasound amplitude of 2 Å for the (153)-reflection. The choice of the reflection with respect to the ultrasound propagation vector [111] influences the satellite separation. Since the angle α between the scattering vector **G** and the ultrasound propagation direction is only 28°, the satellite reflections are closely spaced compared to the (-571)-reflection in figure 4.25b (α = 78°) even at the large ultrasound frequency of 100 MHz

4.3.3. Angular positions of ultrasound excited satellite reflections

A calculated example due to equation 4.8 for the resulting satellite positions at the x-ray energy of 200 keV, the ultrasound frequency of 95.9667 MHz and the (-571)-reflection is shown in figure 4.27. If the ultrasonic wave vector lies parallel to the diffraction vector, the positions of satellites of increasing order are very closely spaced. For the ultrasonic wave along the [111]-direction as well as perpendicular to the scattering vector, the satellites are well separated. The difference of 12° in α between the ultrasonic wave propagation in [111] and perpendicular to **G** does not change the absolute angular positions significantly since the positions depend on sin(θ-α). The Bragg angle θ is small for high energy x-ray diffraction (below 3°, see also chapter 5) and the angle α equals 90° for an ultrasound wave propagation perpendicular to **G** and 78° for the propagation in [111] - direction (figure 4.4). This is already close enough to α = 90° to obtain well separated satellite reflections.

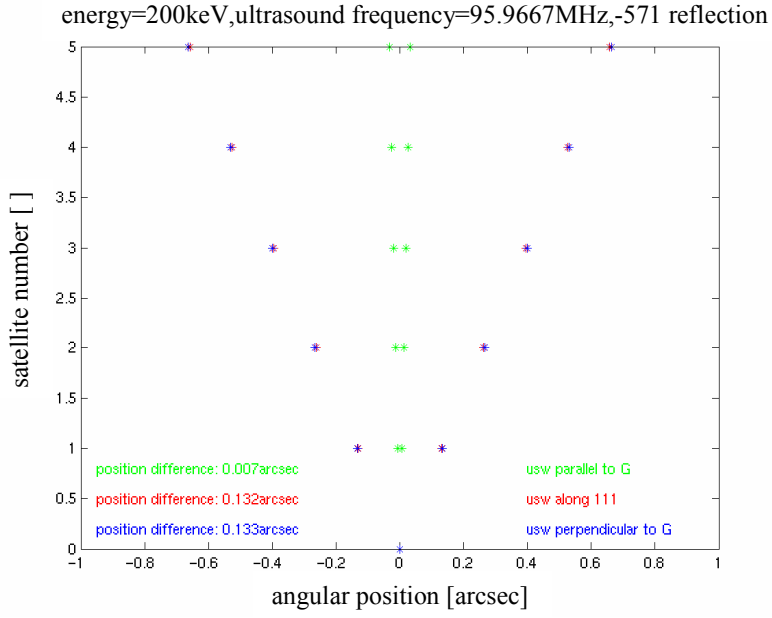

Figure 4.27: Calculated satellite positions for different ultrasound propagation directions at the x-ray energy of 200 keV and the ultrasound frequency of 95.9667 MHz for the (-571)-reflection. The separation of satellite positions is largest if the ultrasound propagation is perpendicular to the scattering vector **G**. The satellite positions are independent of the ultrasound amplitude.

4.3.4. The FWHM of ultrasound excited satellite reflections

The FWHM of the ultrasound excited satellite reflections is plotted in figure 4.28 as a function of the satellite order and ultrasound amplitude. The calculation is based on equation 4.9 for an x-ray energy of 210 keV, the (-571)-reflection, and the ultrasound amplitude vector points in the [111]-direction (longitudinal ultrasound propagating in the reciprocal (111)-direction). The FWHM of the satellite reflections cover a range from 0 to 0.025" for ultrasound amplitudes between 0 and 20 Å. Figure 4.29 shows the distribution of halfwidths for the first satellite now as a function of the x-ray energy and the ultrasound amplitude. The reflection is again (-571) and the conditions of ultrasound excitation remained the same as in figure 4.28. The FWHM does not depend on the sound wave frequency (equation 4.9).

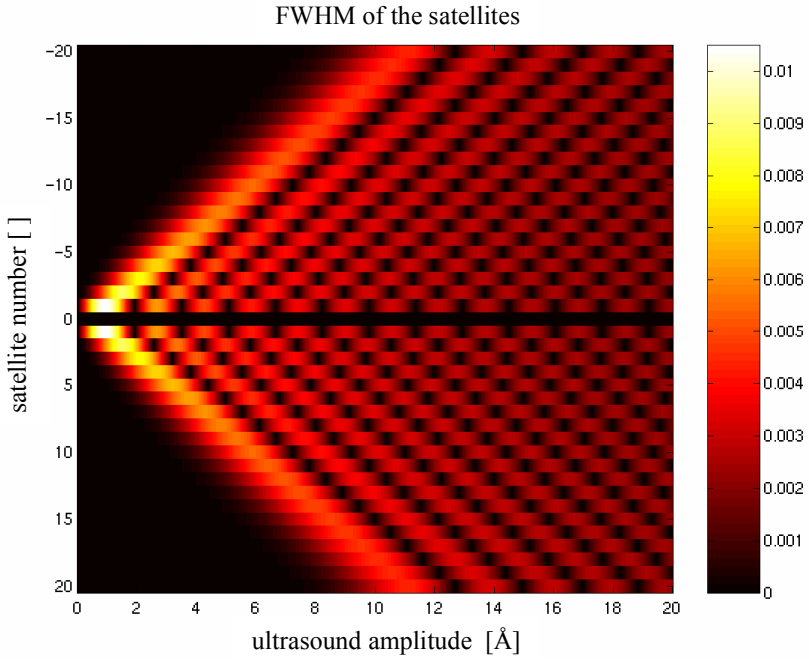

Figure 4.28: The FWHM of the first twenty satellite orders as a function of the ultrasound amplitude. The highest calculated FWHM is already close to the experimental resolution limit of 0.01". The oscillation of the FWHM as a function of the ultrasound amplitude is due to the properties of the Bessel function.

The FWHM of the satellites is oscillating as a function of the ultrasound amplitude and the satellite order (figures 4.28 and 4.29). Different satellite orders do not reach their maximum halfwidth at the same ultrasound amplitude; the maxima are shifted in

amplitude space (figure 4.28). Furthermore, the maxima of the FWHM decrease with increasing ultrasound amplitude (figure 4.29). This is of course closely connected to the characteristics of the Bessel functions of different order (figure 4.3). A FWHM of 0" occurs for a given satellite order, when the Bessel function of the same order reaches 0. Additionally, figure 4.29 shows that the FWHM of the satellites decreases with increasing x-ray energy approximately with an inverse function like it is expected from the theory. For the interpretation of experimental data it will be important to know, which experimental parameters vary the FWHM of the satellite reflections periodically.

Another tendency should be noted. The maxima of the oscillating FWHM are greater for smaller amplitudes and satellite numbers (figures 4.28 and 4.29). But even the highest calculated theoretical value of 0.025" FWHM for a x-ray energy above 80 keV and an ultrasound amplitude range between 0 and 20 Å is quite small as compared to the experimental resolution nowadays achievable on triple-axis diffractometers. The calculated values for the FWHM are already close to the angular resolution limit of 0.01" of the experimental setup on ID 15.

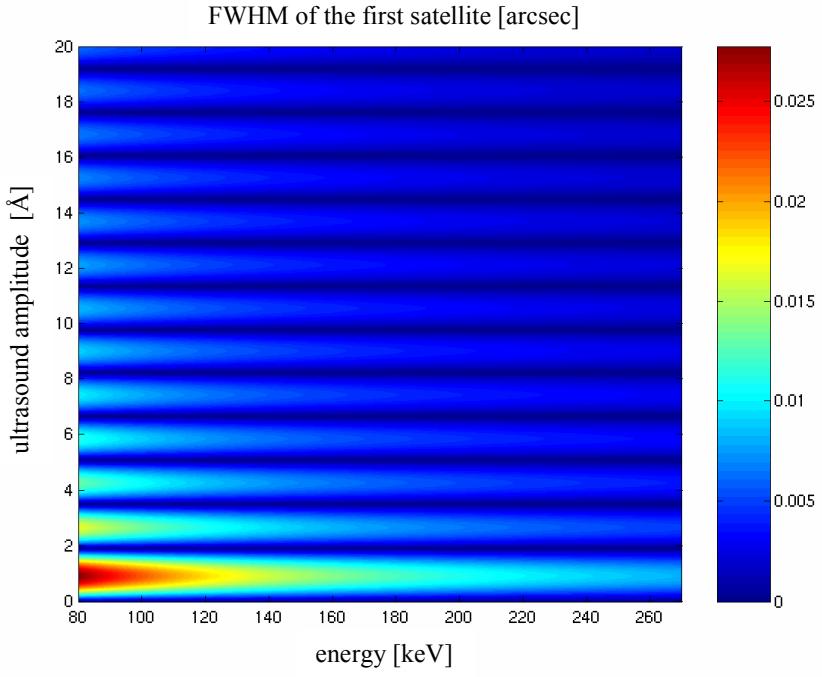

Figure 4.29: The FWHM of the first satellite order as a function of the ultrasound amplitude and the x-ray energy. Higher energies lead to smaller FWHM. The FWHM is oscillating with increasing amplitude with the tendency to smaller values for higher amplitudes.

Chapter 5

Experimental part

The general layout for time-resolved and time-integrated diffraction experiments at the high-energy beamline ID 15 at the European Synchrotron Radiation Facility (ESRF) in Grenoble, France, is described. It is followed by a description of the main parts involved in the set-up together with a detailed discussion of the experimental conditions. The scanning procedures of the high resolution triple-axis diffractometer including the resolution of the instrument at high x-ray energies are treated in detail. The excitation and propagation of ultrasonic waves in crystals is discussed and finally the required timing electronics in order to perform time resolved experiments are presented.

5.1. The high-energy beamline ID 15

The diversity of high-energy x-ray studies has lead to a beamline layout with three different end-stations, which can be operated both independently and simultaneously. An overview of the beamline design is available on the world-wide-web [Exp 03].
The end-station ID 15A is dedicated to operate in an energy range from 30 keV to 500 keV. The spectral ranges available at ID 15A are shown in figure 5.1. It is possible to switch between two insertion devices (ID): an asymmetric permanent magnet multi-pole wiggler (AMPW), or a superconducting wavelength shifter (SCWS) for an increased photon flux at very high energies above 200 keV. The critical energies of these insertion devices are 45 and 96 keV, respectively. After a reconstruction of the beamline in late 2001, the insertion devices were replaced by one asymmetric three-tesla two pole permanent magnet wiggler. However, most of the experiments undertaken in this work were performed using the SCWS.
The incident beam is attenuated by three filters in series, 4 mm of aluminium, 3.5 mm beryllium and 1 mm of carbon. These absorbers are installed permanently in the beamline

to cut out the lower energies and thus to reduce the heat load on the monochromator crystal. An overview of the experimental set-up for the investigation of the time resolved response of ultrasound excitations in perfect silicon crystals is given in figure 5.2. The insertion device (ID) delivers a small white x-ray beam with a source size of 57 x 10 μm^2 (horizontally x vertically). The horizontal aperture is limited to 1.2 µrad.

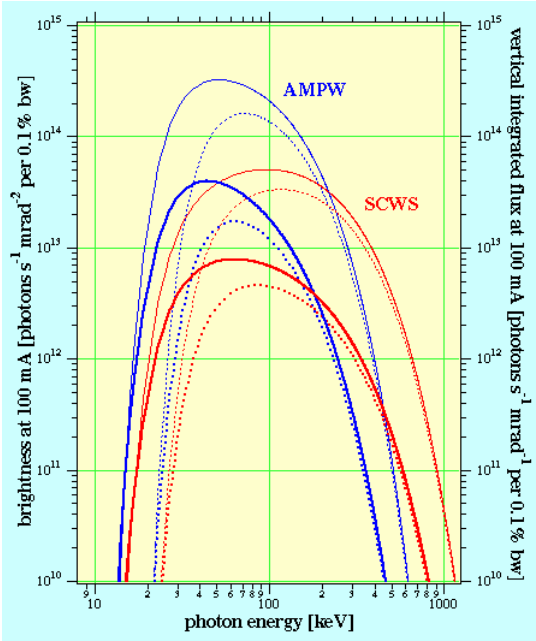

Figure 5.1: Spectral ranges available at ID 15A. Thin lines correspond to the average brightness in the beam centre (left coordinate), thick lines are the vertically integrated values. The solid curves show the spectra of the sources downstream from the permanent filters and the dotted lines are the distribution in the B hutch (the second experimental end-station). After [Exp 03].

The beam passes through the optics hutch into the experimental hutch inside a lead tunnel in order to reduce the background scattering. One permanently installed instrument in the experimental hutch of ID 15A is the high angular resolution triple axis diffractometer, which was used in this work to perform the experiments. The incoming beam is diffracted by the monochromator crystal mounted on a goniometer, by the sample and finally by the analyzer crystal. The diffracted photons are then counted by a cooled germanium solid-state detector.

Figure 5.2: The overall set-up of time-resolved high resolution diffraction experiments at ID 15A. M=Laue monochromator ((111)-cut silicon), S=Sample, A=Analyzer. These three crystals of the diffractometer are identical in our experiments. I=Laser interferometers for a high angular resolution. SPEC is the beamline control software. Details in the text.

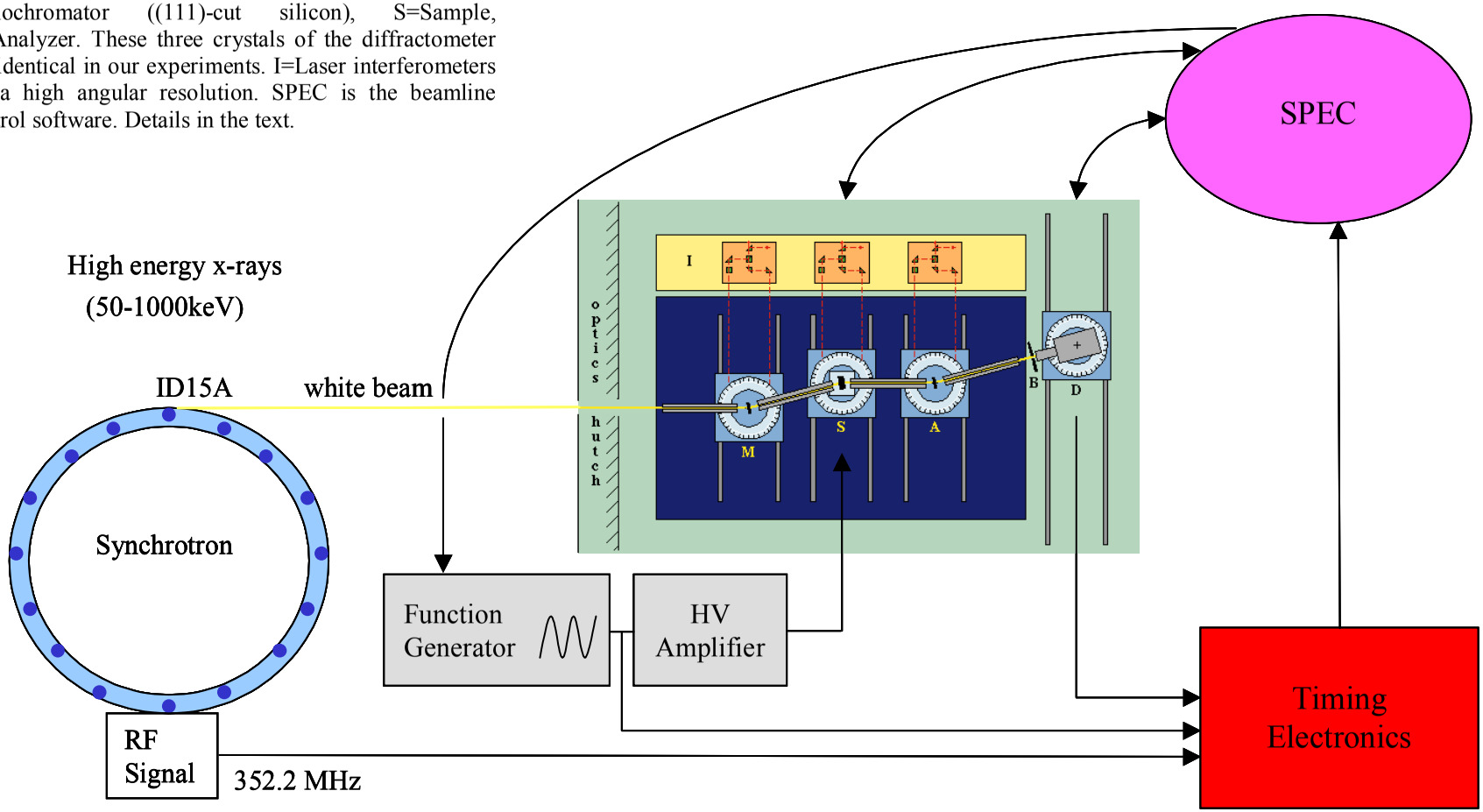

ESRF 16-bunch mode:

16 equally spaced bunches out of 992

Maximum current in storage ring: 90mA

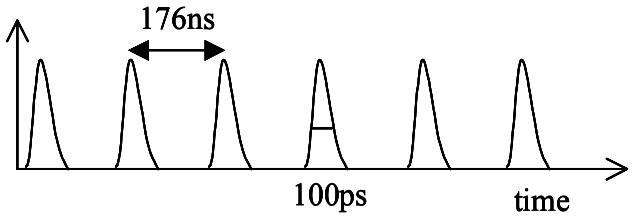

$$\frac{1}{RF}\cdot\frac{992}{16}=176\text{ns} \triangleq 5.68\text{MHz}$$

Time-resolved experiments require single electron bunches well separated from each other with large pulse intensities. A third generation synchrotron source like the ESRF routinely delivers such pulses. Time-resolved experiments are accomplished in 16-bunch mode, which means that only 16 equally spaced electron bunches out of a possible 992 bunches are filled. The maximum total electron current in the storage ring (which is proportional to the x-ray flux) is thereby 90 mA. This is only a factor of two less than the more frequently used multi-bunch operation. The radio-frequency carrier signal of the storage ring is fixed to 352.2 MHz. In 16-bunch mode the x-ray pulses arrive at a frequency of 5.68 MHz to the experimental station, corresponding to a pulse separation of 176 ns. A single x-ray pulse at ESRF has a pulse width of about 100-150 ps.

To achieve the highest possible time resolution around 100-150 ps with this pulsed x-ray source, additional timing electronics have to be implemented to the experimental setup. The detector with its intrinsic response time of 20 ns is unable to achieve this time resolution. Three input signals are indispensable to the timing electronics, which are the detector signal from the registered photons, the radio-frequency carrier signal from the storage ring, and the ultrasonic excitation signal from the frequency generator (figure 5.2). Chapter 5.8 describes the timing electronics, which permit time-resolved studies down to ca. 200 ps resolution. The timing electronics is connected to ‘SPEC’, a UNIX-based computing software package used at the ESRF to control and run experiments and to acquire data. The arrows in figure 5.2, which affiliate the oval flowchart indicating ‘SPEC’ to the components of the setup (diffractometer including detector, function generator, timing electronics), elucidate the particular control structure. ‘SPEC’ controls all motors and axes of the diffractometer and receives a feedback signal from the interferometric laser system, which controls the fine-rotation of monochromator-, sample- and analyser-crystals in the highest angular resolution mode [Lis 98]. The detector position is controlled via ‘SPEC’, too, and the time-integrated photon intensities are returned to this control software. A function generator producing a sinusoidal signal is controlled in frequency and amplitude by ‘SPEC’. This signal is then boosted by a high-voltage (HV) amplifier. A MHz-transducer, bonded to the sample crystal to excite ultrasonic waves, is driven from this amplifier (see chapter 5.7).

5.2. Peculiarities of high-energy x-ray diffraction

Most of the quantities in diffraction theory like the angle of diffraction, the atomic susceptibility, the absorption coefficient and the extinction length are usually expressed as a function of the x-ray wavelength λ. To keep in mind an idea about its value-range at high energies, the x-ray wavelength is plotted in figure 5.3 as a function of the energy. The wavelength is behaving inversely to the x-ray energy:

$$E = hc/\lambda \qquad 5.1$$

In this equation h denotes Planck's constant and c being the vacuum velocity of light.

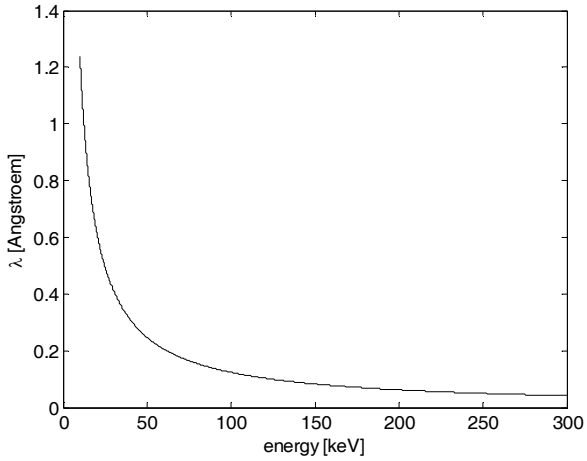

Figure 5.3: X-ray wavelength λ as a function of energy. For high energies λ is below 0.2 Å

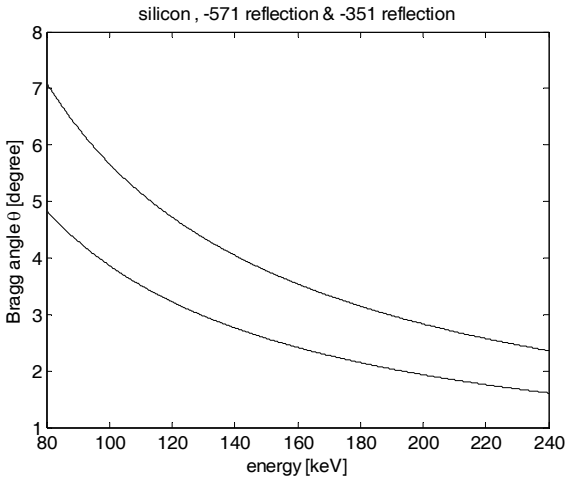

Figure 5.4: Bragg angles θ for x-ray energies between 80 and 240 keV. The upper curve corresponds to the (-351)-reflection and the lower one to (-571).

For a typical energy of 100 keV used in the experiments of this study, the wavelength amounts to 0.124 Å, thus being much smaller than the lattice constant of silicon (a_0 = 5.43 Å). It is also much smaller than ultrasonic wavelengths (in the μm-range), which are being probed in the diffraction experiment. Small x-ray wavelengths result in small diffraction angles due to Bragg's law (chapter 2.1). In high-energy diffraction, the Bragg angles are usually smaller than 10°. As an example, the Bragg angles for the experimentally important (-571)- and (-351)-reflection are plotted as a function of x-ray energies above 80 keV in figure 5.4.

The fact of working with small diffraction angles has an enormous advantage. It favours Laue scattering geometry rather than Bragg geometry, which is much easier to set up experimentally. The set-up requires the installation of an analyser crystal and detector behind the monochromator and the sample crystal. In any case, Laue geometry is preferred since the x-rays should go through the entire (thick) crystal to probe the volume acoustic waves. High energy x-rays permit such a geometry, even for rather large crystals with low absorption.

In the present work, ultrasound excitation in crystals is investigated by means of high-energy x-ray diffraction. The reasons, why it is advantageous to work with high energies, are now discussed.

For the investigation of structural changes due to volume acoustic waves induced by transducers, ultrasound wavelengths are typically found in the higher µm-range, e.g., around 100 µm. A certain number of wavelengths should fit into the crystal in order to realize a superstructure or a diffraction grating, no matter if we are dealing with a travelling or a standing ultrasonic wave. For this reason, the crystal should have dimensions in the mm-range. To penetrate such length-scales with x-rays, high radiation energies are needed. Low energies around 10 keV for example have only a typical penetration depth on the µm-scale and can therefore only probe a negligible part of the modulation period in the crystal. The attenuation lengths as a function of the photon energy for some representative chemical elements are shown in figure 5.5.

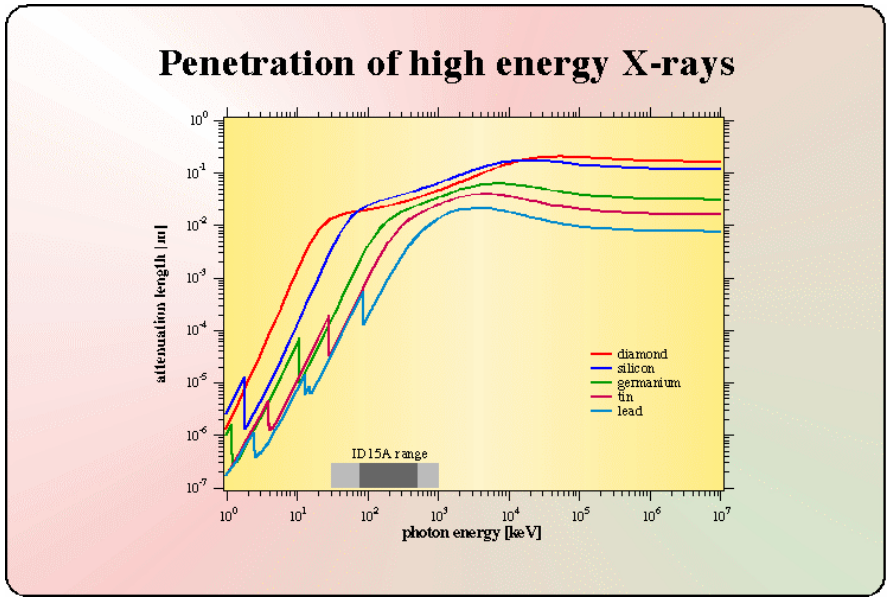

Figure 5.5: The attenuation lengths for the fifth period elements as a function of the x-ray energy. High energies are able to penetrate most materials up to several cm (courtesy of [Exp 03]).

It is clear from this figure, that for various elements the penetration depth becomes at least an order of magnitude larger in the range above 10 to 100 keV. The absorption edges of the different elements located in the lower energy regime are also visible.
The attenuation length is simply the reciprocal of the total absorption coefficient μ. Different processes influence the absorption of x-radiation in a material. The most important ones in the energy range between 1 keV and 1000 keV are elastic (Rayleigh) scattering, inelastic (Compton) scattering and the photoelectric effect, which is also an inelastic procedure and commonly called 'true absorption' [Int 92]. Figure 5.6 shows the absorption coefficient for these different interaction channels for elemental silicon.

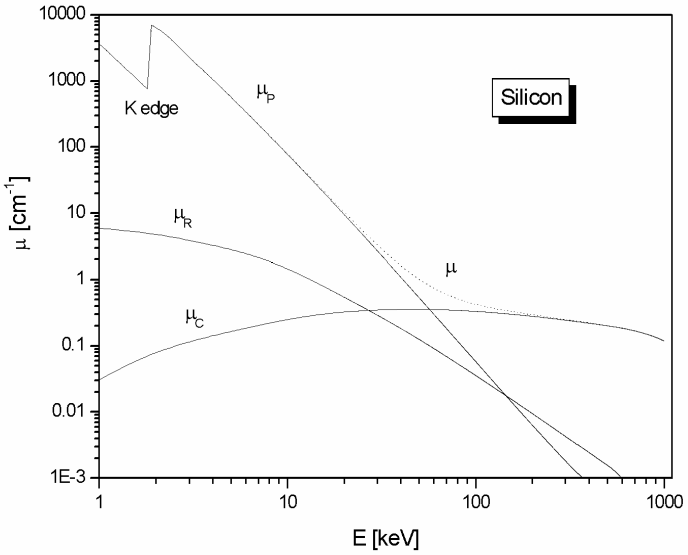

Figure 5.6: The total absorption coefficient μ (dotted curve) and the absorption coefficients for photoelectric absorption, Rayleigh and Compton scattering. At high energies the absorption due to Compton scattering is dominating. The curves are calculated based on XOP [XOP 02].

The process of pair production has its onset above 1 MeV and is out of the plotted μ-range. The dominating process below 30 keV is the photoelectric effect, between 100 keV and 1 MeV Compton scattering dominates, while at intermediate energies both mechanisms contribute to the absorption coefficient. Rayleigh scattering has only a minor contribution between 30 keV and 130 keV. The total absorption coefficient is then calculated as the sum of the individual contributions:

$$\mu = \mu_P + \mu_C + \mu_R \qquad 5.2$$

This sum is also indicated as a dotted curve in figure 5.6. On a double-logarithmic scale, the coefficient of photoelectric absorption for silicon is nearly linearly decreasing with increasing energy above the K-edge absorption energy. Thus much less x-radiation is absorbed through the photoelectric effect at very large energies. Around 60 keV, where the Compton scattering exhibits a broad maximum, both photoelectric and Compton absorption are nearly equal in strength. Since the Compton scattering starts to dominate the absorption process at even higher energies, the total absorption coefficient decreases with a smaller slope on an already low absorption level. E.g., at 100 keV the photoelectric part of the absorption amounts to 0.06 cm^{-1}, the Compton part to 0.33 cm^{-1} (table 6.1). The attenuation of a parallel and monochromatic x-ray beam in a material is given by

$$I = I_0 \cdot \exp(-\mu T) \quad , \qquad 5.3$$

in which I_0 describes the incoming intensity, I the transmitted intensity, μ the material dependent total linear absorption coefficient and T the crystal thickness.
For a 5 mm thick silicon crystal and an x-ray energy of 100 keV only 19% of the radiation intensity is absorbed, of which the photoelectric absorption contributes to a 3% transmission decrease. For 200 keV the total intensity reduction decreases to 14%.

Table 5.1: The absorption coefficients for photoelectric absorption, Rayleigh and Compton scattering at 100 and 200 keV x-ray energy.

	E = 100 keV	*E = 200 keV*
Rayleigh [cm^{-1}]	0.04	0.010
Compton [cm^{-1}]	0.33	0.281
Photoelectric [cm^{-1}]	0.06	0.006
Total μ [cm^{-1}]	0.43	0.297

The situation can be much different when dealing with perfect crystals. The treatment is far more cumbersome, e.g., consider the anomalous Borrmann transmission through a thick crystal. Here, the absorption coefficient varies along the crystals exit surface. After [Bat 64] the condition for a Borrmann thick crystal is $\mu \cdot T > 6$ or even bigger than 10. In our case the value of $\mu \cdot T$ amounts to 0.22 for a silicon crystal of 5 mm

thickness. The total absorption coefficient including Compton scattering at 100 keV is taken from table 6.1. For higher energies this value would be smaller, which means that for our experimental conditions $\mu \cdot T$ is too small to be governed by the Borrmann anomalous transmission. In addition, we should connect this result to the discussion of chapter 2.6 and 2.7 for thick and thin crystals. In the language of Batterman [Bat 64] the experimental conditions for a 5 mm thick silicon crystal in the x-ray energy range between 100 kev and 200 keV lie within the thin crystal regime with respect to absorption, since $\mu \cdot T < 1$. Therefore we do not take into account absorption for the calculation of the intensity distribution of diffracted x-rays (chapters 2.6 and 4). In chapter 2.6 the intensity distribution was calculated in Laue geometry without absorption as a function of the thickness parameter A. In the language of Zachariasen [Zac 45], thick and thin crystals are distinguished via A, if absorption does not need to be taken into account. For a 5 mm thick silicon crystal, the (-571)-reflection and an x-ray energy of 100 keV, A yields 37.3 due to equation 2.17. For the x-ray energy of 200 keV the thickness parameter A = 18.6. Thus these experimental conditions are well within the thick crystal regime $A >> 1$ without absorption.

Another argument favouring high x-ray energies deals with the resolution of the instrument. Not only higher reflection orders, but also higher energies allow achieving a superior angular resolution, because the width of the rocking curve of a reflection decreases accordingly, and as a consequence, the FWHM of the instrument resolution function decreases. This is important, because changes in the intensity distribution of diffracted x-rays induced by ultrasound excitation are expected to lie close to the main reflection, even for high frequencies well above the x-ray acoustic resonance. This fact was worked out in detail in chapter 4. Another aspect is important, namely that for increasing energy just above the x-ray acoustic resonance the ultrasonically induced satellite positions move away from the main reflection, which permits their facilitated detection. In contrast to these advantages a compromise has to be found for the values of the x-ray energy, since the main reflections as well as those of the satellites become also sharper at higher energies and can then easily descend below the detection limit of the diffractometer. This limit is given by the mechanical angular resolution possibilities of the triple axis diffractometer, which is 0.01 arcsec. The

following paragraphs are dedicated to deal with the instrument resolution and the scanning procedures.

5.3. The high-resolution triple-axis diffractometer

The triple-axis diffractometer is mounted on a granite optical table with a size of 3m x 2m x 0.4m, and weights 5.6 tons to reduce vibrations transmitted by the surrounding. The monochromator, sample and analyser crystals are each mounted on massive towers. These rotation towers are mounted on translation stages (figure 5.2). Eulerian cradles are installed on each tower in order to align the crystals in a way that the scattered beam remains in the horizontal plane. The angular alignment of the crystals in the horizontal scattering plane is realised by a course rotation of the towers coupled to a high-resolution fine rotation. The coarse rotations are DC-motor driven, while piezo-actuators control the fine rotations. They are coupled by weak link devices. Interferometric read-outs provide an accuracy of 0.01" for the rotation angles. This is necessary because high order reflections at high energies cause the rocking curves to become very narrow, what leads at the same time to the high instrumental resolution. Furthermore, the relative orientation of the three crystals is substantial to align the diffraction vectors (figure 5.7). Therefore it is important to monitor and adjust the rotation of all axes simultaneously. This is realised by a laser interferometer, which is mounted on top of the optical table. This single source provides a laser beam for three individual interferometer set-ups. These interferometers monitor each axis independently by measuring the optical path differences that are induced by mirrors, which are firmly mounted to the body of the towers. The detected signals are read by a feedback system, which controls the piezo-actuators to provide a long time stability of better than 0.1 arcsec [Lis 98b].

The monochromator crystal is covered by a massive lead tank with a 10 x 10 mm^2 aperture towards the sample crystal. In addition, long steel collimators with a 5 mm aperture are placed between the monochromator and the sample, the sample and the analyser and the analyser and the detector in order to reduce the background scattering (figure 5.2).

The nitrogen-cooled energy dispersive germanium solid-state detector is mounted on another bench behind the optical table. If the crystals are in diffraction position for a

certain reflection, the detector follows automatically by translating and turning the detector aperture in the direction of the diffracted beam. It is not necessary to control the detector angle as accurate as for the diffracting crystals since the detection window is larger than the aperture of the collimators. However, the analyser crystal acts as a high precision slit in front of the detector. The entire diffractometer can be run in double-axis or triple-axis mode, thus with or without diffraction on the analyser crystal. Figure 5.7 shows a schematic top view of the three crystals of the diffractometer in diffracting position in the horizontal scattering plane.

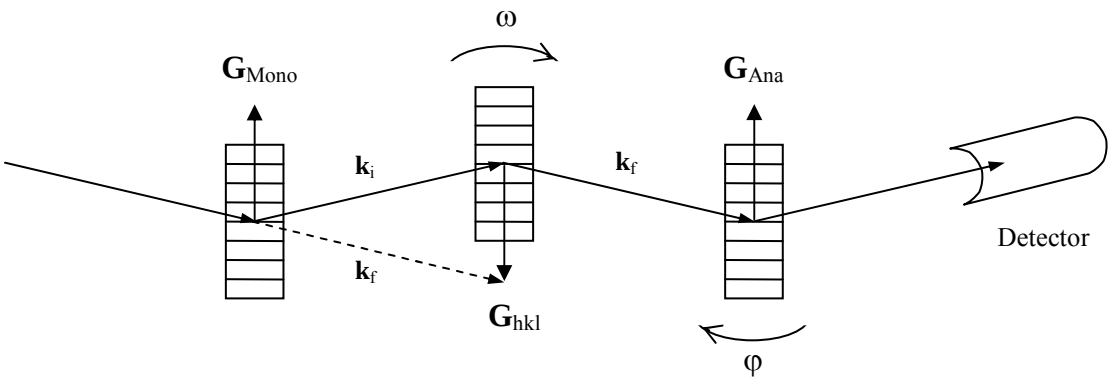

Figure 5.7: Schematic view of the triple-crystal diffractometer for high energy synchrotron radiation. The monochromator diffracts the wavevector $\mathbf{k_i}$ out of the white incident beam. The sample and analyser crystals (second and third) are rotated by ω and φ in order to obtain scattering distributions in reciprocal space.

5.4. Scanning procedures and the non-dispersive set-up

The possible scanning procedures are visualized in figure 5.8. Depending on the chosen reflection (hkl) and the desired energy, the monochromator selects the incoming wave vector $\mathbf{k_i}$ in magnitude and direction.

The sample reflection defines the scattering vector **G**, the scattered wave vector is called $\mathbf{k_f}$. The angle between $\mathbf{k_i}$ and $\mathbf{k_f}$ is twice the Bragg angle, 2θ. In the described condition a reciprocal lattice point satisfies Bragg's law and diffracted photons thus reach the detector.

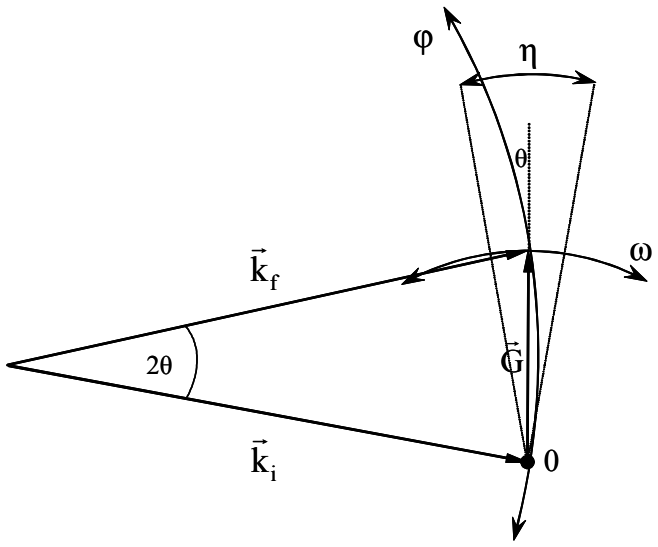

Figure 5.8: The scanning procedure for reciprocal space maps. The wavevectors for the incident and diffracted beam are $\mathbf{k_i}$ and $\mathbf{k_f}$. **G** is the reciprocal lattice vector. Rotating the sample corresponds to a transverse scan (ω-scan) while an analyser scan (φ-scan) probes along the Ewald sphere. Since the Bragg angles θ are small at high energies, an analyser scan differs only little from a longitudinal scan. A transverse scan measures the mosaic distribution of a crystal whereas a longitudinal scan probes for the lattice parameter distribution.

Turning the sample corresponds to a scan of the scattering vector **G** around the origin of the reciprocal space (ω-scan). The measured intensity distribution is called a rocking curve, because probing perpendicular to **G** gives information about the mosaicity (or perfection) of a sample crystal.

Including the third axis of the instrument (the analyser crystal mounted on the third tower) corresponds to a rotation of the diffracted wave vector $\mathbf{k_f}$ around the sample's scattering angle 2θ (figure 5.7) and thus to a scan along the Ewald sphere (φ-scan). This probes mainly the reciprocal lattice vector **G** and thus gives information about the distribution of lattice parameter variations, but is also influenced by the mosaicity of the sample crystal (the scanning direction is tilted by θ compared to the longitudinal component of **G**, figure 5.8).

Rotating the analyser crystal with respect to the sample at different points of the rocking curve leads to a complete mapping of the reciprocal space around one lattice point. The mosaic spread of a crystal within an angular distribution η around the average direction causes a broadening of the reciprocal lattice points in the transverse

direction and does not affect the longitudinal scattering vector distribution unless mosaic size effects come into account. To investigate the longitudinal variations of the scattering vector it is sufficient to probe the Ewald sphere with the analyser crystal only, instead of a typical θ-2θ scan. This is because at high energies the Bragg angles θ are quite small. The opening of the detector is large enough to collect all the scattered photons and does not need to be moved. To conclude, it is still possible to measure the lattice parameter variation with longitudinal resolution possibilities even if a sample eventually shows a mosaic spread that deteriorates the transverse resolution distinctively.

$\Delta G_{\perp}$ and $\Delta G_{||}$ are the perpendicular and parallel components of the variation ΔG with respect to the scattering vector **G**. To achieve the unblurred reciprocal space intensity distribution from the measured data in real space (combined ω-φ-scans), the following coordinate transformation has to be accomplished [Lis 98b]:

$$\begin{pmatrix} \Delta G_{\parallel}/G \\ \Delta G_{\perp}/G \end{pmatrix} = \begin{pmatrix} 1/2\tan\theta & 0 \\ 1/2 & 1 \end{pmatrix} \cdot \begin{pmatrix} \Delta\varphi \\ \Delta\omega \end{pmatrix} \qquad 5.5$$

In the discussion of the scanning procedures the dispersive and non-dispersive scanning mode should also be mentioned. Imagine that the rays of a divergent incident beam hit the reflecting planes of a monochromator crystal. Each ray would therefore have a slightly different Bragg angle. A different wavelength for each incident angle is thus selected for diffraction, which leads to dispersion of the exiting rays. A second crystal, diffracting in the same scattering plane, may be positioned to rotate the scattered beam in the same sense (+ + - configuration) or in the inverse sense (+ – -geometry). Rotating the second crystal in the first case brings successively one ray after the other in Bragg condition. This is called dispersive geometry and the technique is appropriate to probe the beam divergence. In the second case all the rays have also their own Bragg angles, but the lattice planes corresponding to the different rays have to be parallel to fulfil the Bragg condition. This means that all the rays violate the Bragg condition simultaneously, when the crystal is rotated. The beam divergence, in the present case around 3”, does therefore not influence the double-crystal reflection process in this mode. This configuration is called non-dispersive set-

up. This technique is thus sensitive only to sample parameters like the lattice spacing and the mosaic spread. But even the + – -geometry may already be dispersive, if the scattering vectors of both crystals are different, thus if the d-spacing corresponding to the chosen reflections are different. If one wants to work in the non-dispersive mode, the reflections with their corresponding d-spacing values should be chosen as close as possible. Here again, higher order reflections present better possibilities to match the d-spacing values of both crystals. If the analyser crystal is also included in the set-up, the (+ – +) –geometry would represent the non-dispersive mode. In the experiments undertaken in this work, the non-dispersive set-up was exclusively used, thus the (+ – +) –geometry or the (– + –) –geometry and, in addition, identical crystals with exactly the same reflection were investigated.

5.5. High angular resolution

Let us call the half-width of the rocking curve of a perfect crystal $\Delta\theta^{HW}$. If the crystals used as the sample and the analyser are identical and the diffractometer is set to the non-dispersive mode, one has to set as an uncertainty for the resolution element in ω and φ the double of the half-width of a single crystal:

$$\Delta\omega = 2\Delta\theta^{HW} \qquad 5.6a$$

$$\Delta\varphi = 2\Delta\theta^{HW} \qquad 5.6b$$

Inserting these values in equation 5.5 leads to the following resolution for the parallel and the perpendicular component of the scattering vector:

$$\Delta G_{\parallel}/G = \Delta\theta^{HW}/\tan\theta$$
$$\Delta G_{\perp}/G = 3\Delta\theta^{HW} \qquad 5.7a\text{-}b$$

The half-width of the rocking curve itself is a function of the reflection order and the energy (i.e., the Bragg angle) of the following form [Zac 45]:

$$\Delta\theta^{HW} = \Delta\theta^{HW}(\tan\theta, 1/h, 1/k, 1/l) \qquad 5.8$$

It turns out that the resolution parallel to the diffraction vector increases with increasing reflection order because the half-width decreases accordingly. The situation is different for the resolution perpendicular to the diffraction vector. Here it increases not only with increasing reflection orders, but also with increasing energies, since the Bragg angle decreases. It follows that the transverse resolution may be an order of magnitude better than the longitudinal one, which is on the order of 10^{-7} and 10^{-6}, respectively. It should be recalled that the resolution possibilities at higher energies have to be compromised with the mechanical stability of the instrument controlled by the laser-interferometric method, what presents actually a sampling capability of the angular positions of the crystals of 0.01''- 0.02''.

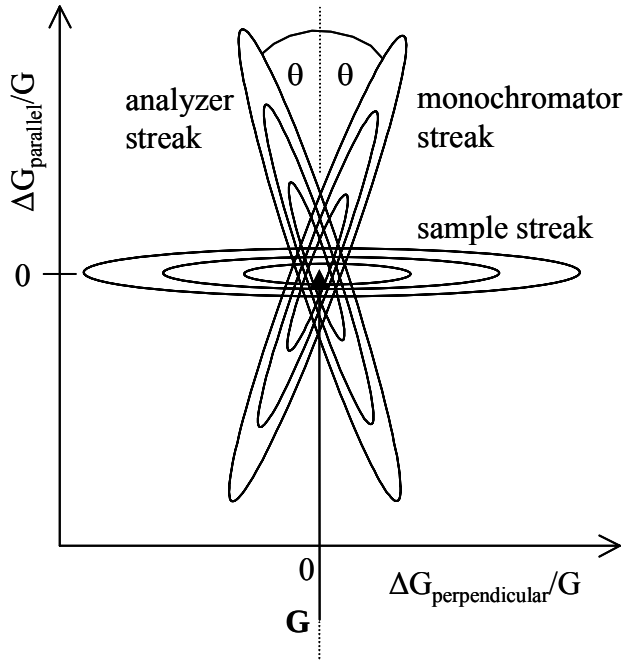

Figure 5.9: A schematic view of an ideal reciprocal space map in coordinates parallel and perpendicular to the reciprocal lattice vector G. The ellipses represent contour lines of the intensity distribution. The analyser and monochromator streak are tilted by the Bragg angle θ with respect to the longitudinal direction. The sample streak lies along the perpendicular component.

A schematic view of the resolution elements in the reciprocal space is sketched in figure 5.9. The ellipses represent contour-lines. The sketched intensity distributions

come from the intrinsic crystal half-widths and are called resolution streaks. They are only resolvable, if the sample crystal itself does not present a too poor quality, which would result in a broadening of the reciprocal lattice point. The inclination of the monochromator and analyser streak by θ with respect to the direction parallel to the scattering vector and the sample's streak extension in the direction perpendicular to the scattering vector becomes evident from figure 5.8. Such a representative reciprocal space map was measured for the (-351)-reflection at the energy of 100 keV and presented in [Lis 98b].

5.6. The instrument resolution function

A resolution function of the triple-axis diffractometer in two crystal mode (without analyser) is presented in figure 5.10. This is realised by a scan in ω and corresponds to the integration over the analyser-scanning angle φ. The resolution function is recorded for the (-571)-reflection at the x-ray energy of 200 keV. For comparison, the measured and the calculated curve are plotted together. The shapes are rather similar, the theoretical curve being a Lorentzian. The half-width of the measured rocking curve amounts to 0.065", the theoretical half-width is calculated to 0.04". As a first approximation the calculation of the theoretical curve is based on the convolution of the rocking curves of two perfect silicon crystals (equation 2.19). This already leads to an acceptable result. The deviation of the measured curve is due to a broadening that is influenced by different contributions. First, the crystals may not be fully perfect. Second, there might be a contribution of neighbouring wavelengths $\lambda \pm \Delta\lambda$ impinging on the monochromator crystal, and third, the divergence of the incoming beam on the monochromator may also cause a broadening. This is not contradictory to the discussion of the non-dispersive set-up, since the last two points mentioned here do not affect the scattering by two consecutive crystals. But that does not mean that the rocking curve of the monochromator may not be broadened due to its acceptance of different wavelengths of the white beam and ray directions within its intrinsic bandwidth. In other words, the set-up does not probe the dispersion, but the dispersion broadens the resolution function of the set-up.

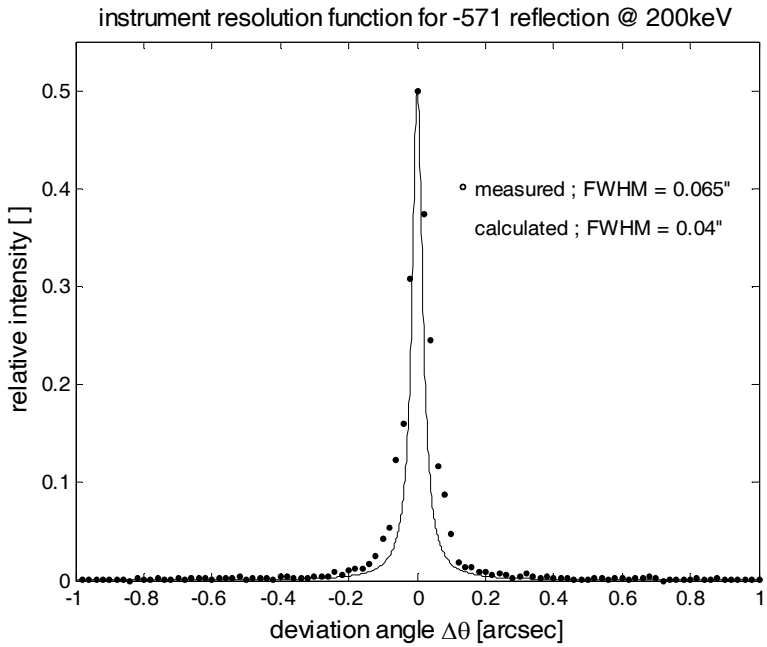

Figure 5.10: The resolution function of the triple-axis diffractometer in two-crystal mode for the (-571)-reflection at the x-ray energy of 200 keV. The angle $\Delta\theta$ indicates the deviation from the Bragg angle θ. The FWHM of the theoretical curve is smaller.

5.7. The sample: ultrasound in crystals

Piezoelectric $LiNbO_3$-transducers (Valpey-Fisher) were bonded to the (111)-surface of nearly perfect silicon crystals, in most cases with a thickness of 5 mm. Clean machine oil was used as bonding medium. The transducers with a resonance frequency either of 5, 20 or 30 MHz were normally driven in an overtone frequency around 100-150 MHz and excited the ultrasonic waves in the crystal.

A schematic view of the combined real- and reciprocal space scattering geometry is presented in figure 5.11. A monochromatic x-ray beam with an incoming wave vector $\mathbf{k_i}$ is reflected on the perturbed lattice planes of the crystal. The outgoing wave vector $\mathbf{k_f}$ forms the angle θ with the set of diffracting lattice planes. The scattering vector **G** is by definition perpendicular to this set of lattice planes. The angle between the scattering vector and the reciprocal direction parallel to the surface is called β, the parallel direction being in most cases (-110). The direction of the ultrasound wave

vector κ is supposed to point in the direction perpendicular to the crystal surface, hence the (111)-direction. The angle between this ultrasound direction and the scattering vector is called α.

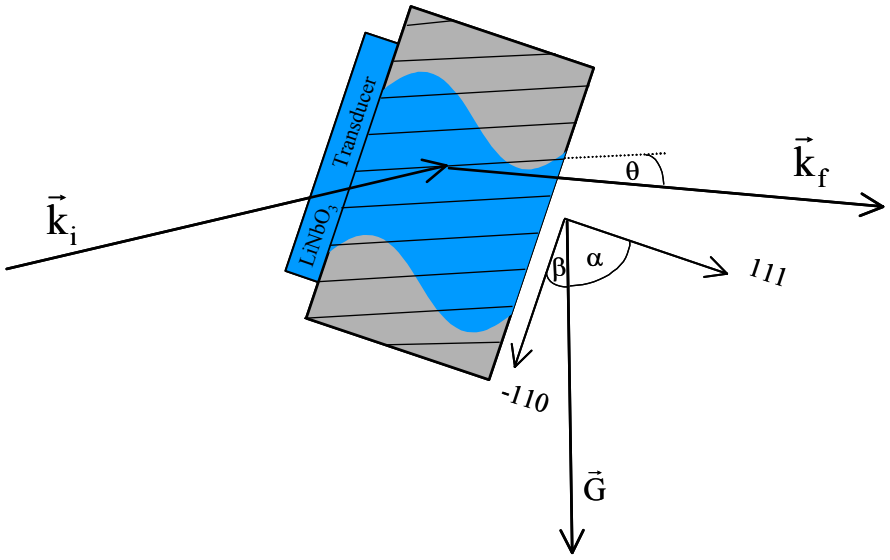

Figure 5.11: Diffraction on an ultrasound excited silicon crystal. The lattice planes are not parallel to the (-110) face because an asymmetric reflection has to be chosen for resolution reasons. The angle of asymmetry is called β and the angle between the ultrasound propagation direction and the reciprocal lattice vector is α.

If the ultrasound wavelength exceeds the interatomic distances by far, the lattice nature of the crystals can be neglected. Since ultrasound wavelengths are typically in the μm-range and the interatomic distances are only a few Ångstrøm, this condition is certainly fulfilled. In this case ultrasonic or elastic waves in crystals are described in the framework of the elasticity theory of solids. Therein, the elastic moduli play a central role. In general, 21 different elastic moduli have to be considered [Ash 76]. In crystals with cubic symmetry the number of independent elastic moduli reduces to only three, namely c_{11}, c_{12} and c_{44}.

The description of the dynamic elastic behaviour of a solid has to start with the equation of motion, which can be written as indicated in equations 5.9a-c [War 69].

$$\begin{aligned}
\frac{\partial \sigma_x}{\partial x} + \frac{\partial \tau_{xy}}{\partial y} + \frac{\partial \tau_{zx}}{\partial z} &= \rho \frac{\partial^2 u}{\partial t^2} \\
\frac{\partial \sigma_y}{\partial y} + \frac{\partial \tau_{xy}}{\partial x} + \frac{\partial \tau_{yz}}{\partial z} &= \rho \frac{\partial^2 v}{\partial t^2} \\
\frac{\partial \sigma_z}{\partial z} + \frac{\partial \tau_{zy}}{\partial y} + \frac{\partial \tau_{zx}}{\partial x} &= \rho \frac{\partial^2 w}{\partial t^2}
\end{aligned} \qquad 5.9a\text{-}c$$

In these equations, t represents the time dependence and ρ the density of the material. σ and τ express the normal and shearing stresses, respectively, and ε and γ stand for the normal mutatis mutandis the shearing strains.

Hooke's law links the stresses with the strains via the elastic moduli. This is written down in equation 5.10a-f.

$$\begin{aligned}
\sigma_x &= c_{11}\varepsilon_x + c_{12}\varepsilon_y + c_{12}\varepsilon_z \\
\sigma_y &= c_{12}\varepsilon_x + c_{11}\varepsilon_y + c_{12}\varepsilon_z \\
\sigma_z &= c_{12}\varepsilon_x + c_{12}\varepsilon_y + c_{11}\varepsilon_z \\
\tau_{yz} &= c_{44}\gamma_{yz} \\
\tau_{zx} &= c_{44}\gamma_{zx} \\
\tau_{xy} &= c_{44}\gamma_{xy}
\end{aligned} \qquad 5.10a\text{-}f$$

Together with the definitions of the normal and the shearing strains, in which u, v and w represent the components of displacement at the position x, y and z (equations 5.11a-f), the equation of motion becomes a linear partial differential equation of second order.

$$\begin{aligned}
\varepsilon_x &= \partial u/\partial x \\
\varepsilon_y &= \partial v/\partial y \\
\varepsilon_z &= \partial w/\partial z \\
\gamma_{yz} &= \partial v/\partial z + \partial w/\partial y \\
\gamma_{zx} &= \partial w/\partial x + \partial u/\partial z \\
\gamma_{xy} &= \partial u/\partial y + \partial v/\partial x
\end{aligned} \qquad 5.11a\text{-}f$$

A travelling plane wave 'Ansatz' for the variables u, v and w inserted into the equation of motion leads to the following three simultaneous conditions to determine the velocities and vibration directions of the possible elastic waves:

$$\begin{aligned}
&\left\{c_{11}\,l^2 + c_{44}\left(m^2+n^2\right) - \rho v^2\right\} A + \left(c_{12}+c_{44}\right) lmB + \left(c_{12}+c_{44}\right) lnC = 0 \\
&\left(c_{12}+c_{44}\right) lmA + \left\{c_{11}\,m^2 + c_{44}\left(n^2+l^2\right) - \rho v^2\right\} B + \left(c_{12}+c_{44}\right) mnC = 0 \\
&\left(c_{12}+c_{44}\right) nlA + \left(c_{12}+c_{44}\right) mnB + \left\{c_{11}\,n^2 + c_{44}\left(l^2+m^2\right) - \rho v^2\right\} C = 0
\end{aligned} \qquad 5.12a\text{-}c$$

If **κ** represents the propagation direction of the ultrasonic wave, the direction cosines with respect to the reciprocal lattice base vectors are called l, m and n. For the vibration direction **a** (and hence the amplitude), the direction cosines are named with A, B and C. For a specified propagation direction equation 5.12a-c represents a set of homogeneous equations in the variables A, B and C. To obtain non-trivial solutions the determinant of the coefficients must vanish, which leads to the equations of the sound velocities.

As an example, the velocities for the [111]-direction of a cubic crystal are calculated. Therefore, l, m and n have to be set to $1/\sqrt{3}$. The solution of equation 5.12a-c results in three possible waves, one pure longitudinal ultrasonic wave and two degenerated cases of pure transverse ones. The conditions for the vibrational directions as well as the results for the sound velocities are given by equations 5.13a-c.

$$\begin{aligned}
v_1 &= \sqrt{\frac{c_{11}+2c_{12}+4c_{44}}{3\rho}} & A_1 = B_1 = C_1 &= 1/\sqrt{3} \\
v_2 &= \sqrt{\frac{c_{11}-c_{12}+c_{44}}{3\rho}} & A_2 + B_2 + C_2 &= 0 \\
v_3 &= \sqrt{\frac{c_{11}-c_{12}+c_{44}}{3\rho}} & A_3 + B_3 + C_3 &= 0
\end{aligned} \qquad 5.13a\text{-}c$$

For silicon, the three elastic moduli values are c_{11} = 165 GPa, c_{12} = 64 GPa and c_{44} = 79 GPa [deL 56], the density has the value $\rho = 2.33 \cdot 10^3$ kg/m^3 [Ash 76]. This gives

finally the possible velocities for the [111]-direction in silicon, 9334 m/s for the longitudinal mode and 5075 m/s for the two transverse modes.

It should be noted that for other directions than [100], [110] or [111] the three possible waves are still independent, but no longer neither pure longitudinal nor pure transverse [War 69].

Furthermore it should be mentioned that these ultrasound propagation velocities are required in the simulation program SIMSAT (chapter 4) in order to calculate the length of the ultrasound wave vector κ, which is, together with the propagation direction, responsible for the angular position of eventually induced satellite reflections. The calculation of these velocities is already included in the program for all required propagation directions.

Eigenresonances and ultrasound velocities: We expect to observe strongest effects on the diffracted intensity distribution, if a standing ultrasonic wavefield is excited in the silicon crystal. In order to obtain the eigenresonances of the crystal, the diffraction angle $\Delta\theta$ is set on the tail of an unperturbed rocking curve. Applying an excitation frequency in the low frequency range is accompanied by a broadening of the rocking curve (chapter 4). The ultrasound frequency is then successively changed in the low frequency regime and the diffracted intensity is recorded.

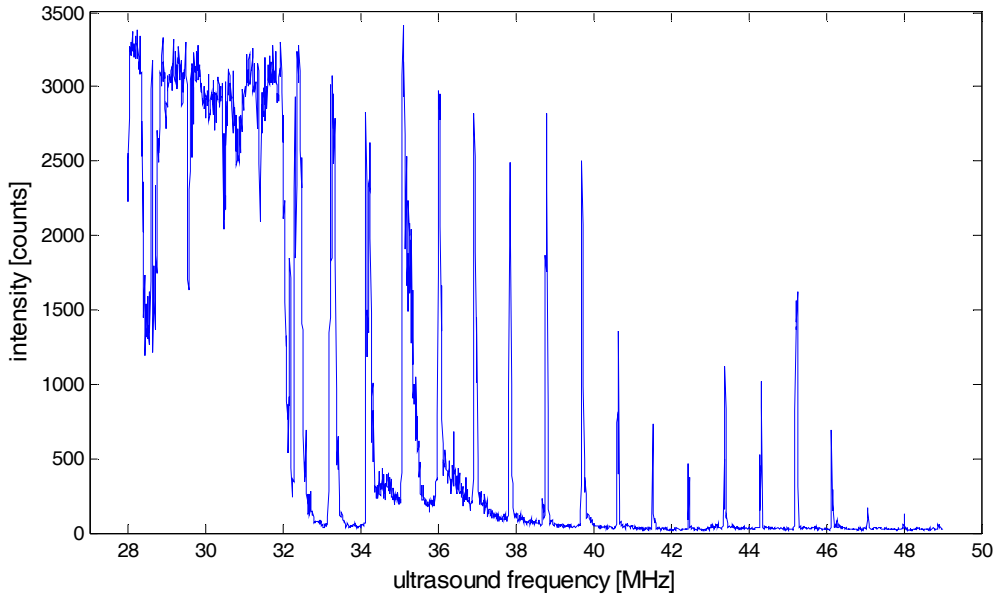

Figure 5.12: A frequency scan on the tail of the rocking curve for the (-571)-reflection at the x-ray energy of 200 keV and an excitation voltage of 0.2 V. The diffraction angle $\Delta\theta$ is set to 0.4 arcsec beside the peak value of the rocking curve intensity distribution. Then the ultrasound frequency is successively changed in steps of 0.01 MHz and the diffracted intensity is recorded for 0.2 s. Close to the transducer resonance frequency of 30 MHz a large resonance distribution is measured. At larger frequencies resonances of the 5 mm thick silicon crystal are observed.

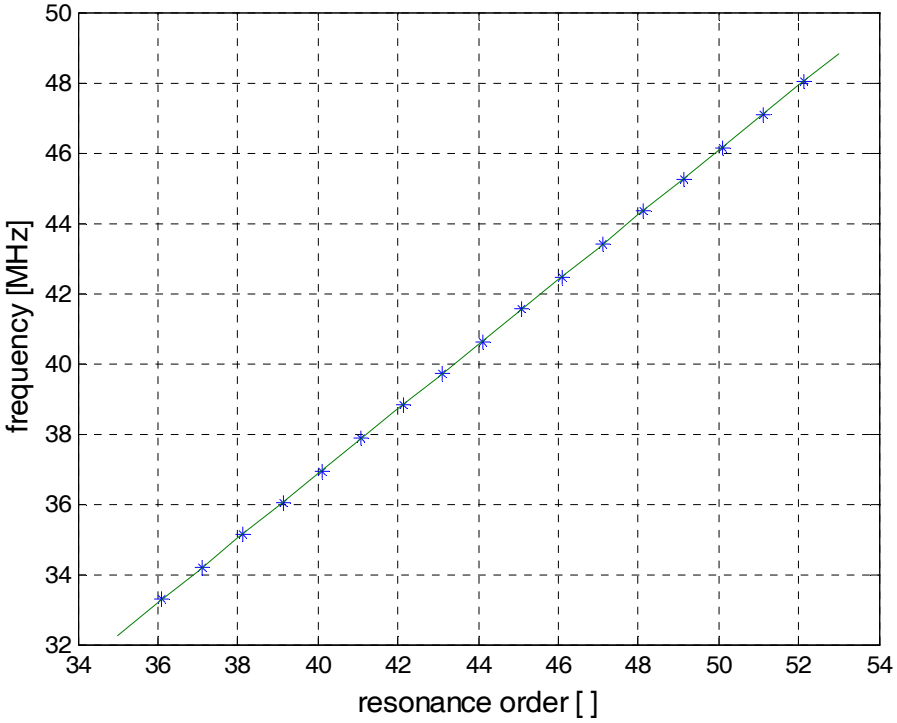

Figure 5.13: The resonance frequencies of figure 5.12 as a function of the resonance order. The resonance frequencies increase linearly with a gradient of 0.92 MHz ± 0.02 MHz. The resonance orders are nearly integers. They are obtained by extrapolating the linear function to the origin 0.

If the crystal is vibrating in an eigenresonance, the intensity increase should be largest (Hoc 97, Lis 98). Figure 5.12 shows a frequency scan with a step size of 0.01 MHz at the x-ray energy of 200 keV and an excitation voltage of 0.2 V at an angle $\Delta\theta = 0.4$ arcsec beside the peak intensity value of the (-571)-reflection. Around the transducer main resonance frequency of 30 MHz a large resonance distribution is measured. At ultrasound frequencies between 33 MHz and 49 MHz resonance frequencies of the crystal are observed, for which the diffracted intensity achieves maxima. A shape-preserving interpolant [Mat 02] is fitted to the data in order to determine the resonance frequencies, which yields a mean value of successive resonance frequencies of $\Delta f = 0.92$ MHz ± 0.02 MHz. The resonance frequencies show therefore a linear increase. This result is shown in figure 5.13, where the resonance frequencies are plotted as a function of resonance order n. The resonance orders are obtained by extrapolating the linear function to the origin 0, which means that the resonance frequencies f_n should follow $f_n = \Delta f \cdot n$. This gives nearly integer values for the resonance orders n (figure 5.13). Assuming that a standing ultrasonic wave is excited

in the crystal, we can determine the ultrasound velocity from the frequency gradient Δf with $v_1 = 2 \cdot \Delta f \cdot T$, T being the crystal thickness of 5 mm. This is due to the fact that an integer number of half the ultrasound wavelength should fit into the crystal. The result for the ultrasound velocity is $v_1 = 9200$ m/s, which is close to the value 9334 m/s for a propagation in the expected [111]-direction. However, for high ultrasound frequencies the situation is different. For high ultrasound frequencies separated satellite reflections are expected rather than a broadening of the rocking curve, if the excitation amplitude remains constant (chapter 4). But it is still possible to observe resonances. Figure 5.14 shows a frequency scan in the range from 122 MHz to 124 MHz with a step size of 0.005 MHz at the x-ray energy of 261 keV and an excitation voltage of 0.05 V at an angle $\Delta\theta = 0.2$ arcsec beside the peak intensity value of the (-571)-reflection. In this experiment a 40 MHz transducer was bonded to the (111)-face of a 10 mm thick silicon crystal. The detailed structure of the resonance intensity distribution is unclear.

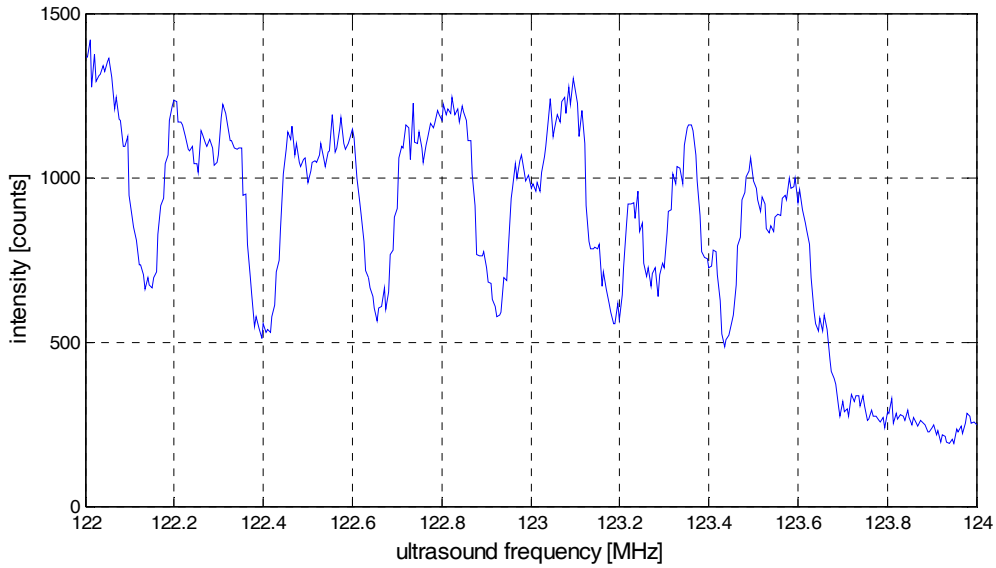

Figure 5.14: A frequency scan in the high frequency regime on the tail of the rocking curve for the (-571)-reflection at the x-ray energy of 261 keV and an excitation voltage of 0.05 V. The diffraction angle $\Delta\theta$ is set to 0.2 arcsec beside the peak value of the rocking curve intensity distribution and the ultrasound frequency is successively changed in steps of 0.005 MHz. The diffracted intensity is recorded for 0.2 s at each frequency. Broad resonances of the 10 mm thick silicon crystal are obtained with an increment of 0.26 MHz.

It is still possible to determine the periodicity of this resonance structure to $\Delta f = 0.26$ MHz. This yields an ultrasound velocity of 5200 m/s, which is far from the velocity in the [111]-direction. In chapter 6 the most probable propagation direction for a high excitation frequency is determined to point in the [012]-direction. Taking into account

an effective crystal thickness due to the longer travelling path in [012]-direction, which is due to the angle between the [111] and the [012]-direction, the ultrasound velocity is determined from the resonance frequencies with $v_2 = 2 \cdot \Delta f \cdot T_{eff} = 2 \cdot \Delta f \cdot T \cdot (5/3)^{1/2}$. This yields 6713 m/s for the ultrasound velocity, which is in the range of the propagation velocity for the [012]-direction of 5823 m/s, whereby it should be remembered that the resonance frequencies in figure 5.14 are very broad with nearly 0.2 MHz. Frequency scans in the high frequency and especially in intermediate frequency ranges need further investigations.

5.8. Time-resolution in x-ray diffraction: The timing electronics

As discussed in chapter 4, the ultrasound excitation of crystals can provoke time-dependent changes in the diffraction process. Therefore, time-resolving electronics are needed to observe those changes. A schematic view of the timing electronics is shown in figure 5.15.

The signal registered from the germanium-detector is amplified and serves as input signal for two different units. One chain of units consists of a timing filter amplifier, a constant fraction discriminator and a logic shaper and delay. This chain determines the arrival of the photon pulses already quite accurate in time (about 20 ns). The timing filter amplifier shapes the pulses with a fast rise time to minimize the noise contribution to the time resolution and allows a further wideband amplification of the signals. The constant fraction discriminator reduces the timing jitter. It is not this component that achieves the highest time resolution, but it is important to keep the jitter small in order to avoid that several photons fall into the time window of this chain. The logic shaper and delay then shapes the signal in a way that it can be treated by the logic AND-unit. The resulting signal of this chain is visualized with the help of a snapshot of the oscilloscope's screen (figure 5.15).

In the second chain of components the pulses from the detector are discriminated to the right photon energy. They are brought into coincidence in the logic unit with the channel indicating at what time the photon arrived, after being shaped properly. This signal of the energy-resolving channel is also shown on the oscilloscope snapshot.

Finally, the radiofrequency signal of the storage ring (‘bunch clock’) indicates very accurately the possible arrival of a photon from the synchrotron and represents the third part of the three-level coincidence. This signal is treated in the following way. To be able to handle the signal, it must be divided from the high MHz-regime to the low MHz-regime. This frequency is still much higher than the frequency of actually registered photons at the detector so that no photons can be missed. Before being transferred to the logic unit, the signal is deformed to a rectangular pulse by the discriminator. The resulting signal from the discriminator is also shown on the oscilloscope snapshot in figure 5.15. From this record the higher ‘bunch clock’ frequency compared to the two detector signals is also obvious.

The output of the logic unit indicates a measured photon with the correct energy very precise in time. The precision and the jitter follows from the most accurate channel, the treated radiofrequency signal from the storage ring. The output signal serves as a start signal to the ‘Time-to-Amplitude Converter’ (TAC).

On the other hand, the frequency generator signal, which drives the transducer to excite ultrasonic waves in the crystal, is triggered in a way that it gives always at the same relative period the stop signal for the time-counting. Also this signal has to be divided down and discriminated to be accepted from the TAC. For the TAC, it serves as a stop signal. Also all the outputs of these units, the frequency generator, the divider and the discriminator, are visualized with a snapshot of the oscilloscope screen in figure 5.15.

The philosophy of the timing electronics up to this point is recapitulated in the upper right part of the scheme in figure 5.15. The actual photon events with the right energy and very well known in time give the start signal to the TAC, the triggered signal from the frequency generator tells the TAC to stop. Thus the time difference between the photon arrival and the excitation through the ultrasound is measured and converted into an analogue amplitude value by the TAC. After the digitalisation of this amplitude value by the ‘Amplitude-to-Digital Converter’ (ADC), it is stored as one event in the corresponding channel of the ‘Multi Channel Analyser’ (MCA). Thereby the AIM serves as the device support for the MCA record with its 8192 channels, thus the AIM is the providing memory allocation.

This procedure repeats in a stroboscopic way until enough statistics is achieved in the channels of the MCA. These data are communicated via the fast Ethernet to the computing unit. A plot of the counted photons in the different channels is shown on

the lower right-hand side in figure 5.15, which is the output information of the whole electronics. After the calibration the channels are converted into a time scale. Therefore the plot represents the time-dependent intensity development at one single point of the rocking curve (or at any diffraction angle). If at all the other diffraction angles of the rocking curve the same procedure is repeated and thus the development of the intensity as a function of time is measured at different diffraction angles, a whole time pattern is recorded by putting all of them together. The time pattern represents therefore the intensity distribution as a function of both variables, diffraction angle $\Delta\theta$ and time t. Such a completed time pattern is shown in chapter 6, figure 6.22, where the experimental results are discussed.

Timing Electronics

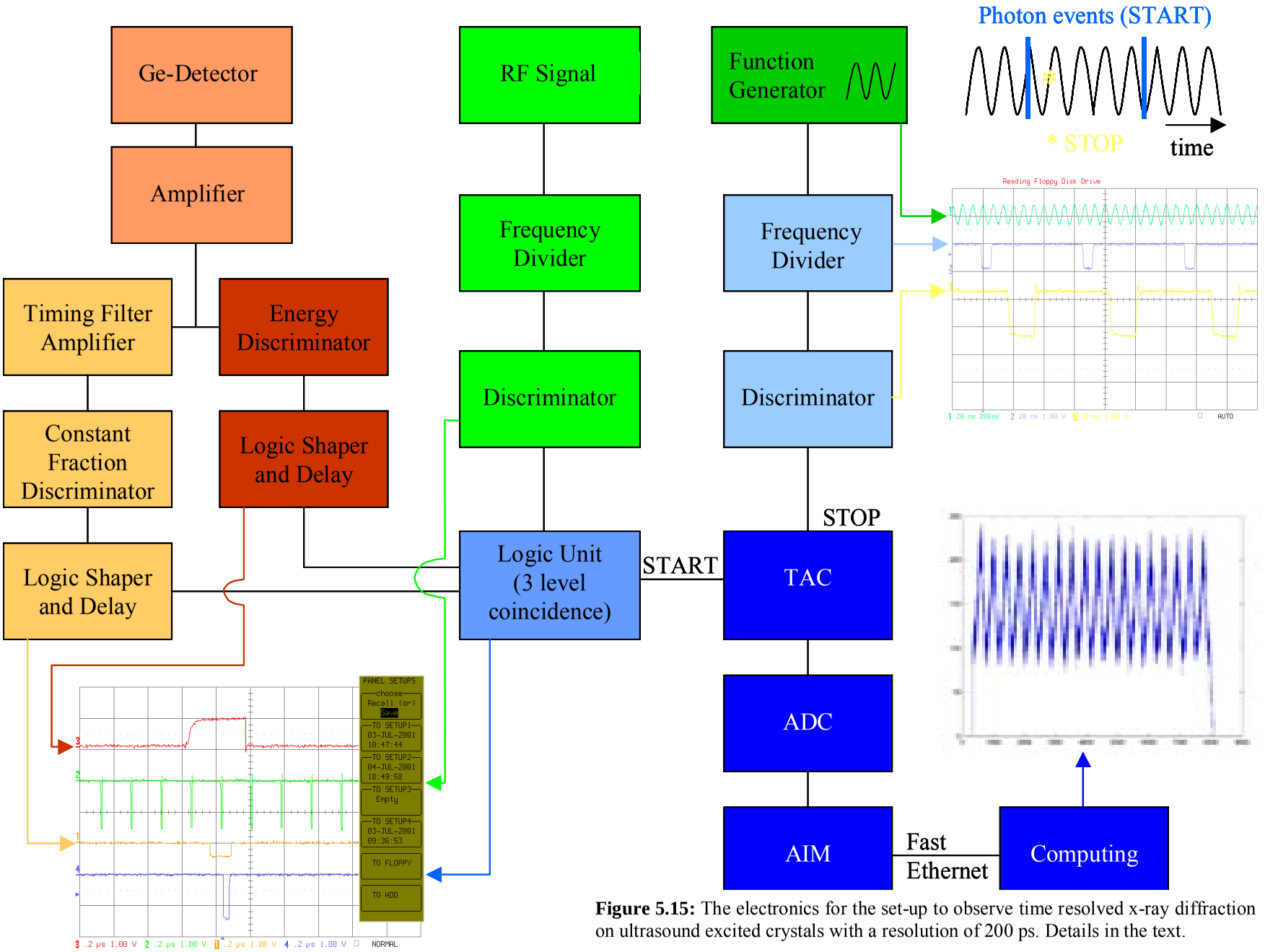

Figure 5.15: The electronics for the set-up to observe time resolved x-ray diffraction on ultrasound excited crystals with a resolution of 200 ps. Details in the text.

Chapter 6

Results and discussion: Comparison of experimental data and simulations

6.1. Determination of sound propagation direction and angular satellite positions

On the basis of the calculations performed with SIMSAT for the actual experimental conditions, we are now able to compare the measured data with the simulations. For a $LiNbO_3$ longitudinal transducer bonded to a 5 mm thick silicon crystal like it is shown in figure 5.11 we expect to excite longitudinal ultrasonic waves in the [111]-direction. At the x-ray energy of 200 keV and an ultrasound frequency of 95.9667 MHz we measured well above the x-ray acoustic resonance condition ($\Delta = 13.9 >> 1$), thus ultrasound excited satellite reflections should in principle be observable. After adjusting the ultrasound frequency to an Eigenresonance of the silicon crystal as described in chapter 5.7, we indeed managed to resolve five diffraction satellites on each side of the main reflection (-571) at the ultrasound frequency of 95.9667 MHz (figure 6.1).

The excitation voltage amplitude was set to 0.5 V on the frequency generator. Via $\mathbf{Ga} \approx n$ the number n of measured satellites gives an indication for the value of the ultrasound amplitude, which is about 2.5 Å. Obviously, this value of the ultrasound amplitude falls into the high amplitude regime since more than only one diffraction satellite is observed. For the simulation of this experiment the ultrasound amplitude was therefore set to 2.5 Å in order to match the number of excited satellites from the experimental observation. But from figure 6.1 and figure 6.2 it becomes clear that the measured satellite positions do not match the simulated ones.

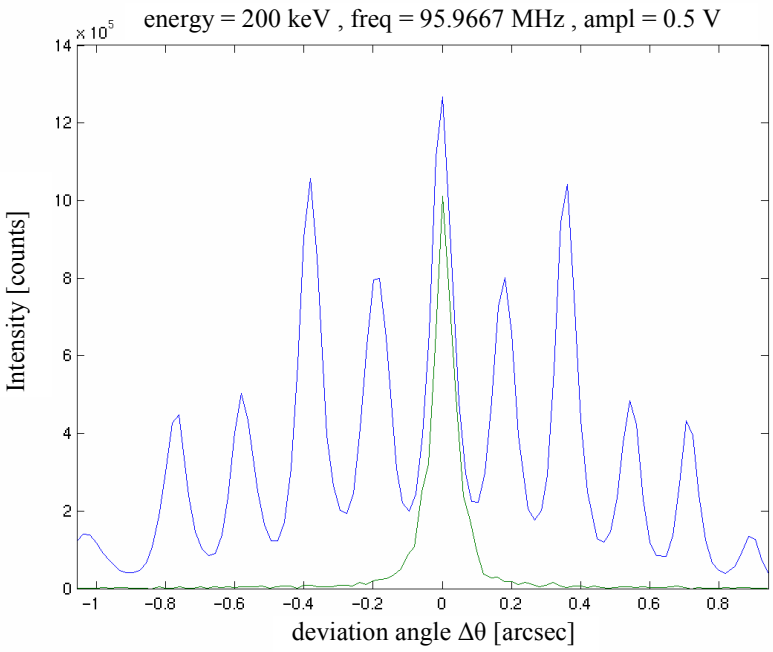

Figure 6.1: Measured ultrasound excited satellite reflections around the (-571) silicon reflection at the x-ray of 200 keV, the ultrasound frequency of 95.9667 MHz and an excitation voltage of 0.5 V. The angular scale is relative to the exact Bragg angle. The increment in Δθ is 0.02 arcsec, the accumulation time per data point is 50 s. The green curve represents the instrument resolution measured on the unexcited silicon crystal at 200 keV.

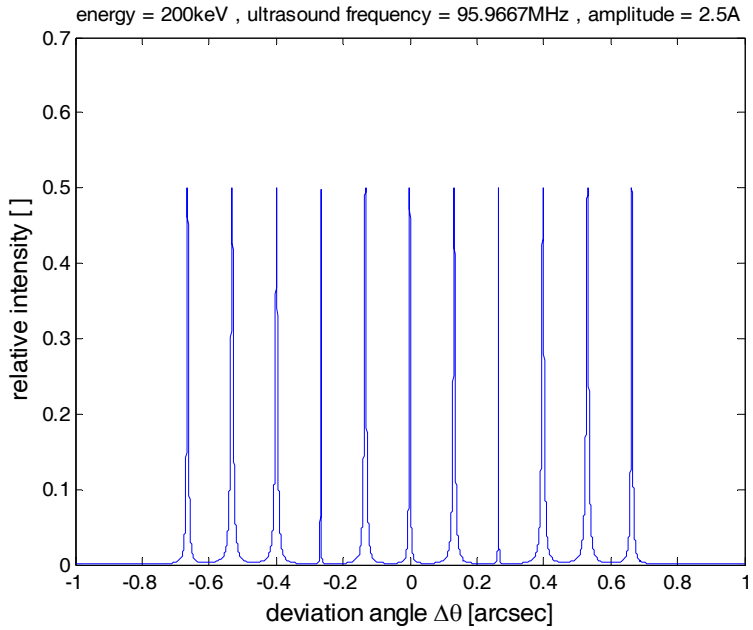

Figure 6.2: Simulated ultrasound excited satellite reflections of the (-571) silicon reflection. The x-ray energy and ultrasound frequency is set to the experimental values of 200 keV and 95.9667 MHz. The ultrasound propagation direction is assumed to point in the [111]-direction with the sound velocity of 9334 m/s for a longitudinal wave. The ultrasonic amplitude is chosen to 2.5 Å in order to match the measured number of satellite reflections. The increment in Δθ is 0.0001 arcsec. The theoretical satellite positions do not fit the observed ones.

Determination of the satellite positions from the measurement and calculating the satellite positions with the kinematical theory (equation 4.8) and the dynamical theory (equation 4.9) leads to the satellite Bragg angles shown in figure 6.3. As expected for high x-ray energies, the satellite positions calculated with the kinematical and the dynamical theory do not differ much. The difference would be hardly detectable with the smallest possible angular stepwidth of the diffractometer of 0.01". The difference between the satellite positions calculated with both theories as compared to the measured positions is much larger, i.e. on the order of 0.08"-0.38". In addition, the measured set of satellite positions is not symmetric with respect to the main reflection. The angular positions of the satellite system seem to be inclined to the left-hand side of the main reflection.

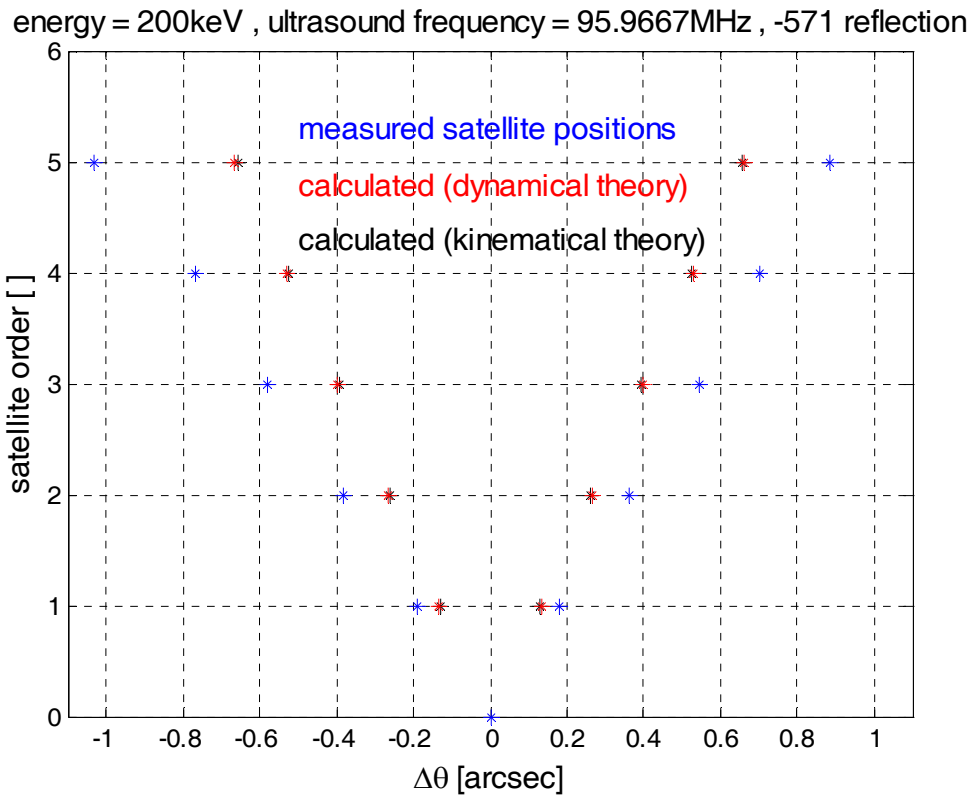

Figure 6.3: Comparison of measured and calculated satellite positions. The calculations due to kinematical and dynamical theory do not differ much at high x-ray energy of 200 keV. The system of measured satellite positions is inclined to lower diffraction angles. The difference between measurement and calculation is already 0.38 arcsec for the fifth satellite.

Assuming that the excited ultrasonic wave does not propagate along the expected [111]-direction, a reciprocal space map is most helpful to analyze the actual direction of the excited ultrasonic wave in the silicon crystal. Figure 6.4 displays the measured high-resolution reciprocal space map of the region around the (-571) reflection including the satellite system. The data in the figure is transformed from the originally measured ω-φ -scans to the reciprocal space coordinates parallel and perpendicular to the diffraction vector **G** via equation 5.5. Even the resolution streaks of the satellite reflections are clearly visible, which is an indication of the good quality of the high resolution setup, the diffracting crystals and the statistical certainty of the measurement. Such resolution streaks of highly resolved reflections were schematically shown in figure 5.9 and their origin explained in chapter 5.5. The black arrow in figure 6.4 indicates the direction of the diffraction vector **G**; the white line represents the projection of the sound direction within the scattering plane passing through the maxima of the measured two-dimensional satellite intensities. The angle between the diffraction vector and the white line is determined to $\alpha = 56°$. The complementary angle of 124° is equivalent for the propagation direction of the ultrasonic wave.

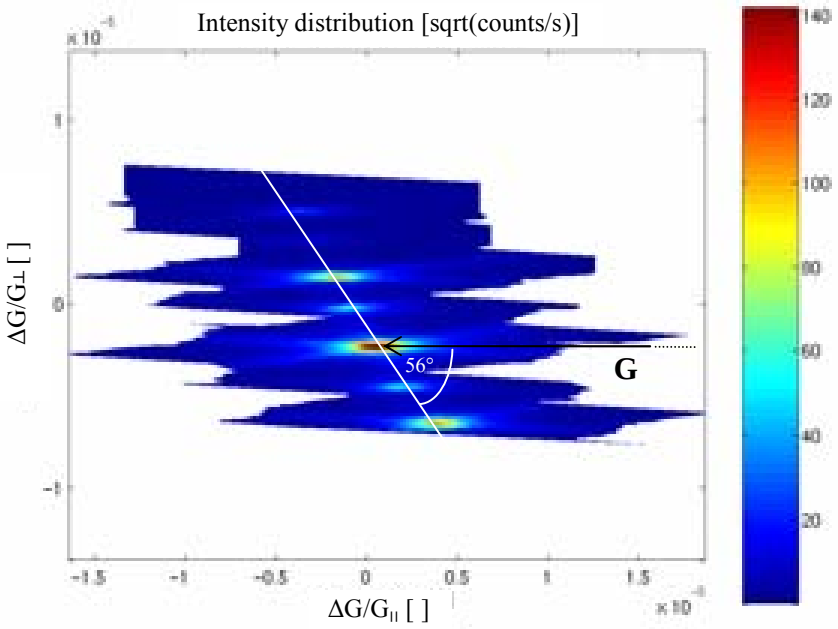

Figure 6.4: High resolution reciprocal space map to determine the ultrasound propagation direction. The original stepwidth of the angular scan is 0.02 arcsec in ω and 0.01 arcsec in φ. The x-ray energy is 200 keV and the ultrasound frequency 220.6 MHz. We assume that the ultrasonic wave does not change its propagation direction in the high frequency regime. The total scanning time is 2 h with an integration time of 0.2 s at each point of the reciprocal space.

To determine the ultrasonic wave propagation direction from this intensity map, a schematic view of the experimental situation is displayed in figure 6.5. In the most general case, the ultrasonic wave vector **κ** may point in any direction of the reciprocal space. It can therefore also point out of the scattering plane as assumed in figure 6.5.

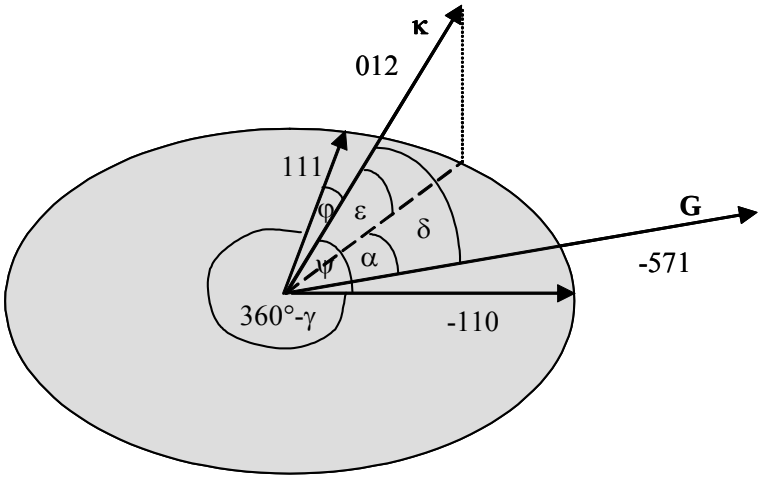

Figure 6.5: Geometry for the ultrasound wave vector **κ** lying out of the scattering plane. The plane is determined by the (111) and (-110) reciprocal lattice vectors. The scattering vector **G** lies in the scattering plane. The angle α is measured in the reciprocal space map experiment.

The angle of the projection of **κ** onto the scattering plane is denoted ε. The angle between this projection and the diffraction vector **G** is α and represents the angle determined from the measurement. The angle between **κ** and **G** is called δ. The relation between the projection angle ε, the angle α between the projection of **κ** onto the scattering plane and **G**, and the angle δ between **κ** and **G** is given by

$$\cos\delta = \cos\alpha \cdot \cos\varepsilon \tag{6.1}$$

Equation 6.1 is the law of spherical right triangles [War 69].

Since the angles ε and α are unknown, we need at least one more reciprocal lattice vector to define the scattering plane. The scattering plane can be defined by the (111) reciprocal lattice vector of the (111)-cut silicon crystal and the (-110) reciprocal lattice vector perpendicular to it (i.e. $\gamma = 90°$). The diffraction vector **G** lies in this plane. φ is the angle between the reciprocal lattice vector (111) and the ultrasound wave vector **κ**, ψ the angle

between (-110) and **κ**. The angle between the ultrasound wave vector and the scattering plane spanned by two reciprocal lattice vectors is calculated to [Mer 91, p. 141]

$$\cos\varepsilon = \frac{1}{\sin\gamma} \cdot \sqrt{\cos^2\varphi + \cos^2\psi - 2\cos\varphi\cos\psi\cos\gamma} \qquad (6.2)$$

The solution for the most probable direction of the ultrasound wave vector **κ** is then obtained by systematic trial and error. For a list of Miller indices (hkl) indicating the propagation direction of the ultrasonic wave, the angle α is calculated via equations 6.1 and 6.2. The list contains all possible combinations of the indices h, k, l for $-2 \leq h,k,l \leq 2$. Only the set of indices (hkl) = (012), (hkl) = (120), (hkl) = (0-1-2) and (hkl) = (-1-20) yield α = 56.25° respectively α = 123.75°. All other combinations of (hkl) lead to different angles for α, which are at least several degrees off the measured value. The list of calculated angles α for the different propagation directions (hkl) can be found in appendix A.2. It should be noted that the directions of vectors pointing to a reciprocal lattice point (hkl) are identical to directions [hkl] in real crystal space due to the cubic symmetry of the silicon crystal.

To obtain the sound velocities for the [012] direction, equations 5.12a-c for the propagation of elastic waves in cubic crystals are solved (the direction cosines have to be set to l = 0, m = $1/\sqrt{5}$, n = $2/\sqrt{5}$). This results in three velocities

$$v_1 = \sqrt{\frac{c_{44}}{\rho}} \qquad (6.3)$$

$$v_{2,3} = \sqrt{\frac{c_{11} + c_{44}}{2\rho} \pm \sqrt{\left(\frac{c_{11} + c_{44}}{2\rho}\right)^2 - \frac{9c_{11}c_{44}}{25\rho^2}}} \quad , \qquad (6.4)$$

corresponding to a pure transverse mode, a quasi-longitudinal mode, and a quasi-transverse mode, respectively. Possible sound velocities for the [012]-direction are then

v_1 = 5823 m/s, v_2 = 9782 m/s and v_3 = 3006 m/s. The calculation of the satellite positions based on v_1 and the propagation direction [012] by the kinematical (equation 4.8) and the dynamical (equation 4.9) theory match the measured satellite diffraction angles very well. The results are plotted in figure 6.6.

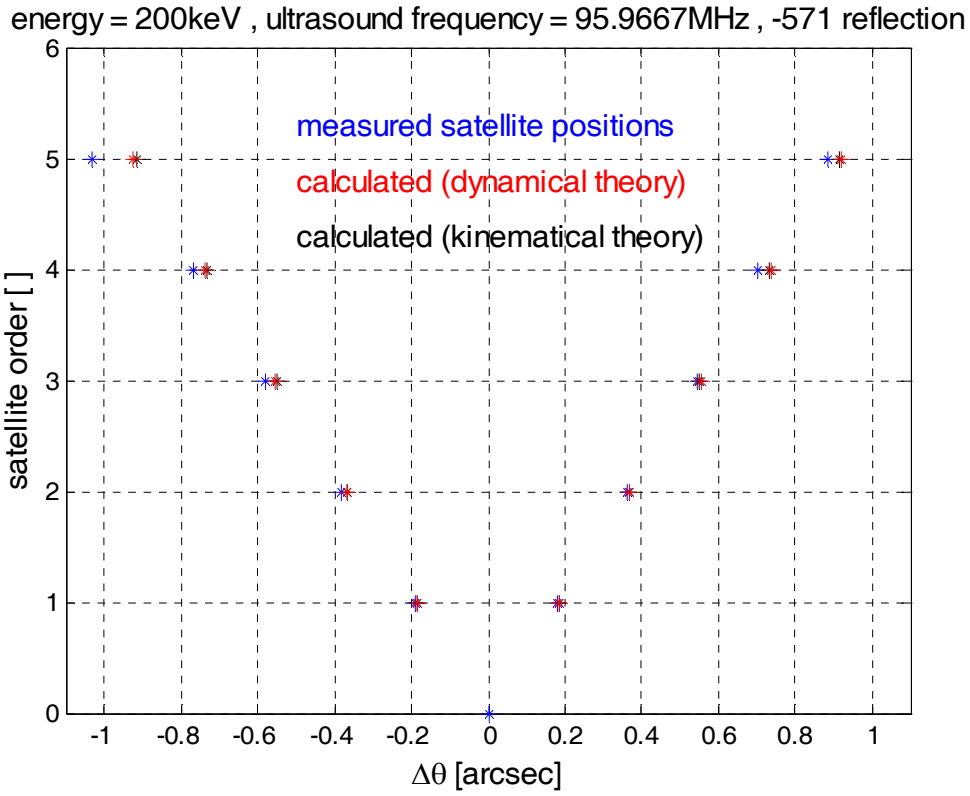

Figure 6.6: Comparison of measured and calculated satellite positions for a transverse ultrasonic wave propagating in the [012]-direction with the velocity of 5823 m/s. The positions of the satellites match very well.

The asymmetry in the measured satellite positions, especially for higher order satellite reflections, is explained by the long term drift of the triple-axis diffractometer. A scan like it is shown in figure 6.1 takes about 1h in order to obtain a very high counting statistics. The long term stability of the instrument was determined to be on the order of 0.1 arcsec [Lis 97]. The largest deviation between the calculated satellite positions and the measured ones is observed for the fifth order satellite on the left side of the main reflection. This deviation is determined to 0.11 arcsec, which lies in the range of the long term stability of the instrument.

6.2 Comparison of measured and simulated intensity distributions

The intensity distribution of the satellite system measured at the x-ray energy of 200 keV, the ultrasound frequency of 95.9667 MHz, and the excitation voltage of 0.5 V is shown in figure 6.7. The data was obtained by a ω-scan around the (-571)-reflection of the excited silicon sample measured without analyzer. In the same plot the instrumental resolution function measured at the same x-ray energy of 200 keV without ultrasonic excitation is shown.

In chapter 6.1 the most probable ultrasound propagation direction was determined to point in the [012]-direction. The simulation according to equation 4.5 describing the high amplitude case for the x-ray energy of 200 keV and an ultrasound frequency of 95.9667 MHz as in the experiment is shown in figure 6.8. The ultrasound amplitude vector is assumed to point in the [100]-direction and thus perpendicular to the ultrasound propagation direction [012]. This is because the determination of the sound propagation in chapter 6.1 showed that we are dealing with a transverse ultrasonic wave. Only the ultrasound velocity of 5823 m/s for the transverse wave yielded the measured satellite positions. From the discussion in chapters 4.5 and 4.6 it should be kept in mind, however, that the ultrasound amplitude vector affects the number of excited diffraction satellites and their FWHM, but not the angular satellite positions. The absolute value of the ultrasound amplitude was set to 3.8 Å, since this is resulting in five diffraction satellites on each side of the main reflection, the same number of satellites as were completely resolved by the experiment within the measured Δθ-range.

In figure 6.8 the instrument resolution function for the x-ray energy of 200 keV is plotted as well. This shows that the resolution element of the instrument with a FWHM of 0.065 arcsec is much broader than the calculated FWHM of the satellites. In addition, the FWHM of the satellites differ from one satellite to the other. The maximum values of the calculated satellite intensities are always 0.5, which is not observed in the experimental data. Moreover, the measured maximum values of the satellite intensities vary from one satellite to the other. In order to compare the simulation directly with the measured data, the result of the simulation has to be convoluted with the instrument resolution function.

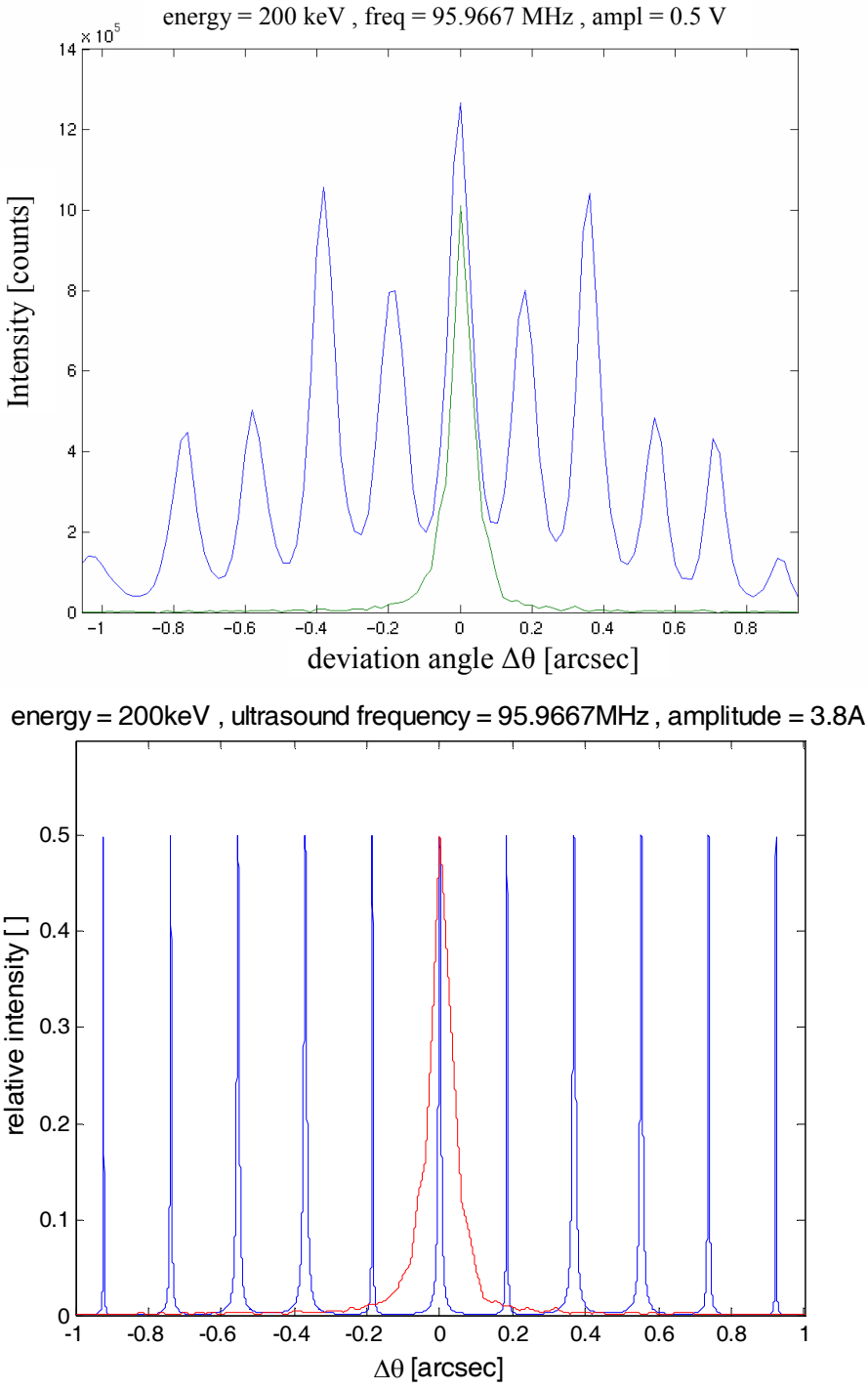

Figure 6.7 (top): Measured ultrasound excited satellite reflections around the (-571) silicon reflection like in figure 6.1. The interpretation of the angular satellite positions is now different since the ultrasound propagation direction turned out to be [012]. The green curve represents the instrument resolution function at 200 keV.

Figure 6.8 (bottom): Corresponding simulation of the satellite system with the ultrasound propagation in [012]-direction at a velocity of the transverse wave of 5823 m/s. The measured instrument resolution function normalized to 0.5 is also plotted (in red) to indicate that the FWHM is bigger than the FWHM of the calculated satellites. An ultrasound amplitude of 3.8 Å is chosen in order to obtain five diffraction satellites on each side of the main reflection.

For the convolution of the simulated intensity distribution with the measured instrumental resolution function the increment in $\Delta\theta$ has to be identical for both. In the simulation the stepsize is set to 0.0001 arcsec in order to resolve the sharp satellite reflections (figure 6.8), the resolution function is measured with a stepsize of 0.02 arcsec. Therefore the increment in $\Delta\theta$ is decreased down to 0.0001 arcsec by a linear interpolation of the intensity distribution of the resolution function in order to carry out the required convolution. The result of this convolution is presented in figure 6.9 together with the experimental data normalized to the maximum intensity value of 0.5 for the main reflection. The result is quite striking. It already explains why the maximum satellite intensities can not all have the same value in the measurement. Due to the instrumental resolution the differing FWHM of the diffraction satellites is not directly resolved in the measurement, but is expressed via the different height of the satellite reflections. This is clearly shown after convoluting the simulation with the instrumental resolution function. It also explains that the measured FWHM of all satellites lies in the range of the FWHM of the resolution function.

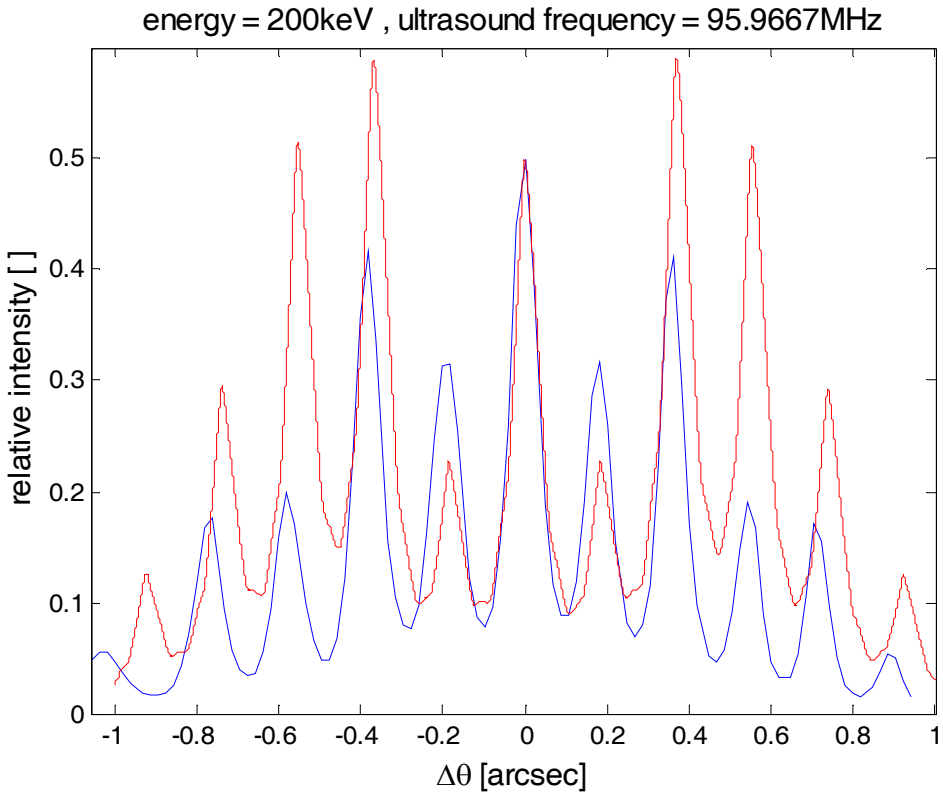

Figure 6.9: Comparison of measured (blue) and calculated (red) intensity profiles for the ultrasound excited satellite reflections. The maxima of the satellite reflections are influenced through the ultrasound amplitude which is a priori unknown. The amplitude is set to 3.8 Å, which fits qualitatively the measured intensity distribution.

The different maximum values of the measured satellite intensities are therefore caused by a resolution effect, but the intensity distribution of the convoluted diffraction satellites still does not completely match the measured satellite system. The intensity of the simulated main reflection after convolution, however, already fits nearly perfect. One reason for the differences between the measured satellite intensity distribution and the convolution of the simulated satellites with the resolution function is the unknown absolute value of the ultrasound amplitude. The value of **a** projected on **G** can change the FWHM of the satellites and thus the intensity values in the measurement. Another reason will become clear by the discussion of energy scans in chapter 6.3. It will be shown, that the satellite reflections behave fully dynamic; thus crystal thickness effects change the satellite intensities. The theory presented in chapter 4 treats the satellite reflections in the thick crystal limit, but our chosen experimental conditions with respect to x-ray energy, crystal thickness and ultrasound amplitude allow us to measure satellite reflections in the dynamical regime.

Small amplitude regime: An example of the measured intensity distribution for the (-351)-reflection of the silicon crystal excited in the small ultrasound amplitude regime at the x-ray energy of 146 keV and an ultrasound frequency of 144.797 MHz is shown in figure 6.10. In the small amplitude regime only one diffraction satellite is excited on each side of the main reflection. The instrument resolution function of the unexcited crystal at the x-ray energy of 146 keV is also plotted in figure 6.10. This shows that the main reflection is not broadened due to the ultrasonic excitation, which is expected from the diffraction theory of the small amplitude regime (chapter 4) once the satellite reflection is separated from the main reflection. The FWHM of the main reflection begins to oscillate only in the limit of large excitation amplitudes. The simulation (figure 6.10) shows a smaller FWHM of the satellites and the main reflection as compared to the measurement, which is 0.19 arcsec for the measured main reflection and 0.06 arcsec for the calculated one and 0.2 arcsec for the measured satellite reflection compared to 0.008 arcsec for the calculated FWHM of the satellite reflection. In the simulation a second order satellite reflection, which is not fully excited, appears in the diffraction profile due to the chosen ultrasound amplitude of 0.5 Å.

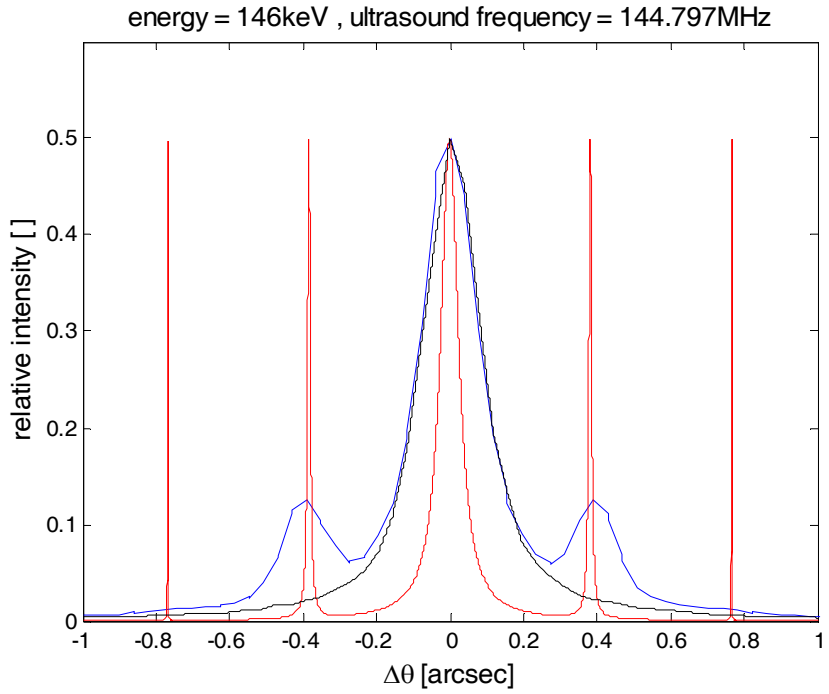

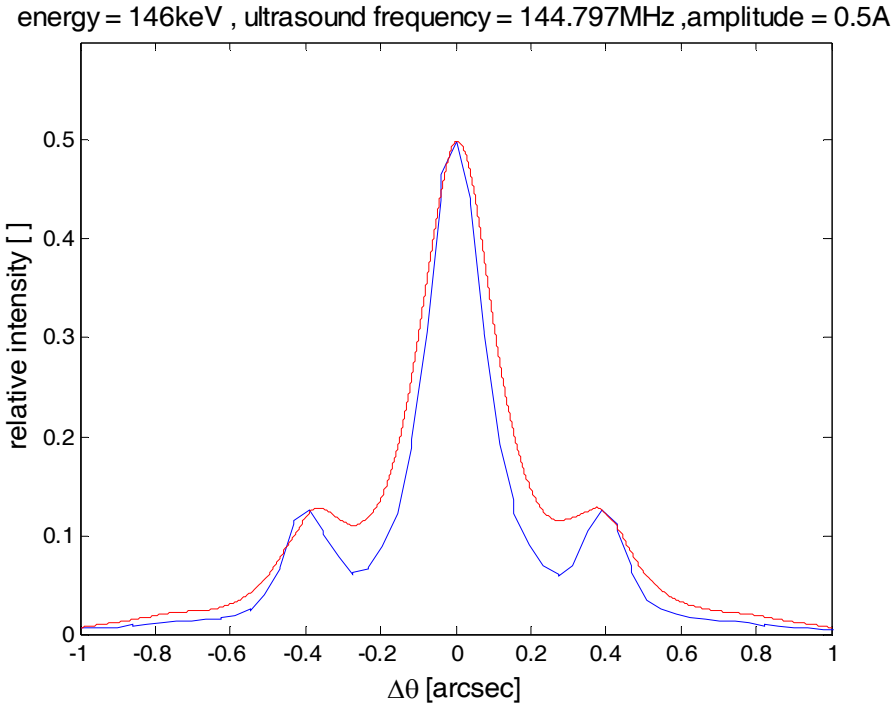

Figure 6.10 (top): Measured ultrasound excited satellite reflections (blue) at the (-351) silicon reflection in the small amplitude regime. The FWHM of the instrument resolution function (black) did not change. The red curve represents the simulation at the x-ray energy of 146 keV and the ultrasound excitation frequency of 144.797 MHz.

Figure 6.11 (bottom): The red curve corresponds to the convolution of the simulation (red in figure 6.7) and the instrumental resolution function (black in figure 6.7), which fits the measurement (in blue) quite well. The ultrasound amplitude is set to 0.5 Å in order to match the maximum intensity of the satellite reflections.

The simulation is obtained assuming that the ultrasonic wave is as well in this case propagating in the [012]-direction. The calculated angular satellite position matches the experimentally observed one within the stepsize in $\Delta\theta$ of the measurement, which was only 0.0392 arcsec in this experiment. The center of gravity of the measured satellite intensity distribution differs thereby only by 0.0158 arcsec from the simulated peak position of the satellite reflection.

The expected observable intensity distribution is obtained by the convolution of the simulated intensity profile with the measured resolution function of the diffractometer at the x-ray energy of 146 keV. The result is shown in figure 6.11 together with the measured intensity distribution. The ultrasound amplitude is set to 0.5 Å in the simulation in order to match the maximum intensity of the satellite reflection. A slightly larger FWHM of the central reflection by 0.04 arcsec is the main difference of the intensity profiles, which is most probably caused by the measured resolution function, which could as well only be measured with a stepsize of 0.0392 arcsec.

The result of the measured and simulated intensity distribution in the small amplitude regime compared to large amplitudes shows that the main and satellite reflections are not yet governed by full dynamical diffraction. The satellite reflections can still be treated in the framework of the thick crystal approximation (chapter4) like it is the case for the main reflections of the unexcited crystal. Only at large amplitudes effects due to the complete dynamical diffraction behavior of the satellites and the main reflection come into account.

6.3 Analysis of x-ray energy scans

In the following experiment x-ray energy scans are carried out by changing successively the Bragg angle of the monochromator crystal. The corresponding x-ray energies are obtained by a combination of Bragg's law (equation 2.5) with equation 5.1. Since the Bragg angle changes with energy, the sample crystal is simultaneously translated such that the incident x-ray beam remains on the same spot on the sample. The initial x-ray energy is 224.83 keV. The sample is excited with an ultrasound frequency of 102.385 MHz. At this resonance frequency ultrasound excited satellite reflections are observed. During the experiment the conditions of the ultrasonic excitation are not changed. A ω-scan of the (-571) reflection of silicon is then carried out in steps of $\Delta\omega = 0.025$" in the range of ±2". The x-ray energy is then successively changed from 224.83 keV to 199.86 keV in steps of about 0.4 keV and the ω-scan is repeated at each energy.

Over this x-ray energy range we measure changes of the maximum values of the satellite intensities as a function of energy. Ten out of 70 measured rocking curves with energy increments of about 3 keV for the incident x-ray energy are presented in figure 6.12.

The maximum intensity of the first order satellite initially increases relative to the intensity of the main reflection with decreasing x-ray energy. After reaching a maximum value, it decreases again. It can therefore be assumed that the satellite intensities vary periodically with x-ray energy. In this particular measurement, the maximum intensity of the first order satellite achieves the same value as the maximum intensity of the main reflection at the x-ray energy of 210.24 keV. It seems, however, that the satellites of higher order do not follow exactly the same intensity evolution in this energy range. The second order satellite, for example, does not change its maximum intensity value as much as the first order satellite and does not reach the same maximum intensity as the main reflection in the investigated x-ray energy range.

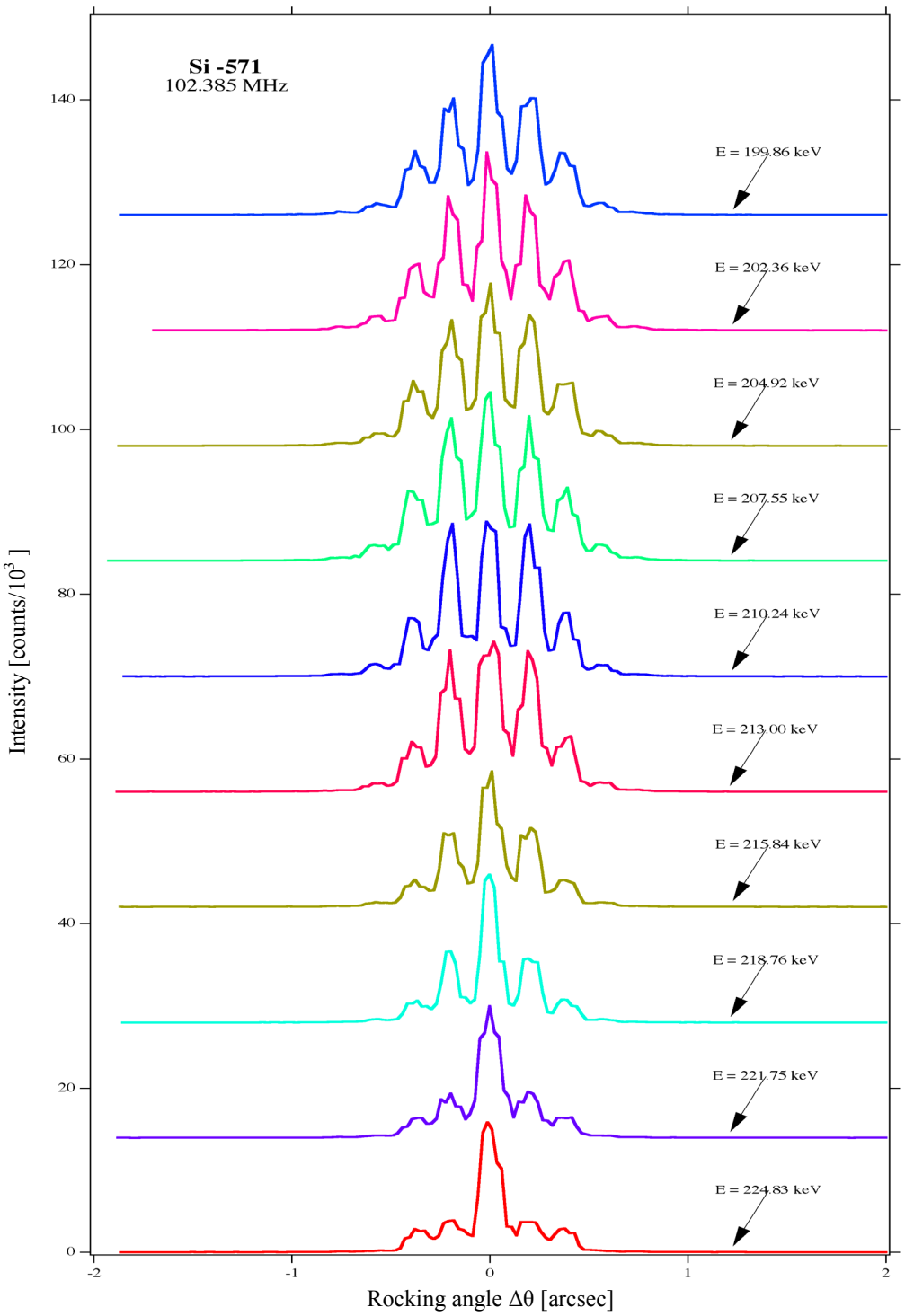

Figure 6.12: Measured intensity profiles of ultrasound excited satellite reflections at different x-ray energies in the range of 199 keV to 225 keV. The peak intensity of the first order satellites first grows and then decreases with increasing x-ray energy. At 210.24 keV the first order satellite peak intensity reaches the same value as the main reflection.

In order to analyze these observations in more detail, the integrated intensities of the satellites and the main reflection are determined. These are obtained by fitting a Lorentz profile in the least-squares sense to the measured data, independently for both satellites and the main reflection. This results in the integrated intensities for the main reflection, the first and the second order satellite shown in figure 6.13. Before fitting the data, the intensity distributions are normalized to the beam current in the storage ring. This is necessary because the synchrotron beam current changes distinctively during the total scanning time of 5h 45min.

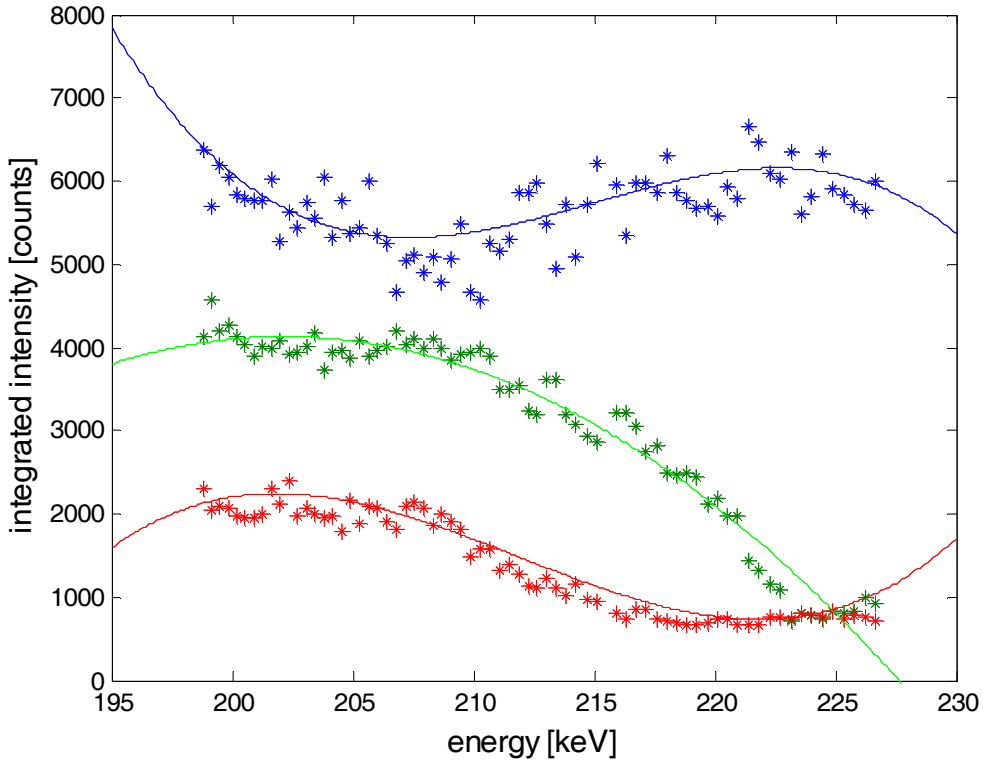

Figure 6.13: The integrated intensities of the main reflection and the satellite reflections for the intensity distributions shown in figure 6.12. The integrated intensities are oscillating as a function of the x-ray energy in the measured range between 198 keV and 227 keV. The fit curves serve as a guide to the eye.

The blue data points in figure 6.13 correspond to the integrated intensities of the main reflection at all measured x-ray energies in the range between 198 keV and 227 keV. The green data points correspond to the first order and the red points to the second order satellite reflection. The polynomial fits to the data points serve as a guide to the eye. The integrated intensities of both satellite reflections and even the main reflection exhibit a

part of an oscillation period as a function of the x-ray energy. The x-ray energy for the maximum integrated intensity is determined to 202.2 keV for the first order satellite.

How can such an evolution of the satellite intensities with changing x-ray energy be explained? In chapter 4.4 the simulations of diffraction on ultrasound excited crystals were discussed. Figure 4.25 shows the dependence of the satellite intensity distribution as a function of the x-ray energy and the deviation angle $\Delta\theta$ for the high amplitude regime. Figure 4.14 shows the same for the low amplitude regime. For the simulation shown in figure 4.25 the ultrasound frequency was set to 102.385 MHz, i.e., the same value as in the experiment. Summarizing the observations from these simulations, we note that neither the maximum intensity of the satellite reflections changes as a function of energy, nor do the angular positions of the satellites change (beyond 20 keV). The FWHM of the satellite reflections decreases with increasing energy. In the experiment the satellite reflections remain at the same Bragg angle for different x-ray energies, just as predicted by the simulation, but contrarily to the simulation the maximum values of the satellite intensities do oscillate. Remembering the discussion in the previous paragraph, the decrease of the FWHM of the satellite reflections with increasing energy could lead to a decrease of the maximum values of the satellite intensities due to convolution effects with the instrument resolution. But this effect can not explain the oscillation of the integrated satellite intensity with increasing x-ray energy.

To explain the oscillatory dependence of the satellite intensities as a function of the x-ray energy, the dependence of the intensity distribution on the thickness parameter A in the framework of the dynamical diffraction theory is revitalized (chapter 2.6). The decrease of A leads to an oscillation of the diffracted intensity in the center of the diffraction pattern (figure 2.12). At a fixed crystal thickness the increasing x-ray energy forces A to decrease (equation 2.17 and figure A.2). Figure 6.14 shows the intensity distribution for the (-571) main reflection as a function of the deviation angle $\Delta\theta$ and the x-ray energy for a crystal thickness of 5 mm calculated on the basis of equation 2.18. The figure ranges from $-0.05'' \leq \Delta\theta \leq 0.05''$ in Bragg angle and from $100\ \text{keV} \leq E \leq 3000\ \text{keV}$ in x-ray energy. This range up to extremely high x-ray energies of 3000 keV is chosen to show the transition to the kinematical limit.

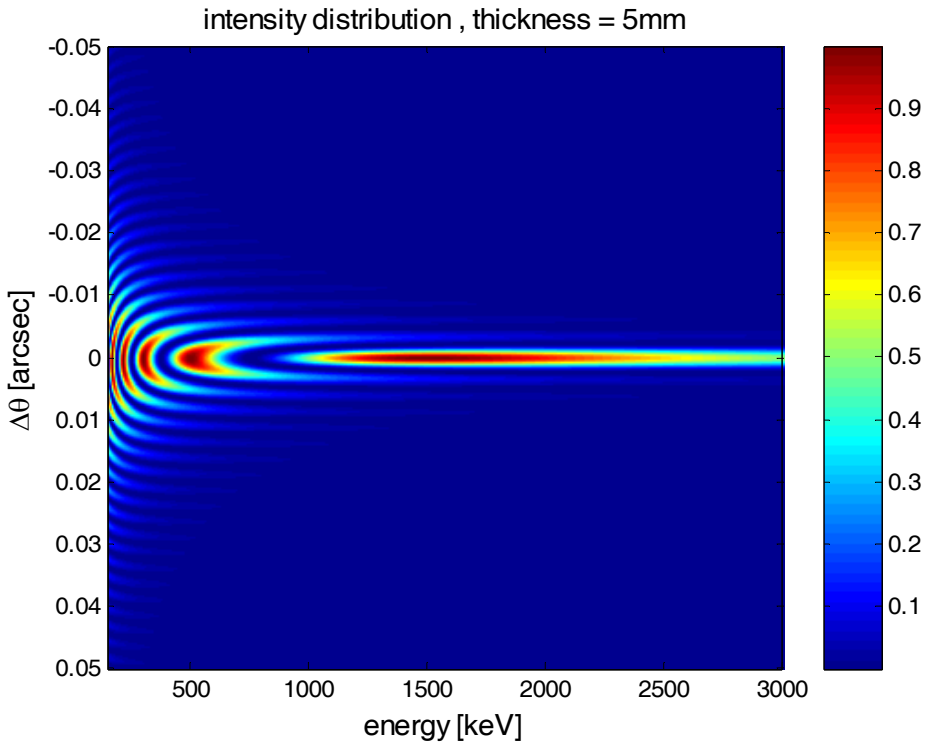

Figure 6.14: Calculated intensity profiles as a function of x-ray energy for a 5 mm thick silicon crystal. The intensity is oscillating between 0 and 1 in the center of the diffraction profile until the extinction length exceeds the crystal thickness and the kinematical limit is approached. The idea to explain oscillations of satellite intensities with energy is based on such a dynamical theory approach.

At lower energies many extinction lengths fit into the crystal, which allows using the thick crystal approximation to smear out the intensity oscillations as a function of $\Delta\theta$. Only at the x-ray energy of 1495 keV the extinction length equals exactly twice the crystal thickness and the intensity oscillates one last time in the center of the diffraction pattern before the extinction length becomes much larger than the crystal thickness with further increasing energy. At extremely large extinction lengths diffraction phenomena merge into the kinematical limit. Since we are measuring around 210 keV (i.e. much less than 1495 keV) the thick crystal approximation remains valid for the main reflection of the unexcited crystal. Exciting the crystal with large ultrasound amplitudes leads to an increased extinction length of the main reflection. The extinction lengths of the satellite reflections are generally larger than the extinction length of the main reflection of the unexcited crystal due to the modulation by the Bessel function. If the extinction lengths

of the satellites and the main reflection achieve values in the range of the crystal thickness, the thick crystal approximation is not valid any more. It can therefore be expected that at large ultrasound amplitudes the extinction lengths of satellite reflections already approach crystal thickness at x-ray energies, where the main reflection of the unexcited crystal can still be treated in the thick crystal approximation. Figure 6.15 aids the explanation of the oscillating satellite intensity maxima. Provided that the extinction lengths of the satellites and the main reflection are already in the range of the crystal thickness, an increasing x-ray energy can then drive the extinction length of the satellites and the main reflection over the crystal thickness and intensity oscillation phenomena like shown in figure 6.14 can already occur at x-ray energies around 200 keV. The satellites and the main reflection behave then fully dynamic. The fact that even the main reflection oscillates as a function of the x-ray energy in figure 6.13 gives a clear indication that the complete satellite system including the main reflection behaves fully dynamic. To elaborate this idea in further detail, the extinction lengths of the satellites are calculated as a function of x-ray energy and ultrasound amplitude.

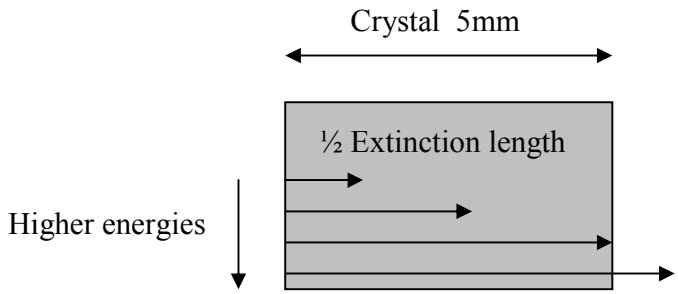

Figure 6.15: Scheme to explain satellite intensity oscillations as a function of x-ray energy. Contrary to the main reflection of the unexcited crystal the extinction length of the satellite reflections grows over the crystal thickness with increasing x-ray energies.

6.3.1 Extinction length of the first order satellite and determination of the ultrasound amplitude

The extinction length of a satellite reflection can be calculated with

$$\Lambda_{sat} = \frac{\lambda\sqrt{\gamma_h\gamma_0}}{C_s\left|\chi_{sat}\right|\sqrt{dT^2+1}} \quad , \tag{6.5}$$

where the electric susceptibility of the unperturbed lattice in equation 2.15 is replaced by the electric susceptibility of the satellite reflection. The electric susceptibility of the satellite reflection of order n is given by [Ent 84]

$$\chi_{sat} = \left|J_n(\vec{G}\cdot\vec{a})\right|\cdot\chi_{hkl} \tag{6.6}$$

χ_{hkl} is the electric susceptibility of reflection (hkl) of the unperturbed lattice and J_n is the n^{th}-order Bessel function corresponding to the satellite reflection of order n. The electric susceptibility χ_{sat} of a satellite reflection of order n is calculated due to equation 6.6 provided that the satellite reflections can be treated independently from each other if they are well separated in the high frequency regime.

The extinction length of a satellite reflection is then a function of the x-ray energy and the ultrasound amplitude **a** for a given reflection (hkl) and surface cut of the crystal. The deviation parameter dT is determined relative to the angular satellite position and is therefore set to 0 for the exact Bragg angle of the satellite position.

Figure 6.16 shows the extinction length of the first order satellite in the x-ray energy range from 150 keV to 250 keV and for ultrasonic amplitudes between 0 and 50 Å. It is due to the properties of the Bessel function (chapter 4.4) that the extinction length oscillates as a function of the ultrasound amplitude. At the same time, the extinction length of the first order satellite reflection increases nearly linear with increasing x-ray energy.

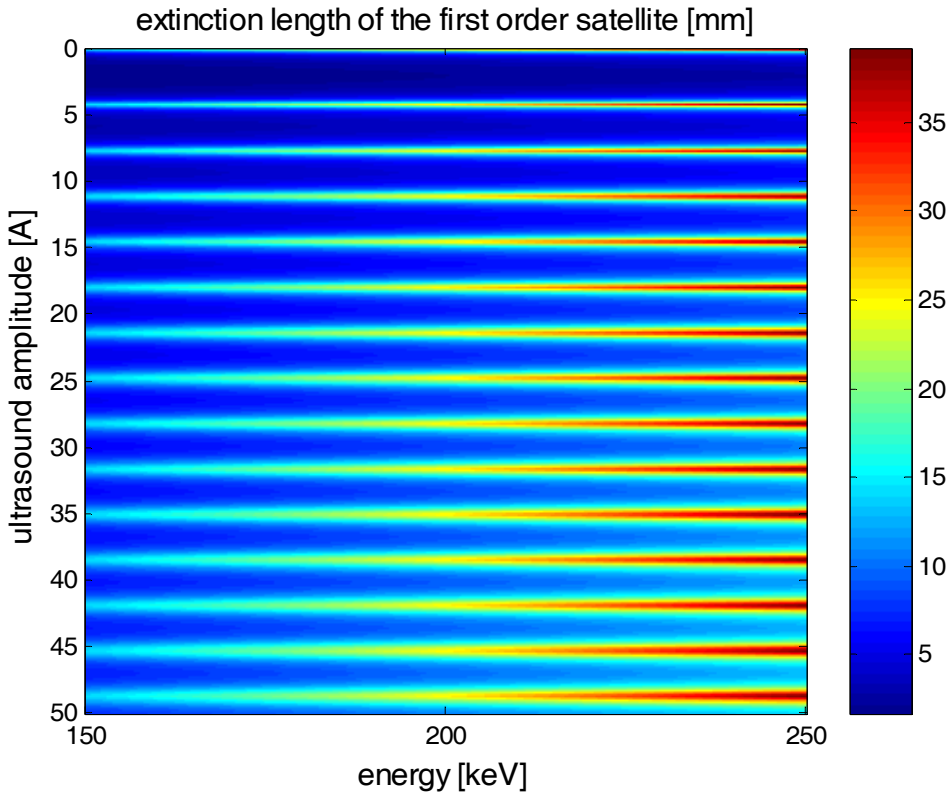

Figure 6.16: Extinction length of the first order satellite at the silicon (-571)-reflection as a function of x-ray energy and ultrasound amplitude. The extinction length is periodic with ultrasound amplitude and can exceed twice the crystal thickness with increasing energy.

For a transverse ultrasonic wave traveling along the [012]-direction with an ultrasound amplitude vector in the [100]-direction and an absolute value of the amplitude of 3.834 Å the extinction length of the first satellite is visualized in figure 6.17 as a function of the x-ray energy between 150 keV and 250 keV. Indeed, for this ultrasound amplitude the extinction length of 10 mm - equal to twice the crystal thickness - is achieved at the x-ray energy of 202.2 keV. But it is not the only possible ultrasound amplitude, which fulfills the condition that the extinction length of the first order satellite has to amount to twice the crystal thickness, and thus the first order satellite intensity achieves a maximum at the x-ray energy of 202.2 keV.

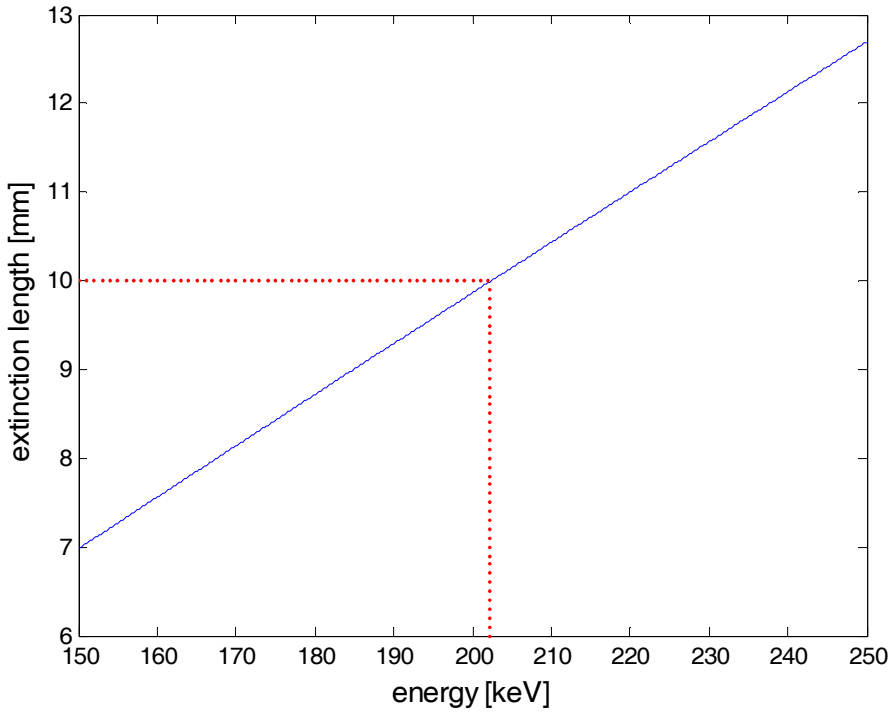

Figure 6.17: Extinction length of the first order satellite reflection as a function of x-ray energy at the ultrasound amplitude of 3.83 Å. At 202.2 keV the extinction length amounts to twice the crystal thickness (10 mm), where the satellite peak intensity reaches a maximum (see figure 6.13).

This is illustrated in figure 6.18, which shows the dependence of the extinction length of the first order satellite on the ultrasound amplitude at the constant x-ray energy of 202.2 keV. In principle, all ultrasound amplitudes, for which the extinction length achieves 10 mm, represent possible solutions for the actual excited ultrasound amplitude in the crystal during the experiment presented in figure 6.12. These are represented graphically by the intersection points of the green curve in figure 6.18 with the blue extinction length curve.

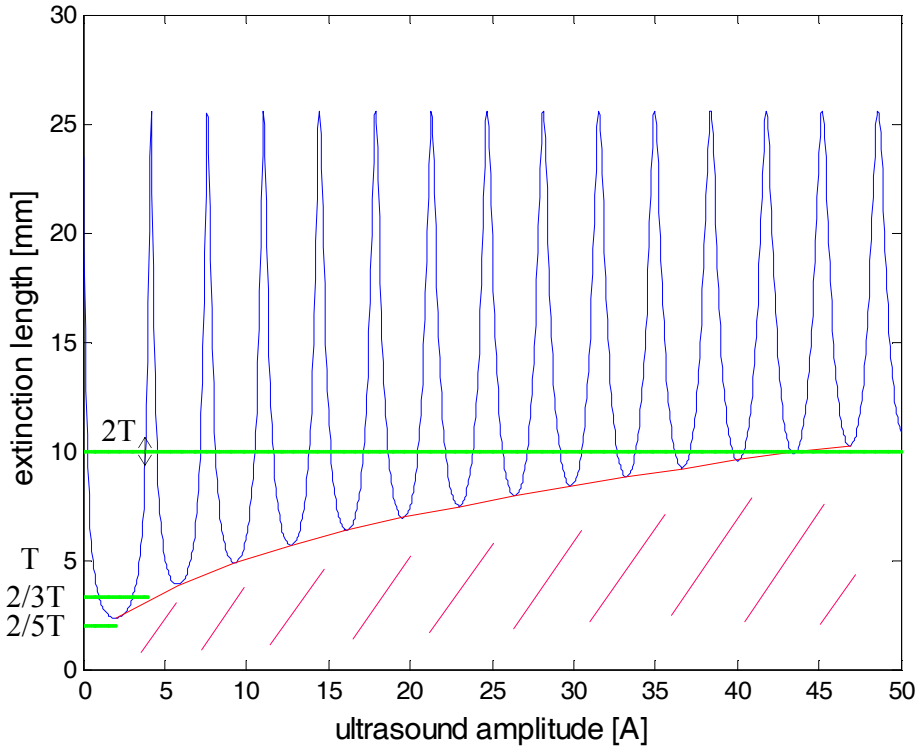

Figure 6.18: Extinction length (blue curve) of the first order satellite reflection as a function of ultrasound amplitude at the x-ray energy of 202.2 keV. The increasing ultrasound amplitude varies the extinction length periodically. If the extinction length amounts to twice or 2/3 of the crystal thickness, the satellite peak intensity is maximal. If twice the crystal thickness falls below the red curve, the oscillation effect of the satellite peak intensity can not be observed any longer (regime of a thin crystal). If twice the crystal thickness is much greater than the peak value of the extinction length (i.e. 27.6 mm), the thick crystal regime is reached.

Furthermore, intensity maxima for the first order satellite are expected at values (n integer):

$$T = (2n+1)/2 * \Lambda_{sat} \tag{6.7}$$

For a crystal thickness of T = 5 mm the extinction length of the first order satellite can only have the two possible values, 2T and 2T/3. Smaller extinction lengths do not exist for any ultrasound amplitude (figure 6.18). The number of excited satellite reflections in the measurement shown in figure 6.12 is n =3. Taking into account the measured number of satellite reflections via the scalar product **Ga** ≈ n, the two ultrasound amplitude values

3.83 Å and 3.08 Å corresponding to an extinction length of 10 mm and 10/3 mm, respectively, result in three excited satellite reflections. They are therefore the most probable amplitude values of the transverse ultrasonic wave propagating along the [012]-direction in the silicon crystal. However, the larger amplitude value of 3.83 Å is more evident, since it results in three fully excited satellite reflections n = 3.5 compared to n = 2.8 for the smaller ultrasound amplitude of 3.08 Å.

Three more general conclusions can be drawn according to figure 6.18. The increasing ultrasound amplitude causes a periodic variation of the extinction length. It should therefore be possible to observe a periodic behavior of the satellites intensity maxima as well in a series of rocking curves measured at different ultrasound amplitudes at a constant x-ray energy. This effect will be shown in paragraph 6.4. Second, if the crystal thickness T is smaller than half of the absolute minimum of the extinction length curve (figure 6.18), no intensity oscillation effect will be observable at all (regime of a thin crystal). The red curve through the local minima of the extinction length indicates twice the minimum value for the crystal thickness and the ultrasound amplitude values up to 50 Å, for which the intensity oscillation will be observable. For a crystal thickness below these minimum values the extinction length of the first order satellite exceeds the crystal thickness and the kinematical approximation for the satellite reflection dominates. If, on the other hand, twice the crystal thickness is much greater than the peak value of the extinction length (i.e. 27.6 mm), the thick crystal regime is reached. Third, with the precise knowledge of the extinction length of a satellite reflection, it is consequently possible to accurately measure structure factors of ultrasound excited superlattices (equations 6.6 and 2.12). Moreover, with the knowledge of the ultrasound amplitude, in principle, even the structure factor of the silicon crystal lattice can be deduced very accurately. The accuracy is given by the fact that a small change in the ultrasound amplitude is followed by a large change in the extinction length (figure 6.18). In the next paragraph the determination of the structure factor will be discussed.

6.3.2 Determination of the superlattice structure factor

Based on equations 6.5 and 6.6 the extinction lengths of the first order satellite were calculated as a function of x-ray energy and ultrasound amplitude. On the other hand, the measurement presented in figure 6.12 showed that the maximum integrated satellite intensity occurs at the x-ray energy of 202.2 keV. Since we know that the extinction length has to amount to twice the crystal thickness (i.e. 10 mm) at this x-ray energy for a maximum satellite intensity, the electric susceptibility of the first satellite can be calculated via equation 6.6. Thus, combining equations 6.6 and 2.13, the product of the absolute value of the first order Bessel function with the absolute value of the structure factor of the reflection can be defined as the structure factor of the ultrasound excited superlattice for the first order satellite. It can then be calculated via $|F_{sat}| = |\chi_{sat}|/|\chi_{hkl}| \cdot |F_{hkl}|$ without knowing the excited ultrasound amplitude. For the silicon (-571)-reflection, an extinction length Λ_{sat} = 10 mm and an x-ray energy of 202.2 keV, we thus achieve a value of $|F_{sat}|$ = 2.64. On the other hand, if we take into consideration the excited ultrasound amplitude determined to a = 3.83 Å (chapter 6.3.1), the absolute value of the structure factor for the silicon (-571)-reflection can be determined via $|F_{hkl}| = |F_{sat}|/|J_1(\mathbf{Ga})|$. This yields $|F_{-571}|$ = 21.18 in agreement with the theoretical value of 21.21.

6.3.3 Higher order satellites

The extinction lengths of the first three satellite orders and the main reflection (0^{th} order) as a function of the x-ray energy between 150 keV and 250 keV are plotted in figure 6.19. The calculation is based on equation 6.5 for the ultrasound amplitude direction [100] with an ultrasound amplitude of 3.83 Å. When the extinction length of the first order satellite amounts to twice the crystal thickness, its peak intensity should become maximal. This was observed in the experiment (figure 6.12) at 202.2 keV and agrees well with the calculation presented in figure 6.17. However, the extinction lengths of the 0^{th}, second and third order satellites within the same x-ray energy range are different. The extinction lengths of the main reflection, the second and third order satellite do not reach

2T = 10 mm in the investigated x-ray energy range. But their peak intensity can still reach a maximum, if the extinction length amounts to 2/3T (equation 6.7). In fact, the second order satellite does achieve this value at the x-ray energy of 228 keV, while the zero order satellite has a maximum at 193.5 keV. Unfortunately, these values lie outside the measured x-ray energy range (figure 6.12), but the fact that different satellite orders reach their maximum value in the peak intensity at different x-ray energies explains nicely, why the diffraction satellites do not behave identically as a function of increasing x-ray energy. In addition, the increase of the extinction length of the higher order satellites and the zero order satellite, i.e., the main reflection, is much less pronounced in the plotted energy range than for the first order satellite. Therefore, the overall change of their intensities is expected to be less than that for the first order satellite within the measured energy range. These two observations are in complete agreement with the measurement presented in figures 6.12 and 6.13.

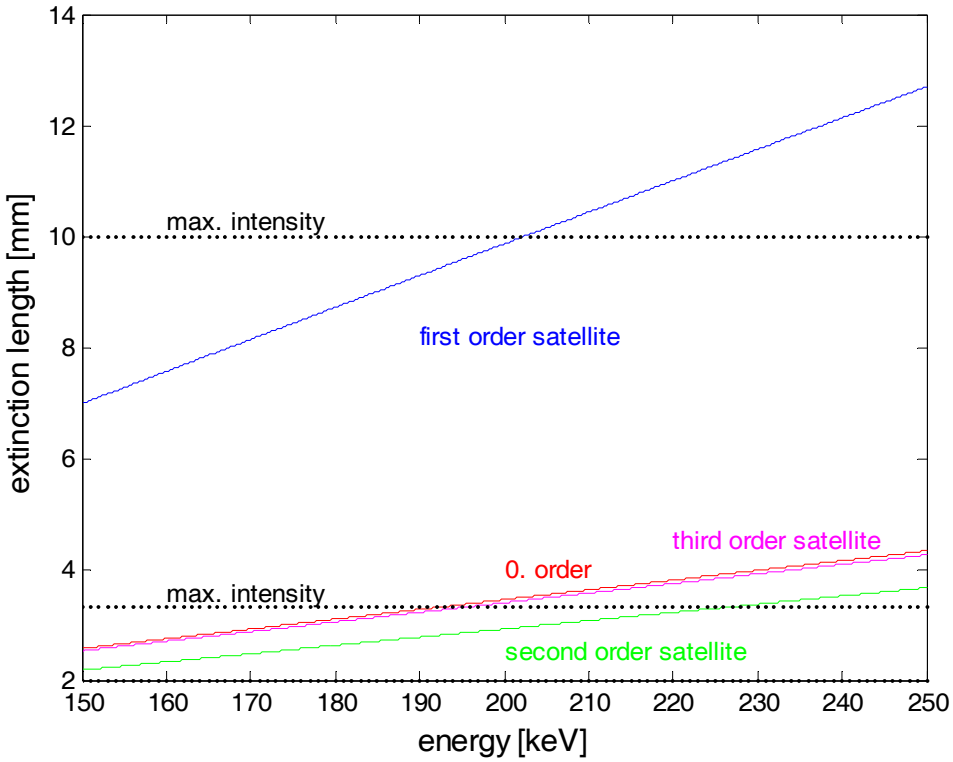

Figure 6.19: Extinction lengths of the first three order satellite reflections as a function of x-ray energy at the ultrasound amplitude of 3.83 Å. The extinction lengths of the different satellite orders amount to 2T or 2/3T at different energies. The second order satellite achieves its maximum intensity at 228 keV, the 0^{th} -order satellite at 193.5 keV.

6.4 Ultrasound amplitude scans

Due to the calculation (figure 6.18; equation 6.5), ultrasound amplitude variations (the presented range lies between 0 and 50 Å) are followed by a periodic change of the extinction length of a given satellite reflection. If the extinction length surpasses thereby twice the crystal thickness or, more generally, follows equation 6.7, the satellite peak intensity will go through a maximum. At ultrasound amplitudes where the extinction length amounts to the value of the crystal thickness, the satellite intensity will pass a minimum. This has been observed in a series of rocking curve scans of the (-351)-reflection at excitation voltages between 0 and 1 V (figure 6.20). The ultrasound frequency was 144.797 MHz in this experiment. At a transducer voltage of 0.4 V the peak intensity of the first order satellite is smaller than at 0.2 V and at 0.8 V. At voltages higher than 0.8V, the peak intensity of the first order satellite increases further. The interpretation of this observation has to be considered only preliminary yet since a second effect overlaps the satellite intensity distribution. The FWHM of the satellite reflections always exhibit a periodic behavior as a function of ultrasound amplitude regardless of the crystal thickness (figure 4.26). Convolution with the instrument resolution function also leads to a periodic behavior of the peak intensity of the satellite reflection (see chapter 6.2). Since both effects can not be separated, it is difficult to further analyze the data quantitatively.

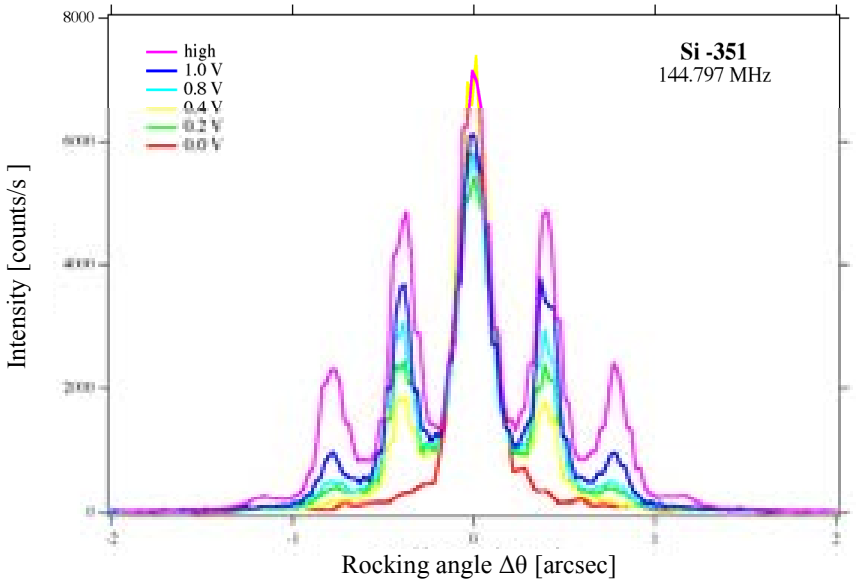

Figure 6.20: Intensity profiles of ultrasound excited satellites of the (-351) silicon reflection at different transducer voltage amplitudes between 0 and 1V. The peak intensity of the first order satellite goes through a minimum at 0.4 V.

Choice of the reflection:

The angle α between the diffraction vector **G** and the ultrasound propagation vector **κ** affects the angular separation of ultrasound excited satellite reflections. When approaching α = 90°, their separation increases. This was already discussed in chapter 4.5. The experimental verification is now presented. Figure 6.21 shows a series of rocking curve scans for increasing transducer voltages at constant ultrasound frequency (144.797 MHz) as in the measurement presented in figure 6.20, but now for the (153)-reflection. The angle α for the (-351)-reflection and an ultrasound propagation in [012] is calculated to 50.8˚, and for the (153)-reflection to 6.4˚. Obviously the satellite reflections are well separated if the (-351)-reflection is chosen and are not completely resolved for the (153)-reflection. Therefore, the main reflection to investigate ultrasound excited satellite reflections has to be carefully selected, provided that the true ultrasound propagation direction is known beforehand and experimentally well controlled.

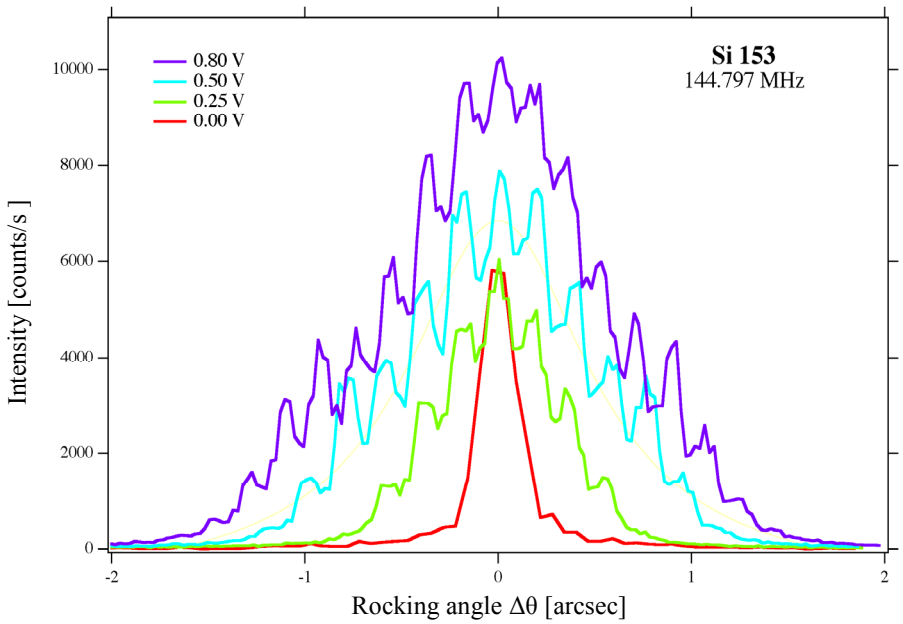

Figure 6.21: Rocking curve scans under identical conditions as in figure 6.20, but measured around the (153)-reflection. The angle α = 6.4° between the scattering vector and the ultrasound wave vector projected onto the scattering plane is too small to resolve clearly the satellite reflections.

6.5 Time resolved evolution of the ultrasound excited satellite system

The time evolution of ultrasound excited satellite intensity distributions is discussed in chapter 4.3 and 4.7 based on the dynamical diffraction theory modified for space-time modulated structures. The simulations for the low amplitude case in the high frequency regime showed that the modulation of the satellite intensities decreases with increasing ultrasound frequencies above the threshold frequency for resonant time modulation ($\Delta \approx 1.4$). For example, at 200 keV and 100 MHz (thus $\Delta \approx 9$, equation 4.2) the maximum intensity change of the first order satellite amounts to 1.2 % of the time-integrated intensity of ½.The accompanying angular shift of this peak intensity is on the order of 0.01". Therefore, it can not be expected to clearly observe those shifts as a function of time.

But another time-dependent effect, which is not yet included in the theory, has to be considered as well. This effect is based on the time dependence of satellite reflections which behave dynamically in the sense of chapter 6.3. The motivation is qualitatively as follows: Since we are exciting standing ultrasonic waves in the silicon crystal, the elongation $u(\mathbf{x},t)$ for such a wave field can be written as:

$$u(\mathbf{x},t) = 2|\mathbf{a}|\cos(\boldsymbol{\kappa}\mathbf{x})\sin(\omega t) \tag{6.8}$$

with $\mathbf{a}$ = amplitude vector, $\boldsymbol{\kappa}$ = wave vector, $\mathbf{x}$ = space coordinate, $\omega/2\pi$ = ultrasound frequency and t = time. Thus the crystal is modulated in space with a time dependent amplitude $a(t) = a\sin(\omega t)$.

On the other hand the satellites and the main reflection exhibit dynamical diffraction behavior at large ultrasound amplitudes due to the results of chapter 6.4. This yields to the following conclusion. The time dependent change of the ultrasound amplitude can drive the extinction length of a satellite reflection beyond the crystal thickness and back during one single oscillation period. This should produce large changes in the diffracted satellite intensity as a function of elapsed time. And indeed, we do observe this effect in the time-resolved experiment.

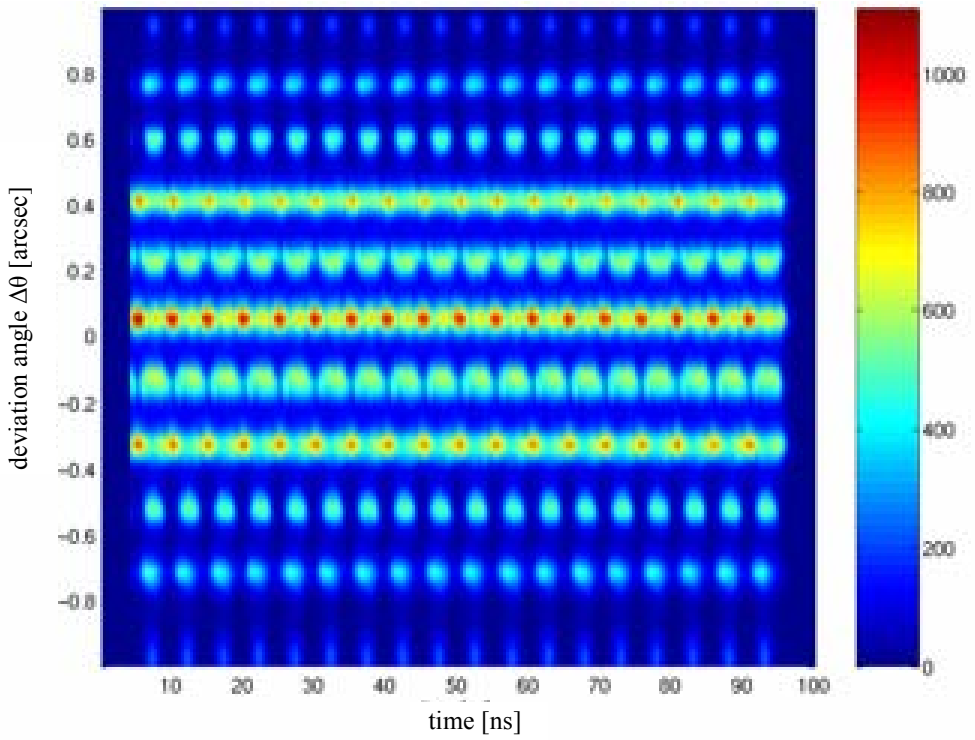

Figure 6.22: Time-resolved diffraction pattern measured at the x-ray energy of 200 keV and the ultrasound frequency of 95.9667 MHz. The amplitude is set to 0.5V. The extinction lengths of the satellite reflections are periodically driven over twice the crystal thickness leading to the distinctive maxima and minima of the satellite intensities. The period of 5.21 ns between the intensity maxima corresponds to twice the excitation frequency. The phase shift between the different satellite orders is due to their different extinction lengths.

The time dependent evolution of the time integrated diffraction pattern of the satellite system as shown in figure 6.1 is presented in figure 6.22 for a time range of 100 ns. The time and diffraction angle resolved intensity distribution is measured at the ultrasound frequency of 95.9667 MHz and a transducer voltage of 0.5 V. All satellite reflections including the main reflection (-571) show nicely the periodicity of the intensity maxima with twice the ultrasound frequency. As predicted in figure 6.23 the satellite reflections of different order are not in phase to each other when they reach their maximum intensity, because the extinction length of different satellite orders is shifted in phase at a given ultrasound amplitude. At large ultrasound amplitudes the extinction length of even and odd satellite orders begins to oscillate in phase. For the (-571)-reflection at the x-ray energy of 200 keV the extinction length of the main reflection and the second order

satellite begin to oscillate in phase at an ultrasound amplitude of about 20 Å (figure 6.23). The extinction length of the first order and third order satellite begin to oscillate in phase at an ultrasound amplitude of about 22 Å. However, at smaller ultrasound amplitudes like 3.8 Å as derived in chapter 6.2 and 6.3.1 the extinction lengths are still out of phase to pass 10 mm or 10/3 mm for a maximum intensity.

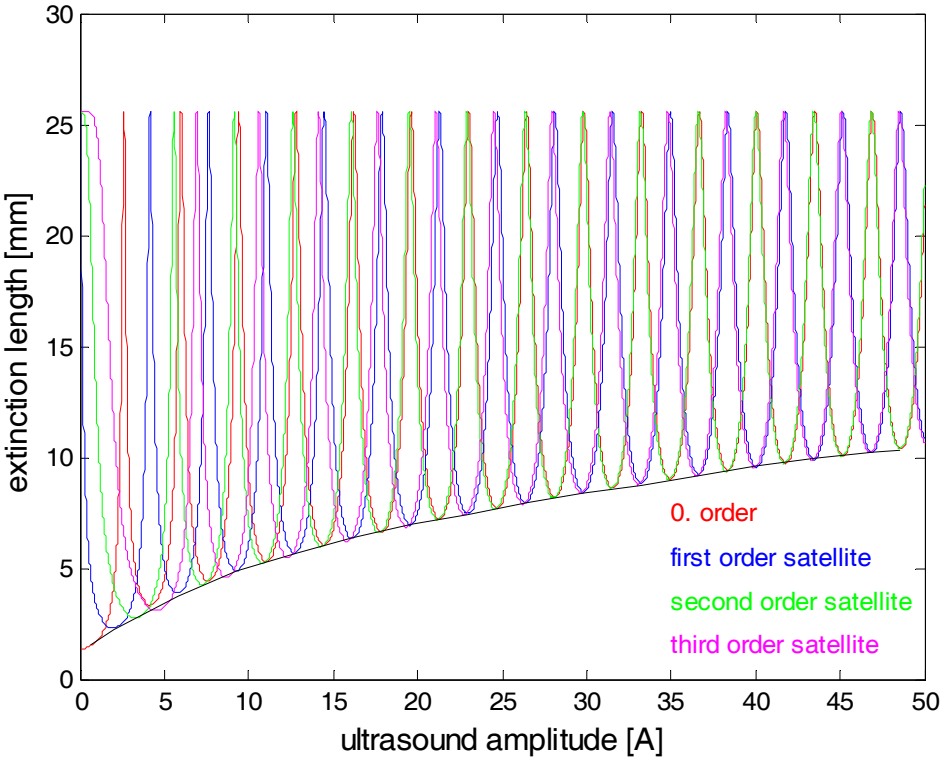

Figure 6.23: The extinction lengths of the first three satellite orders at the x-ray energy of 200 keV as a function of the ultrasound amplitude between 0 and 50 Å. The extinction lengths are shifted in phase for small amplitudes. For large amplitudes even and odd orders begin to oscillate in phase, respectively.

The fact that the frequency of the intensity modulations is twice the experimentally applied ultrasound frequency is not surprising, since the diffraction process does not distinguish between compressed and dilated crystal regions. This observation was already mentioned in [Iol 95b] and is also obvious from figure 6.22.

Chapter 7

Conclusions and outlook

This work treats time-integrated and time-resolved high energy x-ray diffraction on ultrasound excited silicon crystals. High energy synchrotron radiation at a x-ray energy above 80 keV and a high resolution triple-axis diffractometer with a mechanical angular resolution of 0.01 arcsec permitted to resolve for the first time ultrasound excited satellite reflections from acoustic waves in the volume of the crystal. The propagation direction of the transducer-excited waves is determined in the high frequency regime. The high frequency regime is thereby defined via the relation between the extinction length of a given x-ray reflection and the wave length of the ultrasonic wave, which has typically values between 10 μm and 150 μm in the experiments carried out in this work. The transducer is bonded to the (111)-face of the silicon crystal and excites a transverse ultrasound mode in the [012]-direction. To determine this propagation direction high resolution reciprocal space maps are most helpful. High resolution reciprocal space maps enable one to measure the projection of the ultrasound propagation vector onto the scattering plane. Together with the ultrasound propagation velocity of the transverse wave in [012]-direction of 5823 m/s the angular positions of the satellite reflections were confirmed. For future research projects it will be advantageous to measure reciprocal space maps of two independent reflections under the same ultrasound excitation conditions in order to nail down the ultrasound propagation direction definitely. In addition, it would be interesting to simulate the detailed ultrasonic field in the crystal with a finite-element method to verify and to give reasons for this propagation direction of the ultrasonic wave.

In order to understand and simulate time-integrated and time-dependent intensity distributions of main reflections and satellites the computer code SIMSAT was developed in the framework of this thesis. SIMSAT allows simulating time-integrated and time-dependent rocking curve scans of certain x-ray reflections as a function of x-ray energy,

ultrasound frequency and amplitude. The calculations are based on the dynamical diffraction theory of perfect crystals modified for ultrasound modulated crystal structures, which treats main reflection as well as satellite reflections in the limit of thick crystals. Thick crystals are distinguished from thin crystals via the extinction length of a given crystal reflection. If the x-ray energy dependent extinction length is much smaller than the true crystal thickness, the crystal is regarded as thick. Since under the experimental boundary conditions of x-ray energies between 80 keV and 250 keV and crystal thicknesses of 5 mm the thick crystal criterion is always fulfilled, a treatment in the framework of the kinematical theory is excluded. The simulations show the following general aspects of high energy x-ray diffraction on ultrasound excited crystals. First, the FWHM of the satellite reflections are distinctively smaller than the FWHM of the resolution function of the diffractometer, which is 0.065 arcsec at 200 keV. Second, the satellite reflections achieve the same peak intensity value as the main reflection of 0.5. Contrarily to the simulations the measured peak values of the satellite intensity distributions are different compared to each other and the main reflection. The convolution of the calculated intensity distribution for the (-351)-reflection at an ultrasound excitation frequency of 145 MHz with the diffractometers resolution function approaches the measured intensity distribution in the small ultrasound amplitude regime quite well. In the large amplitude regime 5 diffraction satellites were resolved on each side of the (-571)-reflection at an ultrasound excitation frequency of 96 MHz. The convolution of the calculated intensity distribution with the instrumental resolution function shows qualitatively a comparable result as the measured intensity distribution in the large amplitude regime. The remaining intensity differences between simulation and experiment are explained via the fully dynamical diffraction behavior of the satellite reflections. Rocking curve scans in the energy range between 199 keV and 225 keV show a periodic change in the peak intensity of the satellite reflections, which can only be explained by the full dynamic diffraction behavior of the satellite reflections. This means that the extinction lengths of the satellite reflections exceed the extinction length of the main reflection without ultrasound excitation by far and lie in the range of twice the crystal thickness. The increase in the x-ray energy leads then to an increasing extinction length of the satellite reflections passing the value of twice the crystal thickness and thus

to a periodic change of the satellite intensities. At the x-ray energy value, for which the first order satellite reflection achieves the same peak intensity value as the main reflection, the possible excited ultrasound amplitudes are obtained from the relation of satellite extinction length to crystal thickness. Measurements of rocking curves at different ultrasound amplitudes confirmed the dynamic diffraction behavior of the satellite reflections. For the simulation of satellite intensity distributions behaving fully dynamic, the theoretical approach of x-ray diffraction on ultrasound modulated crystals has to be extended to this regime.

Finally, it was possible to follow the development of the intensity distribution of the satellite reflections as a function of time with a resolution of 200 ps. Since the extinction length of the satellite reflections is periodically driven over twice the crystal thickness with the ultrasound excitation frequency, intensity maxima of the satellite reflections are observed with an oscillation period of 5.2 ns. The different satellite orders are shifted in phase. This time dependent behavior of dynamical diffraction satellites is a newly observed effect. It opens the way to a rapid suppression and modulation of the diffracted intensity like it was in principle proposed by Iolin [Iol 95b]. Since a large and time dependent ultrasound amplitude can force the extinction length to pass the crystal thickness several times during one oscillation period, shutter mechanisms with suppression times of 100 ps seem to be achievable.

Appendix A.1.

Deviation parameter dT and thickness parameter A

The deviation parameter dT is plotted as a function of x-ray energy and angular deviation Δθ for the (-351)-reflection of silicon in figure A.1a and for the (-571)-reflection in figure A.1b. The thickness parameter A is plotted as a function of x-ray energy and crystal thickness for the same reflections in figure A.2a and A2.b. It is especially useful to know the values of these dimensionless parameters during an experiment to identify the applicable approximations with respect to thin and thick crystals.

Figure A.1a

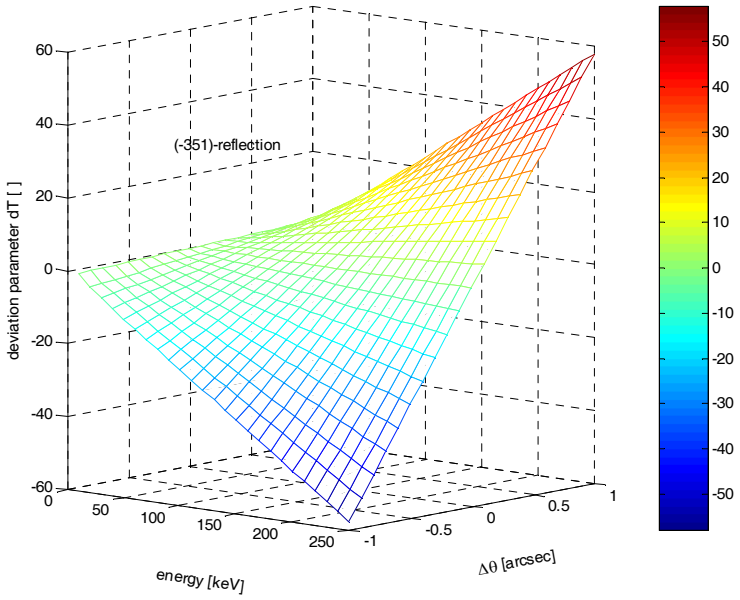

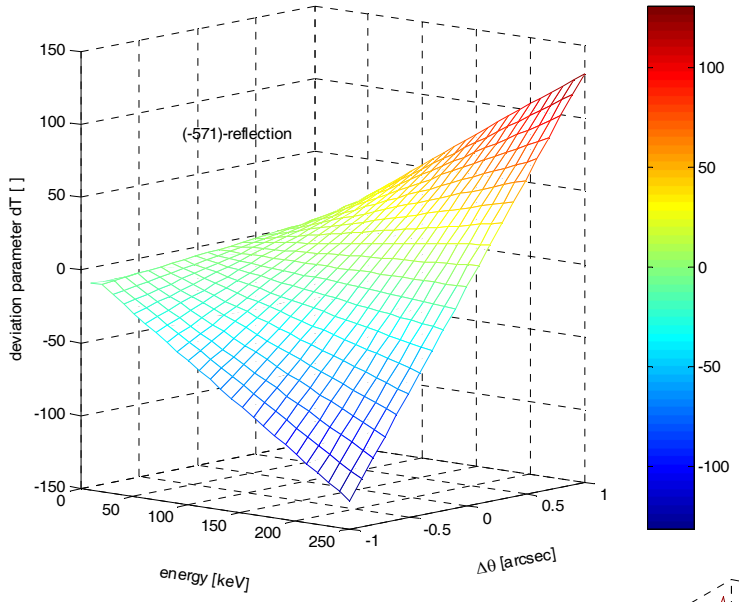

Figure A.1b

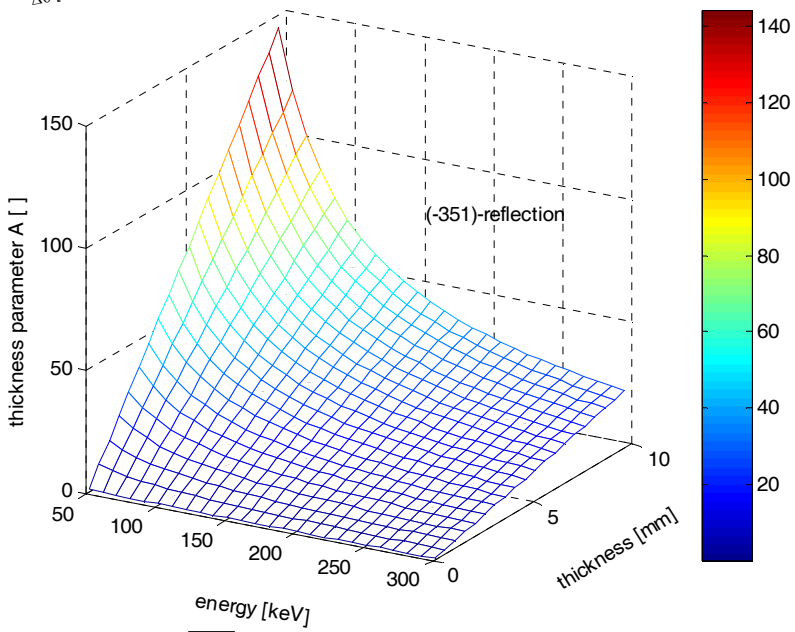

Figure A.2a

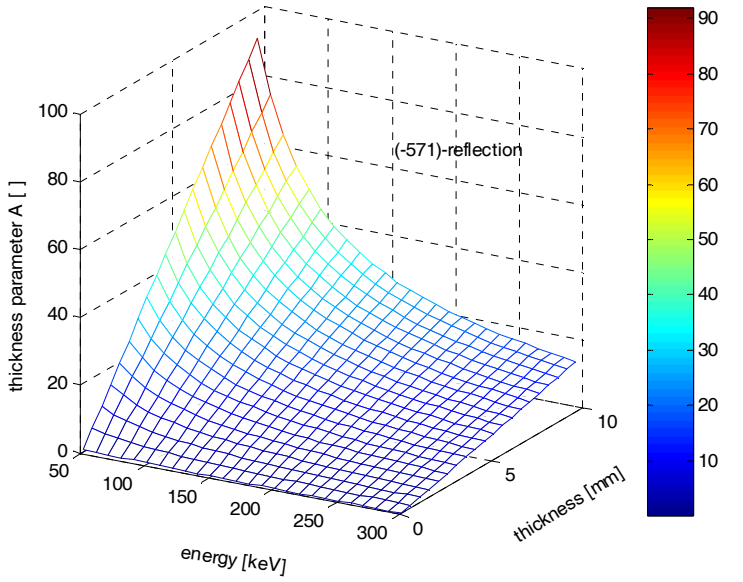

Figure A.2b

Appendix A.2.

List of ultrasound directions projected onto the scattering plane:

The calculation of the angle α in the scattering plane is carried out due to the description in chapter 6.1 based on equations 6.1 and 6.2. The calculations which agree with the measured angle α are marked with *.

h	k	l	α	
-2.0000	-2.0000	-2.0000	101.5370	
-2.0000	-2.0000	-1.0000	101.5370	
-2.0000	-2.0000	0	101.5370	
-2.0000	-2.0000	1.0000	101.5370	
-2.0000	-2.0000	2.0000	101.5370	
-2.0000	-1.0000	-2.0000	87.7734	
-2.0000	-1.0000	-1.0000	84.5131	
-2.0000	-1.0000	0	79.3293	
-2.0000	-1.0000	1.0000	70.0548	
-2.0000	-1.0000	2.0000	50.7685	
-2.0000	0	-2.0000	70.0548	
-2.0000	0	-1.0000	62.3054	
-2.0000	0	0	50.7685	
-2.0000	0	1.0000	33.7446	
-2.0000	0	2.0000	11.5370	
-2.0000	1.0000	-2.0000	50.7685	
-2.0000	1.0000	-1.0000	40.0978	
-2.0000	1.0000	0	26.7621	
-2.0000	1.0000	1.0000	11.5370	
-2.0000	1.0000	2.0000	3.6882	
-2.0000	2.0000	-2.0000	33.7446	
-2.0000	2.0000	-1.0000	23.0739	
-2.0000	2.0000	0	11.5370	
-2.0000	2.0000	1.0000	0.0000	
-2.0000	2.0000	2.0000	10.6707	
-1.0000	-2.0000	-2.0000	115.3005	
-1.0000	-2.0000	-1.0000	118.5608	
-1.0000	-2.0000	0	123.7446	*
-1.0000	-2.0000	1.0000	133.0191	
-1.0000	-2.0000	2.0000	152.3054	
-1.0000	-1.0000	-2.0000	101.5370	
-1.0000	-1.0000	-1.0000	101.5370	
-1.0000	-1.0000	0	101.5370	

-1.0000	-1.0000	1.0000	101.5370	
-1.0000	-1.0000	2.0000	NaN	
-1.0000	0	-2.0000	79.3293	
-1.0000	0	-1.0000	70.0548	
-1.0000	0	0	50.7685	
-1.0000	0	1.0000	11.5370	
-1.0000	0	2.0000	27.6946	
-1.0000	1.0000	-2.0000	50.7685	
-1.0000	1.0000	-1.0000	33.7446	
-1.0000	1.0000	0	11.5370	
-1.0000	1.0000	1.0000	10.6707	
-1.0000	1.0000	2.0000	27.6946	
-1.0000	2.0000	-2.0000	26.7621	
-1.0000	2.0000	-1.0000	11.5370	
-1.0000	2.0000	0	3.6882	
-1.0000	2.0000	1.0000	17.0239	
-1.0000	2.0000	2.0000	27.6946	
0	-2.0000	-2.0000	133.0191	
0	-2.0000	-1.0000	140.7685	
0	-2.0000	0	152.3054	
0	-2.0000	1.0000	169.3293	
0	-2.0000	2.0000	168.4630	
0	-1.0000	-2.0000	123.7446	*
0	-1.0000	-1.0000	133.0191	
0	-1.0000	0	152.3054	
0	-1.0000	1.0000	168.4630	
0	-1.0000	2.0000	129.2315	
0	0	-2.0000	101.5370	
0	0	-1.0000	101.5370	
0	0	0	NaN	
0	0	1.0000	78.4630	
0	0	2.0000	78.4630	
0	1.0000	-2.0000	50.7685	
0	1.0000	-1.0000	11.5370	
0	1.0000	0	27.6946	
0	1.0000	1.0000	46.9809	
0	1.0000	2.0000	56.2554	*
0	2.0000	-2.0000	11.5370	
0	2.0000	-1.0000	10.6707	
0	2.0000	0	27.6946	
0	2.0000	1.0000	39.2315	
0	2.0000	2.0000	46.9809	
1.0000	-2.0000	-2.0000	152.3054	
1.0000	-2.0000	-1.0000	162.9761	
1.0000	-2.0000	0	176.3118	
1.0000	-2.0000	1.0000	168.4630	

1.0000	-2.0000	2.0000	153.2379	
1.0000	-1.0000	-2.0000	152.3054	
1.0000	-1.0000	-1.0000	169.3293	
1.0000	-1.0000	0	168.4630	
1.0000	-1.0000	1.0000	146.2554	
1.0000	-1.0000	2.0000	129.2315	
1.0000	0	-2.0000	152.3054	
1.0000	0	-1.0000	168.4630	
1.0000	0	0	129.2315	
1.0000	0	1.0000	109.9452	
1.0000	0	2.0000	100.6707	
1.0000	1.0000	-2.0000	NaN	
1.0000	1.0000	-1.0000	78.4630	
1.0000	1.0000	0	78.4630	
1.0000	1.0000	1.0000	78.4630	
1.0000	1.0000	2.0000	78.4630	
1.0000	2.0000	-2.0000	27.6946	
1.0000	2.0000	-1.0000	46.9809	
1.0000	2.0000	0	56.2554	*
1.0000	2.0000	1.0000	61.4392	
1.0000	2.0000	2.0000	64.6995	
2.0000	-2.0000	-2.0000	169.3293	
2.0000	-2.0000	-1.0000	180.0000	
2.0000	-2.0000	0	168.4630	
2.0000	-2.0000	1.0000	156.9261	
2.0000	-2.0000	2.0000	146.2554	
2.0000	-1.0000	-2.0000	176.3118	
2.0000	-1.0000	-1.0000	168.4630	
2.0000	-1.0000	0	153.2379	
2.0000	-1.0000	1.0000	139.9022	
2.0000	-1.0000	2.0000	129.2315	
2.0000	0	-2.0000	168.4630	
2.0000	0	-1.0000	146.2554	
2.0000	0	0	129.2315	
2.0000	0	1.0000	117.6946	
2.0000	0	2.0000	109.9452	
2.0000	1.0000	-2.0000	129.2315	
2.0000	1.0000	-1.0000	109.9452	
2.0000	1.0000	0	100.6707	
2.0000	1.0000	1.0000	95.4869	
2.0000	1.0000	2.0000	92.2266	
2.0000	2.0000	-2.0000	78.4630	
2.0000	2.0000	-1.0000	78.4630	
2.0000	2.0000	0	78.4630	
2.0000	2.0000	1.0000	78.4630	
2.0000	2.0000	2.0000	78.4630	

List of symbols and acronyms

A thickness parameter

A, B, C direction cosines of vibration direction

a ultrasound amplitude

a_0 lattice constant

α angle between scattering vector and ultrasound wave vector

$\mathbf{b}_1$, $\mathbf{b}_2$, $\mathbf{b}_3$ reciprocal lattice base vectors

β asymmetry angle

C, C_s x-ray polarization factor

c vacuum velocity of light (ultrasound wave speed only in table 4.1)

c_{11}, c_{12}, c_{44} elastic moduli

χ dielectric susceptibility, atomic susceptibility

χ_{hkl} dielectric susceptibility for (hkl) reflection

χ_0 dielectric susceptibility for (hkl) = (000)

χ_{sat} dielectric susceptibility for a satellite reflection

δ angle between ultrasound wave vector and scattering vector if out of scattering plane

Δ relation between extinction length and ultrasound wave length

$\Delta G_{\|}$ parallel component of scattering vector

$\Delta G_{\perp}$ perpendicular component of scattering vector

$\Delta\theta$ deviation from Bragg angle

$\Delta\theta_n$ angular position of satellite n

$\Delta\theta^{HW}$ FWHM of a satellite reflection

d_{hkl} lattice spacing

dT deviation parameter (in theta)

E x-ray energy

$\mathbf{E}$, $\mathbf{E}_{hkl}$, $\mathbf{E}_m$, $\mathbf{E}_n$, $\mathbf{E}_0$ electric field vector

ε normal strain

ε angle between ultrasound wave vector and scattering plane

Λ extinction length

Λ_{sat} extinction length satellite

F_{hkl} structure factor

f atomic scattering factor

f_n scattering factor of atom n

f_0 atomic scattering factor without correction

f′ anomalous dispersion correction of atomic scattering factor

f″ imaginary part of atomic scattering factor

$\mathbf{G}$, $\mathbf{G}_{hkl}$ reciprocal lattice vector, scattering vector

$\mathbf{G}_{Mono}$, $\mathbf{G}_{Ana}$ scattering vector of monochromator and analyzer

γ shearing strain

γ_h, γ_0 asymmetry parameters

h Planck's constant

h, k, l Miller indices

I (relative) intensity

IM time-dependent intensity distribution

J_0 Bessel function of order 0

J_n Bessel function of order n

K absolute value of refracted x-ray wave vector

$\mathbf{k}$ x-ray wave vector

$\boldsymbol{\kappa}$ ultrasound wave vector

$\mathbf{k}_i$, $\mathbf{k}_f$ initial and final wave vector

$\mathbf{k}_{hkl}$ x-ray wave vector for (hkl) reflection

$\mathbf{k}_0$ absolute value of x-ray wave vector for (hkl) = (000)

l, m, n direction cosines of ultrasound propagation direction

λ x-ray wavelength

λ_{usw} ultrasound wavelength

M time-modulating intensity component

μ absorption coefficient

n_1, n_2, n_3 (hkl) for crystal surface normal

ν x-ray frequency

ω angular ultrasound frequency

ω scanning angle perpendicular to Ewald sphere

φ scanning angle along Ewald sphere

φ angle between crystal surface normal and ultrasound wave vector (chapter 6)

ψ angle between crystal surface parallel and ultrasound wave vector

p_1, p_2, p_3 (hkl) for crystal surface parallel

Γ pendellösungs-length

r propagation vector

ρ density

σ normal stress

τ shearing stress

T, t_0 crystal thickness

t time

θ Bragg angle

uswfreq ultrasound frequency (in SIMSAT)

uswh, uswk, uswl (hkl) for ultrasound propagation direction (in SIMSAT)

u, v, w displacement components of elastic wave propagation

$\mathbf{v}_1$, $\mathbf{v}_2$, $\mathbf{v}_3$ ultrasound velocities

V volume of crystallographic elemental cell

x, y, z coordinates of elastic wave propagation

x_n, y_n, z_n coordinates of atom n in crystallographic unit cell

Comments:

a) Miller indices hkl are written in brackets (hkl) to distinguish clearly from the text.
b) Directions in real crystal space are denoted in brackets [xyz], the direction of a vector in reciprocal space pointing to a reciprocal lattice point (hkl) is denoted as the (hkl)-direction.
c) Vector notation '→' and **bold letters** are used synonymously to mark a vector.

ADC amplitude-to-digital converter

AE acousto-electric

AIM accumulation interface memory

DS Dispersion surface

FWHM full width at half maximum

HFVAW high frequency volume acoustic wave

ID insertion device

La Laue point

Lo Lorentz point

MCA multi channel analyzer

LFVAW low frequency volume acoustic wave

RF radio frequency

SAW surface acoustic wave

SIMSAT program code ‘simulation of satellites’

TAC time-to-amplitude converter

VAW volume acoustic wave

XAR x-ray acoustic resonance

Bibliography

[Ash 76] N.W. Ashcroft and N.D. Mermin, Solid state physics, Saunders College Publishing, 1976

[Bro 89] I.N. Bronstein and K.A. Semendjajew, Taschenbuch der Mathematik, Verlag Harri Deutsch, 1989

[Dal 02a] T. d'Almeida, M. Di Michiel, M. Kaiser, T. Buslaps and A. Fanget, Time-resolved x-ray diffraction measurements on CdS shocked along the c axis, Journal of Applied Physics 92(3), 1715 (2002)

[Dal 02b] T. d'Almeida, M. Kaiser, M. Di Michiel, T. Buslaps, A. Fanget, Time-resolved x-ray diffraction on laser-shocked crystals, Surface scattering and diffraction for advanced metrology II, Proceedings of SPIE 4780, 176 (2002)

[Exp 03] http://www.esrf.fr/exp_facilities/id15a/handbook/handbook.html

[Fox 31] G.W. Fox and P.H. Carr, The effect of piezo-electric oscillation on the intensity of x-ray reflections from quartz, Phys. Rev. 37, 1622 (1931)

[Gia 85] C. Giacovazzo and H.L. Monaco, Fundamentals of crystallography, Oxford University Press, 1985/1994

[Hoc 97] R. Hock, Beugung von Neutronen und hochenergetischer Röntgenstrahlung an schwingenden Silicium Kristallen, Habilitationsschrift Universität Würzburg, 1997

[Lis 98b] K.-D. Liss, A. Royer, T. Tschentscher, P. Suortti and A.P. Williams, On high-resolution reciprocal-space mapping with a triple-crystal diffractometer for high-energy x-rays, J. Synchrotron Rad. 5, 82 (1998)

[Lis 03] K.-D. Liss, M. Kaiser, J. Hlinka, F. Denoyer, R. Hock, R. Currat, Kinetics of the field induced commensurate to ferro-electric phase transition in thiourea, J. Phys. D: Appl. Phys. 36, A172 (2003)

[Mat 02] MatLab, The language of technical computing, Version 6.5.0, 2002

[Mer 91] G. Merziger und T. Wirth, Repetitorium der höheren Mathematik, Feldmann Verlag, 1991

[Sak 94] J.J. Sakurai, Modern quantum mechanics, Addison-Wesley, 1994

[War 69] B.E. Warren, X-ray diffraction, Dover Publications, 1969/1990

[XOP 02] X-ray oriented programs, European Synchrotron Radiation Facility, 2002; and: M. Sanchez del Rio, XOP: A multiplatform graphical user interface for synchrotron radiation spectral and optics calculations, SPIE proceedings 3152, 148 (1997)

Dynamical diffraction theory

[Aut 61] A. Authier, Etude de la transmission anormale des rayons x dans les cristaux de silicium, Bull. Soc. Franç. Minér. Crist. LXXXIV, 51 (1961)

[Bat 64] B.W. Batterman and H. Cole, Dynamical Diffraction of x-rays by perfect crystals, Reviews of modern physics 36(3), 681 (1964)

[Bru 76] O. Brümmer und H. Stephanik, Dynamische Interferenztheorie, Akademische Verlagsgesellschaft Geest & Portig K.-G., 1976

[Dar 14a] C.G. Darwin, The theory of x-ray reflection, Phil. Mag. 27, 315 (1914)

[Dar 14b] C.G. Darwin, The theory of x-ray reflection, Phil. Mag. 27, 675 (1914)

[Ewa 16a] P.P. Ewald, Zur Begründung der Kristalloptik, Teil I Dispersionstheorie, Ann. Phys. 49, 1 (1916)

[Ewa 16b] P.P. Ewald, Zur Begründung der Kristalloptik, Teil II Theorie der Reflexion und Brechung, Ann. Phys. 49, 117 (1916)

[Ewa 17] P.P. Ewald, Zur Begründung der Kristalloptik, Teil III Die Kristalloptik der Röntgenstrahlen, Ann. Phys. 54, 519 (1917)

[Hae 01] J. Härtwig, Hierarchy of dynamical theories of x-ray diffraction for deformed and perfect crystals, J. Phys. D: Appl. Phys. 34(10A), A70 (2001)

[Lau 31] M. von Laue, Die Theorie der Röntgenstrahlinterferenzen in neuer Form, Ergebn. Exakt. Naturwiss. 10, 133 (1931)

[Pin 78] Z.G. Pinsker, Dynamical scattering of x-rays in crystals (Springer series in solid-state sciences; volume 3), Springer-Verlag, 1978

[Sla 58] J.C. Slater, Interaction of waves in crystals, Reviews of modern physics 30(1), 197 (1958)

[Tan 76] B.K. Tanner, X-ray diffraction topography (International series in the science of the solid state; volume 10), Pergamon Press, 1976

[Zac 45] W.H. Zachariasen, Theory of x-ray diffraction in crystals, John Wiley and Sons Inc., 1945

X-ray diffraction on volume acoustic waves (VAW):

Acousto-electric phonons (AE)

[Möh 70] W. Möhling, G.O. Müller, H. Peibst, and E. Schnürer, X-ray diffraction analysis of acoustoelectric phonons, Phys. Stat. Sol. (a) 2, 725 (1970)

[Köh 70] R. Köhler, W. Möhling, and H. Peibst, Intensity relations in Laue case reflections of perfect crystals containing nearly monochromatic lattice vibrations, Phys. Stat. Sol. 41, 75 (1970)

[Lem 70] H. Lemke, G.O. Müller, and E. Schnürer, Acousto-electric phonon distributions measured by X-ray Brillouin scattering, Phys. Stat. Sol. 41, 539 (1970)

[Kie 73] J. Kies, R. Köhler, W. Möhling und H. Peibst, Untersuchungen zum Übergang vom dynamischen zum kinematischen Reflexionsvermögen, Z. Naturforsch. 28 a, 610 (1973)

[Köh 73] R. Köhler, W. Möhling, and H. Peibst, Mean acoustoelectric frequencies as determined by x-ray diffraction, Phys. Stat. Sol. (b) 56, K21 (1973)

[Köh 74a] R. Köhler, W. Möhling, and H. Peibst, Influence of acoustic lattice vibrations on dynamical X-ray diffraction, Phys. Stat. Sol. (b) 61, 173 (1974)

[Köh 74b] R. Köhler, W. Möhling, and H. Peibst, Evaluation of acoustoelectric wave vectors and amplitudes from X-ray diffraction experiments, Phys. Stat. Sol. (b) 61, 439 (1974)

[Car 71] D.G. Carlson, A. Segmüller, E. Mosekilde, H. Cole, and J.A. Armstrong, X-ray diffraction from piezoelectrically amplified shear waves in the 50-GHz range, Appl. Phys. Lett. 18(8), 330 (1971)

[LeR 75] S.D. LeRoux, R. Colella, and R. Bray, X-ray diffraction studies of acoustoelectrically amplified phonon beams, Phys. Rev. Lett. 35(4), 230 (1975)

[LeR 76] S.D. LeRoux, R. Colella, and R. Bray, Effect of acoustoelectric phonons on anomalous transmission of x-rays, Phys. Rev. Lett. 37(16), 1056 (1976)

[Col 82] R. Colella, Multiple Diffraction of x-rays, Z. Naturforsch. 37a, 437 (1982)

[Cha 83] L.D. Chapman, R. Colella, and R. Bray, X-ray diffraction studies of acoustoelectrically amplified phonons, Phys. Rev. B 27(4), 2264 (1983)

X-ray acoustic resonance (XAR)

[Ent 77] I.R. Entin, Effect of resonant suppression of the anomalous transmission of x-rays by ultrasound, JETP Lett. 26(5), 269 (1977)

[Ent 78a] I.R. Entin, E.V Suvorov. N.P. Kobelev, and Ya.M Soifer, X-ray acoustic resonance in a perfect silicon crystal, Sov. Phys. Solid State 20(5), 754 (1978)

[Ent 78b] I.R. Entin, Theoretical and experimental study of x-ray acoustic resonance in perfect silicon crystals, Phys. Stat. Sol. (b) 90, 575 (1978)

[Ent 79] I.R. Entin, Dynamic diffraction of x-rays by a crystal with a periodic displacement field, Sov Phys. JETP 50(1), 110 (1979)

[Ent 81] I.R. Entin and K.P. Assur, Silicon-crystal rocking curves under x-ray acoustic resonance conditions, Acta Cryst. A 37, 769 (1981)

[Ent 88a] I.R. Entin and I.A. Smirnova, The effect of x-ray beam intensity oscillations as a function of the amplitude of ultrasound excited in a crystal, Phys. Stat. Sol. (a) 106, 339 (1988)

[Ent 91] I.R. Entin, V.I. Khrupa, and O.V. Petrosyan, Resonance acoustic method of high-precision x-ray structure factor determination in perfect and slightly imperfect silicon, Phys. Stat. Sol. (a) 127, 321 (1991)

[Khr 91a] V.I. Khrupa and I.R. Entin, Effect of structural distortions on the spatial distribution of the intensity of diffracted beam under x-ray acoustic resonance conditions, Sov. Phys. Solid State 33(6), 1023 (1991)

[Nos 93] V.L Nosik, Theoretical Investigation of X-ray Acoustic Resonance in Ideal Crystals, Cryst. Rep. 38(2), 158 (1993)

[Iol 95a] E.M. Iolin, E.A. Raitman, V.N Gavrilov, B.N. Kuvaldin and L.L. Rusevich, The effect of ultrasound on the diffraction in a deformed crystal under the conditions of x-ray acoustic resonance, J. Phys. D: Appl. Phys. 28, A281 (1995)

High frequency volume acoustic waves (HFVAW)

[Ass 82] K.P. Assur and I.R. Entin, Effect of ultrasonic vibrations on dynamic diffraction: the Bragg geometry, Sov. Phys. Solid State 24(7), 1209 (1982)

[Ent 84] I.R. Entin and I.A. Puchkova, Oscillatory dependence of the intensity of x-ray reflections on the amplitude of ultrasound excited in a crystal, Sov. Phys. Solid State 26(11), 1995 (1984)

[Ent 88b] I.R. Entin, Dynamical and Kinematical X-Ray Diffraction in Crystals Strongly Disturbed by Ultrasonic Vibrations, Phys. Stat. Sol. (a) 106, 25 (1988)

[Khr 91b] V.I. Khrupa, I.R. Entin, and L.I. Datsenko, On the Transition of the Dynamical Case of X-Ray Diffraction to the Kinematical One in Perfect and Real Silicon Crystals Distorted by Ultrasound, Phys. Stat. Sol. (a) 125, 451 (1991)

[Nos 91a] V.L. Nosik, Theory of dynamic diffraction of x-rays in the Laue case in a crystal distorted by ultrasound. I. Four-wave approximation, Sov. Phys. Crystallogr. 36(5), 610 (1991)

[Nos 91b] V.L. Nosik, Theory of dynamic diffraction of x-rays in the Laue case in a crystal distorted by ultrasound. II. Integral reflecting capacity of a vibrating crystal, Sov. Phys. Crystallogr. 36(5), 615 (1991)

[Ent 85] I.R. Entin, On the Suppression of X-Ray Anomalous Transmission by Acoustic Oscillations, Phys. Stat. Sol. (b) 132, 355 (1985)

[Pol 87] I.V Polikarpov and V.V. Skadorov, X-Ray Dynamical Diffraction in Crystals Being Subjected to the Action of Ultrasonic Waves, Phys. Stat. Sol. (b) 143, 11 (1987)

[Pol 88] I.V Polikarpov and V.V. Skadorov, X-Ray Bragg Dynamical Diffraction in Crystals Weakly Deformed by Ultrasonic Waves, Phys. Stat. Sol. (b) 149, 435 (1988)

[Pol 94] I.V. Polikarpov, V. Panov and H.D. Bartunik, Dynamical Adjustment of Crystal Reflectivity by Large-Amplitude Ultrasonic Excitation for Synchrotron X-ray Monochromatization, J. Appl. Cryst. 27, 453 (1994)

[Pol 96] I. Polikarpov, X-ray diffraction in crystals in the presence of laser-induced dynamic gratings, J. Phys. D: Appl. Phys. 29, 2148 (1996)

[Pol 97] I. Polikarpov and E. Zolotoyabko, Effect of absorption on dynamical Bragg diffraction of x-rays on a crystal modulated by strong ultrasound, J. Phys. D: Appl. Phys. 30, 2591 (1997)

[Iol 95b] E.M. Iolin, Rapid Suppression and Modulation of the Diffracted Beam in a Single Crystal Excited by Ultrasound, Acta Cryst. A51, 897 (1995)

[Pol 98] I. Polikarpov and V.V. Skadorov, Resonance Time Modulation of X-ray Diffraction in Crystals Deformed by Ultrasound, J. Appl. Cryst. 31, 388 (1998)

[Iol 88] E.M. Iolin, E.A. Raitman, B.N. Kuvaldin, and E.V. Zolotoyabko, Anomalous influence of high-frequency ultrasound on radiation diffraction in deformed single crystals, Sov. Phys. JETP 67(5), 989 (1988)

[Zol 92a] E. Zolotoyabko and V. Panov, Interference of x-ray diffraction trajectories in a strained crystal undergoing ultrasonic excitation, Acta Cryst. A48, 225 (1992)

[Zol 95a] E. Zolotoyabko and B. Sander, X-ray diffraction profiles in strained crystals undergoing ultrasonic excitation: The Laue case, Acta Cryst. A51, 163 (1995)

Low frequency volume acoustic waves (LFVAW)

[Hau 75] A. Hauer and S.J. Burns, Observation of an x-ray shuttering mechanism utilizing acoustic interruption of the Borrmann effect, Appl. Phys. Lett. 27(10), 524 (1975)

[Har 67] K. Haruta, Intensity of x-rays diffracted from an elastically vibrating single-crystal plate, J. Appl. Phys. 38(8), 3312 (1967)

[Lis 97a] K.D. Liss, A. Magerl, A. Remhof and R. Hock, Ultrasound-Induced Gradient Crystals Observed by High-Energy X-rays, Acta Cryst. A53, 181 (1997)

[Lis 97b] K.D. Liss, A. Magerl, R. Hock, A. Remhof and B. Waibel, Towards a new (Q, t) regime by time-resolved X-ray diffraction: Ultrasound excited crystals as an example, Europhys. Lett. 40(4), 369 (1997)

[Lis 98] K.D. Liss, A. Magerl, R. Hock, B. Waibel, A. Remhof, The investigation of ultrasonic fields by time resolved X-ray diffraction, Proceedings of SPIE 3451, 117 (1998)

X-ray diffraction on surface acoustic waves (SAW)

[Zol 92c] E. Zolotoyabko, E. Jacobsohn, and D. Shechtman, B. Kantor and J. Salzman, Acoustic field study in layered structures by means of x-ray diffraction, J. Appl. Phys. 71(7), 3134 (1992)

[Zol 94] E. Zolotoyabko, B. Sander, Y. Komem and B. Kantor, The Ultrasound-Induced Narrowing Effect of Rocking Curves in Strained Silicon Crystals, Acta Cryst. A50, 253 (1994)

[San 95] B. Sander, E. Zolotoyabko and Y. Komem, The dynamics of rocking curves in strained (001) Si crystals undergoing ultrasonic excitation, J. Phys. D: Appl. Phys. 28, A287 (1995)

[Zol 97] E. Zolotoyabko, X-ray Diffraction from Superlattices Formed by Surface Acoustic Waves, Surf. Invest. 12, 369 (1997)

[Ros 97] D.V. Roshchupkin, I.A. Schelokov, R. Tucoulou, M. Brunel, X-ray diffraction on a multilayer mirror modulated by surface acoustic waves, Nucl. Instr. Meth. B 129, 414 (1997)

[Ros 98] D.V. Roshchupkin, R. Tucoulou, A. Masclet, M. Brunel, I.A. Schelokov, A.S. Kondakov, X-ray diffraction by standing surface acoustic waves, Nucl. Instr. Meth. B 142, 432 (1998)

[Zol 98] E. Zolotoyabko and I. Polikarpov, X-ray Bragg Diffraction in a Strong Acoustic Field, J. Appl. Cryst. 31, 60 (1998)

[Sau 98] W. Sauer, T.H. Metzger, J. Peisl, Y. Avrahami, E. Zolotoyabko, X-Ray diffraction under surface acoustic wave excitation, Physica B 248, 358 (1998)

[Sau 99] W. Sauer, M. Streibl, T.H. Metzger, A.G.C. Haubrich, S. Manus, A. Wixforth and J. Peisl, A. Mazuelas, J. Härtwig and J. Baruchel, X-ray imaging and diffraction from surface phonons on GaAs, Appl. Phys. Lett. 75(12), 1709 (1999)

[Tuc 00] R. Tucoulou, R. Pascal, M. Brunel, O. Mathon, D.V. Roshchupkin, I.A. Schelokov, E. Cattan and D. Remiens, X-ray diffraction from perfect silicon crystals distorted by surface acoustic waves, J. Appl. Cryst. 33, 1019 (2000)

[Tuc 01] R. Tucoulou and F. de Bergevin, O. Mathon, D. Roshchupkin, X-ray Bragg diffraction of $LiNbO_3$ crystals excited by surface acoustic waves, Phys. Rev. B 64, 134108 (2001)

[Zol 02] E. Zolotoyabko and J.P Quintana, Time and phase control of x-rays in stroboscopic diffraction experiments, Rev. Sci. Instr. 73(3), 1643 (2002)

Applications of ultrasound excited crystals

[Zol 92b] E. Zolotoyabko, I. Polikarpov, V. Panov and D. Schvarkov, Determination of crystal imperfection by x-ray diffraction in a strong acoustic field, J. Appl. Cryst. 25, 88 (1992)

[Zol 93] E. Zolotoyabko, B. Sander, Y. Komem, B. Kantor, Improved strain analysis in semiconductor crystals by x-ray diffractometry enhanced with ultrasound, Appl. Phys. Lett. 63(11), 1540 (1993)

[Mkr 86] A.R. Mkrtchyan, M.A. Navasardian, R.G. Gabrielyan, L.A. Kocharian and R.N. Kuzmin, Controlled Focusing of the Å Wavelength Radiation in case of the Ultrasound Modulation or Temperature Gradient, Sol. Stat. Com. 59(3), 147 (1986)

[Nos 94a] V.L. Nosik, Dynamical X-ray Focusing under Conditions of the X-ray Acoustic Resonance: I. Focusing in Perfect Crystals, Cryst. Rep. 39(4), 526 (1994)

[Nos 94b] V.L. Nosik, Dynamical X-ray Focusing under Conditions of the X-ray Acoustic Resonance: II. Focusing in an Elastically Bent Crystal, Cryst. Rep. 39(6), 887 (1994)

[Rev 95] C. Revol, J. Baruchel, D. Bellet, G. Marot, P. Théveneau and F. Zontone, A vibrating monochromator for the 'diffraction topography' beamline of the ESRF, J. Phys. D: Appl. Phys. 28, A262 (1995)

[Pol 99a] I. Polikarpov, R.T. de Oliveira and E. Zolotoyabko, Acoustically adjustable $LiNbO_3$ double-crystal monochromator for synchrotron radiation, Rev. Sci. Instr. 70(5), 2230 (1999)

[Pol 99b] I. Polikarpov and V.V. Panov, Ultrasound adjustable Laue-Laue double-crystal x-ray monochromator, J. Phys. D: Appl. Phys. 32, 2083 (1999)

[Pol 98] I. Polikarpov, R.T. de Oliveira, and C. Cusatis, Double-crystal diffractive modulator of synchrotron radiation, Rev. Sci. Instr. 69(6), 2218 (1998)

[Tuc 97] R. Tucoulou, D.V. Roshchupkin, I.A. Schelokov, M. Brunel, L. Ortega, E. Ziegler, M. Lingham, C. Mouget, S. Douillet, High frequency electro-acoustic chopper for synchrotron radiation, Nucl. Instr. Meth. B 132, 207 (1997)

[Tuc 98] R. Tucoulou, D.V. Roshchupkin, O. Mathon, I.A. Schelokov, M. Brunel, E. Ziegler and C. Morawe, High-Frequency X-ray Beam Chopper Based on Diffraction by Surface Acoustic Waves, J. Synchrotron Rad. 5, 1357 (1998)

Topography on VAW

[Sac 67] E.J. Saccocio, M.A. Lopez and K.J. Lazara, X-ray images of ultrasonic waves in a crystal, J. Appl. Phys. 38(1), 309 (1967)

[Ent 78c] I.R. Entin, Investigation of the dispersion surface of x-ray radiation in a perfect crystal by the x-ray acoustic resonance method, Sov. Phys. Solid State 20(7), 1230 (1978)

[Zhe 89] Y. Zheng, A. Zarka and B. Capelle, Pendellösung fringes in stroboscopic x-ray section topography of weakly excited quartz resonators, Acta Cryst. A 45, 275 (1989)

[Epe 96] Y. Epelboin, Simulation of synchrotron white-beam topographs. An algorithm for parallel processing: Application to the study of piezoelectric devices, J. Appl. Cryst. 29, 331 (1996)

[Epe 99] Y. Epelboin, V. Mocella and A. Soyer, Optical characteristics of synchrotron sources and their influence in the simulation of x-ray topographs, Phil. Trans. R. Soc. Lond. A 357, 2731 (1999)

[Moc 00] V. Mocella, Y. Epelboin and J.P. Guigay, X-ray dynamical diffraction: the concept of a locally plane wave, Acta Cryst. A 56, 308 (2000)

Topography on SAW

[Wha 82] R.W. Whatmore, P.A. Goddard, B.K. Tanner & G.F. Clark, Direct imaging of travelling Rayleigh waves by stroboscopic X-ray topography, Nature 299, 44 (1982)

[Zol 99] E. Zolotoyabko, D. Shilo, W. Sauer, E. Pernot and J. Baruchel, Stroboscopic x-ray topography in crystals under 10-µm-surface acoustic wave excitation, Rev. Sci. Instr. 70(8), 3341 (1999)

[Zol 98] E. Zolotoyabko, D. Shilo, W. Sauer, E. Pernot and J. Baruchel, Visualization of 10 μm surface acoustic waves by stroboscopic x-ray topography, Appl. Phys. Lett. 73(16), 2278 (1998)

[Zol 95b] E. Zolotoyabko, E. Jacobsohn, H. Bartunik, I. Polikarpov, I. Koelln, H.G. Krane, Visualization of acoustic fields in surface acoustic wave devices by means of X-ray topography, Nucl. Instr. Meth. B 97, 346 (1995)

[Moc 99] V. Mocella and Y. Epelboin, White-beam topography of Rayleigh waves: a numerical study, J. Appl. Cryst. 32, 154 (1999)

X-ray diffraction on optically excited crystals

[Sae 91] P. Saeta, J.-K. Wang, Y. Siegal, N. Bloembergen, and E. Mazur, Ultrafast Electronic Disordering during Femtosecond Laser Melting of GaAs, Phys. Rev. Lett. 67(8), 1023 (1991)

[Gle 95a] E.N. Glezer, Y. Siegal, L. Huang, and E. Mazur, Laser-induced band-gap collapse in GaAs, Phys. Rev. B 51(11), 6959 (1995)

[Sok 95] K. Sokolowski-Tinten, J. Bialkowski, and D. von der Linde, Ultrafast laser-induced order-disorder transitions in semiconductors, Phys. Rev. B 51(20), 14186 (1995)

[Gle 95b] E.N. Glezer, Y. Siegal, L. Huang, and E. Mazur, Behavior of $\chi^{(2)}$ during a laser-induced phase transition in GaAs, Phys. Rev. B 51(15), 9589 (1995)

[Hua 98] Li Huang, J. Paul Callan, Eli N. Glezer, and Eric Mazur, GaAs under Intense Ultrafast Excitation: Response of the Dielectric Function, Phys. Rev. Lett. 80(1), 185 (1998)

[Sok 98a] K. Sokolowski-Tinten, J. Bialkowski, A. Cavalleri, and D. von der Linde, Transient States of Matter during Short Pulse Laser Ablation, Phys. Rev. Lett. 81(1), 224 (1998)

[Sok 98b] K. Sokolowski-Tinten, J. Bialkowski, and M. Boing, A. Cavalleri, D. von der Linde, Thermal and nonthermal melting of gallium arsenide after femtosecond laser excitation, Phys. Rev. B III.58(18), R11805 (1998)

[Sta 94] P. Stampfli and K.H. Bennemann, Time dependence of the laser-induced femtosecond lattice instability of Si and GaAs: Role of longitudinal optical distortions, Phys. Rev. B 49(11), 7299 (1994)

[Sil 96] P.L. Silvestrelli, A. Alavi, M. Parrinello, and D. Frenkel, Ab initio Molecular Dynamics Simulation of Laser Melting of Silicon, Phys. Rev. Lett. 77(15), 3149 (1996)

[DeC 01a] M.F. DeCamp, D.A. Reis, P.H. Bucksbaum, and R. Merlin, Dynamics and coherent control of high-amplitude optical phonons in bismuth, Phys. Rev. B 64, 092301 (2001)

[Ris 97] C. Rischel, A. Rousse, I. Uschmann, P.-A. Albouy, J.-P. Geindre, P. Audebert, J.-C. Gauthier, E. Förster, J.-L. Martin & A. Antonetti, Femtosecond time-resolved X-ray diffraction from laser-heated organic films, Nature 390, 490 (1997)

[Rou 99a] A. Rousse, C. Rischel, I. Uschmann, E. Förster, P.-A. Albouy, J.-P. Geindre, P. Audebert, J.-C. Gauthier and A. Antonetti, Subpicosecond X-ray diffraction study of laser-induced disorder dynamics above the damage threshold of organic solids, J. Appl. Cryst. 32, 977 (1999)

[Rou 01] A. Rousse, C. Rischel, S. Fourmaux, I. Uschmann, S. Sebban, G. Grillon, Ph. Balcou E. Förster, J.-P. Geindre, P. Audebert, J.-C. Gauthier & D. Hulin, Non-thermal melting in semiconductors measured at femtosecond resolution, Nature 410, 65 (2001)

[Feu 01] T. Feurer, A. Morak, I. Uschmann, Ch. Ziener, H. Schwoerer, E. Förster, R. Sauerbrey, An incoherent sub-picosecond X-ray source for time-resolved X-ray-diffraction experiments, Appl. Phys. B 72, 15 (2001)

[Kul 00] G. Kulcsár, D. AlMawlawi, F.W. Budnik, P.R. Herman, M. Moskovits, L. Zhao, and R.S. Marjoribanks, Intense Picosecond X-Ray Pulses from Laser Plasmas by Use of Nanostructured "Velvet" Targets, Phys. Rev. Lett. 84(22), 5149 (2000)

[Rou 99b] A. Rousse, Dynamique atomique à l'échelle subpicoseconde : état de l'art, J. Phys. IV France 9, Pr5-57 (1999)

[Ros 99] C. Rose-Petruck, R. Jimenez, T. Guo, A. Cavalleri, C. W. Siders, F. Ráksi, J. A. Squier, B. C. Walker, K. R. Wilson & C. P. J. Barty, Picosecond-milliångstrøm lattice dynamics measured by ultrafast X-ray diffraction, Nature 398, 310 (1999)

[War 99] J. Wark, Table-top picosecond sources, Nature 398, 284 (1999)
[Sid 99] C. W. Siders, A. Cavalleri, K Sokolowski-Tinten, Cs. Tóth, T. Guo, M. Kammler, M. Horn von Hoegen, K. R. Wilson, D von der Linde, C. P. J. Barty, Detection of Nonthermal Melting by Ultrafast X-ray Diffraction, Science 286, 1340 (1999)

[Cav 00] A. Cavalleri, C. W. Siders, F. L. H. Brown, D. M. Leitner, Cs. Tóth, J. A. Squier, C. P. J. Barty, and K. R. Wilson, K Sokolowski-Tinten, M. Horn von Hoegen, and D von der Linde, M. Kammler, Anharmonic Lattice Dynamics in Germanium Measured with Ultrafast X-Ray Diffraction, Phys. Rev. Lett. 85(3), 586 (2000)

[Cav 01a] A. Cavalleri, C. W. Siders, C. Rose-Petruck, R. Jimenez, Cs. Tóth, J. A. Squier, C. P. J. Barty, and K. R. Wilson, K Sokolowski-Tinten, M. Horn von Hoegen, and D von der Linde, Ultrafast x-ray measurement of laser heating in semiconductors: Parameteres determining the melting threshold, Phys. Rev. B 63, 193306 (2001)

[Cav 01b] A. Cavalleri, Cs. Tóth, C. W. Siders, and J. A. Squier, F Ráksi, P. Forget and J. C. Kieffer, Femtosecond Structural Dynamics in VO_2 during an Ultrafast Solid-Solid Phase Transition, Phys. Rev. Lett. 87(23), 237401 (2001)

[Sok 01] K Sokolowski-Tinten, C. Blome, C. Dietrich, A. Tarasevitch, M. Horn von Hoegen, and D von der Linde, A. Cavalleri, J. A. Squier, M. Kammler, Femtosecond X-Ray Measurement of Ultrafast Melting and Large Acoustic Transients, Phys. Rev. Lett. 87(22), 225701 (2001)

[Sch 96] R.W. Schoenlein, W.P. Leemans, A.H. Chin, P. Volfbeyn, T.E. Glover, P. Balling, M. Zolotorev, K.-J. Kim, S. Chattopadhyay, C.V. Shank, Femtosecond X-ray Pulses at 0.4 Å Generated by 90º Thomson Scattering: A Tool for Probing the Structural Dynamics of Materials, Science 274, 236 (1996)

[Lee 96] W.P. Leemans, R.W. Schoenlein, P. Volfbeyn, A.H. Chin, T.E. Glover, P. Balling, M. Zolotorev, K.-J. Kim, S. Chattopadhyay, and C.V. Shank, X-Ray Based Subpicosecond Electron Bunch Characterization Using 90º Thomson Scattering, Phys. Rev. Lett. 77(20), 4182 (1996)

[Sch 00] R.W. Schoenlein, S. Chattopadhyay, H.H.W. Chong, T.E. Glover, P.A. Heimann, C.V. Shank, A.A. Zholents, M.S. Zolotorev, Generation of Femtosecond Pulses of Synchrotron Radiation, Science 287, 2237 (2000)

[Lar 98] J. Larsson, P.A. Heimann, A.M. Lindenberg, P.J. Schuck, P.H. Bucksbaum, R.W. Lee, H.A. Padmore, J.S. Wark, R.W. Falcone, Ultrafast structural changes measured by time-resolved X-ray diffraction, Appl. Phys. A 66, 587 (1998)

[Lin 00] A.M. Lindenberg, I.Kang, S.L. Johnson, T. Missalla, P.A. Heimann, Z. Chang, J. Larsson, P.H. Bucksbaum, H.C. Kapteyn, H.A. Padmore, R.W. Lee, J.S. Wark, and R.W. Falcone, Time-Resolved X-Ray Diffraction from Coherent Phonons during a Laser-Induced Phase Transition, Phys. Rev. Lett. 84(1), 111 (2000)

[Rei 01] D.A. Reis, M.F. DeCamp, P.H. Bucksbaum, R. Clarke, E. Dufresne, M.Hertlein, R. Merlin, R. Falcone, H. Kapteyn, M.M. Murnane, J. Larsson, Th. Missalla, and J.S. Wark, Probing Impulsive Strain Propagation with X-Ray Pulses, Phys. Rev. Lett. 86(14), 3072 (2001)

[Buc 99] P.H. Bucksbaum, R. Merlin, The phonon Bragg switch: a proposal to generate sub-picosecond X-ray pulses, Solid State Communications 111, 535 (1999)

[DeC 01b] M.F. DeCamp, D.A. Reis, P.H. Bucksbaum, B. Adams, J.M Caraher, R. Clarke, C.W.S. Conover, E.M. Dufresne, R. Merlin, V. Stoica & J.K. Wahlstrand, Coherent control of pulsed X-ray beams, Nature 413, 825 (2001)

[Kra 01] F. Krausz and C. Spielmann, Slick switching of X-rays, Nature 413, 784 (2001)

[Bel 02] C. Belzile and J.C. Kieffer, C.Y. Cote, T. Oksenhendler and D. Kaplan, Jitter-free subpicosecond streak cameras (invited), Rev. Sci. Instr. 73(3), 1617 (2002)

[Ada 02] B.W. Adams, Manipulation and detection of x-rays on the femtosecond time scale (invited), Rev. Sci. Instr. 73(3), 1632 (2002)

[Chu 95] F.N. Chukhovskii and E. Förster, Time-Dependent X-ray Bragg Diffraction, Acta Cryst. A51, 668 (1995)

[War 99] J.S. Wark and R.W. Lee, Simulations of femtosecond X-ray diffraction from unperturbed and rapidly heated single crystals, J. Appl. Cryst. 32, 692 (1999)

Acknowledgments

I would like to express my thanks to all the people who have contributed to make this thesis possible. My deep gratitude goes especially to Professor Dr. Rainer Hock for accepting to be the academic advisor of this thesis. His constant support and readiness for scientific discussions cannot be overestimated. I am much obliged to Professor Dr. Andreas Magerl for receiving me in his group and to Professor Dr. Hartmut Fuess for co-refereeing this thesis.

Many thanks for the constant support and help to all the staff members of beamline ID 15 at the European Synchrotron Radiation facility in Grenoble, where this work was carried out. Special thanks to Dr. Thierry d'Almeida for a lot of interesting discussions and who also proved a true friend in troubled times at the beamline. I would also like to thank Dr. Klaus-Dieter Liss for his support. His excellent experimental skills contributed a lot to make the experiments on ID 15 successful.
I warmly thank Prof. Dr. Christian Bressler for the proofreading of the manuscript.

Mein ganz besonderer Dank geht an meine Eltern, ohne deren Unterstützung diese Arbeit nicht möglich gewesen wäre. Je voudrais aussi remercier Mlle Carole Perlongo pour tout le support pendant cette période assez difficile.

Thanks

Maik Kaiser

Geburtsdatum: 01. März 1970

Geburtsort: Mainz

Nationalität: deutsch

Chemin de Boston 19
1004 Lausanne
Schweiz
Tel. +33663715642
Email: maik.kaiser@epfl.ch

Bildungsgang

1999	Diplom in Physik, Technische Universität Darmstadt
1993	Vordiplom in Physik, Technische Universität Darmstadt
1990-91	Studium der Elektrotechnik, Technische Universität Darmstadt
1989	Abitur, Staatliches Gymnasium zu St. Katharinen, Oppenheim

Beruflicher Werdegang

Seit 07/1999 Doktorarbeit am Lehrstuhl für Kristallographie und Strukturphysik der Friedrich-Alexander-Universität Erlangen-Nürnberg und an der European Synchrotron Radiation Facility, Grenoble, Frankreich:

Hochenergie-Röntgenbeugung an ultraschallangeregten Kristallen

- Hochenergie-und hochauflösende Röntgenbeugung am Dreiachsendiffraktometer
- Zeitaufgelöste Röntgenbeugung ultraschallangeregter Kristalle im 200 ps-Bereich
- Dynamische Röntgenbeugung periodisch modulierter Kristalle
- Simulation zeitunabhängiger und zeitabhängiger Intensitätsverteilungen gebeugter Röntgenstrahlung an ultraschallangeregten Kristallen
- Schockwellen in Kristallen angeregt durch gepulste Hochleistungslaser
- Elektrisch angeregte Phasenübergänge in Kristallen bei tiefen Temperaturen

1997-1998 Diplomarbeit am Fachbereich Materialwissenschaft, Technische Universität Darmstadt, und am Hahn-Meitner-Institut (HMI), Berlin:

Struktur und Morphologie von WS_2 van der Waals-Epitaxieschichten

- Preparation und in-situ Charakterisierung molekularstrahl-epitaktisch (MBE) gewachsener Schichtlagen im Ultrahochvakuum (UHV)
- Elektronenspektroskopie für chemische Analyse (ESCA; XPS, UPS)
- Niederenergetische Elektronenbeugung (LEED) gitterfehlangepasster Schichten
- Röntgenbeugung an dünnen Schichten (Zweikreis-und Vierkreisdiffraktometer)
- Rasterelektronenmikroskopie (SEM) und Rastertunnelmikroskopie (STM)
- Phasenreinheit, Morphologie, Schichtdicken, Schichtgitterkonstanten und Grenzflächenspannung dünner Schichten

Erlangen, Grenoble, Lausanne im Dezember 2003